Ole Andre Øiseth

Dynamic behaviour of cable-supported bridges subjected to strong natural wind

NTNU – Trondheim
Norwegian University of
Science and Technology

Preface

This thesis is submitted in partial fulfilment of the requirements for the degree *philosophiae doctor* at the Norwegian University of Science and Technology (NTNU), Trondheim, Norway. The work has been carried out at the Faculty of Engineering Science and Technology, Department of Structural Engineering, under the supervision of Professor Ragnar Sigbjörnsson and Associate Professor Anders Rönnquist

Abstract

This thesis discusses wind-induced dynamic response of slender cable-supported bridges. The focus has been on prediction of the flutter stability limit and the buffeting response in strong winds. The thesis consists of journal papers that are either submitted or published.

Multimode flutter has recently been shown to be the governing phenomenon for the aeroelastic stability limit of long-span cable-supported bridges. In this thesis the multimode flutter phenomenon is thoroughly studied. It is concluded that the most important indicator of possible multimode effects is the shape-wise similarity of the vertical and torsional vibration modes since flutter will not occur if the still-air vibration modes are shape-wise dissimilar. When the stability limit of a long-span bridge is assessed, the shape-wise similarity of all possible mode combinations should be evaluated first. Then the system should be grouped into uncoupled subsystems. The subsystem involving the still-air torsional vibration mode with the lowest natural frequency will most likely provide the lowest stability limit. If this subsystem consists of more than two vibration modes, multimode effects will occur. The reduction of the stability limit will be small if the shape-wise similarities of the vibration modes are not of the same order of magnitude, or if the system consists of two torsional and one vertical mode, and the torsional modes are well separated. If these conditions are not fulfilled, the flutter stability limit should be assessed using a multimode approach.

The self-excited forces are particularly important when the wind-induced dynamic response or the flutter stability limit is assessed for slender bridges. The self-excited forces can be modelled simply using quasi-steady theory. Since the quasi-steady theory is frequency independent, the model may be used in both the time and frequency domains. However, it is well known that the traditional quasi-steady theory may severely underestimate the flutter stability limit since no aerodynamic torsional damping is introduced into the model. In this thesis a novel modified quasi-steady theory is suggested. The method takes advantage of that the self-excited forces are most important at the natural frequencies of the combined structure and flow system. This implies that curves providing a frequency-independent description of the self-excited forces can be fitted to the experimental data in the important reduced-frequency range corresponding to the natural frequencies of the system. The suggested model has been applied for the Hardanger Bridge in a comprehensive case study, and it is concluded that the model provides wind-induced response and flutter stability limits of good accuracy.

Simplified methods for assessment of the flutter stability limit are still considered important in preliminary designs and when designing medium-span bridges where multimode effects will not reduce the flutter stability limit significantly. The most popular approach is still Selberg's formula, published almost 50 years ago. Selberg's formula provides the flutter stability limit with reasonable accuracy if the aerodynamic properties of the cross section are similar to those of a flat plate, and the vertical and torsional modes have an identical shape. In this thesis an alternative analytical approach to Selberg's formula is suggested. The formulae presented are based on the fundamental flutter equations, and the simplified solution is developed by introducing two assumptions. (*i*) The quasi-steady model for the self-excited forces outlined above is introduced in the equations of motion. (*ii*) The critical frequency is assumed to be on the torsional branch of the solution system and can be approximated by the uncoupled system of equations. It is demonstrated that by introducing these two approximations, the complexity of the flutter equations is significantly reduced, and if the still-air damping is neglected, a closed-form solution of the flutter stability limit may be obtained. The formula presented is very similar to Selberg's formula, but contains coefficients taking into account the actual aerodynamic properties of the cross section and the possible imperfect shape-wise similarity of the vibration modes. The formulae presented are tested for a range of hypothetical structural configurations, in addition to the properties of a few well-known bridges, considering the aerodynamic properties of two cross sections. It is concluded that the proposed formulae provide results of adequate accuracy, and that they can be regarded as engineering approximations of the critical flutter velocity.

This thesis also discusses unsteady modelling of the self-excited forces in the time domain. A comprehensive case study, where the wind-induced dynamic response of a slender suspension bridge is assessed in the time domain, is presented. Here, the self-excited forces have been modelled, using rational functions, indicial functions, a novel modified rational function approach explained and introduced in this thesis, and a further developed modified quasi-steady theory. The quasi-steady model is a further development of the model outlined above. As explained above, in the modified quasi-steady theory suggested in this thesis, the experimental results of the aerodynamic derivatives are approximated with curves providing a frequency-independent description of the self-excited forces in the important reduced-frequency range. This implies that the self-excited forces may be accurately modelled at frequencies corresponding to one horizontal, one vertical, and one torsional vibration mode. The further development presented here is to uncouple the aeroelastic system utilizing the right- and left-hand eigenvectors. This implies that the experimental results for the aerodynamic derivatives may be accurately approximated for all the natural frequencies of the aeroelastic system. It is concluded that all the unsteady models evaluated provide an adequate description of the self-excited forces, but that the unsteady models may be

challenging to fit to the experimental data since the same coefficients are used in the expressions for the imaginary and real part of the transfer functions, which implies that two sets of data have to be approximated using the same coefficients. It is also seen that the quasi-steady model presented provides satisfying results. The results are in fact of higher accuracy than when some of the unsteady models are applied.

As modern bridges become longer, slenderer and lighter, the use of nonlinear methods to evaluate the dynamic response may become necessary. This implies that time domain assessment of the wind-induced dynamic response will become more important in the future. When nonlinearities are introduced into the model, it is an advantage to use the degrees of freedom of the element model directly and not use still-air vibration modes as generalized degrees of freedom. This can be done modelling the self-excited forces at distinct points along the girder, but this will imply that a huge amount of convolution integrals have to be evaluated at each time step. Another approach is suggested in this thesis. The starting point is a traditional beam element with twelve degrees of freedom, where the convolution integrals are added as aerodynamic degrees of freedom in each node. This implies that the convolution integrals do not need to be evaluated explicitly, since their value is calculated just like the response of the structure. Four different aeroelastic beam elements have been developed and tested. It is concluded that the elements provide wind-induced dynamic response and flutter stability limits that correspond very well to results predicted by the traditional multimode approach in the frequency domain.

Accurate modelling of the wind field is a crucial issue when predicting the dynamic response of long-span bridges. The wind field is most commonly modelled as a multivariate Gaussian stationary and homogeneous stochastic process, where the turbulence components are assumed independent. Since the wind field is affected by the roughness at the site, the turbulence components will become correlated, since three-dimensional eddies are generated by the roughness elements, but this effect is normally neglected. In this thesis the measurements of the fluctuating wind carried out at the Sotra Bride in 1975 are reinvestigated. The cross-spectral densities of all the turbulence components have been determined using auto regressive (AR) models. It is concluded that the cross-spectral density of the u and w components may have a significant influence on the dynamic response, in particular for structures with low natural frequencies. However for the bridge considered, reasonable estimates of the wind-induced dynamic response will still be obtained if the cross-spectral density of the u and w components is neglected, but the accuracy of the modelling will be improved if it is included.

Acknowledgements

Table of contents

Introduction

Since the infamous Tacoma Narrows Bridge collapse in 1940 [1, 2], wind-induced dynamic response has been a crucial issue when designing slender bridges. This incident made bridge engineers all over the world realize that cable-supported bridges may collapse during moderate winds, due to fluid-structure interaction. As a consequence, wind tunnel tests became a natural part of bridge design [3, 4]. As modern bridge design gets slenderer, lighter, and longer, the demand for more accurate and reliable methods to predict wind-induced dynamic response is increasing. This is the reason that wind-induced dynamic response of bridges is still an interesting research subject today, over 70 years after the collapse of the Tacoma Narrows Bridge.

Prediction of wind-induced dynamic response is summarized in Figure 1.
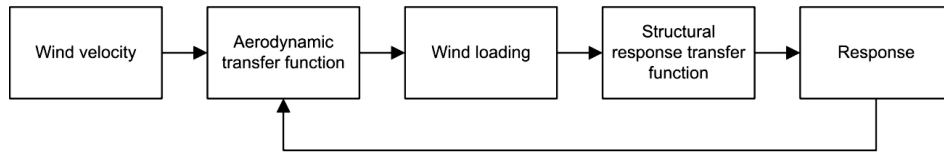
Figure 1: Prediction of wind-induced dynamic response, [5]

Since wind fluctuations are random in nature, prediction of wind-induced dynamic response implies that the statistical properties of the response have to be obtained from the known statistical properties of the wind field. The statistical properties of the wind field are represented by spectral densities in the frequency domain. When assessing the wind-induced response for civil engineering structures, one often relies on existing spectral densities that may be calibrated such that they become suitable for the site in question; for instance, see [6, 7]. There are several expressions for spectral densities, and perhaps the most well known is the Von Karman spectral density that was developed for laboratory turbulence by Von Kármán [8] and suggested by Harris in 1968 for wind engineering applications, see [9]. Another well-known expression for the spectral density of longitudinal turbulence has been suggested by Davenport [10]. The expression is empirical, and it is well known that this spectral density does not give satisfying results when the frequency tends to zero. Kaimal [11] has also suggested an expression for spectral density that has very frequently been used. Solari and Piccardo [12] have done a comprehensive review of existing expressions for spectral densities. They have gathered 14 expressions for the power spectral density of the u component (along the mean wind direction), 9 expressions for the w component (across wind vertically) and 6 expressions for the v component (across wind horizontally). When it comes to the cross-spectral density of the u and w components, only four cross-spectral

densities have been found. The main reason for this is that the spectral density of the u component is most frequently used in response analysis, and there is therefore more information in the literature on this spectral density than, for instance, for the cross-spectral density of the u and w components. Only the u and w components are usually considered for bridges, assuming the cross-spectral density of the components is negligible, e.g., [13-17], but there are some analysis where the cross-spectral density has been included [18-20]. It is stated by Simiu and Scanlan [16] that limited data presently suggest that this is a conservative assumption, but that knowledge of these quantities in applications can improve accuracy. Minh et.al [20] conclude that for the particular case evaluated, the vertical response is overestimated; the torsional response is underestimated, while the horizontal response remains unchanged if the cross-spectral density of the u and w components is neglected.

In addition to the spectral and cross-spectral densities of the u and w components at one point, the spatial properties of the wind field must be considered. On an empirical basis Davenport [21] suggested an exponential expression for the normalized co-spectral density and a zero-phase spectrum

$$\psi_n\left(\Delta m, \omega\right) = \exp\left(-C_{n,m} \frac{\Delta m \omega}{V}\right) \tag{1}$$

Here, $n \in \{u, v, w\}$, $m \in \{x, y, z\}$. This expression is very simple, but it contains two well-known inconsistencies [22-24]. (1) The normalized co-spectral density is positive for all separations, which conflicts with the definition of the turbulence components with a zero mean value. (2) When the frequency tends to zero, the co-spectral density tends to unity. This implies that the turbulence components at two distinct points become fully coherent, which in reality is impossible. Krenk [23] has suggested a modified exponential format assuming locally isotropic turbulence, where the inconsistencies mentioned above are avoided. There are also other alternatives; see [12], where several papers on this matter have been cited. In the time domain, the spectral densities are used to generate time series of the fluctuating wind. The time series can for instance be obtained using Monte Carlo methods, e.g., [25-33] or ARMA methods e.g., [34, 35].

When the properties of the wind field are established, either in terms of cross-spectral densities in the frequency domain or in the time domain in terms of simulated time series of the fluctuating wind at distinct points in space, the aerodynamic load must be obtained. This is usually done through wind tunnel testing with a scaled model. The most popular approach is to use a section model [4], which is a rigid scaled model of the girder supported by a system of springs at each end. The section model may move horizontally, vertically, and rotate. Another alternative is to use a taut strip model [36-38]. This is basically two tensioned strings that cross the wind tunnel. A flexible scaled

2

model of the bridge deck is attached to these strings, which implies that the strings introduce stiffness, while the mass comes mainly from the flexible model of the girder. The third option is to use a scale model of the whole bridge [36, 39, 40]. The wind loading normally considered for a horizontal girder is shown in Figure 2
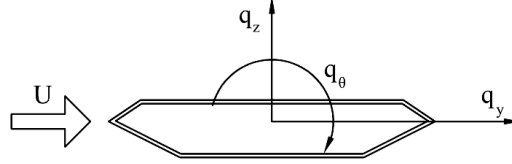
Figure 2: Wind loading acting on a cross section of the bridge deck

As can be seen from the figure, there are three load components acting on the girder. Since the girder is horizontal, only the u and w components of the wind field are relevant to the wind loading. The transfer function outlined in Figure 1 can be defined in both the frequency domain and the time domain. In the frequency domain the cross-spectral density matrix of the wind loading may be expressed as

$$\mathbf{S_q}\left(\omega, \Delta x\right) = \mathbf{B}_q\left(\omega\right)\mathbf{S_u}\left(\omega, \Delta x\right)\mathbf{B}_q^*\left(\omega\right) \tag{2}$$

Here, the matrix $\mathbf{S_u}$ contains the auto and cross-spectral densities of the u and w components. The matrix $\mathbf{B_q}$ contains the aerodynamic transfer functions that are functions of frequency and dependent on the mean wind velocity and the dimensions and aerodynamic properties of the girder. The contents in matrix $\mathbf{B_q}$ can be obtained from wind tunnel tests using one of the approaches outlined above. If the aerodynamic model has been linearized, the time domain counterpart of Eq. (2) can, be written as.

$$\mathbf{q}\left(t\right) = \int_{-\infty}^{t} \mathbf{b}_q\left(t - \tau\right)\mathbf{u}\left(\tau\right)d\tau \tag{3}$$

Here, $\mathbf{q}$ is the distributed action; $\mathbf{b_q}$ contains the aerodynamic impulse response functions, and $\mathbf{u}$ contains the velocity components. The matrices $\mathbf{b_q}$ and $\mathbf{B_q}$ constitute a pair of Fourier transforms.

After establishing the aerodynamic loading, either in terms of a cross-spectral density matrix in the frequency domain or in the time domain as time series of the aerodynamic loading at distinct points along the structure, the dynamic response may be determined using the finite element method [41-43]. The response can be obtained using the degrees of freedom of the element model directly, but presently, the most popular approach seems to be using selected still-air vibration modes as generalized degrees of freedom in the assessment of the wind-induced dynamic response.

As can be seen in Figure 1, the aerodynamic loading may be dependent on the response of the structure. This effect is due to self-excited forces that are generated by the structure's motion. The most popular unsteady model for the self-excited forces, suggested by Scanlan and Tomko [44] reads:

$$q_y^{Se} = \frac{1}{2}\rho V^2 B\left(KP_1^* \frac{\dot{r}_y}{V} + KP_2^* \frac{B\dot{r}_\theta}{V} + K^2 P_3^* r_\theta + K^2 P_4^* \frac{r_y}{B} + KP_5^* \frac{\dot{r}_z}{V} + K^2 P_6^* \frac{r_z}{B} \right)$$

$$q_z^{Se} = \frac{1}{2}\rho V^2 B\left(KH_1^* \frac{\dot{r}_z}{V} + KH_2^* \frac{B\dot{r}_\theta}{V} + K^2 H_3^* r_\theta + K^2 H_4^* \frac{r_z}{B} + KH_5^* \frac{\dot{r}_y}{V} + K^2 H_6^* \frac{r_y}{B} \right) \quad (4)$$

$$q_\theta^{Se} = \frac{1}{2}\rho V^2 B^2\left(KA_1^* \frac{\dot{r}_z}{V} + KA_2^* \frac{B\dot{r}_\theta}{V} + K^2 A_3^* r_\theta + K^2 A_4^* \frac{r_z}{B} + KA_5^* \frac{\dot{r}_y}{V} + K^2 A_6^* \frac{r_y}{B} \right)$$

Here, V is the mean wind velocity; r_n, $n \in \{y, z, \Theta\}$ symbolizes the horizontal, vertical and torsional response; ρ is the air density; B is the width of the girder, and $K = B\omega/V$ is the reduced frequency of motion. P_n^*, H_n^*, A_n^* $n \in \{1,2,...6\}$ are dimensionless aerodynamic derivatives, which are treated as cross-sectional properties that are functions of the reduced frequency of motion. The response is positive in the same directions as the forces displayed in Figure 2. The expression presented in (4) has not been developed from a theoretical point of view, since it is not possible to develop expressions for the self-excited forces for a general cross section. There are expressions for the self-excited forces for an airfoil developed by Theodorsen [45]. The expressions displayed in (4) can be viewed as an extension of the airfoil theory, and numerous studies have demonstrated the adequacy of the concept. Since the flow around the airfoil is fully attached and not separated, the accuracy of the definition shown in Eg. (4) will be questionable for very bluff cross sections. The aerodynamic derivatives are in most cases determined from wind tunnel tests, e.g., [44, 46, 47], but attempts have also been made to determine them from fluid structure interaction analysis, using computational fluid dynamics software, e.g., [48-50].

The expression presented in Eq.(4) is, strictly speaking, only valid for a single harmonic motion, but the expression can be used to predict the self-excited loading for a more general motion, applying the principle of superposition. When this assumption is introduced, it is possible to develop expressions for the self-excited forces in both the time and frequency domains. The results for the aerodynamic derivatives are known in the frequency domain. To obtain a time domain description of the self-excited forces, curves providing expressions for the transfer functions possible to Fourier transform are therefore used to approximate the experimental data. There are two branches of methods, the rational functions approach, e.g., [14, 51-53], or the indicial functions approach [54-57]. In reality the two methods are almost identical. The rational function formulation has its starting point in the frequency domain, while the indicial function formulation

considers the downwash on the cross section in the time domain. Nevertheless, an expression suitable for Fourier transforming must be selected in both cases, which implies that the expressions used to model the self-excited forces are very similar.

The aeroelastic stability limit is also extremely important when designing slender bridges. The self-excited forces may change the properties of the combined structure and flow system, either such that the system has no total stiffness (the aeroelastic stiffness is negative and equal to the structural stiffness), or such that the system is not able to dissipate energy. A brief historical review of research on flutter instability is given by Matsumoto et al. [58]. The flutter phenomenon was originally investigated in the aeronautical field [59, 60], but the collapse of the Tacoma Narrows Bridge brought the attention of bridge engineers to the phenomenon. Arne Selberg [3] developed an empirical formula for the flutter stability limit, based on work published by Bleich in 1949 and 1950. This empirical formula is well known and is still being widely used today [19]. However, since the formula does not take into account the actual aerodynamic properties of the cross section and the shape-wise similarity of the vibration modes, it may produce seriously inaccurate results. A more accurate approach is to study the properties of the equations of motions for a two-degree-of-freedom system including self-excited forces, where one vertical and torsional still-air vibration modes are used as generalized degrees of freedom. The critical velocity may then be obtained by solving the flutter equations [16, 22]. However, recent bridge projects, e.g., [18, 61], have shown that flutter where several modes interact may provide a lower stability limit than the two-mode case, which implies that the flutter stability limit must be assessed using a multimode approach [18, 62, 63].

Objectives and limitations

The research objectives of this thesis may be summarized as follows:

To improve current understanding of multimode flutter
Since the collapse of the Tacoma Narrows Bridge, bridge designers have learned how to predict the flutter stability limit by using wind tunnel tests with a section model. This approach can only represent a case where two still-air vibration modes couple into the flutter motion. In recent bridge projects multimode effects have reduced the stability limit significantly. One of the research objectives in this work is therefore to improve the current understanding of when a multimode approach should be used to predict the flutter stability limit, and when a bimodal approach is sufficient.

To develop a simple frequency-independent self-excited load model
The quasi-steady theory is frequently used for simplified modelling of self-excited forces. Since the load coefficients are frequency independent, the quasi-steady theory can be used in both the frequency and time domains. The quasi-steady theory is perhaps most convenient in the time domain since no convolution integrals have to be evaluated. However, it is well known that the quasi-steady theory may severely underestimate the flutter stability limit since no aerodynamic torsional damping is introduced. One of the research objectives is therefore to develop a more accurate modified quasi-steady theory to provide adequate estimates of both the stability limit and the wind-induced response.

To develop an alternative analytical expression for the flutter stability limit, including aerodynamic properties and mode shape similarity
Selberg's formula is frequently used to estimate the bimodal flutter stability limit of cable-supported bridges. However, Selberg's formula may provide results that are seriously inaccurate since it does not take the actual aerodynamic properties of the cross section and the shape-wise similarity of the vibration modes into account. One of the research objectives is therefore to develop an alternative analytical solution for the flutter stability limit taking into account the aerodynamic properties and the shape-wise similarity without compromising the accuracy and simplicity that Selberg's formula is well known for.

To compare and improve the current methods for time domain modelling of self-excited forces
There are several methods for modelling self-excited forces in the time domain. One of the objectives of this work is therefore to compare the existing methods and suggest improvements to the modelling to make the calculations more accurate and efficient.

To investigate the importance of the cross-spectral density of the turbulence components for prediction of wind-induced dynamic response of bridges
The wind-induced dynamic response of bridges is most commonly predicted taking into account the along-wind and vertical turbulence components, assuming that the two components are uncorrelated. Some studies have taken the cross-spectral density of u and w components into account. The studies indicate that this effect may influence the dynamic response. One of the objectives of this work is to investigate the possible influence of the cross-spectral density of the turbulence components on the wind-induced dynamic response of cable-supported bridges.

This work's limitations
Vortex-shedding induced vibrations that are typically important at low mean wind velocities will not be dealt with in this thesis. The cross-sectional admittance of the wind loading is not discussed. The response predicted in this thesis has not been compared with experimental data from wind tunnel tests or full-scale measurements.

Present Investigations

The work undertaken during this PhD study is presented as independent journal papers, which are either published or submitted. The three accepted journal papers have been published in *Journal of Wind Engineering and Industrial Aerodynamics*, *Journal of Sound and Vibration* and *Computers and Structures*. The journal paper titles are summarized in Table 1.

Table 1: Citations of the papers included in the thesis

Part	Journal papers
1	Øiseth O, Rönnquist A, Sigbjörnsson R. Simplified prediction of wind-induced response and stability limit of slender long-span suspension bridges, based on modified quasi-steady theory: A case study. Journal of Wind Engineering and Industrial Aerodynamics. (2010)
2	Øiseth O, Sigbjörnsson R. An alternative analytical approach to prediction of flutter stability limits of cable supported bridges. Journal of Sound and Vibration. (2011)
3	Øiseth O, Rönnquist A, Sigbjörnsson R. Time domain modelling of self-excited aerodynamic forces for cable-supported bridges: A comparative study. Computers & Structures. (2011)
4	Øiseth O, Rönnquist A, Sigbjörnsson R. Finite element formulation of the self-excited forces for time-domain assessment of wind-induced dynamic response and flutter stability limit of cable-supported bridges. Submitted for journal publication (2011)
5	Øiseth O, Rönnquist A, Sigbjörnsson R. Effects of cross-spectral densities of atmospheric turbulence on the dynamic response of cable-supported bridges: A case study. Submitted for journal publication (2011)

Declaration of authorship for papers 1-5

In papers 1, 2, 3 and 4, Ole Øiseth implemented the theory and performed all the numerical simulations presented. He also wrote the manuscripts. The co-authors contributed constructive criticism that increased the scientific quality of the papers. In Paper 5 Ole Øiseth performed most of the numerical analysis and wrote the main part of the manuscript. Ragnar Sigbjörnsson drafted the initial outline of the manuscript and performed some initial numerical analysis, which Ole Øiseth further developed. Anders Rönnquist contributed constructive criticism that increased the scientific quality of the paper.

Paper 1

Simplified prediction of wind-induced response and stability limit of slender long-span suspension bridges, based on modified quasi-steady theory: A case study

Øiseth O, Rönnquist A, Sigbjörnsson R

Background

Wind-induced vibration is one of the most important concerns when designing long-span suspension bridges. Most bridge engineers consider prediction of the flutter stability limit particularly important. Bimodal flutter, where two still-air vibration modes interact, has become well known. However, in recent long-span bridge projects, e.g., [18, 61], a reduction of the bimodal stability limit due to interactions between several vibration modes has been observed. A full understanding of multimode flutter has not been achieved, and this paper aims at providing further insight into this phenomenon. When modern bridges become slenderer and lighter, time domain assessment of the dynamic response may become necessary. A model describing self-excited forces in the time domain will therefore become necessary. This can be achieved using indicial or rational functions or quasi-steady theory. The quasi-steady theory is attractive because of its simplicity, but it is well known that the traditional quasi-steady theory may severely underestimate the flutter stability limit since no aerodynamic torsional damping is introduced into the system. This paper therefore aims at developing a modified quasi-steady model with improved accuracy.

Main findings

The bimodal and multimodal stability limits of the Hardanger Bridge are carefully studied in this paper. It is concluded that multimode flutter, where three still-air vibration modes participate, provides the lowest stability limit for the structure. It is also concluded that this is because two still-air vertical modes are shape-wise similar to the same torsion mode, implying that these three still-air vibration modes are coupled when the mean wind velocity is different from zero. The paper illustrates the importance of the shape-wise similarity of the vertical and torsional still-air vibration modes when the still-air vibration modes for flutter assessment are selected. The stability limit is evaluated using quasi-steady theory and aerodynamic derivatives obtained from wind tunnel measurements of a scaled section model. It is concluded that quasi-steady theory severely underestimates the stability limit since no aerodynamic torsional damping is introduced. A novel approximate frequency-independent model is suggested, where curves providing a frequency-independent approximation of the self-excited forces are fitted to the experimental data in the important frequency range. It is concluded that this aerodynamic model provides adequate estimates of both the stability limit and the wind-induced dynamic response for the case considered.

Paper 2

An alternative analytical approach to prediction of flutter stability limits of cable-supported bridges

Øiseth O, Sigbjörnsson R

Background

Selberg's formula [3] is well known to bridge engineers that are designing long-span bridges. It predicts the bimodal flutter stability limit with reasonably accuracy if the vibration modes have a perfect shape-wise similarity and the aerodynamic properties of the cross section are similar to those of a flat plate. This paper aims at developing an alternative to Selberg's formula taking into account the actual shape-wise similarity of the vibration modes and the aerodynamic properties of the cross section. If a simplified bimodal approach is supposed to be useful, multimode effects have to be negligible. Multimode effects are therefore studied carefully in this paper

Main findings

In this paper it has been shown that the flutter equations may be greatly simplified by introducing two approximations. (*i*) It is assumed that the critical frequency is on the torsional branch of the solution system and that the critical frequency may be approximated by the uncoupled system of equations. (*ii*) The aerodynamic derivatives may be approximated by expressions providing a frequency-independent description of the self-excited forces in the important frequency range. It is shown that when these approximations are introduced, the critical velocity may be determined by solving a simple cubic equation, and it is further shown that by neglecting the contribution from still-sir damping, a closed-form solution is achieved. The presented equation is equal to Selberg's formula for a certain combination of coefficients, but provides for including the effects of the cross section's aerodynamic properties and the shape-wise similarity of the vibration modes. The formulae presented have been tested for two different cross sections for a wide range of structural configurations. It is concluded that the formulae provide results of sufficient accuracy for all the cases evaluated and may be used to obtain an engineering approximation of the critical flutter velocity.

Multimode effects have been carefully studied. It is concluded that that the flutter velocity for a pair of modes is not affected by the presence of another pair of shape-wise similar vibration modes if the two pairs are shape-wise dissimilar. This implies that the most important factor for possible multimode effects is the shape-wise similarity of the vibration modes. It is also seen that for a combination of one vertical and two torsional modes, the reduction due to multimode effects is decreasing when the frequency ratio of the torsional modes is increasing. For a combination of two vertical and one torsional vibration modes, a reduction due to multimode effects cannot be neglected even if the two vertical vibration modes are well separated.

Paper 3

Time domain modelling of self-excited aerodynamic forces for cable-supported bridges: A comparative study.

Øiseth O, Rönnquist A, Sigbjörnsson R.

Background

As modern bridges become slenderer and lighter, a nonlinear assessment of the dynamic response may become necessary. Since nonlinearities may be taken into account more easily in the time domain than in the frequency domain, this implies that time domain modelling of the self-excited forces will become more important in the future. There are studies of modelling self-excited forces in time domain, e.g., [13, 14, 51, 54, 55, 57, 64-66], but these studies focus mainly on the fitting of expressions to the experimental data or/and prediction of the flutter stability limit. There are also several different expressions for self-excited forces in the time domain, but there are very few studies comparing the performance of the different approaches.

Main findings

In this paper the wind-induced dynamic response and flutter stability limit of the Hardanger Bridge have been assessed in the time domain. The self-excited forces have been modelled by rational functions, indicial functions, a suggested modified rational function approach and a suggested modified quasi-steady approach. The modified quasi-steady approach has been further developed from the version presented in Papers 1 and 2. An integration scheme, where larger time steps may be used and still avoid amplitude and phase distortion of the self-excited forces, has been suggested and applied successfully in a comprehensive case study. It is concluded that the self-excited load models used provide wind-induced response and stability limit of sufficient accuracy. The unsteady load models provided a poorer least squares fit to the experimental results than the curves used to represent the aerodynamic derivatives in the frequency domain. This is because the unsteady approach requires that two sets of data, representing the real and the imaginary part of the complex transfer functions, are approximated using the same coefficients. The suggested modified rational function approach makes it easier to introduce quasi-steady asymptotes for the self-excited forces outside the reduced velocity range covered by the experimental data. Since the self-excited forces are most important at the natural frequencies of the system, the modified quasi-steady approach suggested in this article provides an accurate representation of the self-excited forces since the self-excited forces corresponding to each natural frequency can be approximated separately. The modified quasi-steady approach presented in this paper actually performs better than some of the unsteady models tested.

Paper 4

Finite element formulation of the self-excited forces for time-domain assessment of wind-induced dynamic response and flutter stability limit of cable-supported bridges.

Øiseth O, Rönnquist A, Sigbjörnsson R.

Background

In most papers discussing modelling self-excited forces by means of indicial or rational functions, the still-air vibration modes are used as generalized coordinates when the wind-induced dynamic response and the stability limit of the aeroelastic system are assessed. This may be a disadvantage when material or geometric nonlinearities are introduced in the model. The dynamic response may be obtained by direct numerical integration if the self-excited forces are modelled at distinct points along the girder. The convolution integrals providing the self-excited forces must then be evaluated numerically for each time step. This requires a huge amount of computational effort. The aim of this paper is therefore to develop an aeroelastic beam element where the self-excited forces are added as unknowns in terms of aerodynamic degrees of freedom such that the convolution integrals do not need to be evaluated explicitly.

Main findings

Four different aeroelastic beam elements have been developed and tested in this paper. The starting point is a two-node beam element with 12 degrees of freedom (three translations and three rotations in each node). The self-excited forces are modelled with rational functions, and the convolution integrals are added as additional variables in the system of equations by means of aerodynamic degrees of freedom. The difference of the four elements is that different shape functions have been used to derive the coefficients in the element matrices related to the aerodynamic degrees of freedom. All the elements developed and tested have provided a converged stability limit that corresponds very well to results provided by a traditional multimode approach. The wind-induced dynamic response has also been obtained using one of the presented elements. The response corresponds very well to results obtained in the frequency domain using still-air vibration modes as generalized coordinates. It may be concluded that, for the current case study, the elements presented provide accurate results for both the stability limit and the wind-induced response. The computational effort required is far less than evaluating the convolution integrals numerically for each time step. The required computational effort is, in fact, much less than was required during the calculations presented in Paper 3, where still-air vibration modes are used as generalized degrees of freedom. This illustrates the effectiveness of the method since the number of degrees of freedom for the finite element model is several times higher than the number of selected still-air vibration modes used in Paper 3.

Paper 5

Effects of cross-spectral densities of wind velocities on the wind-induced dynamic response of cable-supported bridges: A case study

Øiseth O, Rönnquist A, Sigbjörnsson R.

Background

Accurate modelling of the wind field is a crucial issue when predicting the wind-induced dynamic response of long-span cable-supported bridges. The wind field is most commonly modelled as a multivariate Gaussian stationary stochastic process, where the along-wind, across-wind, and vertical velocity components are assumed independent. Since the roughness at the site will influence the wind field, there may be significant correlation of the velocity components. Little information exists on the possible influence of the correlation of the wind velocity components on the dynamic response of bridges.

Main findings

The measurements of the wind velocity components along the Sotra Bridge carried out in 1975 are reinvestigated in this paper. Different from previously published results where the data have been used, this paper focuses mainly on the spectral density of all three velocity components, including the cross-spectral densities of the components. The spatial properties of the wind field considering large separations are also studied. The Sotra Bridge is located in a narrow sound, which is roughly 600 m wide. From the measurements it is clearly seen that the wind field is influenced by the sound. The mean wind velocity is largest at the mid-span of the bridge, while the mean wind velocity is significantly lower closer to the shore. It is also seen that the turbulence intensities are higher at the shore than at the mid-span. The spectral and cross-spectral densities of the wind field have been successfully estimated using auto regressive (AR) models. From the estimated spectral and cross-spectral densities, it is seen that the covariance of the u and w and the u and v components is significant and cannot be disregarded even for large separations along the girder. The wind-induced dynamic response of a simplified model of a suspension bridge has been assessed to investigate the sensitivity of the dynamic response with respect to the modelling of the wind field. It is seen from the results that for the particular case considered the horizontal response is underestimated by 6%; the vertical response is overestimated by 4%, while the torsional response remains unchanged if the cross-spectral density of the u and w components is neglected. The expressions for the spectral densities of the along-wind and vertical turbulence component suggested by von Kármán are fitted to the experimental data from each of the anemometers. It is concluded that reasonable estimates of the dynamic response can be obtained using the average value of the parameters involved for the whole bridge, but that improved accuracy will be achieved if the inhomogeneity of the wind field and the cross-spectral density of the u and w components are taken into account.

Concluding remarks

Several aspects of wind-induced dynamic response of long-span bridges have been dealt with in this thesis. The focus has been on prediction of the flutter stability limit and the buffeting response in strong winds. Neither response due to vortex shedding, nor the effect of aerodynamic admittance functions has been dealt with.

Multimode flutter

It has become well known that flutter where several still-air vibration modes participate may occur, and that the multimode effects may reduce the flutter stability limit of the structure. Multimode effects have been discussed in Papers 1 and 2 of this thesis. It may be concluded that the most fundamental indicator of possible multimode effects is the shape-wise similarity of the torsional and vertical vibration modes since flutter will not occur if the vibration modes are shape-wise dissimilar. If a torsional mode is shape-wise similar to two vertical modes, multimode effects will occur. The reduction will be small if the shape-wise similarities are not of the same order of magnitude. If two torsional modes are shape-wise similar to one vertical mode, multimode effects will occur. The reduction of the stability limit will be small if the two torsional modes are well separated, or the shape-wise similarities of the mode combinations are not of the same order of magnitude.

Frequency-independent modelling of self-excited forces

A frequency-independent model for self-excited forces is convenient since it can be used in both the time and frequency domains. As explained in Paper 1 of this thesis, the traditional quasi-steady theory may be used for this purpose, but since the model does not introduce any aerodynamic torsional damping, the flutter threshold will in most cases be underestimated. In Paper 1 of this thesis, a novel frequency-independent description of the self-excited forces has been suggested. It is demonstrated that the self-excited forces are most important in the frequency range close to the natural frequencies. This implies that curves providing a frequency-independent description of the self-excited forces may be fitted to the experimental results of the aerodynamic derivatives in the important frequency range. It is demonstrated in the case study presented in Paper 1 that this simplified aerodynamic model provides stability limits and wind-induced dynamic response of adequate accuracy for the Hardanger Bridge. Similar results may be expected for other bridges where a reasonably streamlined girder is used.

Simplified prediction of the flutter stability limit

Simplified prediction of the flutter stability limit is still considered important in bridge design. In Paper 2 of this thesis, the frequency-independent aerodynamic model presented in Paper 1 is introduced into the fundamental flutter equations. It is further

shown that by assuming that the critical frequency is on the torsional solution branch of the system of equations, and assuming that it may be approximated by the uncoupled system of equations, an analytical expression for the stability limit may be developed. It is also shown that by neglecting still-air damping, a closed-form solution of the flutter stability limit very similar to Selberg's formula may be developed. The formula includes parameters taking into account the actual aerodynamic properties of the cross section and the shape-wise similarity of the vibration modes. The formulae presented in Paper 2 have been tested for two different cross sections, for a range of hypothetical structural configurations in additional to the structural configurations of a few well-known bridges. It can be concluded that the formulae provide results of good accuracy for all the cases considered, and that they may be used to obtain an engineering approximation of the flutter stability limit of cable-supported bridges if multimode effects does not occur.

Unsteady modelling of self-excited forces in the time domain

Unsteady modelling of self-excited forces in the time domain by means of rational or indicial functions has been studied in Papers 3 and 4 of this thesis. The expressions for the unsteady models may be challenging to fit to experimental data of the aerodynamic derivatives since the same coefficients have to be used to fit the data representing the imaginary and the real part of the complex transfer functions. The indicial or impulse response functions used to model self-excited forces in the time domain correspond to the Fourier transform of the expressions curve fitted to the experimental data of the aerodynamic derivatives. Since experimental results are commonly known only in a very limited frequency range, there will be several combinations of coefficients that provide an acceptable fit to the experimental data, at least for an approximation with several exponential filters. Since the behaviour of the transfer function outside the range covered by experimental data will be different, the indicial or impulse response functions will also have strongly different characteristics. To improve the overall behaviour of the transfer function, it is possible to use quasi-steady theory as an asymptotic value when the frequency goes to zero. A transfer function facilitating introduction of these asymptotes has been suggested in Paper 3. Since the rise time of the indicial or aerodynamic impulse response functions may be much shorter than the shortest period of interest, time steps much smaller than what is usually necessary when calculating the dynamic response of slender structures need to be used to avoid amplitude and phase distortion of the self-excited forces. An integration method, where the time steps can be kept as usual, is therefore suggested and applied successfully in a comprehensive case study.

Even when the integration scheme presented in Paper 3 is introduced, the computational effort required to calculate the dynamic response for a relatively small number of still-air vibration modes is large. In Paper 4 of this thesis a different approach is considered.

16

Here, the convolution integrals providing the self-excited forces in the time domain are added as additional unknowns in the system of equations in terms of aerodynamic degrees of freedom in each node of traditional beam elements. This approach has provided accurate stability limits and wind-induced dynamic response and requires far less computational effort than evaluating the convolution integrals numerically at each time step. Since the displacement degrees of freedom of the element model are used directly in the calculations, geometric and material nonlinearities can be much more easily introduced into the calculations than when still-air vibration modes are used as generalized coordinates.

Effects of cross-spectral densities of turbulence components on wind-induced response

The influence of the cross-spectral densities of turbulence components on the wind-induced dynamic response is studied in paper 5 of this thesis. The measurements of the fluctuating wind along the Sotra Bridge carried out in 1975 are reinvestigated. It is seen from the results that there is a significant correlation of the turbulence components. The identified spectral and cross-spectral densities of the turbulence components are used to predict the spectral densities of the cross-sectional actions acting on a wedge-shaped box girder. It is seen that for the considered cross section, the cross-spectral density of the vertical and along-wind component may have a significant influence on the horizontal and vertical actions, in particular at low frequencies, while the influence on the torsional action seems to be negligible. The identified cross-spectral densities of the atmospheric turbulence are used to predict the wind-induced dynamic response of a simplified model of a suspension bridge. From the result it is seen that the horizontal response is underestimated by 6%; the vertical response is underestimated by 4%, while the torsional response remains unchanged if the cross-spectral density of the u and w components is neglected. It is concluded that the cross-spectral density of the u and w components has little effect on the wind-induced dynamic response of the bridge considered, but that improved accuracy will be achieved if this is included. The aerodynamic admittance functions may have an effect on the result, and it is therefore recommended that this is investigated further.

Suggestions for further work

Multimode flutter has been thoroughly discussed in this thesis. Since aerodynamic derivatives related to the horizontal motion for the cross sections considered have not been available, possible interaction of horizontal modes with the flutter motion has only been briefly discussed. This can therefore be further investigated. It is also possible to carry out a study where a more direct connection between the flutter performance and the design of the suspension bridge is considered. For instance, the shape-wise similarity of the vertical and torsional vibration modes may depend on the position of the towers along the bridge, the sag of the main cables, and if there are one or two main cables. As pointed out in this thesis, significant multimode effects are present for the Hardanger Bridge [67], while it is reported that for the Messina Strait Bridge no significant multimode effects are present [68]. Although some of the parameters mentioned above will be given by the landscape at the site, an insight into how the basic geometry of the suspension bridge can affect the flutter performance may be useful in the initial design.

The modified quasi-steady theory suggested in this thesis has only been tested for relatively streamlined girders. How the load model will perform for more bluff cross sections and twin- deck cross sections should be investigated.

The aeroelastic beam elements developed in this thesis have been used successfully to predict the wind-induced dynamic response and the stability limit of a simplified model of a suspension bridge. It is recommended to test the elements on a more realistic structure where material and geometrical nonlinearities are included. It is also recommended that the robustness and the accuracy of the elements are tested, considering several structural and aerodynamic configurations.

It is shown in this thesis that the cross-spectral density of the horizontal along-wind and vertical across-wind turbulence components may have influence on the cross-sectional actions in the low-frequency range. Taking measurements of the fluctuating wind is therefore recommended to evaluate how this cross-spectral density is affected by the separation of the two points considered. The possible influence of the aerodynamic admittance functions has not been taken into account in this thesis. A Study of the effect of the cross-spectral densities of the turbulence components on the cross-sectional actions when the aerodynamic admittance is taken into account is therefore recommended.

Probabilistic modelling of wind-induced dynamic response and the flutter stability limit may become an important topic in the future. The parameters used in the modelling of the wind field, buffeting actions, self-excited actions and the structural properties are in reality uncertain, both in terms of scatter in the experimental results and possible model errors when the bridge is scaled for wind tunnel testing. Study is therefore recommended of how uncertainty in the parameters used will affect the uncertainty in the final results. Furthermore, a comparison is recommended of the predicted response with measurements of the dynamic response of a long-span bridge to evaluate overall model uncertainty.

References

[1] Wyatt TA. Bridge aerodynamics 50 years after Tacoma Narrows - part I: The Tacoma Narrows failure and after. Journal of Wind Engineering and Industrial Aerodynamics. 1992;40:317-26.

[2] Walshe DE, Wyatt TA. Bridge aerodynamics 50 years after Tacoma Narrows - part II: A new. Journal of Wind Engineering and Industrial Aerodynamics. 1992;40:327-36.

[3] Selberg A. Oscillation and Aerodynamic Stability of Suspension Bridges. Acta polytechnica scandinavica civil engineering and building construction Series No 13. 1961.

[4] Hjorth-Hansen E. Section model tests. In: Larsen A, editor.Proceedings of Aerodynamics of large bridges. Copenhagen, Denmark1992.

[5] Davenport AG. The buffeting of structures by gusts. Proceedings of Symp Wind effects on buildings and structures. England1963.

[6] Hui MCH, Larsen A, Xiang HF. Wind turbulence characteristics study at the Stonecutters Bridge site: Part I-Mean wind and turbulence intensities. Journal of Wind Engineering and Industrial Aerodynamics. 2009;97:22-36.

[7] Hui MCH, Larsen A, Xiang HF. Wind turbulence characteristics study at the Stonecutters Bridge site: Part II: Wind power spectra, integral length scales and coherences. Journal of Wind Engineering and Industrial Aerodynamics. 2009;97:48-59.

[8] von Kármán T. Progress in the Statistical Theory of Turbulence. Proceedings of the National Academy of Sciences of the United States of America. 1948;34:530-9.

[9] Harris RI. Some further thoughts on the spectrum of gustiness in strong winds. Journal of Wind Engineering and Industrial Aerodynamics. 1990;33:461-77.

[10] Davenport AG. The spectrum of horizontal gustiness near the ground in high winds. Quarterly Journal of the Royal Meteorological Society. 1961;87:194-211.

[11] Kaimal JC, Izumi Y, Wyngaard JC, Cote R. Spectral characteristics of surface-layer turbulence. Quarterly Journal of the Royal Meteorological Society. 1972;98:563-&.

[12] Solari G, Piccardo G. Probabilistic 3-D turbulence modeling for gust buffeting of structures. Probabilistic Engineering Mechanics. 2001;16:73-86.

[13] Chen X, Matsumoto M, Kareem A. Aerodynamic coupling effects on flutter and buffeting of bridges. Journal of Engineering Mechanics. 2000;126:17-26.

[14] Chen XZ, Matsumoto M, Kareem A. Time domain flutter and buffeting response analysis of bridges. Journal of Engineering Mechanics-Asce. 2000;126:7-16.

[15] Strømmen EN. Theory of bridge aerodynamics. Berlin: Springer; 2006.

[16] Simiu E, Scanlan RH. Wind effects on structures fundamentals and applications to design. 3rd ed. New York: Wiley; 1996.

[17] Tubino F, Solari G. Gust buffeting of long span bridges: Double Modal Transformation and effective turbulence. Engineering Structures. 2007;29:1698-707.

[18] Katsuchi H, Jones NP, Scanlan RH. Multimode coupled flutter and buffeting analysis of the Akashi-Kaikyo bridge. Journal of Structural Engineering-Asce. 1999;125:60-70.

[19] Simiu E, Miyata T. Design of buildings and bridges for wind a practical guide for ASCE-7 standard users and designers of special structures. Hoboken, N.J.: Wiley; 2006.

[20] Minh NN, Miyata T, Yamada H, Sanada Y. Numerical simulation of wind turbulence and buffeting analysis of long-span bridges. Journal of Wind Engineering and Industrial Aerodynamics. 1999;83:301-15.

[21] Davenport AG. Response of slender line like structures to a gusty wind. The institution of civil engineers. 1962;23:389-408.

[22] Dyrbye C, Hansen SO. Wind loads on structures. Chichester: Wiley; 1997.

[23] Krenk S. Wind field coherence and dynamic wind forces. In: Næss AK, Steen, editor. IUTAM Symposium on Advances in Nonlinear Stochastic Mechanics. Dordrecht: Kluwer; 1995. p. XIII, 510 s.

[24] Hansen SO, Krenk S. Dynamic along-wind response of simple structures. Journal of Wind Engineering and Industrial Aerodynamics. 1999;82:147-71.

[25] Matheson MJ, Holmes JD. Simulation of the dynamic response of transmission lines in strong winds. Engineering Structures. 1981;3:105-10.

[26] Deodatis G. Simulation of ergodic multivariate stochastic processes. Journal of Engineering Mechanics. 1996;122:778-87.

[27] Shinozuka M. Monte Carlo solution of structural dynamics. Computers and Structures. 1972;2:855-74.

[28] Shinozuka M, Jan CM. Digital simulation of random processes and its applications. Journal of Sound and Vibration. 1972;25:111-28.

[29] Kim HK, Shinozuka M, Chang SP. Geometrically nonlinear buffeting response of a cable-stayed bridge. Journal of Engineering Mechanics. 2004;130:848-57.

[30] Shinozuka M, Yun CB, Seya H. Stochastic methods in wind engineering. Journal of Wind Engineering and Industrial Aerodynamics. 1990;36:829-43.

[31] Aas-Jakobsen K, Strommen E. Time domain calculations of buffeting response for wind-sensitive structures. Journal of Wind Engineering and Industrial Aerodynamics. 1998;74-6:687-95.

[32] Aas-Jakobsen K, Strommen E. Time domain buffeting response calculations of slender structures. Journal of Wind Engineering and Industrial Aerodynamics. 2001;89:341-64.

[33] Mann J, Krenk S. Fourier simulation of a non-isotropic wind field model. In: Schuëller GI, Shinozuka M, Yao JTP, editors. ICOSSAR '93, the 6th International Conference on Structural Safety and Reliability, Innsbruck, Austria,9-13 August 1993. Rotterdam: A.A. Balkema; 1993. p. 1669-74.

[34] Mignolet MP, Spanos PD. MA to ARMA modeling of wind. Journal of Wind Engineering and Industrial Aerodynamics. 1990;36:429-38.

[35] Li Y, Kareem A. ARMA representation of wind field. Journal of Wind Engineering and Industrial Aerodynamics. 1990;36:415-27.

[36] Davenport AG. The response of suspension bridges to wind action. In: Holand I, Kavlie D, Moe G, Sigbjörnsson R, editors.Proceedings of International research seminar on Safety of structures under dynamic loading held in june 1977 at the Norwegian Institute of Technology. Trondheim, Norway1978.

[37] Ma RJ, Chen AR. Determination of flutter derivatives by a taut strip model. Journal of Wind Engineering and Industrial Aerodynamics. 2007;95:1400-14.

[38] Tanaka H, Davenport AG. Response of taut strip models to turbulent wind. ASCE J Eng Mech Div. 1982;108:33-49.

[39] Zhu LD, Wang M, Wang DL, Guo ZS, Cao FC. Flutter and buffeting performances of Third Nanjing Bridge over Yangtze River under yaw wind via aeroelastic model test. Journal of Wind Engineering and Industrial Aerodynamics. 2007;95:1579-606.

[40] Fujino Y, Ito M, Shino I, Iwamoto M, Hikami Y-I, Tatsumi M, et al. Wind tunnel study of long-span suspension bridge under smooth and turbulent flow. Journal of Wind Engineering and Industrial Aerodynamics. 1990;33:313-22.

[41] Chopra AK. Dynamics of structures: theory and applications to earthquake engineering. Upper Saddle River, N.J.: Pearson Prentice Hall; 2007.

[42] Cook RD. Concepts and applications of finite element analysis. New York: Wiley; 2002.

[43] Zienkiewicz OC, Taylor RL. The finite element method. 5th ed. Oxford: Butterworth-Heinemann; 2000.

[44] Scanlan RH, Tomko JJ. Airfoil and bridge deck flutter derivatives. Journal of the Engineering Mechanics Division. 1971;97:1717-37.

[45] Theodorsen T. General theory of aerodynamic instability and the mechanism of flutter NACA Report No. 496. Washington DC1934.

[46] Jakobsen JB. Fluctuating wind load and response of a line-like engineering structure with emphasis on motion-induced wind forces. Trondheim: Department of Structural Engineering, Norwegian Institute of Technology; 1995.

[47] Jakobsen JB, Hjorth-Hansen E. Determination of the aerodynamic derivatives by a system-identification-method. Journal of Wind Engineering and Industrial Aerodynamics. 1995;57:295-305.

[48] Huang L, Liao H, Wang B, Li Y. Numerical simulation for aerodynamic derivatives of bridge deck. Simulation Modelling Practice and Theory. 2009;17:719-29.

[49] Sarwar MW, Ishihara T, Shimada K, Yamasaki Y, Ikeda T. Prediction of aerodynamic characteristics of a box girder bridge section using the LES turbulence model. Journal of Wind Engineering and Industrial Aerodynamics. 2008;96:1895-911.

[50] Zhu ZW, Gu M, Chen ZQ. Wind tunnel and CFD study on identification of flutter derivatives of a long-span self-anchored suspension bridge. Computer-Aided Civil and Infrastructure Engineering. 2007;22:541-54.

[51] Caracoglia L, Jones NP. Time domain vs. frequency domain characterization of aeroelastic forces for bridge deck sections. Journal of Wind Engineering and Industrial Aerodynamics. 2003;91:371-402.

[52] Yagi T. Wind-induced instabilities of structures. Stockholm: Kungl. tekniska högskolan, Institutionen för byggkonstruktion.; 1997.

[53] Bucher CG, Lin YK. Stochastic stability of bridges considering coupled modes. Journal of Engineering Mechanics-Asce. 1988;114:2055-71.

[54] Borri C, Costa C, Zahlten W. Non-stationary flow forces for the numerical simulation of aeroelastic instability of bridge decks. Computers & Structures. 2002;80:1071-9.

[55] Borri C, Hoffer R. Aeroelastic wind forces on flexible bridge girders. Meccanica. 2000;35:1-15.

[56] Costa C, Borri C. Application of indicial functions in bridge deck aeroelasticity. Journal of Wind Engineering and Industrial Aerodynamics. 2006;94:859-81.

[57] Salvatori L, Borri C. Frequency- and time-domain methods for the numerical modeling of full-bridge aeroelasticity. Computers & Structures. 2007;85:675-87.

[58] Matsumoto M, Mizuno K, Okubo K, Ito Y, Matsumiya H. Flutter instability and recent development in stabilization of structures. Journal of Wind Engineering and Industrial Aerodynamics. 2007;95:888-907.

[59] Bisplinghoff RL, Ashley H. Principles of aeroelasticity. New York: Wiley; 1962.

[60] Fung YC. An introduction to the theory of aeroelasticity. New York: Wiley; 1955.

[61] Katsuchi H, Jones NP, Scanlan RH, Akiyama H. Multi-mode flutter and buffeting analysis of the Akashi-Kaikyo bridge. Journal of Wind Engineering and Industrial Aerodynamics. 1998;77-8:431-41.

[62] Agar TJA. Aerodynamic flutter analysis of suspension bridges by a modal technique. Engineering Structures. 1989;11:75-82.

[63] Jain A, Jones NP, Scanlan RH. Coupled flutter and buffeting analysis of long-span bridges. Journal of Structural Engineering-Asce. 1996;122:716-25.

[64] Borri C, Costa C. A parametric study of indicial function models in bridge deck aeroelasticity. Wind and Structures. 2004;7:405-20.

[65] Caracoglia L, Jones NP. A methodology for the experimental extraction of indicial functions for streamlined and bluff deck sections. Journal of Wind Engineering and Industrial Aerodynamics. 2003;91:609-36.

[66] Chen XZ, Kareem A. Nonlinear response analysis of long-span bridges under turbulent winds. Journal of Wind Engineering and Industrial Aerodynamics. 2001;89:1335-50.

[67] Øiseth O, Rönnquist A, Sigbjörnsson R. Simplified prediction of wind-induced response and stability limit of slender long-span suspension bridges, based on modified quasi-steady theory: A case study. Journal of Wind Engineering and Industrial Aerodynamics. 2010;98:730-41.

[68] D'Asdia P, Sepe V. Aeroelastic instability of long-span suspended bridges: a multi-mode approach. Journal of Wind Engineering and Industrial Aerodynamics. 1998;74-6:849-57.

Paper I

Ole Øiseth, Anders Rönnquist, Ragnar Sigbjörnsson

Simplified prediction of wind-induced response and stability limit of slender long-span suspension bridges, based on modified quasi-steady theory: A case study.

Simplified prediction of wind-induced response and stability limit of slender long-span suspension bridges, based on modified quasi-steady theory: A case study

Ole Øiseth, Anders Rönnquist, Ragnar Sigbjörnsson*

Department of Structural Engineering, Norwegian University of Science and Technology, 7491 Trondheim, Norway

ARTICLE INFO

ABSTRACT

The Hardanger Bridge is currently under construction in Norway. It will have a main span of 1310 m and a girder that is only 18.3 m wide, which implies that wind-induced vibration is a major concern in the design. Buffeting response and flutter analysis of the Hardanger Bridge are treated in this paper. The self-excited forces are modelled using aerodynamic derivatives obtained from free vibration tests, quasi-steady theory, and a suggested modified quasi-steady theory. The stability limit predicted using aerodynamic derivatives corresponded well with the wind tunnel results, while the quasi-steady theory severely underestimated the critical mean wind velocity for the section model used in the wind tunnel tests. A new set of modified quasi-steady coefficients are suggested, where the experimental results of the aerodynamic derivatives are used to obtain frequency-independent model coefficients. The critical velocities predicted by the modified quasi-steady coefficients differ only by 4–5% from estimates based on the aerodynamic derivatives. The response predicted by the suggested simplified aerodynamic model is also presented, and the results indicate that adequate estimates are achieved.

1. Introduction

One of the essential tasks in modern bridge design is to avoid excessive levels of wind-induced vibration. Self-excited vibration, such as galloping and flutter, are of particular interest, since these phenomena may cause devastating effects, leading to structural collapse like the infamous Tacoma Narrows bridge failure. Since cable-supported bridges can be vulnerable to flutter, this instability phenomenon has been the subject of intensive research efforts in bridge engineering. The present state of the art is the multimode approach, in which coupling effects from several still-air vibration modes are considered (Agar, 1989; Chen et al., 2000; Jain et al., 1996b). It is widely recognized that coupled flutter, where several vibration modes interact may occur, and that the multimode effects may be stabilizing or destabilizing, as shown, among others, by Chen and Kareem (2008) and Katsuchi et al. (1999). Crucial questions are: Which of the still-air vibration modes are involved? Which of the aerodynamic derivatives are most influential? How can an effective flutter control be

achieved? These issues have been addressed in several papers (Bartoli and Mannini, 2008; Chen and Kareem, 2008; Chen, 2007; Larsen et al., 1995; Matsumoto et al., 2007; Matsumoto et al., 2008).

The question regarding the effective flutter control is of growing interest as the span length of suspension bridges increases. This has resulted in a variety of techniques to reduce or suppress the aeroelastic response, which is a key issue, with respect to traffic safety, structural fatigue, and related maintenance, as well as prevention of collapse under extreme conditions. The most common control methods applied can roughly be divided into: (a) flow pattern control and (b) vibration mode control. Flow pattern control is dealing with aerodynamic optimisation of the shape of the cross section, application of guide vanes, a central slot or central stabilizer (see, for instance, Yang and Ge, 2009, for further details). Moreover the application of moving control surfaces, which may be either active or passive, has also been discussed in the literature (Omenzetter et al., 2000; Wilde and Fujino, 1998; Wilde et al., 1999). Vibration mode control, on the other hand, is primarily based on the application of mechanical devices (e.g., tuned mass dampers) that may be either passive or active (Gu et al., 2002; Kwon and Park, 2004; Körlin and Starossek, 2007; Larsen et al., 1995).

In some applications, e.g., in order to study how structural nonlinearities affect the response, time domain analyses may be the most effective approach. Since the description of the

* Corresponding author.
E-mail addresses: ole.oiseth@ntnu.no (O. Øiseth), anders.ronnquist@ntnu.no (A. Rönnquist), ragnar.sigbjornsson@ntnu.no (R. Sigbjörnsson).

Nomenclature

A_m	aerodynamic admittance function
A_n^*, H_n^*, P_n^*	aerodynamic derivatives
A_n	coefficient, rational functions
a_n, h_n, p_n	modified quasi-steady coefficients
$\mathbf{B}_q$	buffeting load coefficient matrix
B, D	width and height of the girder
d_l	coefficient, rational functions
$\mathbf{M}, \mathbf{C}, \mathbf{K}$	mass, damping, and stiffness matrices
C_D, C_L, C_M	force coefficients
$\mathbf{E}_n$	impedance matrix
$G_n, \mathbf{G}_n$	the Fourier transform of variable n, a vector containing Fourier transforms
i	the imaginary unit
K	reduced frequency
κ	roughness coefficient
L	span length
$\tilde{m}_z, \tilde{m}_\theta$	modal equivalent and evenly distributed mass and mass moment of inertia
$\mathbf{q}$	cross sectional load vector
$\tilde{\mathbf{Q}}, \tilde{Q}_i$	modal load vector or modal load
$\mathbf{r}, \dot{\mathbf{r}}, \ddot{\mathbf{r}}$	displacement, velocity, and acceleration vector
S or $\mathbf{S}$	auto or cross-spectral density, cross-spectral density matrix
t	time
V	mean wind velocity
$x, \Delta x, x_r$	span-wise coordinate, span-wise separation, position
z	height above ground or water
$\eta, \boldsymbol{\eta}$	generalized coordinate or vector containing all generalized coordinates
ξ_n	still-air damping ratio

ρ	air density
$\boldsymbol{\varphi}_n, \boldsymbol{\phi}$	vibration mode or matrix containing all selected vibration modes
$\phi_y, \phi_z, \phi_\theta$	components in the vibration mode vector
ω, ω_n	circular frequency and natural circular frequency

Subscripts/superscripts

ae	aerodynamic
buff	buffeting
D, L, M	drag, lift, moment
r	response, position
Se	self-excited
tot	total
T	transpose
u, w	along-wind, across-wind vertically
y, z, θ	horizontal, vertical, rotation
V	wind property
0	still-air
–	mean value
~	modal property
′	derivative
.	time derivative
*	complex conjugate
−1	matrix inverse

Abbreviations

AD	aerodynamic derivatives
MQSC	modified quasi-steady coefficients
QST	quasi-steady theory

self-excited forces suggested by Scanlan and Tomko (1971) contains frequency-dependent coefficients, frequency dependency has to be transformed into time dependency before the experimental results can be used in the time domain. This can be achieved by using indicial functions (Borri et al., 2002; Scanlan et al., 1974) or rational functions (Chen et al., 2000; Chen and Kareem, 2001). Another and perhaps simpler approach is to use quasi-steady theory, since it is valid in both time and frequency domain. To explore the possibility of using quasi-steady theory for multimodal response and stability prediction of narrow long-span suspension bridges, we have selected the Hardanger Bridge (Fig. 1), which is currently entering the construction phase in Norway.

The Hardanger Bridge will be the longest suspension bridge in Norway and among the top 10 longest suspension bridges in the world, with a total length of 1380 m, including a main span of 1310 m. The bridge towers are 186 m high, and the headroom under the girder is 55 m. Since the bridge will have only two traffic lanes and one lane for bicycles and pedestrians, it is unusually narrow; the width of the girder is 18.3 m and the distance between the two cables is only 14.5 m. This implies that the bridge will be one of the slenderest long-span suspension bridges in the world (see Table 1). The geometry of the girder is shown in Fig. 2. To improve its aerodynamic performance, guide vanes are applied. The 10-min design mean wind velocity is 38 m/s, corresponding to a mean return period of 50 years.

Extensive analysis of the buffeting response and stability limits is presented as follows. However, vortex shedding that typically dominates the response at low mean wind velocities will not be dealt with herein. The quasi-steady approach is simpler than
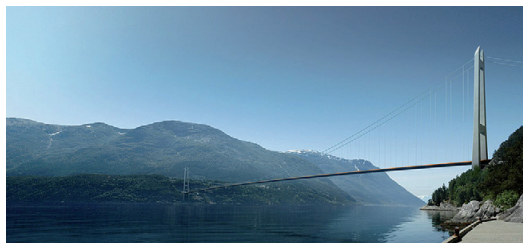
Fig. 1. Artist's view of the Hardanger Bridge across the Hardanger Fjord in the western part of Norway (www.vegvesen.no, 2009).

Table 1
Main span and width of some well-known bridges (www.wikipedia.org, 2009).

Bridge name	Main span (m)	Width (m)	Country
Akashi-Kaikyō Bridge	1991	35.5	Japan
Xihoumen Bridge	1650	36	China
Great Belt Bridge	1624	31	Denmark
Runyang Bridge	1490	39.2	China
Humber Bridge	1410	28.5	United Kingdom
Jiangyin Suspension Bridge	1385	–	China
Tsing Ma Bridge	1377	41	China
The Hardanger bridge	1310	18.3	Norway
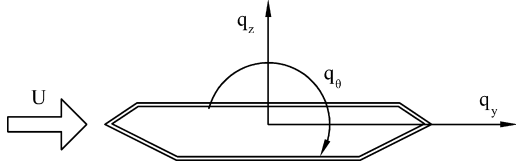
Fig. 2. Aerodynamic forces acting on a cross section of the bridge deck. The section shown is that one of the Hardanger Bridge.

unsteady models, but the traditional quasi-steady theory underestimates the stability limit of the Hardanger Bridge severely, compared with the results when aerodynamic derivatives are used. In the case at hand, the traditional quasi-steady theory is therefore judged inadequate to model the self-excited forces in coupled flutter or buffeting response analysis. In the following, a modified set of quasi-steady coefficients is introduced, where the frequency dependency is accounted for in an average sense. This is achieved by assuming the damping terms and the stiffness terms of the aerodynamic derivatives to be proportional to the reduced wind velocity and to the squared reduced mean wind velocity, respectively. A general polynomial expression will obviously give a more accurate fit to the experimental data than the constraints introduced. However, the approximation suggested is found to give fairly good fits to the important aerodynamic derivatives for the Hardanger Bridge. Similar results may be expected for other bridges, which have a girder with similar aerodynamic properties. The new modified quasi-steady coefficients are not intended to replace frequency-dependent force coefficients, but may serve as an approximation giving adequate accuracy for engineering purposes.

2. General relations

The equations used in the present case study, comprising the classical multimode theory, are summarised in this section. A comprehensive detailed overview can be found in the literature (e.g., Chen et al., 2000; Jain et al., 1996a; Katsuchi et al., 1998) along with notable textbooks (Dyrbye and Hansen, 1997; Simiu and Miyata, 2006; Simiu and Scanlan, 1996; Strømmen, 2006). It is assumed that the bridge may be treated as a line-like structure. It is taken for granted that the wind field can be approximated as locally stationary and homogenous; furthermore that the wind action and displacements, all referred to the shear centre of the cross section, can be divided into a time invariant mean and a randomly fluctuating part. The displacement components and the distributed forces are defined as (see Fig. 2).

$$\mathbf{r}_{tot}(x,t)=\bar{\mathbf{r}}(x)+\mathbf{r}(x,t),\bar{\mathbf{r}}(x)=\begin{bmatrix}\bar{r}_y & \bar{r}_z & \bar{r}_\theta\end{bmatrix}^T,\mathbf{r}(x,t)=\begin{bmatrix}r_y & r_z & r_\theta\end{bmatrix}^T$$

$$\mathbf{q}_{tot}(x,t)=\bar{\mathbf{q}}(x)+\mathbf{q}(x,t),\bar{\mathbf{q}}(x)=\begin{bmatrix}\bar{q}_y & \bar{q}_z & \bar{q}_\theta\end{bmatrix}^T,\mathbf{q}(x,t)=\begin{bmatrix}q_y & q_z & q_\theta\end{bmatrix}^T$$

(1)

where $\bar{r}_n$ and r_n, $n\in\{y, z, \theta\}$ symbolises the mean and fluctuating part of the displacement components, respectively, and $\bar{q}_n$ and q_n, $n\in\{y, z, \theta\}$ represents the mean and fluctuating part of the distributed action. The displacements are positive in the same directions as the wind action is displayed in Fig. 2.

In the following, we focus on the variance of the randomly fluctuating displacement components. The solution is based on a straightforward modal superposition approach introducing the mode shapes as generalized coordinates. Thus, an adequate number of natural modes and corresponding undamped natural frequencies are required. Axial displacements in the span-wise direction of the girder are disregarded. Hence, the structural

displacements in a Cartesian coordinate system are represented by the sum of the products of selected natural mode shapes, $\boldsymbol{\varphi}_i$, and the corresponding generalized coordinates, η_i

$$\mathbf{r}(x,t)=\boldsymbol{\Phi}(x)\boldsymbol{\eta}(t), \qquad \boldsymbol{\Phi}(x)=\begin{bmatrix}\boldsymbol{\varphi}_1 & \cdots & \boldsymbol{\varphi}_i & \cdots & \boldsymbol{\varphi}_{N_{mod}}\end{bmatrix}$$

$$\boldsymbol{\eta}(t)=\begin{bmatrix}\eta_1 & \cdots & \eta_i & \cdots & \eta_{N_{mod}}\end{bmatrix}^T, \quad \boldsymbol{\varphi}_i=\begin{bmatrix}\phi_y & \phi_z & \phi_\theta\end{bmatrix}^T$$

(2)

where ϕ_n, $n\in\{y, z, \theta\}$ symbolises the horizontal, vertical, and torsional deformation along the girder. The modal wind action vector is expressed as

$$\tilde{\mathbf{Q}}_{tot}=\begin{bmatrix}\tilde{Q}_1 & \cdots & \tilde{Q}_i & \cdots & \tilde{Q}_{N_{mod}}\end{bmatrix}^T_{tot} \quad where \quad \tilde{Q}_i=\int_L\left(\boldsymbol{\varphi}_i^T(\mathbf{q}_{Buff}+\mathbf{q}_{Se})\right)dx$$

(3)

Here L is the span length. The cross sectional action, $\mathbf{q}_{tot}=\mathbf{q}_{Buff}+\mathbf{q}_{se}$, is divided into a buffeting part, $\mathbf{q}_{Buff}$, and a self-excited part, $\mathbf{q}_{se}$, containing the total drag, lift, and moment action per unit length of the structure. The aeroelastic self-excited forces may be represented by aeroelastic derivatives introduced by Scanlan and Tomko (1971). Using matrix notation, this can be expressed as follows in the frequency domain

$$\mathbf{G}_{\mathbf{q}_{Se}}(x,V,\omega)=\mathbf{C}_{ae}(V,\omega)\mathbf{G}_{\dot{\mathbf{r}}}(x,\omega)+\mathbf{K}_{ae}(V,\omega)\mathbf{G}_{\mathbf{r}}(x,\omega)$$

$$\mathbf{C}_{ae}=\frac{\rho B^2}{2}\omega\begin{bmatrix}P_1^* & P_5^* & BP_2^* \\ H_5^* & H_1^* & BH_2^* \\ BA_5^* & BA_1^* & B^2A_2^*\end{bmatrix}, \quad \mathbf{K}_{ae}=\frac{\rho B^2}{2}\omega^2\begin{bmatrix}P_4^* & P_6^* & BP_3^* \\ H_6^* & H_4^* & BH_3^* \\ BA_6^* & BA_4^* & B^2A_3^*\end{bmatrix}$$

(4)

where $\mathbf{G}_{\dot{\mathbf{r}}}(x,\omega)$ and $\mathbf{G}_{\mathbf{r}}(x,\omega)$ are the Fourier transforms of the velocity and displacement response, respectively, ρ is air density, ω is the circular frequency of motion, B is the width of the girder, and P_n^*, H_n^*, A_n^*, $n\in\{1,2, ..., 6\}$ are the dimensionless aerodynamic derivatives that are functions of the reduced frequency defined as $K=(B\omega)/V$, where V is the mean wind velocity. Thus, the dynamic equilibrium conditions expressed in the modal coordinates can be expressed in the frequency domain as follows:

$$\tilde{\mathbf{M}}_0\mathbf{G}_{\ddot{\boldsymbol{\eta}}}(\omega)+(\tilde{\mathbf{C}}_0-\tilde{\mathbf{C}}_{ae}(V,\omega))\mathbf{G}_{\dot{\boldsymbol{\eta}}}(\omega)+(\tilde{\mathbf{K}}_0-\tilde{\mathbf{K}}_{ae}(V,\omega))\mathbf{G}_{\boldsymbol{\eta}}(\omega)=\mathbf{G}_{\tilde{Q}_{Buff}}(\omega)$$

(5)

Here, $\mathbf{G}_{\boldsymbol{\eta}}$ is the Fourier transform of the displacement response in modal coordinates; $\tilde{\mathbf{M}}_0$ is the modal mass matrix; $\tilde{\mathbf{C}}_0$ represents the modal damping matrix; $\tilde{\mathbf{K}}_0$ symbolises the stiffness matrix; $\tilde{\mathbf{C}}_{ae}(V,\omega)$ is the modal aerodynamic damping matrix, and $\tilde{\mathbf{K}}_{ae}(V,\omega)$ represents the modal aerodynamic stiffness matrix. A matrix with a zero index indicates that the properties are referred to still air conditions. The elements of the modal aerodynamic stiffness and damping matrices may then be calculated by

$$\tilde{K}_{nm}^{(ae)}(V,\omega)=\int_L(\boldsymbol{\varphi}_n^T\mathbf{K}_{ae}(V,\omega)\boldsymbol{\varphi}_m)dx$$

$$\tilde{C}_{nm}^{(ae)}(V,\omega)=\int_L(\boldsymbol{\varphi}_n^T\mathbf{C}_{ae}(V,\omega)\boldsymbol{\varphi}_m)dx$$

(6)

where L is the span length. $\mathbf{G}_{Q\,Buff}(\omega)$ is the complex buffeting wind action defined by

$$\mathbf{G}_{\tilde{Q}\,Buff}(\omega)=[\cdots G_{\tilde{Q}\,Buff_i}\cdots]^T, \quad G_{\tilde{Q}\,Buff_i}(\omega)=\int_L\boldsymbol{\varphi}_i^T(x)\mathbf{B}_{\mathbf{q}}(\omega)\mathbf{G}_v(x,\omega)dx$$

$$\mathbf{G}_v(x,\omega)=\begin{bmatrix}G_u & G_w\end{bmatrix}^T$$

$$\mathbf{B_q}(\omega) = \frac{\rho V B}{2} \begin{bmatrix} 2(D/B)\overline{C}_D A_{yu} & ((D/B)C'_D - \overline{C}_L)A_{yw} \\ 2\overline{C}_L A_{zu} & (C'_L + (D/B)\overline{C}_D)A_{zw} \\ 2B\overline{C}_M A_{\theta u} & BC'_M \cdot A_{\theta w} \end{bmatrix} \qquad (7)$$

where G_u, $n \in \{u, w\}$ are the Fourier transforms of the turbulence components in the vertical and horizontal direction, respectively; A_{mn}, $m \in \{y, z, \theta\}$ $n \in \{u, w\}$ symbolizes the cross sectional admittance functions; D denotes the height of the girder and $\overline{C}_n, C'_n, n \in \{D \text{ (drag)}, L \text{ (Lift)}, M, \text{ (Moment)}\}$ are the mean value and the derivative of the static wind force coefficients, respectively. The elements in the modal wind action spectral matrix may then be defined as follows:

$$S^+_{Q\ Buff_{ij}}(\omega) = \int_L \int_L \boldsymbol{\varphi}^T_i(x_1)\mathbf{B}_q(\omega)\mathbf{S}^+_V(\Delta x, \omega)\mathbf{B}^T_q(\omega)\boldsymbol{\varphi}_j(x_2)dx_1\,dx_2$$

$$\mathbf{S}^+_V(\Delta x, \omega) = \begin{bmatrix} S^+_{uu}(\Delta x, \omega) & S^+_{uw}(\Delta x, \omega) \\ S^+_{uw}(\Delta x, \omega) & S^+_{ww}(\Delta x, \omega) \end{bmatrix} \qquad (8)$$

Here, $\mathbf{S}^+_V(\Delta x, \omega)$ contains the cross-spectral densities of the velocity components of the wind field at two points with separation Δx; S^+_{uu} represents the cross-spectral density of the horizontal along-wind component; S^+_{ww} symbolizes the cross-spectral density of the vertical component, and S^+_{uw} is the cross-spectral density of the horizontal and vertical components. The spectral response matrix, containing the auto- and cross-spectra of the response components, is given by

$$\mathbf{S}^+_R(\omega, x_r) = \boldsymbol{\Phi}(x_r)\left[\mathbf{E}^{-1}_\eta(\omega)\mathbf{S}^+_{Q\ Buff}(\omega)\mathbf{E}^{-1^*}_\eta(\omega)\right]\boldsymbol{\Phi}^T(x_r)$$

$$\mathbf{E}_\eta(V, \omega) = \left[-\tilde{\mathbf{M}}_0\omega^2 + (\tilde{\mathbf{C}}_0 - \tilde{\mathbf{C}}_{ae}(V, \omega))i\omega + (\tilde{\mathbf{K}}_0 - \tilde{\mathbf{K}}_{ae}(V, \omega))\right] \qquad (9)$$

where $\mathbf{E}_\eta(V, \omega)$ is the impedance matrix. Applying this equation, the variances and covariance of the response components at the point x_r may be obtained by frequency domain integration.

The stability limit of an aeroelastic system may be defined by the combination of frequency and mean wind velocity that gives a singular impedance matrix (sometimes referred to as complex dynamic stiffness matrix). The flutter equations have been developed on this basis (Dyrbye and Hansen, 1997), and the criterion has been used for multimode calculations in Jain et al. (1996a) and Katsuchi et al. (1999). Since the impedance matrix is complex, it is convenient to use the modulus of its determinant as the stability indicator. Thus, the stability limit may be obtained by the following complex polynomial
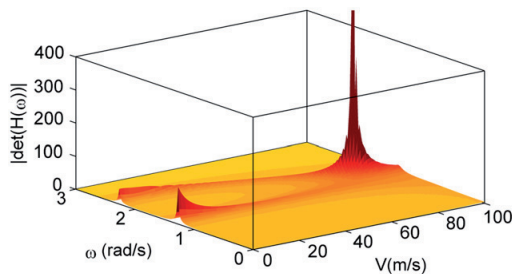
$$|\det(\mathbf{E}_\eta(\omega, V))| = 0 \qquad (10)$$

Fig. 3. The modulus of the determinant of the complex frequency response matrix, expressed as a function of frequency and mean wind speed.

Hence, the instability condition may be identified by an iterative search for the singular values. The determinant value is calculated for a sequence of velocities and frequencies rendering results similar to those shown in Fig. 3, where it is the determinant of the frequency response matrix that has been plotted producing a more illustrative representation. The search procedure is to identify the position of the peak in Fig. 3 and recalculate a small area around it with a denser grid on both axes, which will provide a lower determinant value. The procedure may be repeated until the determinant reaches a specified low value providing the required accuracy of the critical wind speed.

3. Modified quasi-steady modelling

Wind force coefficients, represented by their averages and derivatives, obtained from static wind tunnel tests may be used to quantify the self-excited forces. This is done by expressing the force coefficients as functions of the effective angle of attack, taking the motion of the cross section into account. The self-excited forces can then be approximated as follows (Davenport, 1962), see also for instance (Strømmen, 2006)

$$q_{y\ Se}(t) = \frac{1}{2}\rho V^2 B\left(-2(D/B)\overline{C}_D\frac{\dot{r}_y}{V} - ((D/B)C'_D - \overline{C}_L)\frac{\dot{r}_z}{V} + (D/B)C'_D r_\theta\right)$$

$$q_{z\ Se}(t) = \frac{1}{2}\rho V^2 B\left(-2\overline{C}_L\frac{\dot{r}_y}{V} - (C'_L + (D/B)\overline{C}_D)\frac{\dot{r}_z}{V} + C'_L r_\theta\right)$$

$$q_{\theta\ Se}(t) = \frac{1}{2}\rho V^2 B^2\left(-2\overline{C}_M\frac{\dot{r}_y}{V} - C'_M\frac{\dot{r}_z}{V} + C'_M r_\theta\right) \qquad (11)$$

Since the force coefficients are frequency-independent, the quasi-steady theory may be used to estimate the self-excited forces, both in time and frequency domain. However, since the measurements are carried out on a fixed section model, the theory is only valid when the oscillation period of the structure is high, relative to the time it takes, for a parcel of air, to travel past the cross section (which implies high reduced velocities). As pointed out by Hjorth-Hansen (1993), the quasi-steady theory does not provide any damping contribution related to the torsional motion, which is a weakness of this approach for cross sections, where experiments indicate the opposite. The torsional damping can, however, be included in the model by selecting a velocity reference point different from the shear centre. In the airfoil theory, the $^3/_4$ point is traditionally used (see for instance Fung (1955)), but as pointed out by Scanlan et al. (1974), this is a consequence of the simplicity of the airfoil, and cannot be used directly for a bluff body. Borri and Costa (2004) have introduced torsional damping by using the leading edge of the profile as a reference point, assuming that the action is driven by phenomena occurring at the edge. However, according to Borri and Costa (2004), this assumption is considered valid only when the shape of the profile is fairly "aerodynamic", and the flow separation does not affect the section aerodynamics significantly.

An alternative approach is suggested below, where the experimental results obtained for the aerodynamic derivatives are used to estimate frequency-independent aerodynamic coefficients. The self-excited forces, expressed in the frequency domain, using the aerodynamic derivatives, can generally be written as follows (Scanlan and Tomko, 1971)

$$q_y = \frac{1}{2}\rho V^2 B\left(KP^*_1\frac{\dot{r}_y}{V} + KP^*_2\frac{B\dot{r}_\theta}{V} + K^2 P^*_3 r_\theta + K^2 P^*_4\frac{r_y}{B} + KP^*_5\frac{\dot{r}_z}{V} + K^2 P^*_6\frac{r_z}{B}\right)$$

$$q_z = \frac{1}{2}\rho V^2 B\left(KH^*_1\frac{\dot{r}_z}{V} + KH^*_2\frac{B\dot{r}_\theta}{V} + K^2 H^*_3 r_\theta + K^2 H^*_4\frac{r_z}{B} + KH^*_5\frac{\dot{r}_y}{V} + K^2 H^*_6\frac{r_y}{B}\right)$$

$$q_\theta = \frac{1}{2}\rho V^2 B^2 \left(KA_1^* \frac{\dot{r}_z}{V} + KA_2^* \frac{B\dot{r}_\theta}{V} + K^2 A_3^* r_\theta + K^2 A_4^* \frac{r_z}{B} + KA_5^* \frac{\dot{r}_y}{V} + K^2 A_6^* \frac{r_y}{B} \right)$$

$$(12)$$

Here, $K=(\omega B)/V$ is the reduced frequency. During the present case study, the authors observed that the frequency dependency of some of the load coefficients (e.g., $K^2 H_3^*$) is weak for the bridge deck section considered. Hence, the self-excited forces can be modelled as frequency-independent, if the aerodynamic derivatives are approximated by the following expressions:

$$X_i^*(K) = x_i(1/K) \text{ when } i = 1,2,5 \text{ and } X_i^*(K) = x_i(1/K)^2 \text{ when } i = 3,4,6$$

$$(13)$$

where $X \in \{P,H,A\}$ and $x \in \{p,h,a\}$. This approximation is in fact similar to a rational function approach, but without the unsteady terms; see for instance Eq. (12a) in (Borri et al., 2002) or Eq. (9) in (Chen et al., 2000). A general polynomial expression obviously gives a more accurate fit to the experimental data than the constraints introduced in Eq. (13), but as will be shown in the numerical case study, these simplified expressions give fairly accurate results for a partially streamlined bridge deck cross section in wide reduced frequency ranges. The accuracy depends on the characteristics of the aerodynamic derivatives. If the important aerodynamic derivatives related to the velocities (H_1^*, H_2^*, A_1^*, A_2^*) and displacements (H_3^*, H_4^*, A_3^*, A_4^*) do not have an approximately linear or quadratic trend in an important reduced velocity range, the approximation becomes less accurate. However, most streamlined or partially streamlined cross sections fulfil these requirements. The validity of the approximation depends on how well the suggested expressions fit the experimental data. This is an advantage, since it enables the accuracy of the approximation to be assessed computationally. Based on these approximations,

the self-excited forces can be estimated as follows:

$$q_{y\,Se} = \frac{1}{2}\rho V^2 B \left(p_1 \frac{\dot{r}_y}{V} + p_2 \frac{B\dot{r}_\theta}{V} + p_3 r_\theta + p_4 \frac{r_y}{B} + p_5 \frac{\dot{r}_z}{V} + p_6 \frac{r_z}{B} \right)$$

$$q_{z\,Se} = \frac{1}{2}\rho V^2 B \left(h_1 \frac{\dot{r}_z}{V} + h_2 \frac{B\dot{r}_\theta}{V} + h_3 r_\theta + h_4 \frac{r_z}{B} + h_5 \frac{\dot{r}_y}{V} + h_6 \frac{r_y}{B} \right)$$

$$q_{\theta\,Se} = \frac{1}{2}\rho V^2 B^2 \left(a_1 \frac{\dot{r}_z}{V} + a_2 \frac{B\dot{r}_\theta}{V} + a_3 r_\theta + a_4 \frac{r_z}{B} + a_5 \frac{\dot{r}_y}{V} + a_6^* \frac{r_y}{B} \right) \quad (14)$$

Here, the parameters p_i, h_i and a_i are defined by Eq. (13) and derived applying experimentally defined aerodynamic derivatives and an appropriate measure of goodness-of-fit for the velocity range under consideration. It is seen that this model has more terms than the expressions of the buffeting theory given by Eq. (11). In particular, the additional coupling terms and the torsional damping term will give a more accurate description of the coupled flutter instability phenomenon.

4. Case study: the Hardanger Bridge

An eigenvalue analysis is carried out for the Hardanger Bridge subjected to dead loads, applying the computer program ALVSAT (Sintef, 1996). A total of 24 (the first 8 horizontal, 8 vertical and 8 torsional) vibration modes and corresponding undamped natural frequencies in still-air conditions were extracted. The vertical and torsional vibration modes are plotted in Fig. 4, and the basic properties of the 24 modes are summarised in Table 2. Since the main cables and the sides of the girder are coupled in the vertical direction, and the contribution from the mass of the two towers is negligible, the evenly distributed modal equivalent mass and mass moment of inertia are equal for all the vertical and torsional vibration modes, respectively. The mode shapes, however, are
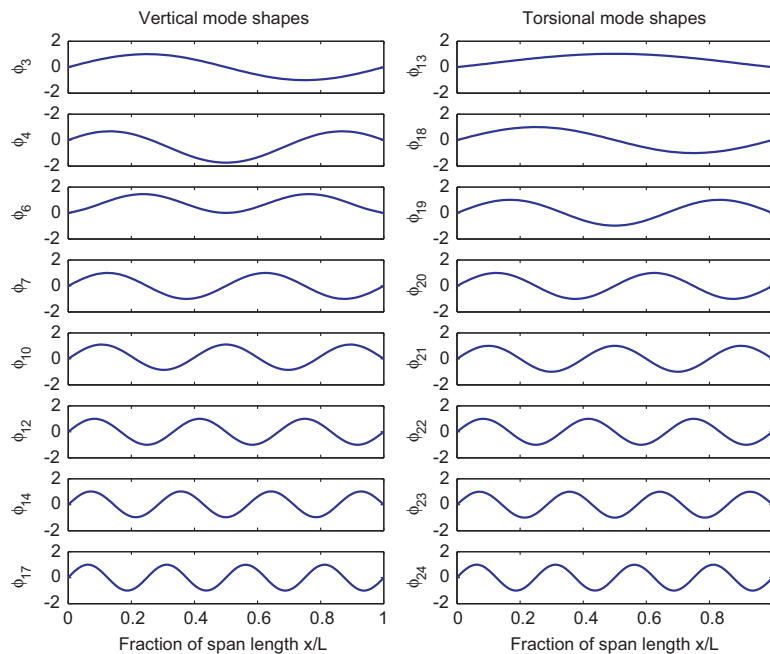

Fig. 4. The 16 first vertical and torsional still-air vibration modes for the Hardanger Bridge.

Table 2
Natural frequencies, damping ratios and modal equivalent evenly distributed mass or mass moment of inertia for the first 24 vibration modes of the Hardanger Bridge.

Mode no.	Natural frequency ω_i (rad/s)	Damping ratio ξ	Modal equivalent evenly distributed mass/mass moment of inertia $\tilde{m}_n$
1	0.32	0.005	10,470 (kg/m)
2	0.62	0.006	9400 (kg/m)
3	0.69	0.005	12,820 (kg/m)
4	0.89	0.006	12,820 (kg/m)
5	1.06	0.007	9510 (kg/m)
6	1.27	0.007	12,820 (kg/m)
7	1.34	0.007	12,820 (kg/m)
8	1.49	0.009	34,550 (kg/m)
9	1.57	0.010	34,190 (kg/m)
10	1.74	0.010	12,820 (kg/m)
11	1.86	0.015	9710 (kg/m)
12	2.10	0.015	12,820 (kg/m)
13	2.23	0.005	426,000 (kg/m m2)
14	2.53	0.020	12,820 (kg/m)
15	2.49	0.020	12,480 (kg/m)
16	2.63	0.025	11,020 (kg/m)
17	2.97	0.025	12,820 (kg/m)
18	3.37	0.006	426,000 (kg/m m2)
19	5.10	0.009	426,000 (kg/m m2)
20	6.76	0.012	426,000 (kg/m m2)
21	8.45	0.015	426,000 (kg/m m2)
22	10.14	0.020	426,000 (kg/m m2)
23	11.83	0.025	426,000 (kg/m m2)
24	13.515	0.030	426,000 (kg/m m2)

Table 3
Critical mean wind velocities, frequencies and reduced velocities for a selection of mode combinations for the Hardanger Bridge when the aerodynamic derivatives are used to describe the self-excited forces.

Mode combination	Critical velocity V_{CR} (m/s)	Critical frequency ω_{CR} (rad/s)	Reduced critical velocity $V_{CR}/(B\omega_{CR})$
4 and 13	98	1.18	4.5
6 and 13	84	1.54	3.0
3 and 18	138	1.95	3.9
4 and 19	229	2.31	5.4
7 and 20	281	3.82	4.0
4, 6, 13	78	1.63	2.6
3, 4, 6, 13, 18	78	1.63	2.6
8 vert.+8 torsional	79	1.63	2.7
24 modes.	79	1.63	2.7

different (see Fig. 4). The span length is $L = 1310$ m, the width and height of the partially streamlined girder displayed in Fig. 2 are $B = 18.3$ m and $D = 3.33$ m, respectively. The density of the air is assumed to be $\rho = 1.25$ kg/m³, and the cross-spectral densities of the wind field are assumed to be given by

$$S_{uu}^+(\omega) = \frac{40.58 V z \kappa}{(1+9.74\omega z/V)^{5/3}} \exp\left(-1.4\frac{\Delta x \omega}{V}\right)$$

$$S_{ww}^+(\omega) = \frac{0.82 V z \kappa}{(1+0.79\omega z/V)^{5/3}} \exp\left(-\frac{\Delta x \omega}{V}\right)$$

$$S_{uw}^+(\omega) = -\frac{2.23 V z \kappa}{(1+1.67\omega z/V)^{7/3}} \exp\left(-\frac{\Delta x \omega}{V}\right) \quad (15)$$

Here, κ is the roughness coefficient at the site that is assumed to be 0.0031. The spectral densities have been adjusted to predict the turbulence intensities, given by Statens-vegvesen (2006). The aerodynamic derivatives for the Hardanger Bridge are obtained by the procedure described by Jakobsen and Hjorth-Hansen (1995) and are given by Hansen et al. (2006) by a second-order polynomial expression. Since experimental data related to the horizontal motion are not available, the quasi-steady aerodynamic derivatives are used for the following terms:

$$P_1^* = -2\overline{C}_D \frac{D}{B}\left(\frac{1}{K}\right) \quad P_5^* = \left(\overline{C}_L - C'_D \frac{D}{B}\right)\left(\frac{1}{K}\right) \quad P_3^* = C'_D \frac{D}{B}\left(\frac{1}{K}\right)^2$$

$$H_5^* = -2\overline{C}_L\left(\frac{1}{K}\right) \quad A_5^* = -2\overline{C}_M\left(\frac{1}{K}\right) \quad P_2^* = P_4^* = P_6^* = H_6^* = A_6^* = 0 \quad (16)$$

where the static force coefficients from Hansen et al. (2006) are $\overline{C}_D = 0.70$, $C'_D = 0$, $\overline{C}_L = -0.25$, $C'_L = 2.4$, $\overline{C}_M = 0.01$ and $C'_M = 0.74$.

Two factors are found to greatly influence which of the modes are most likely to couple into a flutter motion: (1) the degree of shape-wise similarity and (2) the separation of the natural frequencies of the shape-wise similar vertical and torsional vibration modes. The critical mean wind velocity for a selection

of shape-wise similar mode combinations are given in Table 3, together with the critical flutter frequencies and the corresponding critical reduced velocities. Usually, it is the first vertical and torsional vibration modes that provide the lowest critical velocity, but as can be seen from the results, this is not the case for the Hardanger Bridge. The mode shape integrals, where perfect shape-wise similarity will obviously give 1, are estimated for combinations of modes 4 and 13 and modes 6 and 13 below.

$$\frac{\int_L \phi_4 \phi_{13}\,dx}{\int_L \phi_4^2\,dx}\frac{\int_L \phi_{13}\phi_4\,dx}{\int_L \phi_{13}^2\,dx} = 0.41 \quad \frac{\int_L \phi_6 \phi_{13}\,dx}{\int_L \phi_6^2\,dx}\cdot\frac{\int_L \phi_{13}\phi_6\,dx}{\int_L \phi_{013}^2\,dx} = 0.57 \quad (17)$$

As can be seen, modes 6 and 13 are significantly more shape-wise similar than modes 4 and 13. In addition, the natural frequencies of modes 6 and 13 are less separated than the natural frequencies of modes 4 and 13, and will therefore give a lower critical mean wind velocity. Since the stability limit converges when modes 4, 6 and 13 are used in the calculations, the results given in Table 3 indicate that the instability phenomenon is multimode-coupled flutter, where three still-air vibration modes give significant contributions. When all the modes presented in Fig. 4 are considered, the critical mean wind velocity increases by 1 m/s, which is probably because mode 13 is weakly shape-wise similar to mode 10. When the horizontal still-air vibration modes are included in the analysis, the critical mean wind velocity remains unchanged. The critical reduced velocity ranges 2.5–4.7, implying that the experimental data available for the aerodynamic derivatives must be extrapolated for some of the mode combinations.

The stability limits obtained for a selection of mode combinations, when the traditional quasi-steady theory is used to model the self-excited forces are shown in Table 4. Compared with the results presented in Table 3, the quasi-steady theory underestimates the critical velocity by over 40%, providing a stability limit that is very close to the design velocity, which is considered unacceptable. The main reason for this is as pointed out in Section 3, that the quasi-steady theory does not provide any torsional damping to the system. In our case study, the aerodynamic torsional damping is positive, for the considered cross section of the Hardanger Bridge, and will therefore increase the stability limit. This might not be the case for other types of cross sections.

To be able to determine frequency-independent force coefficients from the experimental results of the aerodynamic derivatives, it is important to know which of the aerodynamic derivatives are most important for an accurate prediction of the

self-excited forces. A study is carried out of how the stability limit for modes 4, 6 and 13 changes when the aerodynamic derivatives for the Hardanger Bridge are scaled separately by a factor λ. The results concerning H_n^* and A_n^*, $n \in \{1, 2, ..., 4\}$ are given in Table 5, and, as can be seen, it is $A_1^*, A_2^*, A_3^*, H_3^*$ and, to some extent, H_1^* that significantly influence the stability limit, while the other aerodynamic derivatives have a very little or minor influence. The importance of A_1^*, A_2^*, A_3^* and H_3^* in flutter stabilisation has also been pointed out by Matsumoto et al. (2007), Chen and Kareem (2008), and Chen (2007).

Least square fits of the expressions suggested in Eq. (13) are performed on the experimental results of the aerodynamic derivatives for the Hardanger Bridge given in (Hansen et al., 2006). The results plotted in Fig. 5 show that the approximate expressions represent the experimental results for the important aerodynamic derivatives with apparently fair accuracy. The largest discrepancy is for A_2^*, for which a second-order expression would give a better fit to the data. This implies that the approximation overestimates the torsional damping at low reduced velocities, while it underestimates the damping at higher reduced velocities. It is important to notice that low values of the aerodynamic derivatives H_1^* and A_2^* give conservative results, while high values of the other aerodynamic derivatives give a lower stability limit. The resulting force coefficients are given below

$$h_1 = -2.734 \quad h_2 = 0.206 \quad h_3 = 2.271 \quad h_4 = -0.208$$
$$a_1 = -0.823 \quad a_2 = -0.258 \quad a_3 = 0.726 \quad a_4 = -0.037 \tag{18}$$

To investigate how well the modified quasi-steady coefficients describe the self-excited forces, the critical mean wind velocity is recalculated. The results given in Table 6 confirm that the approximate expressions give an accurate description of the self-excited forces, since the calculated critical mean wind velocities differ only by about 3% from the results presented in Table 3, where the frequency-dependent model with the aerodynamic derivatives have been used. The accuracy of the

critical frequency is within 5% for the combinations of modes 4 and 13 and the combination of modes 6 and 13, while the prediction of the critical frequency for the combination of modes 4 and 13 is less accurate. This is because the critical flutter
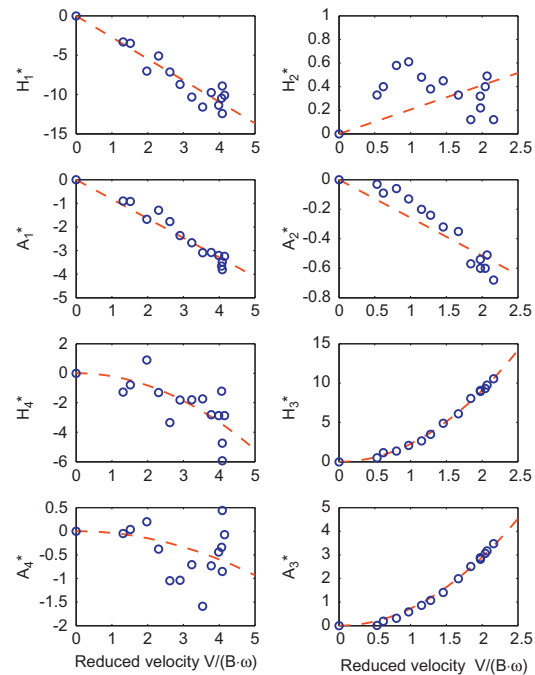

Fig. 5. The aerodynamic derivatives for the cross section of the Hardanger Bridge. Open circles refer to data obtained in wind tunnel tests, and dashed lines represents constraint curves (see Eq. (14)) fitted to the data.

Table 4
Critical mean wind velocities, frequencies and reduced velocities for a selection of mode combinations for the Hardanger Bridge when the traditional quasi-steady theory is used to describe the self-excited forces.

Mode combination	Critical velocity V_{CR} (m/s)	Critical frequency ω_{CR} (rad/s)	Reduced critical velocity, $V_{CR}/(B\omega_{CR})$
4 and 13	59	1.93	1.7
6 and 13	50	2.02	1.4
4, 6 and 13	44	2.07	1.2

Table 6
Critical mean wind velocities, frequencies and reduced velocities for a selection of mode combinations for the Hardanger Bridge when the modified quasi-steady coefficients are used to describe the self-excited forces.

Mode combination	Critical velocity V_{CR} (m/s)	Critical frequency ω_{CR} (rad/s)	Reduced critical velocity $V_{CR}/(B\omega_{CR})$
4 and 13	93	1.40	3.6
6 and 13	80	1.66	2.6
4, 6 and 13	74	1.75	2.3

Table 5
Percentage change of the stability limit for the Hardanger Bridge for a combination of modes 4, 6 and 13 when each flutter derivative has been scaled separately by the factor λ.

Scaling factor λ	Aerodynamic derivatives							
	H_1^*	H_2^*	H_3^*	H_4^*	A_1^*	A_2^*	A_3^*	A_4^*
0.0	−4%	2%	–	1%	–	−37%	114%	0%
0.2	−4%	–	–	–	–	−26%	62%	–
0.4	−3%	–	–	–	–	−16%	36%	0%
0.6	−2%	–	9%	–	14%	−9%	20%	0%
0.8	−1%	–	4%	–	4%	−4%	8%	0%
1.0	0%	0%	0%	0%	0%	0%	0%	0%
1.2	2%	–	−3%	0%	−3%	4%	−7%	0%
1.4	4%	–	−6%	–	−6%	8%	−12%	0%
1.6	8%	−1%	−9%	−1%	−9%	13%	−17%	0%

velocity for this combination is close to the divergence velocity, which implies that the frequency is reduced rapidly at increasing velocities. The critical reduced velocities range 2.3–3.6, which indicate that the approximation is not sensitive to changes of the critical reduced velocity.

To ensure computationally stable behaviour of the bridge, all complex eigenvalues of the system equation must, as outlined in Section 2, have a negative real part (representing positive damping). If the modified quasi-steady coefficients are used to model the self-excited forces, the response may be estimated by direct numerical integration. Since only the stability limit is of interest, the modal buffeting forces are set to zero. The numerical integration is performed with the well-known Newmark method, applying $\beta = 1/6$ and $\gamma = 0.5$ (see, for instance, Zienkiewicz and Taylor, 2000). The responses for the critical mean wind velocity at $V = 74$ m/s, and higher than the critical mean wind velocity at $V = 77$ m/s, for a combination of modes 4, 6 and 13 given in Table 6, are plotted in Fig. 6. The free vibration response at the critical mean wind velocity clearly appears as an un-damped
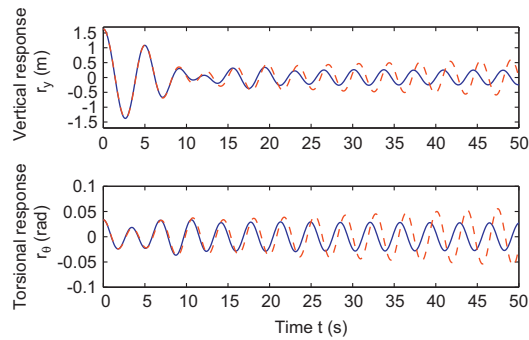

Fig. 6. Free vibration response of modes 4, 6 and 13 at the critical velocity $V = 74$ m/s (solid lines) and higher than the critical $V = 77$ m/s (dashed lines).
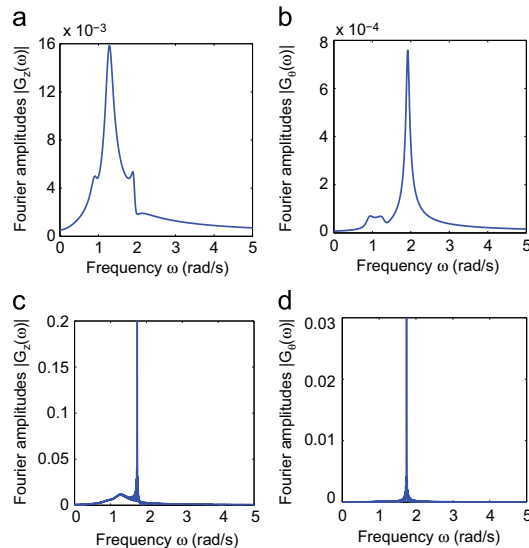

Fig. 7. Fourier amplitude spectra of the free vibration response for a combination of still-air modes 4, 6 and 13. (a) Vertical response, $V = 60$ m/s; (b) torsional response, $V = 60$ m/s; (c) vertical response, $V = 74$ m/s; and (d) Torsional response $V = 74$ m/s.

response. The Fourier amplitude spectra of the time series at mean wind velocities of 60 and 74.5 m/s are plotted in Fig. 7. For the case at 60 m/s, only small coupling effects are present, while a common frequency of 1.75 rad/s dominates both the vertical and torsional response at the onset of coupled flutter. The time domain simulations correspond well with the results presented in Table 6.

Since it is only the flutter vibration mode that has zero damping when the aeroelastic system becomes unstable, all the complex vibration modes other than the flutter vibration mode will be damped out during free vibration, as displayed in Fig. 6. This makes it possible to visualise the flutter vibration mode by calculating the free vibration response for the whole system. The flutter vibration modes (FVM) are shown for a selection of mode combinations in Fig. 8. The FVM are complex and will thus be time-dependent, but the time dependency seems low for the flutter modes in our case. As shown in Fig. 8 and Table 3, mode 13 can couple with both modes 4 and 6, which means that it can participate in two different bimodal flutter phenomena. The flutter vibration modes for the two cases are noticeably different as the combination of modes 4 and 13 gives the largest
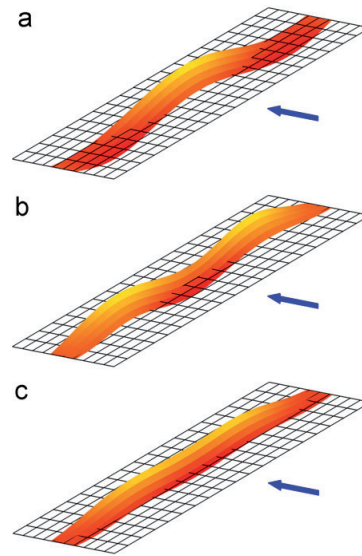

Fig. 8. The flutter vibration mode for combinations of still-air vibration modes (a) 4 and 13; (b) 6 and 13; and (c) 4, 6 and 13.
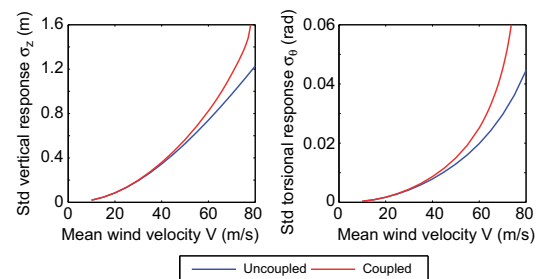

Fig. 9. Comparison of the standard deviation of the buffeting response at the mid-span of the bridge ($x/L = 0.5$) predicted by the uncoupled and coupled system of equations when all the vibration modes presented in Fig. 4 are included.

displacements at the mid-span of the girder, while the combination of 6 and 13 gives the largest displacements at the quarter points of the span. The flutter vibration mode for modes 4, 6 and 13 is quite different from the bimodal combinations as a larger part of the span moves up and down, providing a smaller curvature of the girder with respect to the horizontal axis. When more modes are included, the critical mean wind velocity does not change significantly, and neither does the flutter vibration mode. The time domain simulation of the flutter motion illustrates the possibilities of using the modified quasi-steady theory for response prediction in the time domain.

The effect of modal coupling on the response is illustrated in Fig. 9, where the buffeting response is assessed using a multimode and a mode-by-mode approach. The results indicate that the difference between a multimode and a mode-by-mode calculation is negligible when the mean wind velocity is lower than roughly half the stability limit, and that the difference increases with increasing mean wind velocity. The cross-spectral density of the horizontal and vertical component has negligible influence on the torsional response, while the response in the vertical direction is underestimated by 10% at the design mean wind velocity, if this cross-spectral density is not included.

The buffeting response when the aerodynamic derivatives, the quasi-steady theory, and the suggested modified quasi-steady coefficients are used to model the self-excited forces is shown in Fig. 10. As can be seen, the vertical response when the aero-dynamic derivatives and the modified quasi-steady coefficients are used is nearly identical, while the response when the quasi-steady theory is used is larger than the two other alternatives until the system becomes unstable at a velocity that is much
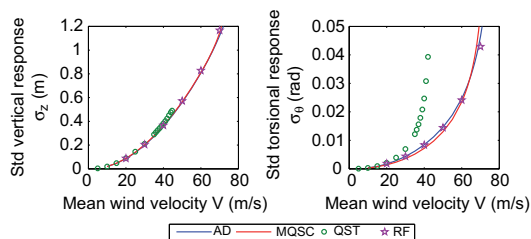
lower than the critical velocity provided by the other models considered. The torsional response when the modified quasi-steady coefficients are used to describe the self-excited forces is slightly lower than when the aerodynamic derivatives have been used. The inaccuracy is 13% at a velocity of 40 m/s, while the quasi-steady theory overestimates the response by 200% at the same velocity. Fig. 11 shows the modal damping and frequencies for a combination of still-air modes 6 and 13. The modified quasi-steady coefficients provide frequencies of good accuracy compared with the aerodynamic derivatives. The damping ratio for the vertical branch is also well captured, but the damping ratio for the torsional branch is not. The figure illustrates that the reason for the inaccuracy of the torsional response provided by the modified quasi-steady coefficients is poor modelling of the torsional damping provided by A_2^*.

The response spectral densities for the torsional and vertical response at a mean wind velocity of 40 m/s are shown in Fig. 12. As expected, the vertical response spectral density is captured with good accuracy, while the torsional response spectral density has a lower peak value, since the modified quasi-steady coefficients provide larger damping to the system than the aerodynamic derivative model. The figure also illustrates that the self-excited forces are most important near the peak in the power spectral density, since the differences are negligible elsewhere. The response provided by the modified quasi-steady coefficients underestimated the torsional response. The reason is that the values of A_2^* in the linear approximation are larger than the experimental data for low reduced velocities, which are

Fig. 10. Comparison of the standard deviations of the vertical and torsional buffeting response at the mid-span of the bridge ($x/L=0.5$) when the aerodynamic derivatives (AD), the modified quasi-steady coefficients (MQSC), the quasi-steady theory (QST) and rational functions (RF) are used to model the self-excited forces. All the vibration modes presented in Fig. 4 have been included.
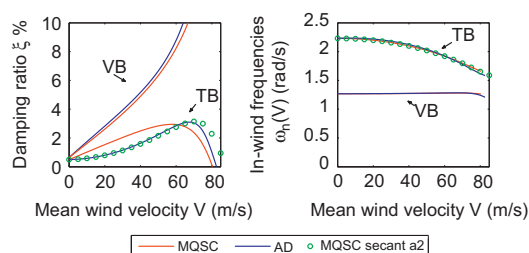

Fig. 12. Power spectral densities for the vertical and torsional response at a mean wind velocity of 40 (m/s) when the self-excited forces have been modelled by the aerodynamic derivatives (AD) and the modified quasi-steady coefficients (MQSC). All the vibration modes presented in Fig. 4 have been included.

Fig. 11. Comparison of the modal damping ratios and the in-wind frequencies for still-air modes 6 and 13 when the aerodynamic derivatives (AD), the modified quasi-steady coefficients (MQSC) and the improved modified quasi-steady coefficients, where a secant approximation have been used for A_2^* (MQSC secant a2), are used to model the self-excited forces. TB refers to the modal branch that corresponds to the torsional mode from still air and VB refers to the modal branch that corresponds to the vertical mode from still air.

Fig. 13. (a) Comparison of the standard deviation of the torsional response when aerodynamic derivatives (AD) and the improved modified quasi-steady coefficients, where A_2^* has been approximated by a secant (MQSC Secant a_2) have been used to model the self-excited forces. (b) Comparison of the power spectral density at a mean wind velocity of 40 m/s predicted by the two load models. All the vibration modes presented in Fig. 4 have been included.

important when the velocity ranges 30–60 m/s. As pointed out above, it is conservative to assume lower values for A_2^*, and a more reasonable fit to the experimental data would be obtained by assuming a smaller a_2. A better approach is to first estimate the torsional in-wind frequency and further calculate the corresponding reduced velocity. The a_2 coefficient may then be adjusted so that better accuracy at this reduced velocity is achieved. As explained above, the approximation of A_2^* must be linear to achieve a frequency-independent description of the self-excited forces. This implies that this aerodynamic derivative may be approximated by a straight line starting in the origin and intersecting the experimental data curve, corresponding to the dominating reduced velocity, at hand (a secant approximation). In Fig. 13, the torsional response and the power spectral density of the torsional response are shown when the secant approximation outlined above has been used for a_2. As can be seen from the figure, the torsional response predicted by this alternative is nearly, exactly the same as the response provided by the aerodynamic derivatives, and the peak in the power spectral density is well captured. The damping predicted by the secant model is shown in Fig. 11, and, as can be seen, the damping of the torsional branch is well captured for all interesting velocities

It is interesting to compare the above-described results obtained using aerodynamic derivatives, quasi-steady theory, and modified quasi-steady theory with results derived by a time domain technique applying the Fourier transformation of the frequency-dependent aerodynamic derivatives, described by smooth curves, fitted to the experimental data. The applied time domain technique is based on a rational function approximation (see, for instance, Bucher and Lin, 1988, for details). This gives the following approximations for the aerodynamic derivatives related to velocities (H_1^*, H_2^*, A_1^*, A_2^*) and displacements (H_3^*, H_4^*, A_3^*, A_4^*),

herein represented by H_4^* and H_1^*.

$$H_4^* = \hat{V}^2 \left(A_1^{(zz)} + \sum_{l=1}^{L} \frac{A_{l+3}^{(zz)}}{\left[(d_l^{(zz)} \hat{V})^2 + 1 \right]} \right), \quad H_1^* = \hat{V} \left(A_2^{(zz)} + \hat{V}^2 \sum_{l=1}^{L} \frac{A_{l+3}^{(zz)} d_l^{(zz)}}{\left[(d_l^{(zz)} \hat{V})^2 + 1 \right]} \right)$$

(19)

Here A_n, $n \in \{1, ..., l+3\}$, and d_l are coefficients determined by least squares fit to the experimental data. The index (zz) indicates that the coefficients are related to the vertical force caused by the vertical motion. The response obtained using rational functions with 1 and 4 exponential filters for the aerodynamic derivatives related to vertical and torsional motion, respectively, is shown in Fig. 10. The outcome is almost identical to the response obtained using frequency domain technique with aerodynamic derivatives (identified by AD in Fig. 10).

The various vibration modes may contribute differently to the response at different points along the girder. This implies that it is possible that the spectral density has more than one peak or has a peak with a different frequency than, for instance, the situation at the mid-span. However, it is common that the response is dominated by one mode in each direction for the entire structure. To illustrate this, the standard deviation of the torsional and vertical response along the girder at a mean wind velocity of 40 m/s is shown in Fig. 14. As can be seen, the modified quasi-steady coefficients capture the response well, especially when a secant approximation is used for A_2^*. It may be concluded that the modified quasi-steady coefficients can produce results with greatly improved accuracy, compared with the traditional quasi-steady approach, and it can provide results with good accuracy, compared with the aerodynamic derivatives, depending on how well the approximation fits the experimental results.
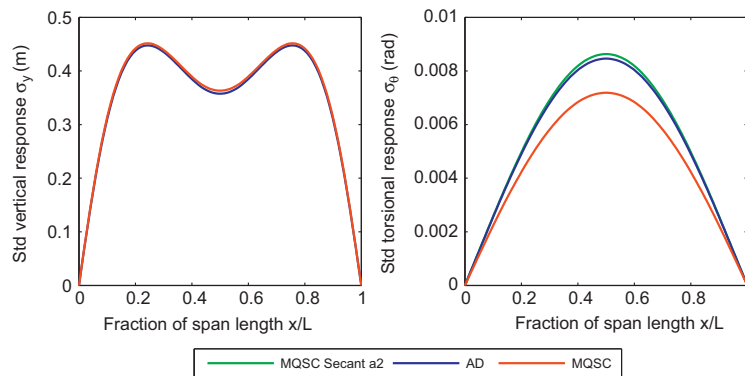
Fig. 14. Comparison of the standard deviations of the vertical and torsional response along the girder at a mean wind velocity of 40 m/s when the aerodynamic derivatives (AD), the modified quasi-steady coefficients (MQSC) and the improved modified quasi-steady coefficients, where a secant approximation has been used for A_2^* (MQSC secant a_2). All the vibration modes presented in Fig. 4 have been included.

Table 7
Comparison of the critical mean wind velocities, frequencies and reduced mean wind velocities provided by the aerodynamic derivatives, the quasi-steady theory, the modified quasi-steady coefficients theory and the critical velocity measured in turbulent flow.

Method of analysis	Critical velocity V_{CR} (m/s)	Critical frequency ω_{CR} (rad/s)	Reduced critical velocity $V_{CR}/(B\omega_{CR})$
Aerodynamic derivatives Eq. (12)	6.83	7.79	2.40
Quasi-steady theory Eq. (11)	3.70	9.50	1.06
Modified quasi-steady theory Eq. (14)	6.52	8.20	2.17
Measured in turbulent flow (wind tunnel experiment)	6.47	–	–

It is also interesting to compare the results provided by the aerodynamic models discussed in this article with the observations in wind tunnel experiments. Numerical stability analyses are therefore carried out on the section model used in wind tunnel experiments (Hansen et al., 2006). The mass of the section model is $\tilde{m}_z = 8793\,g$, and the mass moment of inertia is $\tilde{m}_\theta = 1.23\,gmm^2$. The natural frequency and damping ratio of the vertical vibration mode are $\omega_z = 5.8$ rad/s and $\xi_z = 0.004$ and for the torsional vibration mode $\omega_\theta = 10.1$ rad/s and $\xi_\theta = 0.003$

The stability limits are calculated using the aerodynamic derivatives, the quasi-steady theory and the modified quasi-steady coefficients. The results are given in Table 7. Two of the three approaches provide results with acceptable accuracy. The quasi-steady theory underestimates the stability limit by more than 40%, which is unacceptable for practical purposes. The stability limit obtained by the modified quasi-steady coefficients differs from the results predicted by the aerodynamic derivatives by only 4–5%. Both the aerodynamic derivatives and the modified quasi-steady coefficients overestimate the stability limit, compared with the wind tunnel measurements. The main reason for this is perhaps that the stability limit in the wind tunnel tests is defined as the mean wind velocity, where the vibrations become large, which implies that the experiment will be stopped before the actual theoretical stability limit is reached. Furthermore, the response is large near the stability limit, which implies that the assumption of linearity in Eq. (12) is questionable.

5. Concluding remarks

The critical mean wind velocities have been calculated for several mode combinations for the Hardanger Bridge and the section model used in the wind tunnel tests. The self-excited forces have been modelled using aerodynamic derivatives and the quasi-steady theory, and furthermore by applying a modified quasi-steady approach introduced and explained above. The results presented show that the governing instability phenomenon for the Hardanger Bridge is multimodal coupled flutter, where three still-air vibration modes participate. The multimode effects are accurately captured by the aerodynamic derivatives and the suggested modified quasi-steady theory. The classical quasi-steady theory on the other hand severely underestimated the critical velocity for both the section model and the full-scale bridge, and should not be used to model the self-excited forces unless the design mean wind velocity is well below half the critical mean wind velocity. The modified quasi-steady approach, where the experimental results of the aerodynamic derivatives are used to obtain frequency-independent force coefficients, provided stability limits for both the full-scale bridge and the section model that differ by only 4–5% from the results obtained when the frequency-dependent model with the aerodynamic derivatives are used. The analyses showed that the approximation of torsional damping was more important for the response estimates than the stability limit. However, it has been shown that this uncertainty can be eliminated by adjusting the modified quasi-steady coefficients, so that the important range of reduced velocities is accurately represented. It may be concluded that the modified quasi-steady approach suggested in this study provides adequate estimates for engineering purposes of both the response and the stability limit for the case dealt with here.

The flutter vibration modes have been visualized, and the results clearly illustrate the flutter vibration mode, where the three modes interact, result in a smaller curvature of the girder with respect to the horizontal axis. This provides a motion that is more shape-wise similar in the twisting and vertical directions, relative to the bimodal flutter behaviour. The time domain simulations of the flutter motion illustrate the possibilities of using the modified quasi-steady theory for time domain simulations of the wind-induced response.

References

Agar, T.J.A., 1989. Aerodynamic flutter analysis of suspension bridges by a modal technique. Engineering Structures 11, 75–82.

Bartoli, G., Mannini, C., 2008. A simplified approach to bridge deck flutter. Journal of Wind Engineering and Industrial Aerodynamics 96, 229–256.

Borri, C., Costa, C., 2004. Quasi-steady analysis of a two-dimensional bridge deck element. Computers and Structures 82, 993–1006.

Borri, C., Costa, C., Zahlten, W., 2002. Non-stationary flow forces for the numerical simulation of aeroelastic instability of bridge decks. Computers and Structures 80, 1071–1079.

Bucher, C.G., Lin, Y.K., 1988. Stochastic stability of bridges considering coupled modes. J. Eng. Mech.-ASCE 114, 2055–2071.

Chen, X., Kareem, A., 2008. Identification of critical structural modes and flutter derivatives for predicting coupled bridge flutter. Journal of Wind Engineering and Industrial Aerodynamics 96, 1856–1870.

Chen, X., Matsumoto, M., Kareem, A., 2000. Aerodynamic coupling effects on flutter and buffeting of bridges. Journal of Engineering Mechanics 126, 17–26.

Chen, X., 2007. Improved understanding of bimodal coupled bridge flutter based on closed-form solutions. Journal of Structural Engineering—ASCE 133, 22–31.

Chen, X., Kareem, A., 2001. Nonlinear response analysis of long-span bridges under turbulent winds. Journal of Wind Engineering and Industrial Aerodynamics 89, 1335–1350.

Davenport, A.G., 1962. Response of slender line like structures to a gusty wind. The Institution of Civil Engineers 23, 389–408.

Dyrbye, C., Hansen, S.O., 1997. Wind Loads on Structures. Wiley, Chichester.

Fung, Y.C., 1955. An Introduction to the Theory of Aeroelasticity. Wiley, New York.

Gu, M., Chen, S.R., Chang, C.C., 2002. Control of wind-induced vibrations of long-span bridges by semi-active lever-type TMD. Journal of Wind Engineering and Industrial Aerodynamics 90, 111–126.

Hansen, S.O., Lollesgaard, M., Rex, S., Jakobsen, J.B., Hansen, E.H., 2006. The Hardanger Bridge: Static and Dynamic Wind Tunnel Tests with a Section Model. Svend Ole Hansen ApS, Copenhagen.

Hjorth-Hansen, E. 1993. Fluctuating drag lift and overturning moment for a line-like structure predicted (primarily) from static mean loads.

Jain, A., Jones, N.P., Scanlan, R.H., 1996a. Coupled aeroelastic and aerodynamic response analysis of long-span bridges. Journal of Wind Engineering and Industrial Aerodynamics 60, 69–80.

Jain, A., Jones, N.P., Scanlan, R.H., 1996b. Coupled flutter and buffeting analysis of long-span bridges. Journal of Structural Engineering—ASCE 122, 716–725.

Jakobsen, J.B., Hjorth-Hansen, E., 1995. Determination of the aerodynamic derivatives by a system-identification-method. Journal of Wind Engineering and Industrial Aerodynamics 57, 295–305.

Katsuchi, H., Jones, N.P., Scanlan, R.H., 1999. Multimode coupled flutter and buffeting analysis of the Akashi-Kaikyo bridge. Journal of Structural Engineering—ASCE 125, 60–70.

Katsuchi, H., Jones, N.P., Scanlan, R.H., Akiyama, H., 1998. Multi-mode flutter and buffeting analysis of the Akashi-Kaikyo bridge. Journal of Wind Engineering and Industrial Aerodynamics 77–8, 431–441.

Kwon, S.-D., Park, K.-S., 2004. Suppression of bridge flutter using tuned mass dampers based on robust performance design. Journal of Wind Engineering and Industrial Aerodynamics 92, 919–934.

Körlin, R., Starossek, U., 2007. Wind tunnel test of an active mass damper for bridge decks. Journal of Wind Engineering and Industrial Aerodynamics 95, 267–277.

Larsen, A., Svensson, E., Andersen, H., 1995. Design aspects of tuned mass dampers for the Great-Belt-East-Bridge approach spans. Journal of Wind Engineering and Industrial Aerodynamics 54, 413–426.

Matsumoto, M., Mizuno, K., Okubo, K., Ito, Y., Matsumiya, H., 2007. Flutter instability and recent development in stabilization of structures. Journal of Wind Engineering and Industrial Aerodynamics 95, 888–907.

Matsumoto, M., Okubo, K., Ito, Y., Matsumiya, H., Kim, G., 2008. The complex branch characteristics of coupled flutter. Journal of Wind Engineering and Industrial Aerodynamics 96, 1843–1855.

Omenzetter, P., Wilde, K., Fujino, Y., 2000. Suppression of wind-induced instabilities of a long span bridge by a passive deck-flaps control system: Part I: formulation. Journal of Wind Engineering and Industrial Aerodynamics 87, 61–79.

Scanlan, R.H., Beliveau, J.-G., Budlong, K.S., 1974. Indicial aerodynamic functions for bridge decks. Journal of the Engineering Mechanics Division 100, 657–672.

Scanlan, R.H., Tomko, J.J., 1971. Airfoil and bridge deck flutter derivatives. Journal of the Engineering Mechanics Division 97, 1717–1737.

Simiu, E., Miyata, T., 2006. Design of Buildings and Bridges for Wind a Practical Guide for ASCE-7 Standard Users and Designers of Special Structures. Wiley, Hoboken, N.J.

Simiu, E., Scanlan, R.H., 1996. Wind Effects on Structures Fundamentals and Applications to Design 3rd Ed. Wiley, New York.

Sintef, 1996. "ALVSAT version 3.7 theory manual, user manual and test manual." SINTEF Division of Structural Engineering, Norway.

Statens-vegvesen, 2006. The Hardanger Bridge Design Basis—wind characteristics. The Norwegian Public Roads Administration.

Strømmen, E.N., 2006. Theory of Bridge Aerodynamics. Sprqinger, Berlin.

Wilde, K., Fujino, Y., 1998. Aerodynamic control of bridge deck flutter by active surfaces. Journal of Engineering Mechanics 124, 718–726.

Wilde, K., Fujino, Y., Kawakami, T., 1999. Analytical and experimental study on passive aerodynamic control of flutter of a bridge deck. Journal of Wind Engineering and Industrial Aerodynamics 80, 105–119.

Yang, Y.X., Ge, Y.J., 2009. Aerodynamic flutter control for typical girder sections of long-span cable-supported bridges. Wind Struct. 12, 205–217.

Zienkiewicz, O.C., Taylor, R.L., 2000. The Finite Element Method 5th Ed. Butter-worth-Heinemann, Oxford.

Erratum

Erratum to "Simplified prediction of wind-induced response and stability limit of slender long-span suspension bridges, based on modified quasi-steady theory: A case study" [J. Wind Eng. Ind. Aerodyn. 98 (2010), 730–741]

Ole Øiseth, Anders Rönnquist, Ragnar Sigbjörnsson*

Department of Structural Engineering, Norwegian University of Science and Technology, 7491 Trondheim, Norway

The publisher regrets that on page 730, the first sentence in second column of the Introduction should read:

[…] These issues have been addressed in several papers (Bartoli and Mannini, 2008; Chen and Kareem, 2008; Chen, 2007; Jakobsen and Hjorth-Hansen, 2007; Larsen et al.,1995; Matsumoto et al., 2007; Matsumoto et al., 2008).

Consequently, the following should be added to the list of references (see page 740 in the published paper):

Jakobsen, J.B., Hjorth-Hansen, E., 2007. Arne Selberg's formula for flutter speed in light of multimodal flutter analysis. Twelfth International Conference on Wind Engineering, Cairns, Australia.

The publisher would like to apologise for any inconvenience caused.

Paper II

Ole Øiseth, Ragnar Sigbjörnsson

An alternative analytical approach to prediction of flutter stability limits of cable supported bridges.

An alternative analytical approach to prediction of flutter stability limits of cable supported bridges

Ole Øiseth, Ragnar Sigbjörnsson*

Department of Structural Engineering, Norwegian University of Science and Technology, 7491 Trondheim, Norway

ARTICLE INFO

ABSTRACT

This paper presents a simplified analytical formulation, including closed-form algebraic expressions, for determining the critical flutter velocity of cable supported bridges. The formulae have been developed from the fundamental aeroelastic equations by introducing two assumptions: (1) Flutter derivatives may be approximated by expressions providing a frequency-independent description of self-excited forces. (2) The critical frequency is on the torsional branch of the solution and may be approximated by an uncoupled system of equations. The formulae have been tested for two typical cross sections, for a wide range of hypothetical structural configurations and the structural configurations of some well-known bridges. The numerical results produced by the formulae have been compared with results obtained by complex eigenvalue analysis, and it is concluded that the formulae give satisfactory results for all the cases considered. It is well known that multimodal effects may reduce the stability limits of an aeroelastic system. Hence, multimodal effects have been carefully studied to provide new insight into when a bimodal approach is sufficient, and when a more comprehensive multimodal approach is needed.

© 2011 Elsevier Ltd. All rights reserved.

1. Introduction

Despite great progress in recent years in predicting the flutter stability limit of cable supported bridges, simplified methods are still considered important in the preliminary design of long-span bridges and in the design of medium-span bridges, in particular when approximate methods, e.g. [1–3], are used to evaluate the structural properties. Simplified methods are also convenient when assessing the reliability of cable-supported bridges against flutter failure [4]. Selberg's formula [1,5,34] has been widely used for this purpose since its publication almost 50 years ago. It predicts the stability limit of a bimodal system with reasonable accuracy if the still-air torsional and vertical vibration modes have a perfect shapewise similarity, and the aerodynamic properties of the cross section are similar to those of an ideal flat plate. Selberg's formula may also be combined with an aerodynamic performance index obtained from wind tunnel tests with a scaled section model to enhance its predictability. Independently Rocard developed a formula published in 1963 that is similar to Selberg's formula. The flutter velocity predicted by the two formulae have been compared in [6], and the results deviate from each other by only a few percent. Another formula has been suggested by Nakamura [7], which is identical to Selberg's formula if specific load coefficients are introduced. The simplified solution has been developed by studying the harmonic solution of the bimodal system of equations. Simplified expressions have been developed for the frequency ratio,

---

* Corresponding author.
E-mail addresses: ole.oiseth@ntnu.no (O. Øiseth), ragnar.sigbjornsson@ntnu.no (R. Sigbjörnsson).

the ratio of the complex amplitudes of the vertical and torsional motion, the modal damping ratio and the phase angle between the vertical and torsional motion by neglecting terms of less importance. Gimsing [8] has also suggested a formula, which has been developed using the expression for the aerostatic pressure on the cross section. The formula agrees reasonably well with Selberg's formula. More recently Bartoli and Mannini [9] have developed a simplified approach based on the flutter equations. The importance of each term in the equations has been studied for a range of configurations, and the least significant terms have been neglected to provide the simplified solution. Chen [10] has also contributed an approximate closed-form solution of the flutter stability limit that is similar to Selberg's formula, but with an analytical basis for the aerodynamic performance index. The index depends on the flutter derivatives $H_3^*, A_1^*, A_2^*, A_3^*$, the torsional damping ratio and the shapewise similarity of the still-air vibration modes. The index is a function of reduced frequency, but the frequency dependency is low for some cross sections, which implies that it may be approximated as a constant. All the simplified solutions mentioned above are more or less related to each other since they have been developed from the same fundamental aeroelastic equilibrium conditions, but with different approximations to provide the simplified solution.

In this paper an alternative analytical approach to simplified flutter prediction is presented. The formulae presented have been developed from the fundamental flutter equations [11,12]. Further, it has been assumed that the critical frequency is on the torsion branch of the solution system, to produce a simplified expression. Nakamura [7] has developed a formula for the critical frequency, assuming that the modal frequencies may be approximated by the uncoupled system of equations. This assumption has been confirmed by Chen and Kareem [13], and is adopted in this paper, but with a different expression for the critical frequency. The authors have discovered that the flutter derivatives for some common cross sections may be locally approximated by expressions providing a frequency-independent description of self-excited forces [14]. This implies that the stiffness and damping terms are assumed to be proportional to the squared reduced velocity and the reduced velocity, respectively. This paper shows how this assumption may further simplify the governing equations, making it possible to develop closed-form solutions of the flutter stability limit of cable-supported bridges. The formulae presented are more detailed than the formulae developed by Selberg and Rocard since the effect of imperfect shapewise similarity and the actual aerodynamic properties of the cross section have been included, but simpler than the expressions provided by Chen [10] and Bartoli and Mannini [9], since the simplified aerodynamic model presented above has been introduced in the fundamental aeroelastic equations. The mean wind direction is assumed perpendicular to the bridge, but the theory can be extended for cases with skew wind. In [15,16] it has been shown how the system matrices may be developed for skew winds, and, as can be seen, the flutter derivatives must then be measured at the relevant yaw angle. Further, the influence of the self-excited forces associated with the horizontal degree of freedom has been neglected. In [17] it is shown that for one particular case, the flutter derivatives related to the horizontal motion have a stabilizing effect, but that it is not necessarily conservative to obtain the flutter derivatives with a section model with only two degrees of freedom. On the other hand, it has also been observed, for instance by Katsuchi et al. [18], that the flutter derivatives related to the horizontal motion have a destabilising effect. However, in most cases flutter is generated by a main pair of vertical and torsional modes, with secondary contributions from other modes. This implies that a bimodal consideration with the relevant torsional and vertical vibration modes may serve as an approximation of the critical flutter velocity.

In the formulae presented in this study, the flutter derivatives for the cross section are needed to derive the frequency-independent load coefficients. Experimental results for the flutter derivatives for numerous cross sections have been reported in the literature, and it is common to use girders that are similar to the ones that have been used before when designing cable-supported bridges. This implies that a good estimate of the load coefficients can be found in the published literature; thus, formulae may be used in preliminary designs and when designing medium-span bridges without experimental results of the flutter derivatives. The accuracy of the simplified aerodynamic model presented above is obviously a crucial issue, but most commonly used streamlined or partially streamlined cross sections have flutter derivatives that have a shape where the simplified aerodynamic model presented above gives a satisfying fit to the experimental data in the important reduced-frequency range, see, for instance, the flutter derivatives presented in [19–21]. Su et al. [22] proposed a modified time domain approach, where the traditional quasi-steady theory using static load coefficients, is modified introducing correction coefficients. It is further pointed out by Su et al. [22] that these coefficients do not change significantly with variation in frequency, which supports the suggestion presented above.

The flutter equations provide the stability limit for two still-air vibration modes, but as has been seen in some bridge projects, e.g. [18], flutter where several modes participate may occur, making a multimodal approach necessary. A full understanding of the multimodal flutter phenomenon has not been achieved. Therefore, multimodal effects have been carefully studied in this paper, more specifically, how the shapewise similarity and separation on the frequency axis affects possible reduction of the stability limit. The results presented may be used to evaluate whether a simple bimodal consideration is sufficient or not.

2. Modelling of aeroelastic systems

The dynamic equilibrium condition is defined in still-air modal generalised coordinates. The vibration modes and natural frequencies are obtained using expected (mean) load conditions, such that the geometric stiffness of the structure is properly represented. The self-excited forces are assumed to be given by flutter derivatives obtained from wind tunnel
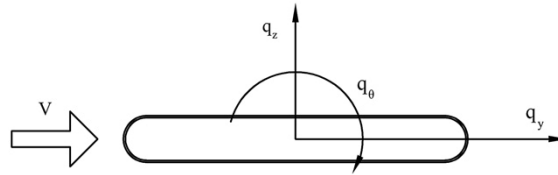
Fig. 1. Aerodynamic forces acting on a cross section of the bridge deck.

tests with a section model [5,23]. It is assumed that the flutter derivatives are valid for the (static) deformation of the structure. The definition of the axis system is shown in Fig. 1, and the displacement components r_y, r_z, r_θ are positive in the same directions as the forces q_y, q_z, q_θ.

The forces acting on a girder can be divided into four parts: (1) a mean value of wind forces, (2) buffeting forces induced by turbulence in the wind field, (3) forces generated by vortex shedding, and (4) self-excited forces generated by the motion of the structure. The focus of the present study is on the self-excited forces defined by the following equations:

$$q_y^{Se} = \frac{1}{2}\rho V^2 B\left(KP_1^* \frac{\dot{r}_y}{V} + KP_2^* \frac{B\dot{r}_\theta}{V} + K^2 P_3^* r_\theta + K^2 P_4^* \frac{r_y}{B} + KP_5^* \frac{\dot{r}_z}{V} + K^2 P_6^* \frac{r_z}{B}\right)$$

$$q_z^{Se} = \frac{1}{2}\rho V^2 B\left(KH_1^* \frac{\dot{r}_z}{V} + KH_2^* \frac{B\dot{r}_\theta}{V} + K^2 H_3^* r_\theta + K^2 H_4^* \frac{r_z}{B} + KH_5^* \frac{\dot{r}_y}{V} + K^2 H_6^* \frac{r_y}{B}\right)$$

$$q_\theta^{Se} = \frac{1}{2}\rho V^2 B^2\left(KA_1^* \frac{\dot{r}_z}{V} + KA_2^* \frac{B\dot{r}_\theta}{V} + K^2 A_3^* r_\theta + K^2 A_4^* \frac{r_z}{B} + KA_5^* \frac{\dot{r}_y}{V} + K^2 A_6^* \frac{r_y}{B}\right) \quad (1)$$

where V is the mean wind velocity, ρ is the air density, B is the width of the girder, $K = B\omega/V$ is the reduced frequency of motion, and P_n^*, H_n^*, A_n^*, $n \in \{1,2,\ldots,6\}$ are the dimensionless flutter derivatives, which are treated as cross sectional properties that are functions of the reduced frequency of motion. In the following it is assumed that the self-excited forces can be treated separately from the other wind-related forces mentioned above.

The flutter equations, [11,12,24] (see also Appendix A), may be used to estimate the critical mean wind velocity. The starting point is a bimodal system, where each mode is restricted to vertical or torsional motion. The modal equilibrium conditions, considering only the self-excited forces, are given as

$$[-\omega^2 \tilde{M}_z + 2\xi_z \omega_z \tilde{M}_z i\omega + \tilde{M}_z \omega_z^2]G_z(\omega) = [\tilde{C}_{zz}i\omega + \tilde{K}_{zz}]G_z(\omega) + [\tilde{C}_{z\theta}i\omega + \tilde{K}_{z\theta}]G_\theta(\omega)$$

$$[-\omega^2 \tilde{M}_\theta + 2\xi_\theta \omega_z \tilde{M}_\theta i\omega + \tilde{M}_\theta \omega_\theta^2]G_\theta(\omega) = [\tilde{C}_{\theta z}i\omega + \tilde{K}_{\theta z}]G_z(\omega) + [\tilde{C}_{\theta\theta}i\omega + \tilde{K}_{\theta\theta}]G_\theta(\omega) \quad (2)$$

where ω is the circular frequency of motion, ξ_n, $n \in \{z,\theta\}$ represents the critical damping ratios of the structure in still air, ω_n, $n \in \{z, \theta\}$ symbolises the still-air natural frequencies (rad/s) of the structure, $G_n(\omega)$, $n \in \{z, \theta\}$, denotes the complex Fourier spectrum of the response, $i = \sqrt{(-1)}$ represents the imaginary unit, and $\tilde{M}_n$, $n \in \{z,\theta\}$, is the modal mass and the mass moment of inertia of the vertical and torsional still-air vibration modes, respectively. The remaining coefficients are given by

$$\tilde{K}_{zz} = \frac{\rho B^2}{2}\omega^2 H_4^* \int_{L_{exp}}\phi_z\phi_z\,dx \qquad \tilde{K}_{z\theta} = \frac{\rho B^2}{2}\omega^2 BH_3^* \int_{L_{exp}}\phi_z\phi_\theta\,dx$$

$$\tilde{K}_{\theta z} = \frac{\rho B^2}{2}\omega^2 BA_4^* \int_{L_{exp}}\phi_\theta\phi_z\,dx \quad \tilde{K}_{\theta\theta} = \frac{\rho B^2}{2}\omega^2 B^2 A_3^* \int_{L_{exp}}\phi_\theta\phi_\theta\,dx \quad (3)$$

$$\tilde{C}_{zz} = \frac{\rho B^2}{2}\omega H_1^* \int_{L_{exp}}\phi_z\phi_z\,dx, \qquad \tilde{C}_{z\theta} = \frac{\rho B^2}{2}\omega BH_2^* \int_{L_{exp}}\phi_z\phi_\theta\,dx$$

$$\tilde{C}_{\theta z} = \frac{\rho B^2}{2}\omega BA_1^* \int_{L_{exp}}\phi_\theta\phi_z\,dx, \quad \tilde{C}_{\theta\theta} = \frac{\rho B^2}{2}\omega B^2 A_2^* \int_{L_{exp}}\phi_\theta\phi_\theta\,dx \quad (4)$$

The stability of the aeroelastic system outlined above is conventionally studied by applying the characteristic equation obtained by expanding the determinant of Eq. (2). This results in a complex polynomial expression of the 4th degree. The roots are in general complex and may hence imply the following three conditions: (1) stable solution resulting in decaying response (positive damping), (2) stable solution describing a steady-state response, setting the limits for stable behaviour (zero damping), and (3) unstable solution characterising a divergent response (negative damping). The following dimensionless coefficients χ_n, $n \in \{z,\theta\}$ $\psi_{z\theta}$, γ and $\hat{V}$ are introduced to make the expressions simpler:

$$\psi_{z\theta} = \frac{\int_{L_{exp}}\phi_z\phi_\theta\,dx}{\int_L \phi_z^2\,dx}\frac{\int_{L_{exp}}\phi_z\phi_\theta\,dx}{\int_L \phi_\theta^2\,dx} \quad \chi_z = \frac{\rho B^2}{\tilde{m}_z} \quad \chi_\theta = \frac{\rho B^4}{\tilde{m}_\theta} \quad \gamma = \frac{\omega_\theta}{\omega_z} \quad \hat{V} = \frac{V}{B\omega_\theta} \quad \hat{\omega}_{CR} = \frac{\omega_{CR}}{\omega_\theta} \quad (5)$$

Here, the coefficient $\psi_{z\theta}$, is a measure of the shapewise similarity of the vertical and torsional mode shapes, where the value zero, on the one hand, indicates that the modes are shapewise dissimilar, and the value one, on the other hand, implies that they match perfectly. If the modes are dissimilar shapewise, the off-diagonal contributions $\tilde{K}_{z\theta}$, $\tilde{K}_{\theta z}$, $\tilde{C}_{z\theta}$, and $\tilde{C}_{\theta z}$ will become zero,

which implies that coupled flutter will not occur. The normalised unstable frequency is denoted as $\hat{\omega}_{CR}$, and since the critical frequency is real, the characteristic equation can be separated into two parts, real and purely imaginary, that each must be equal to zero. This results in the following two expressions:

$$R_4\hat{\omega}_{CR}^4 + R_3\hat{\omega}_{CR}^3 + R_2\hat{\omega}_{CR}^2 + 1 = 0 \tag{6}$$

$$I_3\hat{\omega}_{CR}^3 + I_2\hat{\omega}_{CR}^2 + I_1\hat{\omega}_{CR} + \xi_z\gamma + \xi_\theta = 0 \tag{7}$$

where the coefficients can be expressed as

$$R_4 = 1/4\gamma^2(4 + 2\chi_z H_4^* + 2\chi_\theta A_3^* + \chi_z\chi_\theta(\psi_{z\theta}A_1^*H_2^* - \psi_{z\theta}A_4^*H_3^* - A_2^*H_1^* + A_3^*H_4^*))$$
$$R_3 = \gamma(\xi_\theta\chi_z\gamma H_1^* + \xi_z\chi_\theta A_2^*)R_2 = 1/2(2 + 2\gamma^2 + 8\gamma\xi_z\xi_\theta + \chi_z\gamma^2 H_4^* + \chi_\theta A_3^*) \tag{8}$$

$$I_3 = 1/8\gamma^2(\chi_z\chi_\theta(H_1^*A_3^* - \psi_{z\theta}H_2^*A_4^* - \psi_{z\theta}H_3^*A_1^* + H_4^*A_2^*) + 2(\chi_z H_1^* + \chi_\theta A_2^*))$$
$$I_2 = -1/2(\xi_z\gamma(\chi_\theta A_3^* + 2) + \xi_\theta\gamma^2(\chi_z H_4^* + 2))I_1 = -1/4(\chi_z\gamma^2 H_1^* + \chi_\theta A_2^*) \tag{9}$$

Since the flutter derivatives are functions of reduced frequency, Eqs. (6) and (7) in fact represent a system of equations with two unknowns. It is common to solve these equations graphically. Further details may be found in [11].

The flutter equations are then further developed by assuming that the important flutter derivatives may be approximated by polynomial expressions that provide a frequency-independent description of self-excited forces. This is achieved by assuming flutter derivatives of the following form:

$$X_i^*(K) = x_i(1/K) \quad \text{when } i = 1,2,5 \text{ and } X_i^*(K) = x_i(1/K)^2 \quad \text{when } i = 3,4,6 \tag{10}$$

where $X \in \{P,H,A\}$ and $x \in \{p,h,a\}$. If this assumption is introduced in Eq. (3), the flutter equations can be expressed as follows:

$$R_4\hat{\omega}_{CR}^4 + R_2\hat{\omega}_{CR}^2 + R_0 = 0 \tag{11}$$

$$I_2\hat{\omega}_{CR}^2 + I_0 = 0 \tag{12}$$

where the coefficients are

$$R_4 = \gamma^2 \tag{13}$$

$$R_2 = 1/4\gamma^2\chi_z\chi_\theta(\psi_{z\theta}h_2a_1 + 2 h_4/\chi_\theta + 2a_3/\chi_z - h_1a_2)\hat{V}_{CR}^2$$
$$+ (\gamma\chi_\theta\xi_z a_2 + \gamma^2\chi_z h_1\xi_\theta)\hat{V}_{CR} - (\gamma^2 + 4 \gamma \xi_z\xi_\theta + 1) \tag{14}$$

$$R_0 = 1/4 \gamma^2\chi_z\chi_\theta(h_4a_3 - \psi_{z\theta}h_3a_4)\hat{V}_{CR}^4 - 1/2(\chi_\theta a_3 + \gamma^2\chi_z h_4)\hat{V}_{CR}^2 + 1 \tag{15}$$

$$I_2 = 1/4\gamma^2(\chi_\theta a_2 + \chi_z h_1)\hat{V}_{CR} - (\gamma \xi_z + \gamma^2 \xi_\theta) \tag{16}$$

$$I_0 = 1/8 \gamma^2\chi_z\chi_\theta(h_1a_3 - \psi_{z\theta}h_2a_4 - \psi_{z\theta}h_3a_1 + h_4a_2)\hat{V}_{CR}^3$$
$$-1/2(\gamma\chi_\theta\xi_z a_3 + \gamma^2\chi_z h_4\xi_\theta)\hat{V}_{CR}^2 - 1/4(\gamma^2\chi_z h_1 + \chi_\theta a_2)\hat{V}_{CR} + \xi_\theta + \gamma \xi_z \tag{17}$$

Eqs. (11) and (12) are simpler than Eqs. (6) and (7), in particular, since Eq. (11) can be solved as a second degree equation by simple substitution. The reduced critical frequency may be calculated directly from Eq. (12), and in principle this result may be inserted into Eq. (11) to estimate the reduced velocity, but this renders an expression too complicated for our aim. However, the natural frequencies of the coupled system are, with few exceptions, very close to the natural frequencies of the uncoupled system, where the off-diagonal terms, $\tilde{K}_{z\theta}$, $\tilde{K}_{\theta z}$, and $\tilde{C}_{z\theta}$, have been neglected. This is because the frequencies of a light to moderately damped system are mainly given by the mass and stiffness properties. In addition, the overturning moment related to vertical displacements given by $\tilde{K}_{\theta z}r_z$ is, from a physical point of view, close to zero. This implies that the product of the off-diagonal elements in the stiffness matrix is far less than the product of the elements on the diagonal, which contains both aerodynamic and still-air stiffness. This implies that the modal frequencies can be approximated by the uncoupled system of equations as suggested by Nakamura [7]. The frequency of the torsional and vertical branch of the solution may then be calculated by

$$\omega_{TB} = \sqrt{\left(1 - \frac{1}{2}\chi_\theta\left(\frac{\omega_{TB}}{\omega_\theta}\right)^2 A_3^*\right)}\omega_\theta \quad \text{and} \quad \omega_{VB} = \sqrt{\left(1 - \frac{1}{2}\chi_z\left(\frac{\omega_{VB}}{\omega_z}\right)^2 H_4^*\right)}\omega_z \tag{18}$$

These expressions have to be solved in an iterative manner since the flutter derivatives are functions of the frequency of motion (ω_{TB} for the torsional branch and ω_{VB} for the vertical branch). The expression vertical branch is here used for the velocity-dependent in-wind frequency corresponding to pure vertical motion in still air; similarly, the term torsional branch corresponds to the torsional vibration mode. The approximation presented in Eq. (18) have been used by Dyrbye and Hansen [11] to approximate the frequencies of uncoupled systems and the expression for the frequency of the
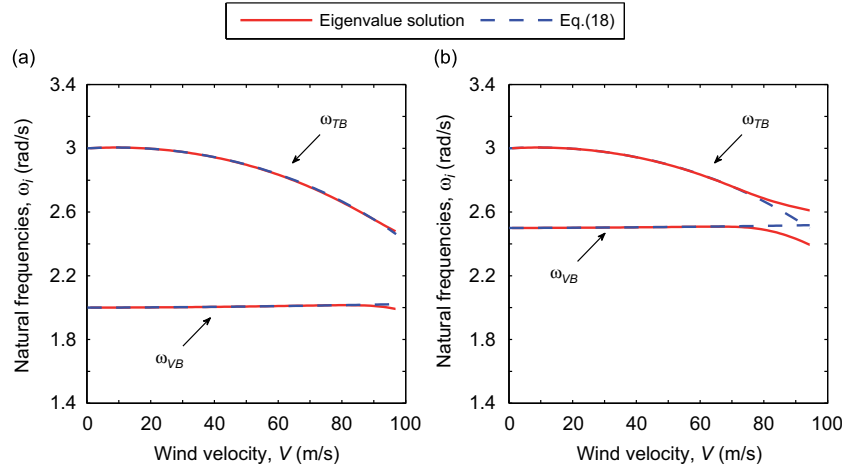
Fig. 2. Comparison of the presented simplified method with an eigenvalue solution: (a) frequency ratio $\gamma=1.5$ and shapewise similarity $\psi_{z\theta}=1.0$ and (b) $\gamma=1.2$ and shapewise similarity $\psi_{z\theta}=0.5$.

torsional branch is slightly different from the expression used by Nakamura [7]. The eigenvalue solution presented in Appendix A, together with the results from Eq. (18), is shown in Fig. 2a for a frequency ratio $\gamma=1.5$ and shapewise similarity $\psi_{z\theta}=1.0$, and in Fig. 2b with a frequency ratio $\gamma=1.2$ and a shapewise similarity $\psi_{z\theta}=0.5$. For the case presented in Fig. 2a, the approximation gives accurate results, while the results are less accurate in Fig. 2b. This is because the frequencies are not well separated; in addition, the off-diagonal terms have been reduced by low shapewise similarity. In the eigenvalue solution the frequencies clearly change path when they are approaching each other, while the frequencies actually cross in the approximate solution, which is not physically correct in this case.

For coupled flutter, the torsion motion is very important since it generates large coupling forces, compared with the vertical motion. This implies that the torsion branch will become unstable at the flutter onset, and when the definition of A_3^* from Eq. (10) is introduced in Eq. (18), the reduced critical frequency may be approximated by

$$\hat{\omega}_{CR} = \sqrt{\frac{\omega_{CR}^2}{\omega_\theta^2}} = \sqrt{\frac{\tilde{M}_\theta \omega_\theta^2 - \tilde{K}_{\theta\theta}}{\omega_\theta^2 \tilde{M}_\theta}} = \frac{1}{2}\sqrt{4 - 2\chi_\theta a_3 \hat{V}_{CR}^2} \tag{19}$$

When this expression is inserted into Eq. (12), the following 3rd degree algebraic equation for the critical velocity emerges:

$$\frac{\gamma^2 \chi_z \chi_\theta}{8}\left(h_4 a_2 - \psi_{z\theta} h_2 a_4 - \psi_{z\theta} h_3 a_1 - \frac{\chi_\theta}{\chi_z} a_2 a_3\right)\hat{V}_{CR}^3 + \frac{1}{2}\xi_\theta \gamma^2 (\chi_\theta a_3 - \chi_z h_4)\hat{V}_{CR}^2 + \frac{1}{4}\chi_\theta a_2(\gamma^2-1)\hat{V}_{CR} + \xi_\theta(1-\gamma^2) = 0 \tag{20}$$

Two approximations were introduced to develop this Equation (a) It has been assumed that the critical frequency may be approximated by equation (19). (b) The second assumption was that the flutter derivatives may be approximated by expressions that give a frequency-independent description of the self-excited forces. The accuracy of this assumption may easily be inspected by investigating the quality of the least squares fit to the experimental data. Since it is only the values of the flutter derivatives at the critical reduced velocity that are used in flutter calculations, the result may be improved if the least squares fit is adjusted to provide better accuracy at the critical reduced velocity. This implies that Eq. (20) must be solved in an iterative manner. However, this has not been necessary for any of the cases in this study, but this approach may be used when dealing with cross sections, where the transfer functions defining the self-excited forces have a more pronounced frequency-dependent characteristic, as is the case for more bluff sections and for twin-deck cross sections. Simplified flutter assessment is not recommended if several of the flutter derivatives have a shape differing strongly from the approximations suggested in Eq. (10).

The formula presented has been developed to describe coupled flutter, and it cannot be expected to give reliable results when the shapewise similarity is close to zero. When the shapewise similarity is zero, there are three aeroelastic instability phenomena that may occur, namely (1) static divergence, (2) torsional flutter, and (3) galloping. Static divergence has a critical frequency equal to zero, which implies that the approximation introduced in Eq. (19) is not valid. The frequency of galloping does not equal the frequency of the torsional branch of the solution system. Theoretically the formula can represent torsional flutter correctly, but this has not been tested in this study since the cross sections dealt with are not suspected to create this instability phenomenon. However, one degree of freedom instability phenomenon may be more easily studied by considering only the relevant equation, and the formula is therefore only relevant for coupled flutter. It is well known that when the frequency ratio γ is approaching unity, the flutter velocity increases dramatically.

This phenomenon will not be taken into account in the flutter formula since, as shown in Fig. 2b, the approximation introduced in Eq. (19) becomes inaccurate.

The formula given in Eq. (20) may be simplified further if the terms h_4 and a_4 are assumed close to zero and negligible. These terms were not included in the original definition of self-excited forces [23], but have been added later for completeness e.g. [12]. Applying the trigonometric solution of the cubic equation, it is possible to develop a closed-form solution based on the reduced equation $x^3 + c_1 x^2 + c_2 x + c_3$ (see [25] for details). When h_4 and a_4 have been neglected, the positive real root for Eq. (20) may then be expressed as

$$\Omega = (\chi_z \psi_{z\theta} h_3 a_1 + \chi_\theta a_2 a_3)$$

$$\alpha = \cos^{-1}\left(\frac{\gamma\sqrt{2}\xi_\theta(-16\xi_\theta^2 a_3^3 \gamma^2 \chi_\theta + 9(\gamma^2-1)((\chi_\theta a_2 a_3(5\Omega - 3\chi_\theta a_2 a_3)) + 3\chi_z^2 \psi_{z\theta}^2 h_3^2 a_1^2))}{\chi_\theta \sqrt{(8\xi_\theta^2 a_3^2 \gamma^2 + 3a_2(\gamma^2-1)\Omega)^3}}\right)$$

$$\frac{V_{CR}}{B\omega_\theta} = 2\sqrt{\frac{16\xi_\theta^2 a_3^2 \gamma^2 + 6a_2(\gamma^2-1)\Omega}{9\gamma^2\Omega^2}}\cos\left(\frac{1}{3}\alpha\right) + \frac{4}{3}\frac{\xi_\theta a_3}{\Omega} \tag{21}$$

The parameter α will become complex when the expression in parentheses exceeds unity. This is not supported by some computer programs, but when this occurs, the problem may be circumvented utilising the trigonometric identity $\cos(n\cos^{-1}(x)) = \cosh(n\cosh^{-1}(x))$. All cubic equations cannot be solved applying the trigonometric solution, but if the expression in the denominator in the parentheses is not equal zero, the trigonometric solution may be used. The torsion damping is also often very low, and when this assumption is introduced in Eq. (20) or (21), the following closed-form solution of the reduced critical velocity emerges

$$\frac{V_{CR}}{B\omega_\theta} = \sqrt{\frac{2a_2(\gamma^2-1)}{\gamma^2\Omega}} \tag{22}$$

This formula will in general give a slightly lower critical velocity than Eqs. (20) and (21) since torsion damping has a positive effect on the critical velocity. The similarity and relation of this formula to Selberg's flutter formula is discussed in Appendix B since Selberg's formula is perhaps the most well known simplified solution. The main reason for the popularity of Selberg's formula is its simplicity. Only few structural parameters are needed to provide an estimate of the critical velocity. However, since Selberg's formula does not account for the aerodynamic properties of bridge sections it may produce a critical velocity that is seriously inaccurate. Therefore it has been recommended to combine Selberg's formula with an aerodynamic performance index accounting for the discrepancy of the aerodynamics of an ideal flat plate and the actual cross section [26]. This aerodynamic performance index is commonly obtained from wind tunnel measurements with a section model and is rarely reported in the literature. It is suggested that Eqs. (20)–(22) may be a realistic alternative to Selberg's formula. In the case of Eq. (22) only four aerodynamic parameters a_1, a_2, a_3 and h_3, and optionally the shapewise similarity factor $\psi_{z\theta}$, are needed in addition to the parameters used in Selberg's formula. These aerodynamic parameters can be obtained from published experimental data of flutter derivatives for a cross section similar to the one in question, while the shapewise similarity may be conservatively assumed perfect. However, the shape wise similarity of the vibration modes is rarely perfect, which implies that evaluation of the shapewise similarity will provide a more accurate and higher critical velocity. Closed form equations for the critical velocity increase the understanding of the influences of the structural and aerodynamic parameters on the critical velocity. This implies that Eq. (21) or (22) may be useful in assessing how an effective flutter control may be achieved.

3. Comparative numerical results

The approximate solutions presented in this study will be tested in this section for a wide range of configurations. There are many factors influencing the stability limit, and it is of course not possible to test the formulae for all possible situations. Therefore, only a few representative cases are tested. In the first two sections, the formula presented in Eq. (21) is evaluated for a range of structural configurations, and two different cross sections have been considered. In the third section, both formulae (Eqs. (21) and (22)) and Selberg's formula are applied to the structural configurations of some well-known cable supported bridges, but with the aerodynamic properties of one of the two cross sections presented below.

3.1. A wedge-shaped box section

A wedge-shaped box section has frequently been used for suspension bridges in recent years, for example, the Severn Bridge (England/Wales), the Humber Bridge (England), and the Askøy Bridge (Norway). Experimental results of the flutter derivatives for the section shown in Fig. 3, which will be referred to as cross section 1 below, are given in [27].

The load coefficients defined in Eq. (10) are calculated by least squares fits to the experimental data, rendering the following results: $h_1 = -2.734$, $h_2 = 0.206$, $h_3 = 2.271$, $h_4 = -0.208$, $a_1 = -0.823$, $a_2 = -0.258$, $a_3 = 0.726$, $a_4 = -0.037$. The approximation and the experimental results of the flutter derivatives are shown in Fig. 4. As pointed out in [28,29], it is A_1^*, A_2^*, A_3^*, H_3^* and, to some extent, H_1^* that are the most important flutter derivatives. As can be seen, the approximate

O. Øiseth, R. Sigbjörnsson / Journal of Sound and Vibration 330 (2011) 2784–2800
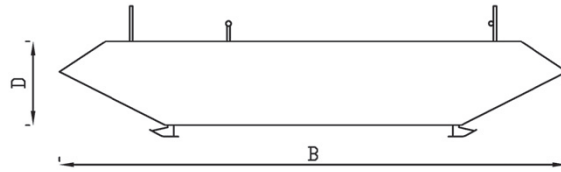
Fig. 3. Wedge-shaped box cross section (cross section 1).
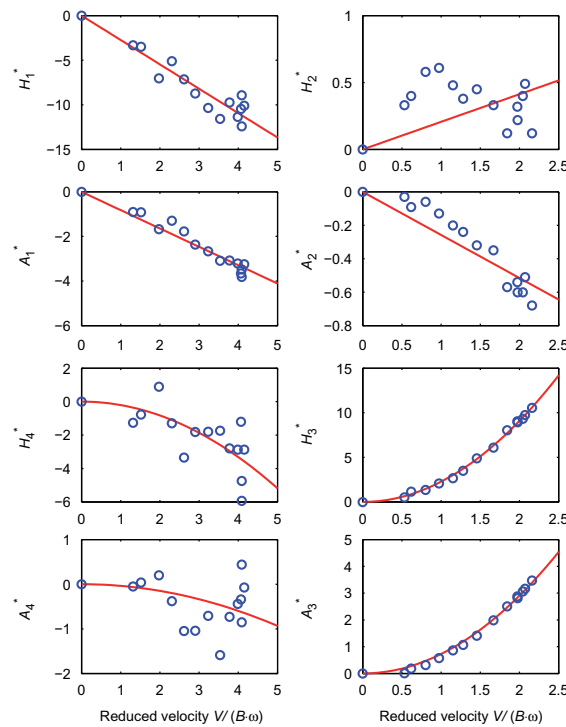
Fig. 4. Flutter derivatives for cross section 1: open circles refer to data obtained in wind tunnel tests, and solid lines represent curves fitted to the data.

expressions provide least squares fits of good accuracy for the important flutter derivatives. The largest discrepancy is for A_2^* for which a second-order expression would give a more optimal fit to the data than the linear one. However, in flutter calculations the functional value of the approximation for the reduced velocity corresponding to the critical velocity is of primary importance but not the overall functional shape. Low values of A_2^* will give conservative results since this will provide less aerodynamic torsional damping. The line representing A_2^* in Fig. 4 provides a reasonable fit to the experimental data in the reduced velocity range $\hat{V} \in [1,\ldots,3]$, and improved results may be obtained if the stability limit is calculated iteratively. The still-air dynamic properties of the structure are assumed to be B=18.3 m, ω_θ=2.23 rad/s, $\omega_\theta = \gamma \omega_z$ rad/s, ξ_z=0.005, ξ_θ=0.005, m_z=12,820 kg/m and m_θ=426,000 kg^2/m. (The structural properties are deemed to be similar to those of the Hardanger Bridge.) The still-air vibration modes are defined by $\phi_z(x)$ and $\phi_\theta(x)$ and are related by the shapewise similarity $\psi_{z\theta}$, defined in Eq. (5). The critical velocities provided by the flutter formula are presented at the top of each row in Table 1, and the results from an eigenvalue solution when the flutter derivatives are used to describe the self-excited forces are presented in parentheses. The accuracy of the approximation is given at the bottom of each row. Similarly, the critical frequencies are shown in Table 2, but with the critical frequency given by Eq. (18) when the critical velocity provided by the eigenvalue solution is used. As can be seen, the flutter formula provides results of good accuracy. The results are less accurate at low frequency ratios and shapewise similarities, but the inaccuracy is still within 10 per cent. The critical frequencies are less accurate, but the critical velocities do not seem to be sensitive to this. The main reason for the inaccuracy is that the torsional frequency is reduced rapidly at high velocities. The small discrepancy in the results provided by the eigenvalue solution and those predicted by the uncoupled system of equations given at the bottom of each cell confirms that the frequencies of the uncoupled system are generally very close to the frequencies of the

Table 1
Critical velocities in m/s for cross section no. 1, expressed as a function of shapewise similarity, $\psi_{z\theta}$, and frequency ratio, γ. The result obtained applying the presented flutter formula, Eq. (21), is presented at the top of each cell, the stability limit calculated by the eigenvalue solution is presented in parentheses, and the percentage difference between the two methods is given at the bottom of each cell.

Shapewise similarity $\psi_{z\theta}$	Frequency ratio, γ												
	1.5	1.6	1.7	1.8	1.9	2.0	2.1	2.2	2.3	2.4	2.5	3.0	4.0
1.0	65	67	70	72	73	75	76	77	78	78	79	81	83
	(67)	(70)	(73)	(76)	(77)	(79)	(80)	(82)	(83)	(84)	(84)	(87)	(90)
	−4%	−4%	−5%	−5%	−5%	−6%	−6%	−6%	−6%	−6%	−7%	−7%	−8%
0.8	68	71	73	75	77	78	79	80	81	82	83	85	87
	(71)	(74)	(77)	(79)	(81)	(83)	(84)	(85)	(86)	(87)	(88)	(91)	(94)
	−4%	−5%	−5%	−5%	−5%	−5%	−6%	−6%	−6%	−6%	−6%	−6%	−7%
0.6	71	75	77	79	81	83	84	85	86	87	87	90	92
	(75)	(79)	(81)	(84)	(86)	(87)	(89)	(90)	(91)	(92)	(92)	(95)	(98)
	−5%	−5%	−5%	−5%	−5%	−5%	−5%	−5%	−5%	−5%	−5%	−6%	−6%
0.4	76	79	82	84	86	88	89	90	91	92	93	95	98
	(84)	(86)	(89)	(91)	(92)	(94)	(95)	(96)	(97)	(97)	(98)	(100)	(103)
	−10%	−8%	−7%	−7%	−6%	−6%	−6%	−6%	−6%	−5%	−5%	−5%	−5%

Table 2
Critical frequencies in rad/s for cross section no. 1, expressed as a function of shapewise similarity, $\psi_{z\theta}$, and frequency ratio, γ. The result obtained applying the presented formula, Eq. (19), is presented at the top of each cell; the stability limit calculated by the eigenvalue solution is presented in parentheses, and the percentage difference between the two methods is given in the third row in each cell, while the result predicted by Eq. (18) at the critical velocity given by the eigenvalue solution is given at the bottom of each cell.

Shapewise similarity $\psi_{z\theta}$	Frequency ratio, γ												
	1.5	1.6	1.7	1.8	1.9	2.0	2.1	2.2	2.3	2.4	2.5	3.0	4.0
1.0	1.87	1.83	1.80	1.77	1.75	1.73	1.71	1.70	1.68	1.67	1.66	1.62	1.58
	(1.83)	(1.78)	(1.73)	(1.68)	(1.65)	(1.61)	(1.58)	(1.55)	(1.53)	(1.51)	(1.49)	(1.41)	(1.33)
	2%	3%	4%	5%	6%	7%	8%	9%	10%	11%	11%	15%	19%
	1.83	1.78	1.73	1.69	1.65	1.61	1.58	1.56	1.53	1.51	1.49	1.42	1.34
0.8	1.83	1.79	1.75	1.72	1.69	1.67	1.65	1.63	1.62	1.60	1.59	1.55	1.50
	(1.78)	(1.72)	(1.66)	(1.62)	(1.58)	(1.54)	(1.50)	(1.47)	(1.45)	(1.42)	(1.40)	(1.32)	(1.23)
	3%	4%	5%	6%	7%	9%	10%	11%	12%	13%	13%	17%	22%
	1.77	1.71	1.66	1.61	1.57	1.53	1.50	1.47	1.44	1.41	1.39	1.31	1.21
0.6	1.78	1.73	1.69	1.65	1.62	1.59	1.57	1.55	1.53	1.51	1.50	1.45	1.39
	(1.72)	(1.65)	(1.59)	(1.54)	(1.49)	(1.45)	(1.41)	(1.38)	(1.35)	(1.32)	(1.30)	(1.21)	(1.10)
	4%	5%	6%	7%	9%	10%	11%	12%	13%	14%	16%	20%	26%
	1.69	1.62	1.56	1.51	1.46	1.42	1.38	1.34	1.31	1.29	1.26	1.16	1.05
0.4	1.71	1.65	1.60	1.56	1.52	1.49	1.46	1.44	1.42	1.40	1.38	1.31	1.24
	(1.61)	(1.55)	(1.49)	(1.43)	(1.38)	(1.34)	(1.30)	(1.26)	(1.23)	(1.20)	(1.17)	(1.07)	(0.95)
	6%	7%	8%	9%	10%	12%	13%	14%	15%	16%	18%	23%	30%
	1.50	1.44	1.38	1.32	1.27	1.22	1.18	1.14	1.11	1.07	1.04	0.93	0.79

coupled system. To investigate the influence of the fit to the experimental data for A_2^*, the case $\psi_{z\theta} = 1.0$ and $\gamma = 2.0$ is recalculated with $a_2 = -0.367$, which represents the experimental data at the critical velocity more accurately. This provides a critical velocity of 80 m/s, which is very close to the eigenvalue solution. Nevertheless, the results are not very sensitive to the approximation of A_2^*, but an improvement of the results can be achieved if the approximation suggested in Eq. (18) is adjusted such that the experimental data at the critical reduced velocity are more accurately represented. If Eq. (22) is used to predict the critical velocity, it is possible to derive a simple expression for the derivative of V_{CR} with respect to a_2:

$$\frac{\partial V_{CR}}{\partial a_2} = \frac{V_{CR}}{2a_2 \left(1 + \frac{\chi_\theta a_2 a_3}{\chi_z \psi h_3 a_1}\right)} \tag{23}$$

The derivative with respect to a_2 at the point defined by the coefficients provided above assuming $a_2 = -0.258$ is $\partial V_{CR}/\partial a_2 = -69.9$. This implies that a ± 0.05 change of a_2 will introduce a ± 3.5 m/s change of the critical velocity. Furthermore, this indicates that it is possible to cover a wide reduced velocity range and still get results with fair engineering accuracy.

3.2. A rectangular cross section

The formula developed in this study is also tested on a rectangular cross section with a height to width ratio of 18. A drawing of the cross section, which will be referred to as cross section 2 in the following, is shown in Fig. 5. The experimental data of the flutter derivatives are taken from [30], and a least squares fit of the expressions defined in Eq. (10) renders the following load coefficients $h_1 = -4.468$, $h_2 = 0.332$, $h_3 = 5.168$, $h_4 = -0.203$, $a_1 = -0.486$ $a_2 = -0.176$, $a_3 = 0.753$, and $a_4 = -0.061$. The approximation and the experimental results of the flutter derivatives are shown in Fig. 6. As can be seen, the approximate expressions provide least squares fits of good accuracy for the important flutter derivatives.

The still-air dynamic properties of the system are assumed to be $\omega_z = 1.00$ rad/s, $\omega_\theta = \gamma \omega_z$ rad/s, $\xi_z = 0.005$, $\xi_\theta = 0.005$, $m_z = 12820$ kg/m and $m_\theta = 426{,}000$ kg^2/m. The still-air vibration modes are defined by $\phi_z(x)$ and $\phi_\theta(x)$ and are related by the shapewise similarity $\psi_{z\theta}$. The width of the girder is taken as $B = 20$ m. The approximation provided by the flutter formula is given at the top of each row in Table 3 while the exact solution is given in parentheses, and the accuracy of the approximation is given at the bottom of each row. The critical frequencies are presented in the same manner in Table 4, but with the critical frequency given by Eq. (18) when the critical velocity provided by the eigenvalue solution is used. The results show that the formula provides critical velocities of good accuracy, and the results become more accurate when the frequency ratio is increasing. The critical frequencies shown in Table 4 are more accurate than those shown in Table 2. The discrepancies of the results predicted by Eq. (18) and the eigenvalue solution are also very small, confirming that the frequencies of the coupled system are very close to the frequencies of the uncoupled system.

To test whether the formula gives accurate results for different mass ratios, a new structural configuration is defined. The damping ratios of the structure in still air ξ_n, $n \in \{z, \theta\}$ are set to 0.005 of critical damping, and the natural frequencies
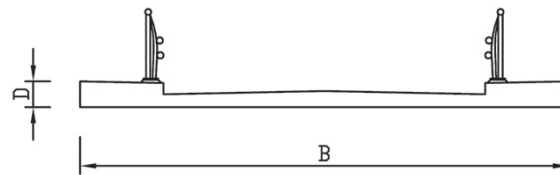

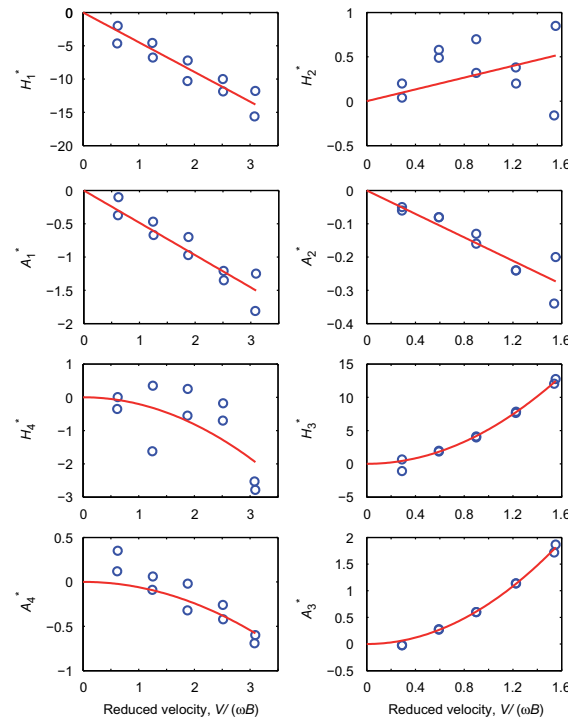**Fig. 5.** Rectangular cross section (cross section 2).

Fig. 6. Flutter derivatives for cross section 2: Open circles refer to data obtained in wind tunnel tests, and solid lines represent curves fitted to the data.

Table 3
Critical velocities in m/s for cross section no. 2, expressed as a function of shapewise similarity, $\psi_{z\theta}$, and frequency ratio, γ. The result obtained applying the presented flutter formula, Eq. (21), is presented at the top of each cell; the stability limit calculated by the eigenvalue solution is presented in parentheses, and the percentage difference between the two methods is given at the bottom of each cell.

Shapewise similarity $\psi_{z\theta}$	Frequency ratio, γ												
	1.5	1.6	1.7	1.8	1.9	2.0	2.1	2.2	2.3	2.4	2.5	3.0	4.0
1.0	35	39	43	47	50	54	57	61	64	68	71	88	120
	(38)	(41)	(45)	(49)	(52)	(56)	(59)	(63)	(66)	(70)	(73)	(90)	(122)
	−7%	−6%	−5%	−4%	−4%	−3%	−3%	−3%	−3%	−3%	−3%	−2%	−2%
0.8	37	41	45	49	53	57	61	65	68	72	75	93	127
	(40)	(44)	(48)	(51)	(55)	(59)	(63)	(66)	(70)	(73)	(77)	(94)	(129)
	−6%	−5%	−4%	−4%	−3%	−3%	−3%	−2%	−2%	−2%	−2%	−1%	−1%
0.6	40	44	49	53	57	61	65	69	73	77	81	100	136
	(42)	(47)	(51)	(55)	(59)	(63)	(66)	(70)	(74)	(78)	(82)	(100)	(137)
	−6%	−5%	−4%	−3%	−3%	−2%	−2%	−2%	−1%	−1%	−1%	−1%	0%
0.4	43	48	53	57	62	66	71	75	79	83	87	108	148
	(46)	(50)	(55)	(59)	(63)	(67)	(71)	(75)	(80)	(84)	(88)	(107)	(146)
	−7%	−5%	−4%	−3%	−2%	−2%	−1%	−1%	−1%	0%	0%	0%	1%

Table 4
Critical frequencies in rad/s for cross section no. 2 expressed as a function of shapewise similarity, $\psi_{z\theta}$, and frequency ratio, γ. The result obtained applying the presented formula, Eq. (19), is presented at the top of each cell; the stability limit calculated by the eigenvalue solution is presented in parentheses, and the percentage difference between the two methods is given in the third row in each cell, while the result predicted by Eq. (18) at the critical velocity given by the eigenvalue solution is given at the bottom of each cell.

Shapewise similarity $\psi_{z\theta}$	Frequency ratio, γ												
	1.5	1.6	1.7	1.8	1.9	2.0	2.1	2.2	2.3	2.4	2.5	3.0	4.0
1.0	1.31	1.37	1.44	1.51	1.58	1.65	1.72	1.79	1.86	1.93	2.00	2.37	3.10
	(1.29)	(1.36)	(1.42)	(1.49)	(1.56)	(1.62)	(1.69)	(1.76)	(1.83)	(1.90)	(1.97)	(2.32)	(3.05)
	1%	1%	1%	1%	1%	1%	1%	2%	2%	2%	2%	2%	2%
	1.30	1.37	1.44	1.50	1.57	1.64	1.71	1.78	1.86	1.93	2.00	2.36	3.09
0.8	1.28	1.34	1.41	1.47	1.53	1.60	1.66	1.73	1.80	1.86	1.93	2.27	2.97
	(1.26)	(1.32)	(1.38)	(1.45)	(1.51)	(1.57)	(1.64)	(1.70)	(1.77)	(1.83)	(1.90)	(2.23)	(2.91)
	1%	1%	2%	2%	2%	2%	2%	2%	2%	2%	2%	2%	2%
	1.27	1.33	1.40	1.46	1.53	1.59	1.66	1.72	1.79	1.86	1.92	2.26	2.96
0.6	1.25	1.30	1.36	1.42	1.47	1.53	1.59	1.65	1.71	1.77	1.84	2.15	2.79
	(1.22)	(1.28)	(1.33)	(1.39)	(1.45)	(1.50)	(1.56)	(1.62)	(1.68)	(1.74)	(1.80)	(2.10)	(2.73)
	2%	2%	2%	2%	2%	2%	2%	2%	2%	2%	2%	2%	2%
	1.23	1.28	1.34	1.40	1.46	1.52	1.58	1.64	1.70	1.76	1.82	2.13	2.77
0.4	1.20	1.24	1.29	1.34	1.39	1.44	1.49	1.54	1.59	1.64	1.69	1.96	2.52
	(1.17)	(1.21)	(1.26)	(1.31)	(1.36)	(1.41)	(1.46)	(1.51)	(1.56)	(1.61)	(1.66)	(1.92)	(2.47)
	3%	3%	2%	2%	2%	2%	2%	2%	2%	2%	2%	2%	2%
	1.15	1.21	1.26	1.31	1.36	1.41	1.46	1.51	1.56	1.62	1.67	1.94	2.49

in still air are assumed to be $\omega_z = 1.0$ rad/s and $\omega_\theta = \gamma\omega_z$, where γ is the frequency ratio. The mass of the bridge deck, hangers and cables are set to $m_z = 1000$ kg/m, and the mass moment of inertia is defined as $m_\theta = m_z R_g^2$ kg, where R_g is the radius of gyration. The radius of gyration is assumed to be between $0.3B$ and $0.5B$, where 0.3, on the one hand, implies that the mass is evenly distributed, and 0.5, on the other hand, implies that the mass is concentrated at the left- and right-hand sides of the girder. The width of the girder is set to $B = 20$ m, and the shapewise similarity of the still-air torsional and vertical vibration modes is assumed perfect, which implies that $\psi_{z\theta} = 1.0$. The critical velocities are calculated for a range of frequency ratios by increasing the still-air torsional natural frequency. The results are shown in Table 5, and the critical frequencies are given in Table 6. As can be seen, the formula provides critical velocities of good accuracy for all the cases evaluated. The critical frequencies shown in Table 6 are also very satisfying.

3.3. Examples of some well-known long-span bridges

It is well known that structural properties, such as frequencies, mass properties, and mode shapes, are just as important to the critical velocity as the aerodynamic properties of the cross section. In [9], structural properties of a few well-known bridges are given. The critical velocity for imaginary bridges having the same structural properties as these bridges, but

Table 5

Critical velocities in m/s for cross section no. 2, expressed as function of radius of gyration, R_g, compared to the width of the girder, B, (R_g/B). The result obtained applying the presented flutter formula, Eq. (21), is presented at the top of each cell; the stability limit calculated by the eigenvalue solution is presented in parentheses, and the percentage difference between the two methods is given at the bottom of each cell.

Radius of gyration/width R_g/B	Frequency ratio, γ												
	1.5	1.6	1.7	1.8	1.9	2.0	2.1	2.2	2.3	2.4	2.5	3.0	4.0
0.30	31	35	38	42	45	48	51	55	58	61	64	79	108
	(34)	(38)	(41)	(44)	(48)	(51)	(54)	(57)	(60)	(63)	(66)	(81)	(111)
	−9%	−8%	−7%	−6%	−5%	−5%	−5%	−5%	−4%	−4%	−4%	−3%	−3%
0.35	34	38	41	45	48	52	55	59	62	65	68	84	115
	(37)	(41)	(44)	(48)	(51)	(55)	(58)	(61)	(65)	(68)	(71)	(87)	(119)
	−9%	−7%	−6%	−6%	−5%	−5%	−5%	−4%	−4%	−4%	−4%	−3%	−3%
0.40	36	40	44	47	51	55	58	62	65	69	72	89	122
	(39)	(43)	(47)	(50)	(54)	(58)	(61)	(65)	(68)	(72)	(75)	(92)	(125)
	−8%	−7%	−6%	−6%	−5%	−5%	−5%	−4%	−4%	−4%	−4%	−3%	−3%
0.5	39	44	48	52	56	60	64	68	71	75	79	97	133
	(42)	(47)	(51)	(55)	(59)	(63)	(67)	(71)	(74)	(78)	(82)	(100)	(137)
	−8%	−7%	−6%	−5%	−5%	−5%	−4%	−4%	−4%	−4%	−4%	−3%	−3%

Table 6

Critical frequencies in rad/s for cross section no. 2, expressed as function of radius of gyration, R_g, compared to the width of the girder, B, (R_g/B). The result obtained applying the presented formula, Eq. (19) is presented at the top of each cell; the critical frequency calculated by the eigenvalue solution is presented in parentheses, and the percentage difference between the two methods is given in the third row in each cell, while the result predicted by Eq. (18) at the critical velocity given by the eigenvalue solution is given at the bottom of each cell.

Radius of gyration/width R_g/B	Frequency ratio, γ												
	1.5	1.6	1.7	1.8	1.9	2.0	2.1	2.2	2.3	2.4	2.5	3.0	4.0
0.30	1,32	1,39	1,45	1,53	1,60	1,67	1,74	1,81	1,88	1,96	2,03	2,40	3,15
	(1,30)	(1,37)	(1,43)	(1,50)	(1,57)	(1,64)	(1,71)	(1,78)	(1,85)	(1,93)	(2,00)	(2,36)	(3,10)
	1%	1%	1%	1%	1%	2%	2%	2%	2%	2%	2%	2%	2%
	1,31	1,38	1,45	1,52	1,59	1,66	1,73	1,81	1,88	1,95	2,02	2,40	3,15
0.35	1,35	1,42	1,50	1,57	1,65	1,72	1,80	1,88	1,96	2,03	2,11	2,51	3,30
	(1,33)	(1,40)	(1,48)	(1,55)	(1,63)	(1,70)	(1,78)	(1,85)	(1,93)	(2,01)	(2,08)	(2,47)	(3,25)
	1%	1%	1%	1%	1%	1%	1%	1%	1%	1%	1%	1%	2%
	1,34	1,41	1,49	1,56	1,64	1,72	1,79	1,87	1,95	2,03	2,10	2,50	3,29
0.40	1,37	1,45	1,53	1,61	1,69	1,77	1,85	1,93	2,01	2,09	2,17	2,58	3,41
	(1,36)	(1,43)	(1,51)	(1,59)	(1,67)	(1,75)	(1,83)	(1,91)	(1,99)	(2,07)	(2,15)	(2,55)	(3,37)
	1%	1%	1%	1%	1%	1%	1%	1%	1%	1%	1%	1%	1%
	1,36	1,44	1,52	1,60	1,68	1,76	1,84	1,92	2,00	2,08	2,16	2,57	3,40
0.50	1,40	1,48	1,57	1,65	1,74	1,82	1,91	1,99	2,08	2,17	2,25	2,69	3,56
	(1,39)	(1,47)	(1,56)	(1,64)	(1,73)	(1,81)	(1,89)	(1,98)	(2,06)	(2,15)	(2,24)	(2,67)	(3,53)
	1%	1%	1%	1%	1%	1%	1%	1%	1%	1%	1%	1%	1%
	1,39	1,48	1,56	1,65	1,73	1,82	1,90	1,99	2,07	2,16	2,25	2,68	3,55

Table 7

Structural properties of well-known bridges together with the critical wind velocity calculated by an eigenvalue solution (EVS), the presented flutter formula (FF) defined in Eq. (21), the undamped version of the flutter formula (UFF) defined in Eq. (22) and Selberg's formula. It has been assumed that the bridges have girders with the same aerodynamic properties as the cross section of the Hardanger Bridge.

	Length L (m)	Width B (m)	Vertical frequency ω_z (rad/s)	Torsional frequency ω_θ (rad/s)	Shapewise similarity $\psi_{z\theta}$	Mass m_z (kg/m)	Moment of inertia, m_θ (kg²/m)	Critical wind velocity V_{CR} (m/s)			
								EVS	FF	UFF	SF
Tacoma	854	12	0.817	1.257	1	4250	177,730	29.6	27.7	25.2	24.5
Bosporus	1074	28	1.018	2.331	1	13,550	1,351,645	91.0	88.1	85.8	78.2
Akashi	1991	35.5	0.402	0.942	1	43,790	9,826,000	77.8	70.6	67	62.1
Normandy	856	23.8	1.382	3.142	1	13,700	633,488	109.7	105.9	104	94.7
Hardanger	1310	18.3	1.270	2.23	0.57	12,820	426,000	84	79	78	62.5

with a cross section with the same aerodynamic properties as the girder of the Hardanger Bridge, is shown in Table 7, in addition to one mode combination for the Hardanger Bridge. The torsional still-air damping ratio ξ_θ has been assumed to be 0.005 of critical damping.

The flutter formulae give accurate results within 3–9% of the complex eigenvalue results for all the cases considered. The undamped version of the flutter formula (Eq. (22)) also provides satisfactory results that are, as expected, lower than the eigenvalue solution. Selberg's formula provides less accurate results than the formulae presented in this paper, and the difference is, as expected, largest where the shapewise similarity is below 1, since it does not take into account imperfect shapewise similarity.

4. Multimodal effects

If a flutter formula, based on a bimodal consideration, is to be useful, a criterion for when a bimodal consideration is sufficient must be developed. The torsional and vertical vibration modes of cable supported bridges often come in shapewise similar pairs, and which of the shapewise similar pairs will give the lowest critical velocity depends on the degree of shapewise similarity, the torsional frequency and the frequency ratio. Three questions regarding the coupling effects will be addressed in this study: (1) Will multimodal effects occur if two bimodal pairs provide nearly the same critical velocities, but are shapewise dissimilar? (2) Will multimodal effects occur if one vertical mode is shapewise similar to two torsional modes? (3) How well separated must two vertical modes that are shapewise similar to the same torsional mode be to avoid multimodal effects?

The damping ratios have been assumed as ξ_n=0.005 of critical damping for all vibration modes; the width of the girder has been assumed B=20 m, and the aerodynamic properties of cross section 2 are used in the calculations.

4.1. Two vertical and two torsional modes

To answer question one, two pairs of shapewise similar modes, where the pairs are shapewise dissimilar, are defined by $\phi_{z1}(x)$, $\phi_{\theta1}(x)$, $\phi_{z2}(x)$ and $\phi_{\theta2}(x)$. This implies that the still-air vibration modes are related by the following shapewise similarities: $\psi_{z1\theta1}$=1.0, $\psi_{z1\theta2}$=0, $\psi_{z2\theta1}$=0, and $\psi_{z2\theta2}$=1.0. The still-air natural frequencies of pair one are set to ω_{z1}=2.5 rad/s, $\omega_{\theta1}$=3.5 rad/s, and the natural frequency of pair two is in the range $\omega_{\theta2}$=[2,…,5] rad/s and ω_{z2}=$\omega_{\theta2}$−1 rad/s. This implies that the distance between the modes on the frequency axis in each pair is equal, and when $\omega_{\theta2}$=3.5, the frequencies coincide. The mass of the system is set to m_z=15,000 kg/m, and the mass moment of inertia is set to m_θ=500,000 kg^2/m. The stability limits are calculated separately for each pair, and both pairs are combined to evaluate possible multimodal effects. The results are shown in Fig. 7.

Since the still-air natural frequencies of pair one are not changed, the bimodal stability limit (dashed line) is constant 90 m/s, while the bimodal stability limit of pair two is increasing from 60 to 117 m/s. The same pattern can be seen on the plot of the critical frequencies. The multimodal calculations perfectly follow the result provided by the bimodal calculations. The stability limit is not affected by the presence of another shapewise similar pair, even when the torsional and vertical frequencies for both pairs are identical ω_{z1}=ω_{z2}=2.5 rad/s and $\omega_{\theta1}$=$\omega_{\theta2}$=3.5 rad/s, which implies that both pairs provide the same stability limit. This could also be proved if the system of equations is studied. If none of the
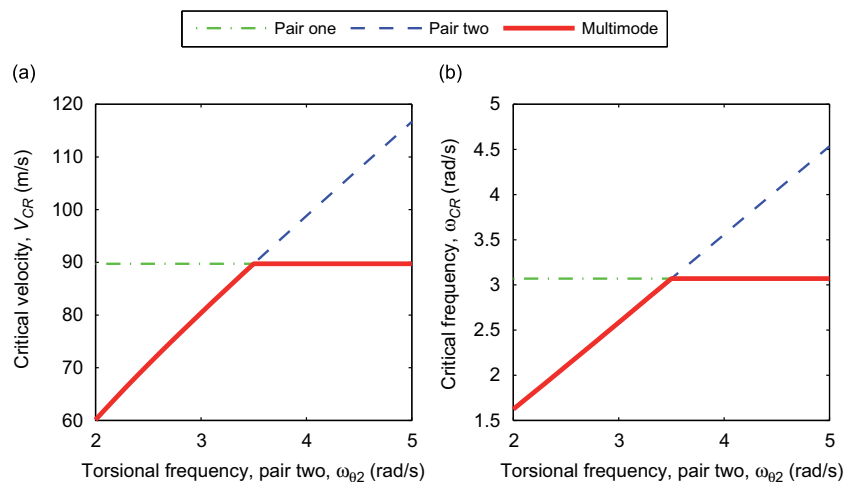

Fig. 7. (a) Critical velocities provided by multimodal calculations (solid line) and bimodal calculations (dashed lines) for a system of shapewise dissimilar pairs and (b) critical frequencies.

vibration modes in pair one is shapewise similar to any of the vibration modes in pair two, the two subsystems will be uncoupled, which implies that they may be solved separately.

4.2. One vertical and two torsional modes

To answer question two, an aeroelastic system, consisting of one vertical and two torsional vibration modes $\phi_z(x), \phi_{\theta 1}(x)$, and $\phi_{\theta 2}(x)$ is defined. The still-air natural frequencies are assumed to be $\omega_{z1}=2.0$ rad/s, $\omega_{\theta 1} \in \{3.0 \ 5.0 \ 8.0\}$ rad/s, and $\omega_{\theta 2}=\omega_{\theta 1} \cdot \Delta$ rad/s, where Δ is in the range [1,...,10]. The mass of the system is set to $m_z=15,000$ kg/m, while the mass moment of inertia is taken as $m_\theta=500,000$ kg^2/m. The stability limit of the vertical, $\phi_z(x)$, and the first torsional mode, $\phi_{\theta 1}(x)$, is calculated first, then the second torsional vibration mode, $\phi_{\theta 2}(x)$, is added to the system, and the percentage change of the stability limit is calculated. The results are shown in Fig. 8. All cases evaluated give similar results: the reduction of the stability limits decreases when the frequency ratio Δ increases. Three separations between the vertical and torsional vibration modes were studied, and all of them followed the same pattern, but the closest separation, when $\omega_{\theta 1}$ is 3 rad/s, seems to decrease faster than the two other cases, which follow each other's pattern nearly perfectly. The case shown in Fig. 8a, where the shapewise similarities are $\psi_{z\theta 1}=1.0$ and $\psi_{z\theta 2}=1.0$, is in reality impossible since this situation implies that the structure has two still-air torsional vibration modes that are identical, but it theoretically represents the upper bound for the reduction of the stability limit. However, the shapewise similarity of the vertical and torsional vibration modes is often not perfect, and when the vertical mode matches the first torsional mode perfectly, and where the same vertical mode is in some degree shapewise similar to the second torsional mode, more specifically
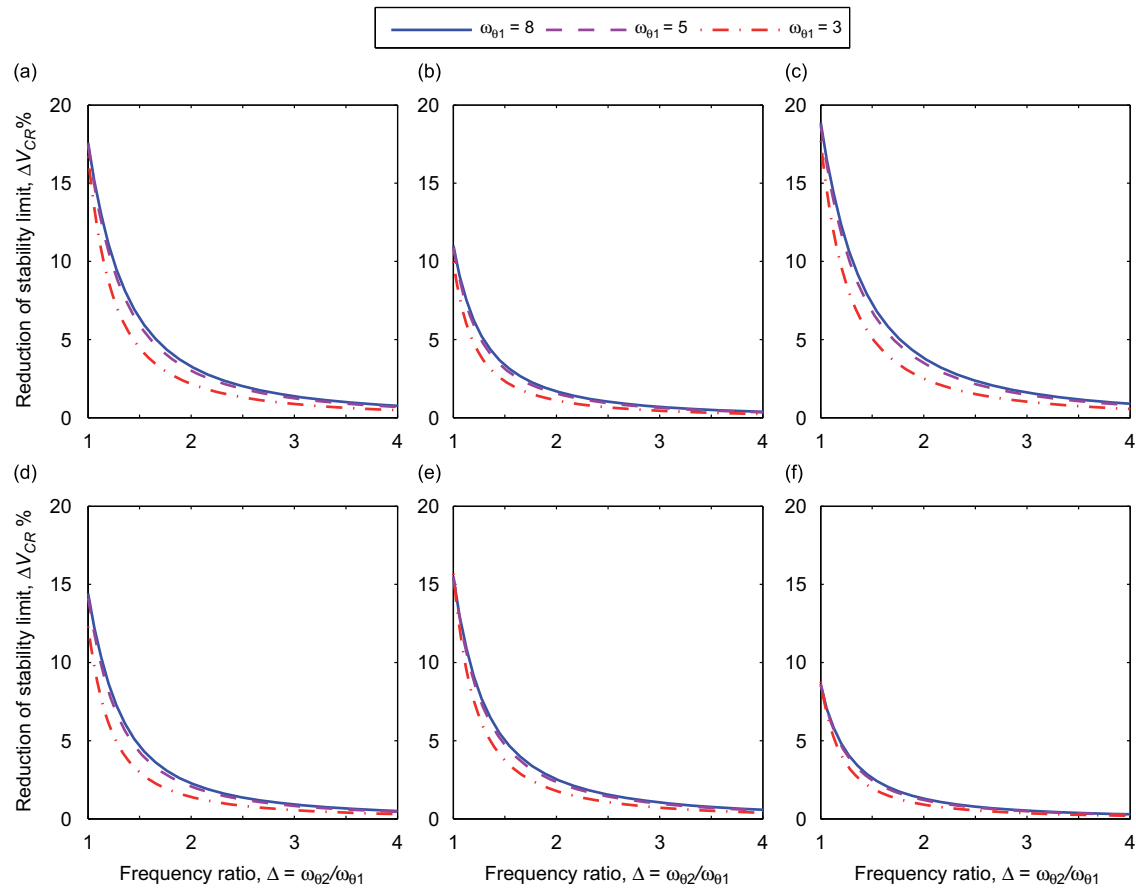

Fig. 8. Percentage reduction of the stability limit, ΔV_{CR}, as a function of the torsional frequency ratio, $\Delta = \omega_{\theta 2}/\omega_{\theta 1}$, for a system with one vertical and two torsional still-air vibration modes: (a) shapewise similarities $\psi_{z\theta 1}=1.0$, $\psi_{z\theta 2}=1.0$, mass properties, $m_z=15,000$ kg/m, $m_\theta=500,000$ kg^2/m. (b) $\psi_{z\theta 1}=1.0$, $\psi_{z\theta 2}=0.5$, $m_z=15,000$ kg/m, $m_\theta=500,000$ kg^2/m. (c) $\psi_{z\theta 1}=0.8$, $\psi_{z\theta 2}=0.8$, $m_z=15,000$ kg/m, $m_\theta=500,000$ kg^2/m. (d) $\psi_{z\theta 1}=0.8$, $\psi_{z\theta 2}=0.4$, $m_z=15,000$ kg/m, $m_\theta=500,000$ kg^2/m. (e) $\psi_{z\theta 1}=1.0$, $\psi_{z\theta 2}=1.0$, $m_z=25,000$ kg/m, $m_\theta=1,500,000$ kg^2/m. (f) $\psi_{z\theta 1}=1.0$, $\psi_{z\theta 2}=0.5$, $m_z=25,000$ kg/m, $m_\theta=1,500,000$ kg^2/m.

$\psi_{z\theta1}$=1.0, $\psi_{z\theta2}$=0.5, is shown in Fig. 8b. The reduction of the stability limit is much lower for this case, compared with the case shown in Fig. 8a and this indicates that the shapewise similarity ratio $\psi_{z\theta1}/\psi_{z\theta2}$ of the two bimodal combinations has great influence on the reduction of the stability limit. Fig. 8c shows results where the shapewise similarities have been assumed to be $\psi_{z\theta1}$=0.8, $\psi_{z\theta2}$=0.8. The results clearly follow the same pattern as those shown in Fig. 8a, but some small differences can be observed since the reduction of the stability limit when the two torsional still-air natural frequencies are identical is a fraction smaller in this case. A situation where the shapewise similarities are $\psi_{z\theta1}$=0.8 and $\psi_{z\theta2}$=0.4 is shown in Fig. 8d. The reduction of the stability limit cannot be directly calculated from the shapewise similarity ratio $\psi_{z\theta1}/\psi_{z\theta2}$ since the results in Fig. 8b and d are not identical, but an estimate can be made.

To investigate how different mass properties affect the results, the same aeroelastic system as outlined above is used, but with a total mass of m_z=25,000 kg/m and a mass moment of inertia of m_θ=1,500,000 kg^2/m. The reduction of the stability limit when the shapewise similarities are $\psi_{z\theta1}$=1.0, and $\psi_{z\theta2}$=1.0 is shown in Fig. 8e, and when this is compared with the results shown in Fig. 8a the results seem to have low sensitivity to changes in the mass properties of the structure. A situation where the shapewise similarities are $\psi_{z\theta1}$=1.0 and $\psi_{z\theta2}$=0.5 is shown in Fig. 8f, and when this figure is compared to the results shown in Fig. 8b, some small differences can be observed.

It may be concluded that reduction of the stability limit caused by multimodal effects is possible if one vertical mode is shapewise similar to two torsional modes. The reduction greatly depends on the separation of the torsional vibration modes on the frequency axis and the shapewise similarity ratio $\psi_{z\theta1}/\psi_{z\theta2}$. Several different structural configurations have been tested, and the results indicate that a reduction below 5% may be expected, for the particular cases tested, if the frequency ratio of the torsional modes is greater than two.
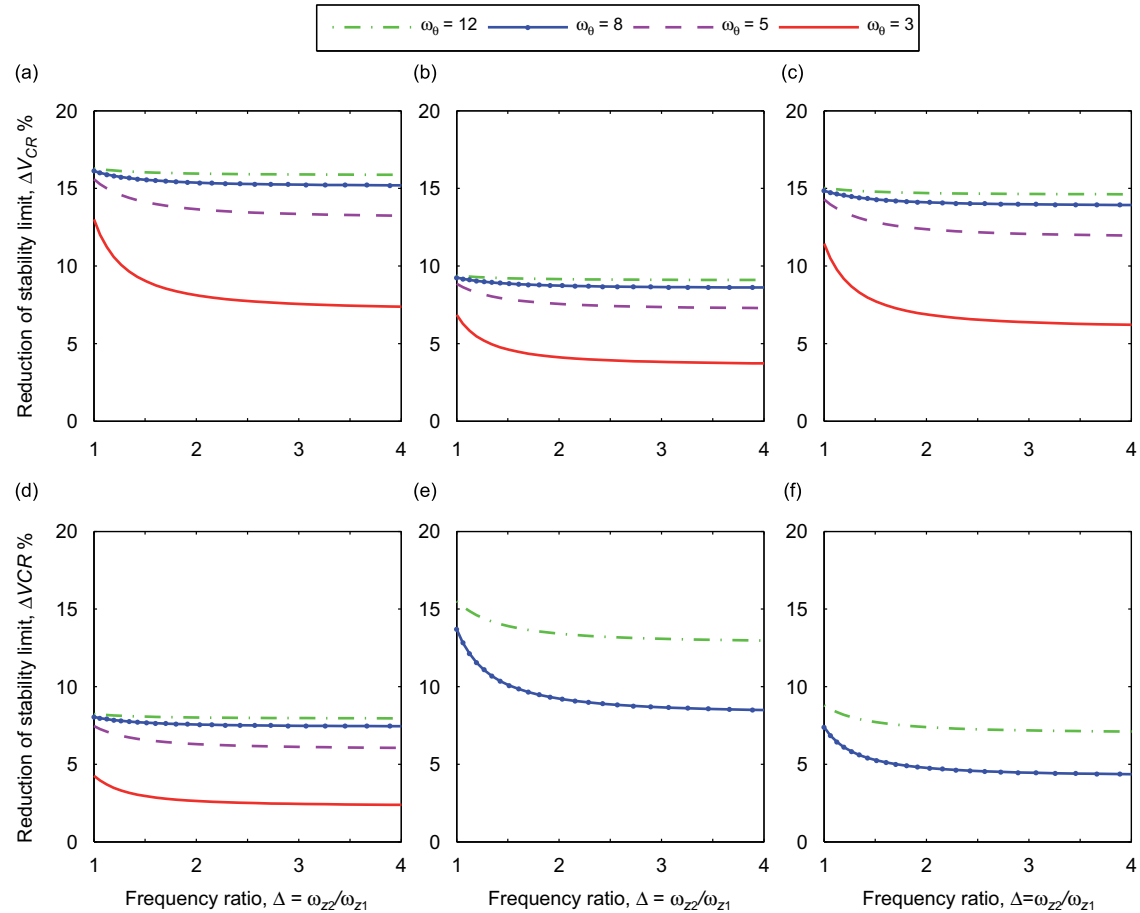

Fig. 9. Percentage reduction of the stability limit, ΔV_{CR}, as a function of the vertical frequency ratio, $\Delta = \omega_{z2}/\omega_{z1}$, for a system with one vertical and two torsional still-air vibration modes. (a) Shapewise similarities $\psi_{z2\theta}$=1.0, $\psi_{z1\theta}$=1.0, mass properties, m_z=15,000 kg/m, m_θ=500,000 kg^2/m. (b) $\psi_{z2\theta}$=1.0, $\psi_{z1\theta}$=0.5, m_z=15,000 kg/m, m_θ=500,000 kg^2/m. (c) $\psi_{z2\theta}$=0.8, $\psi_{z2\theta}$=0.8, m_z=15,000 kg/m, m_θ=500,000 kg2/m. (d) $\psi_{z2\theta}$=0.8, $\psi_{z2\theta}$=0.4, m_z=15,000 kg/m, m_θ=500,000 kg^2/m. (e) $\psi_{z2\theta}$=1.0, $\psi_{z2\theta}$=1.0, m_z=25,000 kg/m, m_θ=1,500,000 kg^2/m. (f) $\psi_{z2\theta}$=1.0, $\psi_{z1\theta}$=0.5, m_z=25,000 kg/m, m_θ=1,500,000 kg^2/m.

4.3. One torsional and two vertical modes

To answer question three stated above, another aeroelastic system is defined. It consists of three still-air vibration modes, two vertical and one torsional, defined by $\phi_{z1}(x), \phi_{z2}(x)$ and $\phi_{\theta}(x)$. The still-air natural frequencies are assumed to be ω_{z2}=2.0 rad/s, $\omega_{\theta} \in \{3.0\ 5.0\ 8.0\ 12.0\}$ rad/s, and $\omega_{z2}=\omega_{z1} \cdot \Delta$ rad/s, where Δ is in the range [1,...,10]. The mass of the system is set to m_z=15,000 kg/m, while the mass moment of inertia is taken as m_{θ}=500,000 kg^2/m. The stability limit of the second vertical, $\phi_{z2}(x)$ and the torsional mode, $\phi_{\theta}(x)$ is calculated first; the first vertical mode is then added to the system, and the percentage change of the stability limit is calculated. The results when the shapewise similarities have been assumed as $\psi_{z2\theta}$=1.0, $\psi_{z1\theta}$=1.0 are shown in Fig. 9a. As can be seen, the reduction of the stability limit due to multimodal effects among one torsional and two vertical modes is somewhat more complicated than where one vertical and two torsional vibration modes are shapewise similar. The frequency ratio Δ is of minor importance when the torsional natural frequency is high, while some dependency of the frequency ratio can be observed when the torsional frequency is low. The reduction of the stability limit converges to a constant value for all situations evaluated, and this implies that a reduction of the stability limit must be expected even when the frequency ratio Δ of the two vertical vibration modes is high. The magnitude of the reduction depends strongly on the torsional natural frequency. The reduction increases with increasing torsional frequency, but as can be seen in the figure, it converges to a constant value. The reduction of the stability limit when the shapewise similarities are $\psi_{z2\theta}$=1.0 and $\psi_{z1\theta}$=0.5 is shown in Fig. 9b. The same pattern as shown in Fig. 9a can be recognised, but the reduction of the stability limit, as expected, strongly depends on the shapewise similarity ratio $\psi_{z2\theta}/\psi_{z1\theta}$ of the still-air vibration modes.

The results when shapewise similarities have been assumed as $\psi_{z2\theta}$=0.8, $\psi_{z1\theta}$=0.8 are shown in Fig. 9c, and, as can be seen, the results follow the same pattern as those shown in Fig. 9a, but the shapewise similarities evaluated here result in less reduction of the stability limit. However, the differences are only one to three percent, which is rather low. A situation where the shapewise similarities are $\psi_{z2\theta}$=0.8, $\psi_{z1\theta}$=0.4 is presented in Fig. 9d, and when this is compared with the curves in Fig. 9b, the results indicate that the reduction of the stability limit cannot be calculated directly from the shapewise similarity ratio $\psi_{z2\theta}/\psi_{z1\theta}$.

To study how a change in the vertical frequency ω_{z2} affects the result, the same aeroelastic system as defined above is used, but with still-air vertical frequencies ω_{z2}=5 rad/s, $\omega_{z2}=\omega_{z1} \cdot \Delta$ rad/s, and $\omega_{z\theta} \in \{8, 12\}$. The results when the shapewise similarities have been assumed to be $\psi_{z2\theta}$=1.0, $\psi_{z1\theta}$=1.0 are shown in Fig. 9e, and, as can be seen, the reduction of the stability limit also depends on the still-air natural frequency ω_{z2} since the curves shown in Fig. 9a are fairly different. A situation where the shapewise similarities have been assumed to be $\psi_{z2\theta}$=1.0, $\psi_{z1\theta}$=0.5 is shown in Fig. 9f. When these results are compared with the curves presented in Fig. 9b, the dependency of the frequency ω_{z2} is also observed here.

It can be concluded that the reduction of the stability limit caused by multimodal effects when one torsional and two vertical still-air vibration modes participate in the flutter motion is more complicated than when one vertical and two torsional modes participate. The reduction depends on the frequency ratio ω_{z2}/ω_{z1}, the torsional frequency ω_{θ}, the vertical frequency, ω_{z2}, and the shapewise similarities. Different from the case with one vertical and two torsional still-air vibration modes, multimodal effects cannot be excluded at high ω_{z2}/ω_{z1} ratios.

5. Concluding remarks

Simplified prediction of flutter stability limits is discussed in this paper emphasising closed form solutions. It has been shown that the established bimodal approach, commonly referred to as the flutter equations, can be greatly simplified if the load coefficients presented in this paper are introduced. The expressions can be further simplified if the critical frequency is assumed to be on the torsional solution branch of the system and can be calculated by the uncoupled system of equations. This results in a simple expression which may be regarded as an engineering approximation of the critical flutter velocity. The expression has been tested for two typical cross sections for a wide range of hypothetical structural configurations, in addition to the structural configurations of a few well-known bridges. The results have been compared with results obtained by a complex eigenvalue analysis. The accuracy of the results has been satisfactory for all the cases evaluated. The presented formulae can be regarded as alternatives to Selberg's formula in preliminary designs of long-span bridges and in the design of medium-span bridges since Selberg's formula does not take into account possible imperfect shapewise similarity and the actual aerodynamic properties of the cross section. Further it has been shown that the expression presented may be simplified further if the contribution from damping is neglected. This results in a formula equal to Selberg's formula if the coefficients are given specific values. The estimate of the stability limit of the bridge may then be improved by using flutter derivatives available in the literature for a cross section similar to the girder of the bridge. It is also possible to use the formulae to study which of the parameters can be adjusted to achieve better aerodynamic performance.

Flutter where several vibration modes participate has been reported in the literature. It is therefore important to make sure that multimodal effects will not reduce the stability limit significantly before a simplified solution based on a bimodal consideration is used. The shapewise similarity is, as shown in this paper, the most important indicator of possible multimodal effects. To evaluate which of the still-air vibration modes participate in the flutter motion, the shapewise similarity of all possible combinations should be evaluated first. Then the vibration modes should be grouped in uncoupled

subsystems. The subsystem containing the still-air torsional vibration mode with the lowest natural frequency will most likely provide the lowest critical velocity. If this subsystem consists of more than two vibration modes, multimodal effects will occur. The reduction will be small if (1) the shapewise similarities are not of the same order of magnitude, which implies that the flutter motion is generated by a main pair of modes, and that the contribution from the secondary modes is small and (2) the subsystem consists of one vertical and two torsional vibration modes, and the two torsional vibration modes are well separated. If there are more than three shapewise similar vibration modes, multimodal calculations should be carried out.

An example where multimodal effects can be neglected, based on the shapewise similarity criterion, is the Messina Strait Bridge. Multimodal calculations of the stability limit of the bridge are presented in [31]. The results presented show that the stability limit remains unchanged when more than one vertical and one torsional still-air vibration mode is included. This is because the vibration modes come in shapewise similar pairs, resulting in uncoupled subsystems consisting of one vertical and one torsional vibration mode. However, the vibration modes are not well separated on the frequency axis, which implies that simplified methods are not recommended.

Participation of horizontal modes in the flutter motion has not been discussed in this study since experimental results of the flutter derivatives associated with horizontal motion are not available for the two cross sections dealt with.

Acknowledgements

Appendix A. The general flutter equation

The stability of an aeroelastic second-order system, where N still-air vibration modes are used as generalised degrees-of-freedom (see Fig. 1), can be predicted considering the following quadratic eigenvalue problem:

$$(S_n^2\tilde{\mathbf{M}}_0 + S_n(\tilde{\mathbf{C}}_0 - \tilde{\mathbf{C}}_{ae}(V,\omega)) + (\tilde{\mathbf{K}}_0 - \tilde{\mathbf{K}}_{ae}(V,\omega)))\mathbf{Z}_n = 0, \quad n = 1,2,\ldots,2N \tag{A.1}$$

Here, $\tilde{\mathbf{M}}_0$ represents the generalised structural mass matrix, $\tilde{\mathbf{C}}_0$ denotes the generalised damping matrix, and $\tilde{\mathbf{K}}_0$ represents the generalised structural stiffness matrix, where the subscript 0 indicates that the matrices contain properties obtained in still air. The function $\tilde{\mathbf{C}}_{ae}(V,\omega_n)$ stands for aerodynamic forces proportional to the velocity of the system, commonly referred to as the aerodynamic damping matrix, while $\tilde{\mathbf{K}}_{ae}(V,\omega_n)$ symbolises aerodynamics forces proportional to the displacement of the system, sometimes referred to as the aerodynamic stiffness matrix. These two matrices are a function of the oscillation frequency, ω, and the wind velocity, V. Furthermore, they also depend on the flutter derivatives (see Eq. (1)). The oscillation frequency, ω, and the wind velocity, V, are treated as continuous and independent variables in the following analysis.

The solution of Eq. (A.1) gives $2N$ eigenvalues, S_n, and corresponding eigenvectors $\mathbf{Z}_n$, where N is the number of degrees-of-freedom. Real roots imply that the system behaviour is non-periodic. When the root S_n is real and positive, the solution reveals exponential divergence; if it is real and negative, the solution exhibits exponential convergence. On the other hand, complex roots result in system behaviour of periodic or oscillatory nature. These roots appear in complex conjugated pairs of the form $S_n = \mu_n + i\omega_n$ and $S_{n+1} = S_n^* = \mu_n - i\omega_n$. The quantity ω_n is the damped natural frequency of the aeroelastic system, while μ_n is a measure of the damping or diverging behaviour of free oscillations. If μ_n is negative, the solution shows exponential convergence corresponding to positive damping of the aeroelastic system. On the other hand, if μ_n is positive, the solution exhibits exponential divergence, which is sometimes interpreted as negative damping of the aeroelastic system. Hence, the stability limit of the aeroelastic system can be defined in terms of the natural frequency, ω_n, and the wind velocity, V, that result in positive real parts of two of the eigenvalues (S_n and S_{n+1}). The lowest wind velocity leading to indifferent behaviour (which corresponds to $\mu_n = 0$) is termed the critical velocity.

The eigenvalue problem, Eq. (A.1), has to be solved by an iterative procedure since the flutter derivatives are functions of the frequency of motion as well as the wind velocity. Further details of the problem formulation and the solution procedure applied herein can be found in [32,33].

Appendix B. Selberg's flutter formula

The widely applied flutter formula, proposed by Selberg, is still used and is referred to in the guidelines of the Norwegian Public Roads Administration [26]. The formula can be expressed as follows, using the notation applied herein:

$$\hat{V}_{CR} = 0.6\sqrt{\left[1 - \left(\frac{1}{\gamma}\right)^2\right]\frac{R_g}{\chi_z B}} \tag{B.1}$$

By comparing this equation to the proposed closed-form flutter formula, Eq. (22), it is seen that the formulae become identical if the aerodynamic coefficients are selected such that the following equation is fulfilled:

$$50a_2\chi_z B - 9R_g(\chi_z h_3 a_1 + \chi_\theta a_2 a_3) = 0 \qquad (B.2)$$

where R_g is the radius of gyration. Similar relations to the other formulae outlined in the introduction can be developed if the approximations suggested in Eq. (10) are introduced:

References

[1] A. Selberg, Oscillation and aerodynamic stability of suspension bridges, *Acta Polytechnica Scandinavica Civil Engineering and Building Construction Series* 13 (1961).

[2] J.R. Banerjee, A simplified method for the free vibration and flutter analysis of bridge decks, *Journal of Sound and Vibration* 260 (2003) 829–845.

[3] G. Vairo, A simple analytical approach to the aeroelastic stability problem of long-span cable-stayed bridges, *International Journal of Computational Methods in Engineering Science and Mechanics* 11 (2010) 1–19.

[4] S. Pourzeynali, T.K. Datta, Reliability analysis of suspension bridges against flutter, *Journal of Sound and Vibration* 254 (2002) 143–162.

[5] E. Simiu, T. Miyata, *Design of Buildings and Bridges for Wind a Practical Guide for ASCE-7 Standard Users and Designers of Special Structures*, Wiley, Hoboken, NJ, 2006.

[6] A.G. Frandsen, Wind stability of suspension bridges application of the theory of thin airfoils, *Bygningsstatiske Meddelelser* 41 (1970) 55–77.

[7] Y. Nakamura, An analysis of binary flutter of bridge deck sections, *Journal of Sound and Vibration* 57 (1978) 471–482.

[8] N.J. Gimsing, *Cable Supported Bridges: Concept and Design*, Wiley, Chichester, 1997.

[9] G. Bartoli, C. Mannini, A simplified approach to bridge deck flutter, *Journal of Wind Engineering and Industrial Aerodynamics* 96 (2008) 229–256.

[10] X.Z. Chen, Improved understanding of bimodal coupled bridge flutter based on closed-form solutions, *Journal of Structural Engineering—ASCE* 133 (2007) 22–31.

[11] C. Dyrbye, S.O. Hansen, *Wind Loads on Structures*, Wiley, Chichester, 1997.

[12] E. Simiu, R.H. Scanlan, *Wind Effects on Structures Fundamentals and Applications to Design*, Wiley, New York, 1996.

[13] X.Z. Chen, A. Kareem, Revisiting multimode coupled bridge flutter: some new insights, *Journal of Engineering Mechanics—ASCE* 132 (2006) 1115–1123.

[14] O. Øiseth, A. Rönnquist, R. Sigbjörnsson, Simplified prediction of wind-induced response and stability limit of slender long-span suspension bridges, based on modified quasi-steady theory: a case study, *Journal of Wind Engineering and Industrial Aerodynamics* 98 (2010) 730–741.

[15] L.D. Zhu, Y.L. Xu, Buffeting response of long-span cable-supported bridges under skew winds—part 1: theory, *Journal of Sound and Vibration* 281 (2005) 647–673.

[16] Y.L. Xu, L.D. Zhu, Buffeting response of long-span cable-supported bridges under skew winds—part 2: case study, *Journal of Sound and Vibration* 281 (2005) 675–697.

[17] X. Zhang, J.M.W. Brownjohn, Some considerations on the effects of the P-derivatives on bridge deck flutter, *Journal of Sound and Vibration* 283 (2005) 957–969.

[18] H. Katsuchi, N.P. Jones, R.H. Scanlan, Multimode coupled flutter and buffeting analysis of the Akashi-Kaikyo bridge, *Journal of Structural Engineering—ASCE* 125 (1999) 60–70.

[19] P.P. Sarkar, L. Caracoglia, F.L. Haan Jr., H. Sato, J. Murakoshi, Comparative and sensitivity study of flutter derivatives of selected bridge deck sections—part 1: analysis of inter-laboratory experimental data., *Engineering Structures* 31 (2009) 158–169.

[20] M. Matsumoto, K. Mizuno, K. Okubo, Y. Ito, Torsional flutter and branch characteristics for 2-D rectangular cylinders, *Journal of Fluids and Structures* 21 (2005) 597–608.

[21] M. Gu, R. Zhang, H. Xiang, Parametric study on flutter derivatives of bridge decks, *Engineering Structures* 23 (2001) 1607–1613.

[22] C. Su, X. Fan, T. He, Wind-induced vibration analysis of a cable-stayed bridge during erection by a modified time-domain method, *Journal of Sound and Vibration* 303 (2007) 330–342.

[23] R.H. Scanlan, J.J. Tomko, Airfoil and bridge deck flutter derivatives, *Journal of the Engineering Mechanics Division* 97 (1971) 1717–1737.

[24] E.N. Strømmen, *Theory of Bridge Aerodynamics*, Springer, Berlin, 2006.

[25] S.M. Selby, *Standard Mathematical Tables*, Chemical Rubber Co., Cleveland, 1973.

[26] Statensvegvesen, *prosjekteringsregler for bruer (Design guidelines for bridges), håndbok 185*, 2006.

[27] S.O. Hansen, M. Lollesgaard, S. Rex, J.B. Jakobsen, E. Hjorth-Hansen, *The Hardanger Bridge: Static and Dynamic Wind Tunnel Tests with a Section Model.*, Svend Ole Hansen ApS, Copenhagen, 2006.

[28] M. Matsumoto, K. Mizuno, K. Okubo, Y. Ito, H. Matsumiya, Flutter instability and recent development in stabilization of structures, *Journal of Wind Engineering and Industrial Aerodynamics* 95 (2007) 888–907.

[29] X. Chen, A. Kareem, Identification of critical structural modes and flutter derivatives for predicting coupled bridge flutter, *Journal of Wind Engineering and Industrial Aerodynamics* 96 (2008) 1856–1870.

[30] S.O. Hansen, M. Lollesgaard, S. Rex, J.B. Jakobsen, E. Hjorth-Hansen, *The Brandangersundet Bridge: Static and Dynamic Wind Tunnel Tests with a Section Model.*, Svend Ole Hansen ApS, Copenhagen, 2007.

[31] P. D'Asdia, V. Sepe, Aeroelastic instability of long-span suspended bridges: a multi-mode approach, *Journal of Wind Engineering and Industrial Aerodynamics* 74(6) (1998) 849–857.

[32] T.J.A. Agar, Aerodynamic flutter analysis of suspension bridges by a modal technique, *Engineering Structures* 11 (1989) 75–82.

[33] L. Salvatori, C. Borri, Frequency- and time-domain methods for the numerical modeling of full-bridge aeroelasticity, *Computers and Structures* 85 (2007) 675–687.

[34] Jakobsen, J.B., Hjorth-Hansen, E., Arne Selberg's formula for flutter speed in light of multimodal flutter analysis. Twelfth International Conference on Wind Engineering, Cairns, Australia.

Ole Øiseth, Anders Rönnquist, Ragnar Sigbjörnsson

Time domain modeling of self-excited aerodynamic forces for cable-supported bridges: A comparative study

Paper III

Time domain modeling of self-excited aerodynamic forces for cable-supported bridges: A comparative study

Ole Øiseth, Anders Rönnquist, Ragnar Sigbjörnsson *

Department of Structural Engineering, Norwegian University of Science and Technology, 7491 Trondheim, Norway

A B S T R A C T

Prediction of the wind-induced dynamic response of suspension bridges, emphasizing self-excited forces, is discussed in this paper. The self-excited forces have been modeled by two commonly applied unsteady models and an unsteady model introduced and explained in this article. A novel frequency-independent approximation of the self-excited forces, which for the suspension bridge considered provides results as accurate as those from the unsteady models, is also presented. An integration method that may reduce the number of time steps necessary to avoid amplitude and phase distortion of the self-excited forces has been introduced and applied successfully in a comprehensive case study.

© 2011 Elsevier Ltd. All rights reserved.

1. Introduction

When designing long-span cable-supported bridges, time domain assessment of the dynamic response is convenient, since structural nonlinearities may be taken more easily into account in the time domain than in the frequency domain. One of the main concerns for long-span bridges is wind-induced dynamic response, which is most commonly predicted using frequency domain methods, where the aeroelastic effects are introduced in terms of experimentally determined aerodynamic derivatives [1–12]. This approach is an extension of classical airfoil theory [13], where Theodorsen's function provides the self-excited forces that are actions generated by the motion of the cross section in the fluid flow. Another well-known aerodynamic function has been developed by Wagner [14]. While Theodorsen's function describes the lift due to circulation about an airfoil oscillating and moving horizontally with constant velocity, the Wagner function describes the growth of circulation or lift on the airfoil at a small, fixed angle of attack, starting impulsively from rest to a uniform velocity. Garrick [15] showed that Theodorsen's function and Wagner's function constitute a pair of Fourier transforms. Likewise, Scanlan et al. [2] suggested that there may be a similar relation between indicial functions in the time domain and aerodynamic derivatives in the frequency domain. The aerodynamic derivatives can be determined by wind tunnel measurements using a scaled section model of the bridge deck, see e.g., [9,16]. Some attempts have also been made to determine the aerodynamic derivatives from fluid–structure interaction models [17–19], where the main challenge is to model the flow around non-structural details like hand rails and guide vanes accurately, since these effects may have a significant influence on the results.

Several methods exist for unsteady modeling of self-excited forces in the time domain. Many of the methods have their origin in the Laplace domain, or equivalent, in the frequency domain when the effect of exponential decay or divergence is assumed to be negligible. A complex transfer function suitable for Fourier transforming is curve-fitted to the experimental data, such that the time domain formulation may be obtained using the Fourier transform applying the convolution theorem. Several transfer functions have been suggested that may be suitable. Yagi [20] applied Roger's approximation and the matrix padé approximation to model the self-excited forces for a bridge deck, but Roger's approximation was more successful. Roger's approximation has also been applied in [21,22]. Roger's approximation is a sum of rational functions, where the denominator is the same for all the transfer functions. Bucher and Lin [23] have used a slightly different approach, where the coefficients in the denominators are determined separately for each transfer function. It is also possible to develop expressions for the self-excited forces considering the downwash on the cross section [14,24]. This results in a formulation that has a more physical basis than the rational function approximations discussed above. However, the indicial functions must also

---

* Corresponding author.
E-mail addresses: ole.oiseth@ntnu.no (O. Øiseth), anders.ronnquist@ntnu.no (A. Rönnquist), ragnar.sigbjornsson@ntnu.no (R. Sigbjörnsson).

Nomenclature

$A_x^{(nm)}$	coefficient number x in the rational function formulation
$A_n^*,\ H_n^*,\ P_n^*$	aerodynamic derivatives
$a_n,\ h_n,\ p_n$	modified quasi-steady coefficients
a_h	distance from the center of the airfoil to the shear center
$a_{inm},\ b_{inm}$	coefficients in the indicial function formulation
$\mathbf{A},\ \mathbf{B}$	state space system matrices
$\beta,\ \gamma$	constants that define the properties of Newmark's method
$B,\ D$	width and height of the girder
$d_x^{(nm)}$	coefficient number x in the rational function formulation
δ	Dirac delta function
M	number of subdivision of the time step
$\mathbf{M},\ \mathbf{C},\ \mathbf{K}$	mass, damping and stiffness matrix
$C_D,\ C_L,\ C_M$	force coefficients
F	aerodynamic transfer function
$\mathbf{F}_{ae}$	a vector that contains the time dependent part of the self-excited forces
$G_n,\ \mathbf{G}_n$	the Fourier transform of variable n, a vector containing Fourier transforms
G_{ij}	mode shape integrals
i	the imaginary unit
I	aerodynamic impulse response function
K	reduced frequency
κ	roughness coefficient
$\mathbf{L},\ L_{nm}$	lower triangular matrix obtained by Cholesky decomposition of the cross spectral density matrix
L	span length
N	number of exponential filters
$P,\ \mathbf{P}$	cross sectional action, vector containing cross sectional actions
ψ	indicial function
$q,\ \mathbf{q}$	cross sectional load
$\mathbf{Q},\ \tilde{Q}_i$	modal load vector, modal load
$r,\ \dot{r},\ \ddot{r}$	displacement, velocity and response acceleration
S or $\mathbf{S}$	auto or cross-spectral density, cross-spectral density matrix
S_k	eigenvalue number k
t	time

τ	integration variable
u	fluctuating horizontal wind velocity
V	mean wind velocity
w	downwash, fluctuating vertical wind velocity
$x,\ \Delta x$	span-wise coordinate, span-wise separation
x_m	time series of the fluctuating wind velocities
$\mathbf{X}_k$	right hand eigenvector number k
$\mathbf{Y}_k$	left hand eigenvector number k
z	height above ground or sea level
$\mathbf{Z}$	state variable
$\eta,\ \boldsymbol{\eta}$	generalized coordinate or vector containing all generalized coordinates
ξ_n	still-air damping ratio for mode no. n
ρ	air density
Φ	Wagner function, or indicial function
$\phi_y,\ \phi_z,\ \phi_\theta$	components in the vibration mode vector
$\omega,\ \omega_n$	circular frequency and natural circular frequency
∞	infinity

Subscripts/superscripts

ae	aerodynamic
$buff$	buffeting
$D,\ L,\ M$	drag, lift, moment
Se	self-excited
T	transpose
$u,\ w$	along-wind velocity, across-wind velocity in vertical direction
$y,\ z,\ \theta$	horizontal displacement, vertical displacement, rotation
0	still-air
$\sim$	modal property
$'$	derivative with respect to angle of attack or τ
$\cdot$	time derivative
$*$	complex conjugate

Abbreviations

AD	aerodynamic derivatives
FD	frequency domain
QST	quasi-steady theory
QSA	quasi-steady asymptotes
TD	time domain

be approximated by functions suitable for Fourier transforming; thus, the main difference of the two methods is the different starting points.

An alternative to unsteady self-excited force models is to use quasi-steady theory [5,6,25,26] to quantify the self-excited forces. In the quasi-steady theory, force coefficients from static wind tunnel measurements are used to quantify the self-excited forces. This implies that the quasi-steady theory may be used in both the time and frequency domains. However, it is well known that the quasi-steady theory may provide inaccurate results for some cross sections, in particular, since no aerodynamic torsional damping is provided. Øiseth et al. [6] propose a modified quasi-steady approach, where curves providing a frequency-independent description of the self-excited forces are fitted to the experimentally determined aerodynamic derivatives in the important frequency range. This approach has also been used to develop simplified expressions for the critical flutter velocity of cable supported bridges [27]. Other approaches have also been suggested in the literature. Borri and Costa [28] have introduced torsional aerodynamic damping by using the leading edge of the profile as reference point, assuming that the action is driven by the phenomena occurring at this edge. Diana et al. [29] have developed a

corrected quasi-steady theory that takes aerodynamic nonlinearities into account. The approach has been developed further in two recent papers [30,31]. In this paper the method suggested by Øiseth et al. [6], focusing on the frequency dependency, has been further developed making it possible to model the self-excited forces accurately at all the natural frequencies of the aeroelastic system.

The unsteady load models discussed above need to be curve-fitted to the experimental data using a nonlinear approach. Since the transfer functions are complex, two sets of data must be curve-fitted to the same coefficients. This implies that the unsteady time domain methods will most likely provide a least squares fit of lower accuracy than the curves used to represent the aerodynamic derivatives in the frequency domain. In this article unsteady and quasi-steady self-excited force models are used to predict the buffeting response of a long-span suspension bridge. Two of the unsteady models discussed above, in addition to an unsteady model suggested in this paper, where quasi-steady asymptotes may be more easily introduced, have been compared. We also present a novel approximate approach, which, when applied to the suspension bridge, provides results as accurate as those produced by the unsteady models. The unsteady self-excited force models give the self-excited forces in terms of convolution integrals in the time

domain. It has been shown in several papers that a time step much smaller than what is usually applied in the dynamic time domain analysis may become necessary to evaluate the convolution integrals with sufficient accuracy to avoid phase and amplitude distortion of the self-excited forces, e.g., [32–34]. In this article an integration scheme that solves this problem has been suggested. When using this integration method, time steps as small as normally recommended in dynamic response calculations are sufficient.

2. Modeling self-excited forces

Self-excited forces are generated by the motion of the structure. Two approaches are currently being used for bridges, namely (1) unsteady models, which take into account how the motion of the structure will affect the flow around it and (2) steady models, where force coefficients measured on a fixed model are used to quantify the self-excited forces. The most common representation of unsteady self-excited aerodynamic forces is given by Scanlan and Tomko [9] as follows (see Fig. 1):

$$q_y^{Se} = \frac{1}{2}\rho V^2 B\left(KP_1^*\frac{\dot{r}_y}{V} + KP_2^*\frac{B\dot{r}_\theta}{V} + K^2 P_3^* r_\theta + K^2 P_4^*\frac{r_y}{B} + KP_5^*\frac{\dot{r}_z}{V} + K^2 P_6^*\frac{r_z}{B} \right)$$

$$q_z^{Se} = \frac{1}{2}\rho V^2 B\left(KH_1^*\frac{\dot{r}_z}{V} + KH_2^*\frac{B\dot{r}_\theta}{V} + K^2 H_3^* r_\theta + K^2 H_4^*\frac{r_z}{B} + KH_5^*\frac{\dot{r}_y}{V} + K^2 H_6^*\frac{r_y}{B} \right)$$

$$q_\theta^{Se} = \frac{1}{2}\rho V^2 B^2\left(KA_1^*\frac{\dot{r}_z}{V} + KA_2^*\frac{B\dot{r}_\theta}{V} + K^2 A_3^* r_\theta + K^2 A_4^*\frac{r_z}{B} + KA_5^*\frac{\dot{r}_y}{V} + K^2 A_6^*\frac{r_y}{B} \right)$$

(1)

Here, V is the mean wind velocity; ρ is the air density; B is the width of the cross section; $K = B\omega/V$ is the reduced circular frequency of motion, and r_n, $n \in \{y, z, \theta\}$ represents the horizontal, vertical and torsional responses that are positive in the same direction as the forces displayed in Fig. 1. P_n^*, H_n^*, A_n^*, $n \in \{1, 2, \ldots, 6\}$ are the dimensionless aerodynamic derivatives, which are characteristic cross-sectional properties given as functions of the reduced-frequency of motion. The aerodynamic derivatives are in practice obtained at discrete harmonic frequencies (commonly presented as reduced frequencies) from wind tunnel experiments applying a scaled section model. Hence, the above equations are strictly only valid for single harmonic motion. However, within the framework of harmonic analysis applying the principle of superposition, Eq. (1) can be extended to any harmonic motion or aperiodic motion applying Fourier integral representation. Consequently, taking the Fourier transform of Eq. (1), the following frequency domain description of the self-excited aerodynamic forces emerges,

$$G_{q_y^{Se}}(\omega) = \frac{1}{2}\rho B^2 \omega^2 \left[(P_1^* i + P_4^*)G_y(\omega) + (P_5^* i + P_6^*)G_z(\omega) \right.$$
$$\left. + B(P_2^* i + P_3^*)G_\theta(\omega) \right]$$

$$G_{q_z^{Se}}(\omega) = \frac{1}{2}\rho B^2 \omega^2 \left[(H_5^* i + H_6^*)G_y(\omega) + (H_1^* i + H_4^*)G_z(\omega) \right.$$
$$\left. + B(iH_2^* + H_3^* r_\theta)G_\theta(\omega) \right]$$

(2)

$$G_{q_\theta^{Se}}(\omega) = \frac{1}{2}\rho B^2 \omega^2 \left[B(A_5^* i + A_6^*)G_y(\omega) + B(A_1^* i + A_4^*)G_z(\omega) \right.$$
$$\left. + B^2(A_2^* i + A_3^*)G_\theta(\omega) \right]$$

which can be further simplified to

$$G_{q_n^{Se}}(\omega) = F_{ny}(\omega)G_y(\omega) + F_{nz}(\omega)G_z(\omega) + F_{n\theta}(\omega)G_\theta(\omega)$$ (3)

Here, $n \in \{y, z, \theta\}$; i is the imaginary unit, and $G_X(\omega)$ is the Fourier transform of $X(t)$, where $X(t) \in \{r_y, r_z, r_\theta, q_y, q_z, q_\theta\}$, and $F_{nm}(\omega)$ symbolises the transfer functions defined in terms of the aerodynamic derivatives, which in this representation are treated as continuous functions of frequency. As shown by Bucher and Lin [23], the time domain description of the self-excited forces can be obtained apply-
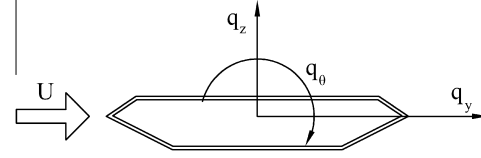

Fig. 1. Aerodynamic forces acting on a cross section of the bridge deck. The structural displacements are positive in the same direction as the forces.

ing the inverse Fourier transform and the convolution theorem. This results in the following equations:

$$q_n^{(Se)}(V, t) = \int_{-\infty}^{t} I_{ny}(t - \tau)r_y(\tau)d\tau + \int_{-\infty}^{t} I_{nz}(t - \tau)r_z(\tau)d\tau$$
$$+ \int_{-\infty}^{t} I_{n\theta}(t - \tau)r_\theta(\tau)d\tau$$

(4)

Here, $n \in \{y, z, \theta\}$. The aerodynamic impulse response functions are defined by the inverse Fourier transform of the transfer functions as follows:

$$I_{nm}(t) = \frac{1}{2\pi}\int_{-\infty}^{\infty} F_{nm}(\omega)e^{i\omega t}d\omega$$ (5)

Here it is assumed that the system is causal, i.e. $I_{nm}(t) = 0$ for $t < 0$. Hence, the upper bounds in the integrals in Eq. (4) can be changed from t to infinity, ∞.

2.1. Unsteady force model 1

The transfer functions are in general only known from experiments at discrete reduced-frequencies. A rational function approximation is frequently used to interpolate the experimental data [20,21,23]; the self-excited lift force related to the vertical motion can then be defined by the following rational function approximation, which will be referred to as force model 1

$$F_{zz}(V, \omega) = \frac{1}{2}\rho V^2\left(A_1^{(zz)} + A_2^{(zz)}\frac{i\omega B}{V} + A_3^{(zz)}\left(\frac{i\omega B}{V}\right)^2 + \sum_{l=1}^{m} \frac{A_{l+3}^{(zz)}i\omega B/V}{i\omega B/V + d_l^{(zz)}} \right)$$

(6)

A_n, $n \in \{1, \ldots, N\}$ are coefficients determined from a nonlinear least squares fit to experimental data. The corresponding impulse response function is given by the inverse Fourier transform of Eq. (6).

$$I_{zz}(t) = \frac{1}{2}\rho V^2\left(A_1^{(zz)}\delta(t) + A_2^{(zz)}\dot{\delta}(t)\frac{B}{V} + A_3^{(zz)}\ddot{\delta}(t)\left(\frac{B}{V}\right)^2 \right.$$
$$\left. + \sum_{l=1}^{m} A_{l+3}^{(zz)}\left(\delta(t) - \frac{d_l^{(zz)}V}{B}e^{\left(-\frac{d_l^{(zz)}V}{B}t\right)} \right) \right)$$

(7)

Here, $\delta(t)$ is the Dirac delta function. Comparing Eqs. (2) and (6), and neglecting added mass effects ($A_3^{(nm)} = 0$), it is seen that the real and imaginary parts of the transfer function, here represented by H_4^* and H_1^*, can be written as:

$$H_4^* = \hat{V}^2\left(A_1^{(zz)} + \sum_{l=1}^{L} \frac{A_{l+3}^{(zz)}}{\left[\left(d_l^{(zz)}\hat{V}\right)^2 + 1 \right]} \right),$$

$$H_1^* = \hat{V}\left(A_2^{(zz)} + \hat{V}^2 \sum_{l=1}^{L} \frac{A_{l+3}^{(zz)}d_l^{(zz)}}{\left[\left(d_l^{(zz)}\hat{V}\right)^2 + 1 \right]} \right)$$

(8)

The lift force related to vertical motion may then be expressed as:

$$q_{zz}(t) = \frac{1}{2}\rho V^2 \left(A_1^{(zz)}r_z(t) + A_2^{(zz)}\frac{B}{V}\dot{r}_z(t) \right.$$
$$\left. + \sum_{l=1}^{m} A_{l+3}^{(zz)} \left(r_z(t) - \frac{d_l^{(zz)}V}{B}\int_{-\infty}^{t} e^{\left(-\frac{d_l^{(zz)}V}{B}(t-\tau)\right)} r_z(\tau)d\tau \right) \right) \quad (9)$$

The self-excited forces should tend to quasi-steady values when the reduced-frequency approaches zero [3]. This is a reduced-frequency range where experimental data for the aerodynamic derivatives may not be available, especially if the aerodynamic derivatives have been obtained by the commonly applied free vibration test. The quasi-steady asymptotes of the transfer function derived from Eq. (8) are

$$\lim_{K \to 0}(K^2 H_4^*) = A_1^{(zz)}, \quad \lim_{K \to 0}(KH_1^*) = A_2^{(zz)} + \sum_{l=1}^{L} \frac{A_{l+3}^{(zz)}}{d_l^{(zz)}} \quad (10)$$

and, as can be seen, both the imaginary and real part of the transfer function goes to quasi-steady values when the reduced-frequency goes to zero. The imaginary part is dependent on both the constant $A_2^{(nm)}$ and the constants in the exponential filters. This implies that $A_2^{(nm)}$ cannot be directly related to the asymptotic quasi-steady contribution related to the structural velocity, which is a disadvantage since a direct comparison with, for instance, the traditional quasi-steady theory becomes more complicated.

2.2. Unsteady force model 2

To derive a force model with simpler quasi-steady asymptotes, the following transfer function is suggested in this article, which will be referred to as force model 2:

$$F_{zz}(V,\omega) = \frac{1}{2}\rho V^2 \left(A_1^{(zz)} + A_2^{(zz)}\frac{i\omega B}{V} + \sum_{l=1}^{m} \frac{A_{l+3}^{(zz)}(i\omega B/V)^2}{i\omega B/V + d_l^{(zz)}} \right) \quad (11)$$

Here, added mass effects have been assumed negligible ($A_3^{(nm)} = 0$). This transfer function model provides the following expression for the real and the imaginary part, here represented by H_4^* and H_1^*, respectively:

$$H_4^* = \hat{V}^2 \left(A_1^{(zz)} - \sum_{l=1}^{L} \frac{A_{l+3}^{(zz)}d_l^{(zz)}}{\left[\left(d_l^{(zz)}\hat{V}\right)^2 + 1\right]} \right),$$

$$H_1^* = \hat{V} \left(A_2^{(zz)} + \sum_{l=1}^{L} \frac{A_{l+3}^{(zz)}}{\left[\left(d_l^{(zz)}\hat{V}\right)^2 + 1\right]} \right) \quad (12)$$

and the quasi-steady asymptotes become:

$$\lim_{K \to 0}(K^2 H_4^*) = A_1^{(zz)}, \quad \lim_{K \to 0}(KH_1^*) = A_2^{(zz)} \quad (13)$$

Taking the inverse Fourier transform of the transfer function, the impulse response function is given by:

$$I_{zz}(t) = A_1^{(zz)}\delta(t) + A_2^{(zz)}\frac{B}{V}\dot{\delta}(t)$$
$$+ \sum_{n=1}^{N} A_{n+3}^{(zz)} \left(\left(d_n^{(zz)}\right)^2 e^{d_n^{(zz)}\frac{V}{B}t}H(t) + \frac{B}{V}\dot{\delta}(t) + d_n^{(zz)}\delta(t) \right) \quad (14)$$

The self-excited forces may then be written as:

$$q_{zz}(t) = \frac{1}{2}\rho V^2 \left(\left(A_2^{(zz)} + \sum_{n=1}^{N} A_{n+3}^{(zz)} \right)\frac{B\dot{r}(t)}{V} \right.$$
$$+ \left(\sum_{n=1}^{N} A_{n+3}^{(zz)}d_n^{(zz)} + A_1^{(zz)} \right)r(t)$$
$$\left. + \frac{V}{B}\int_{-\infty}^{t} \left(\sum_{n=1}^{N} A_{n+3}^{(zz)}(d_n^{(zz)})^2 e^{d_n\frac{V}{B}(t-\tau)} \right)r(\tau)d\tau \right) \quad (15)$$

which may be further simplified through integrating twice by parts:

$$q(t) = \frac{1}{2}\rho V^2 \left(\underbrace{A_1 r(t) + A_2\frac{B\dot{r}(t)}{V}}_{\text{Quasi-steady}} + \underbrace{\int_{-\infty}^{t} \sum_{n=1}^{N} A_{n+3}e^{d_n\frac{V}{B}(t-\tau)}\frac{Br''(\tau)}{V}d\tau}_{\text{Unsteady contribution}} \right) \quad (16)$$

This implies that $A_1^{(nm)}$ and $A_2^{(nm)}$ are the quasi-steady force coefficients, while the exponential filters take the discrepancy of the quasi-steady theory and the experimental results into account.

2.3. Unsteady force model 3

An alternative approach to the rational function formulation, where a function suitable for Fourier transformation is chosen to interpolate the experimental results, is to consider the downwash on the cross section. For the case of an airfoil, the downwash at the 3/4 point may be used to characterize the self-excited forces from circulatory origin [14]:

$$w_i(\tau) = V \cdot r_\theta(\tau) - r'_z(\tau) + r'_\theta(\tau)\left(\frac{1}{2} - a_h\right)\frac{B}{2}$$

$$q_L(t) = \frac{1}{2}\rho VBC'_L \int_{-\infty}^{t} \Phi(t-\tau)\frac{dw(\tau)}{d\tau}d\tau, \quad q_M(t) = \frac{B}{4}(1+a_h)q_L(\tau) \quad (17)$$

where Φ is the well-known Wagner function, and a_h is the distance from the center of the airfoil to the shear center. Several authors, e.g. [2,24], have pointed out that the simple expression outlined above, where only one indicial function is necessary to describe the self-excited forces, is not directly applicable to a bluff section. Bisplinghoff and Ashley [24] suggested a model with two indicial functions, one for the effective angle of attack and one for the angular velocity, and since the aerodynamic center is not as clearly defined as for an airfoil, separate indicial functions are necessary for the lift and overturning moment. Bucher and Lin [23] have pointed out that there may be some redundancy in Eq. (17) since the torsional motion history also contains information on the angular velocity. Costa and Borri [33] and Caracoglia and Jones [35] have used the first two terms in Eq. (17), rendering self-excited aerodynamic forces defined by the following equations, which will be referred to as force model 3,

$$q_L(t) = \frac{1}{2}\rho V^2 BC'_L \left[\int_{-\infty}^{t} \Phi_{Z\theta}(t-\tau)r'_\theta(\tau)d\tau - \frac{1}{V}\int_{-\infty}^{t} \Phi_{ZZ}(t-\tau)r''_z(\tau)d\tau \right]$$

$$q_M^{IF}(t) = \frac{1}{2}\rho V^2 B^2 C'_M \left[\int_{-\infty}^{t} \Phi_{\theta\theta}(t-\tau)r'_\theta(\tau)d\tau - \frac{1}{V}\int_{-\infty}^{t} \Phi_{\theta Z}(t-\tau)r''_z(\tau)d\tau \right] \quad (18)$$

where only the vertical and horizontal components are considered for brevity. The indicial functions are approximated as:

$$\Phi_{nm}(t) = \begin{cases} a_{0nm} - \sum_{i=1}^{N} a_{inm}\exp[-b_{inm}\frac{V}{B}t], & t \geqslant 0 \\ 0, & t < 0 \end{cases} \quad (19)$$

The transfer functions may then be obtained by the Fourier transform:

$$F(\omega) = \int_{-\infty}^{\infty} \Phi(t)e^{-i\omega t}dt = \int_{0}^{\infty} \Phi(t)e^{-i\omega t}dt = \frac{a_{0nm}}{i\omega} - \sum_{i=1}^{N} \frac{a_{inm}}{b_{inm}\frac{V}{B} + i\omega}$$

(20)

which renders the following equivalence scheme, here represented by H_1^*, H_2^*, H_3^* and H_4^*:

$$H_1^* = -C_L'\hat{V}\left[a_{0zz} - \sum_{i=1}^{N} \frac{a_{izz}}{\left(b_{izz}\hat{V}\right)^2 + 1}\right]$$

$$H_2^* = -C_L'\hat{V}\left[\sum_{i=1}^{N} \frac{a_{iz\theta}b_{iz\theta}\hat{V}2}{\left[\left(b_{iz\theta}\hat{V}\right)^2 + 1\right]}\right]$$

$$H_3^* = C_L'\hat{V}2\left[a_{0z\theta} - \sum_{i=1}^{N} \frac{a_{iz\theta}}{\left[\left(b_{iz\theta}\hat{V}\right)^2 + 1\right]}\right]$$

(21)

$$H_4^* = -C_L'\hat{V}2\left[\sum_{i=1}^{N} \frac{a_{izz}b_{izz}}{\left[\left(b_{izz}\hat{V}\right)^2 + 1\right]}\right]$$

An identical equivalence scheme may be obtained for the aerodynamic derivatives related to the self-excited overturning moment, replacing C_L' with C_M' and the first sub index z with θ. The quasi-steady asymptotes of this model are

$$\lim_{K\to0}(KH_1^*) = -C_L'a_{0zz} \quad \lim_{K\to0}(KH_2^*) = -C_L'\sum_{i=1}^{N} \frac{a_{iz\theta}}{b_{iz\theta}}$$

$$\lim_{K\to0}(K^2H_3^*) = C_L'a_{0z\theta} \quad \lim_{K\to0}(K^2H_4^*) = 0$$

(22)

The steady-state values associated with the vertical response (H_4^* and A_4^*) become zero. This is reasonable since the vertical position (displacement) should not affect the load in a steady-state situation. The steady-state values for A_2^* and H_2^* have somewhat more complicated behavior since constraints must be added in the optimization process, while the steady-state values for H_1^*, H_3^*, A_1^* and A_3^* can be easily assigned to one parameter, which is the value that the indicial function tends to.

2.4. Numerical evaluation of the convolution integrals

One of the main problems of using the models presented above to represent the self-excited aerodynamic forces in the time domain is that the time steps must be kept small to be able to evaluate the integral expressions with sufficient accuracy. This is because the indicial or impulse-response functions often have a considerably shorter rise time than the period corresponding to the highest natural frequency of interest. Furthermore, the self-excited forces depend on the motion history, but as has been demonstrated by Borri et al. [32], only the recent part of the motion history is important. Another approach that has been demonstrated in [21,23,36] is to express the dynamic equilibrium in state-space and introduce the integrals as state variables, which implies that the integrals do not have to be evaluated explicitly, but are solved by the numerical integration of the equilibrium equations. In this section an alternative integration approach will be presented. The approach utilizes the fact that additional time steps will only be necessary when the indicial functions have a shorter rise time than the shortest natural period of interest. This implies that the response may be linearly interpolated into an axis with a denser separation before the integrals are evaluated. The response r is known in N points in the interval $0 \leqslant \tau \leqslant t$; each interval, $\Delta\tau$, is subdivided into $(M-1)$ intervals, rendering the following summation formula:

$$\int_{t_{Start}}^{t} \Phi(t-\tau)r(\tau)d\tau = \frac{\Delta\tau}{2(M-1)} \sum_{n=n_{Start}}^{N-1} \sum_{m=1}^{M-1} [r_m\Phi_m + r_{m+1}\Phi_{m+1}]$$

$$r_m = \Delta r\left(\frac{m-1}{M-1}\right) + r_n, \quad \Phi_m = \Phi\left(t - \left(\tau_n + \frac{m-1}{M-1}\Delta\tau\right)\right)$$

$$\Delta\tau = \tau_{n+1} - \tau_n, \quad \Delta r = r_{n+1} - r_n, \quad n_{Start} \approx (t_{Start}/\Delta\tau + 1)$$

(23)

The efficiency of this approach clearly depends on the ratio of the rise time of the indicial function and the period of the response. When the rise time is shorter than the shortest natural period of interest, the procedure is found to be very effective, while the procedure will be less effective when the rise time is longer than the period of the response. Two examples are shown below, where the same indicial function is used in both examples. A harmonic response with a frequency of 0.5 rad/s is used in example one, while a frequency of 2 rad/s is used in example two. The percentage difference of the exact solution and the numerical results obtained by the trapezoidal rule and Eq. (23) is shown in Table 1

$$\Phi(\tau) = \exp(-10\tau) \quad r_1(\tau) = \cos(0.5\tau) \quad r_2(\tau) = \cos(2\tau)$$

$$I_n = \int_0^{10} \Phi(\tau)r_n(\tau)d\tau$$

(24)

The results indicate that the approach suggested in Eq. (23) gives a significant reduction of the necessary number of time steps and is hence more computationally efficient than the trapezoidal rule. If an error less than one percent is required, the number of time steps may be reduced by a factor of 80 in example 1 and by a factor of 11 in example 2. In numerical calculations of the dynamic response of structures it is frequently assumed that the necessary time step is the period of the highest significant vibration mode divided by a factor of 10. In [32–34] time steps of $\Delta\tau = 0.001$ s have been used. This is a much smaller time step than is usually necessary in dynamic analyses of slender bridges with low natural frequencies. The formulae presented above will result in that the time step does not have to be reduced to evaluate the convolution integrals with accuracy sufficient to avoid amplitude and phase distortion of the self-excited forces.

2.5. A novel approximate method

An alternative to the unsteady models presented above is to use quasi-steady theory to model the self-excited aerodynamic forces. The traditional quasi-steady theory does not provide any aerodynamic torsional damping, which, for some cross sections, will result in a significant underestimation of the flutter threshold [6]. However, it is shown in [6] that modified quasi-steady theory, where curve fits providing a frequency-independent description

Table 1
Percentage difference of the exact solution and numerical results obtained by the trapezoidal rule and Eq. (23).

Time step, $\Delta\tau$	Example 1		Example 2	
	Trapezoidal (%)	Eq. (23) (%)	Trapezoidal (%)	Eq. (23) (%)
0.5	400.3565	0.2486	405.0248	3.6431
0.2	107.5532	0.0671	108.9107	1.0614
0.1	31.3262	0.0195	31.6664	0.3122
0.05	8.2030	0.0051	8.2835	0.0819
0.02	1.3306	0.0007	1.3432	0.0133
0.001	0.0033	0.00003	0.3364	0.0033

of the self-excited forces may approximate the experimental data in the important reduced-frequency range with sufficient accuracy. This is achieved if the experimental data for the aerodynamic derivatives are locally approximated by the following expressions:

$$X_i^*(K) = x_i(1/K) \text{ when } i = 1, 2, 5 \quad \text{and}$$

$$X_i^*(K) = x_i(1/K)^2 \text{ when } i = 3, 4, 6 \tag{25}$$

where $X \in \{P, H, A\}$ and $x \in \{p \ h \ a\}$. Inserting these expressions into Eq. (1) provides the following frequency-independent definition of the self-excited forces that may be used in both the time and frequency domain.

$$q_y^{(Se)} = \frac{1}{2}\rho V^2 B \left(p_1 \frac{\dot{r}_y}{V} + p_2 \frac{B\dot{r}_\theta}{V} + p_3 r_\theta + p_4 \frac{r_y}{B} + p_5 \frac{\dot{r}_z}{V} + p_6 \frac{r_z}{B} \right)$$

$$q_z^{(Se)} = \frac{1}{2}\rho V^2 B \left(h_1 \frac{\dot{r}_z}{V} + h_2 \frac{B\dot{r}_\theta}{V} + h_3 r_\theta + h_4 \frac{r_z}{B} + h_5 \frac{\dot{r}_y}{V} + h_6 \frac{r_y}{B} \right) \tag{26}$$

$$q_\theta^{(Se)} = \frac{1}{2}\rho V^2 B^2 \left(a_1 \frac{\dot{r}_z}{V} + a_2 \frac{B\dot{r}_\theta}{V} + a_3 r_\theta + a_4 \frac{r_z}{B} + a_5 \frac{\dot{r}_y}{V} + a_6^* \frac{r_y}{B} \right)$$

Here, $p_n, h_n, a_n, n \in \{1, \ldots, 6\}$ are coefficients determined by fitting the expressions defined in Eq. (26) to the experimental results in the important frequency range. The disadvantage with the modified quasi-steady approach presented in [6] and summarized above is that it is only possible to approximate the aerodynamic derivatives in one reduced-frequency range, which implies that some of the natural frequencies of the aeroelastic system will not be properly covered. Here, as a novel approach utilizing the left and right eigenvectors, it is suggested to uncouple the system of equations. This implies that curves representing the experimental data can be fitted at the reduced velocities corresponding to the natural frequencies of the one degree of freedom system one by one. To uncouple the system it is necessary to reduce the order of the differential equation. Introducing a state variable [37], $\mathbf{Z}(t) = [\dot{\boldsymbol{\eta}} \quad \boldsymbol{\eta}]^T$, the dynamic equilibrium may be rewritten as

$$\mathbf{A\dot{Z}} = \mathbf{BZ}$$

$$\mathbf{A} = \begin{bmatrix} \mathbf{0} & -\tilde{\mathbf{M}}_0 \\ -\tilde{\mathbf{M}}_0 & -(\tilde{\mathbf{C}} - \tilde{\mathbf{C}}_{ae}(V, \omega_k)) \end{bmatrix}, \quad \mathbf{B} = \begin{bmatrix} -\mathbf{M}_0 & \mathbf{0} \\ \mathbf{0} & (\tilde{\mathbf{K}}_0 - \tilde{\mathbf{K}}_{ae}(V, \omega_k)) \end{bmatrix} \tag{27}$$

Here, $\tilde{\mathbf{M}}_0$, $\tilde{\mathbf{C}}_0$ and $\tilde{\mathbf{K}}_0$ represent the still-air modal mass, damping and stiffness matrices, while $\tilde{\mathbf{K}}_{ae}$ and $\tilde{\mathbf{C}}_{ae}$ represent the aerodynamic stiffness and damping matrices, respectively. The eigenvalue problem can then be expressed as follows:

$$\mathbf{BX}_k = S_k \mathbf{AX}_k, \quad \mathbf{Y}_k \mathbf{B} = S_k \mathbf{Y}_k \mathbf{A} \tag{28}$$

Here, $\mathbf{X}_k$ is the right-hand eigenvector; $\mathbf{Y}_k$ is the left-hand eigenvector, and $S_k = a_k + i\omega_k$ is the eigenvalue. As can be seen from Eq. (27), the aerodynamic damping and stiffness matrices are in general frequency-dependent, which implies that the eigenvalue problem must be solved by an iterative approach. If it is assumed that the self-excited forces are most important for the resonant part of the response, the system of equations may be uncoupled. This implies that the aerodynamic stiffness and damping coefficients are assumed constant at varying frequency and equal to the value at the natural frequency of the corresponding one-degree-of-freedom system. The approximation used for the aerodynamic derivatives A_2^* and A_3^* for the natural frequencies $\omega_k \in \{2, 3, 4\}$ at a mean wind velocity of 50 m/s corresponding to the reduced velocities $\hat{V} \in \{1.4, 0.9, 0.7\}$ are shown in Fig. 2. As can be seen from the figure, the aerodynamic derivatives provide a model that is strictly speaking frequency-dependent, which implies that apparently large discrepancies between the frequency-independent approximation and the aerodynamic derivatives may arise. However, the forces
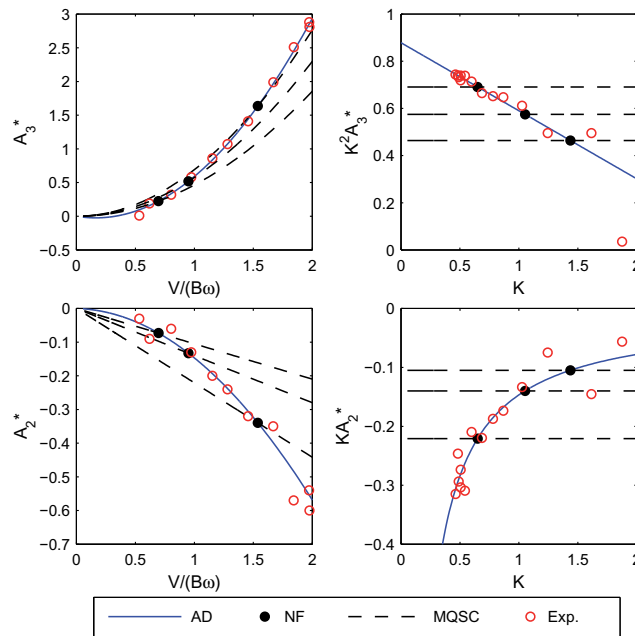

Fig. 2. Illustration of the approximations of the aerodynamic coefficients for three vibration modes. Each solid marker represents a reduced velocity or frequency corresponding to the natural frequency of one of the vibration modes. The blue lines are curves representing the aerodynamic derivatives in the frequency domain, and the black lines represent the approximations used for each complex vibration mode. (For interpretation of the references to color in this figure legend, the reader is referred to the web version of this article.)

proportional to the velocity are commonly most important in a frequency range around the natural frequency for a single-degree-of-freedom system, which indicates that the aerodynamic derivatives associated to the structural velocities will not affect the background turbulence part of the response significantly. The aerodynamic derivatives linked to the displacements of the structure may, on the other hand, affect the background turbulence part of the response; but as will be demonstrated in the present case study, aerodynamic stiffness is for certain structural categories lower than the structural stiffness, in particular for the high natural frequencies, and may in that case result in insignificant inaccuracies. The suggested method will therefore provide fairly accurate numerical results if the difference between the aerodynamic stiffness provided by the frequency-independent approximation and the full frequency-dependent model is smaller than the structural stiffness. The equation of motion may hence be approximated as

$$
\begin{aligned}
&\tilde{A}_{nn} = \mathbf{Y}_n \mathbf{A} \mathbf{X}_n, \quad \tilde{B}_{nn} = \mathbf{Y}_n \mathbf{B} \mathbf{X}_n, \quad \tilde{P}_n = \mathbf{Y}_n \mathbf{P}(t) \\
&\tilde{A}_{nn} \dot{y}_n(t) = \tilde{B}_{nn} y_n(t) - \tilde{P}_n(t) \\
&\mathbf{Z}(t) = \sum_{n=1}^{N} \mathbf{X}_n y_n
\end{aligned}
\tag{29}
$$

This implies that a time domain solution is possible without the use of convolution integrals to define the self-excited forces. The evaluation of the convolution integrals is computationally demanding. A case with 10 vibration modes implies that 100 combinations of mode shapes have to be evaluated. Each combination involves nine integral expressions, similar to the expression given in Eq. (9), for each exponential filter. Compared to this the approach suggested in this section requires much less computational effort.

3. Case study: The Hardanger Bridge

To evaluate the self-excited force models presented above, we have selected the Hardanger Bridge displayed in Fig. 3, which is currently under construction in Norway. The Hardanger Bridge will become the longest suspension bridge in Norway and among the top 10 longest suspension bridges in the world, with its total length of 1380 m, including a main span of 1310 m. Since the bridge will only have two traffic lanes and one lane for bicycles and pedestrians, it is unusually narrow; the width of the girder is 18.3 m and the distance between the two cables only 14.5 m. An eigenvalue analysis is carried out for the bridge subjected to dead loads, applying the computer program ALVSAT [38]. A total of 24 (the first 8 horizontal, 8 vertical and 8 torsional) vibration modes and corresponding undamped natural frequencies were extracted (see [6] for further details).

3.1. Simulation of the wind field

The density of the air is assumed to be $\rho = 1.25$ kg/m³, and the co-spectral densities of the wind field are assumed to be given by:

$$
\begin{aligned}
S_{uu}^{+}(\omega) &= \frac{40.58 V z \kappa}{(1 + 9.74 \omega z/V)^{5/3}} \exp\left(-1.4 \frac{\Delta x \omega}{V}\right) \\
S_{ww}^{+}(\omega) &= \frac{0.82 V z \kappa}{(1 + 0.79 \omega z/V)^{5/3}} \exp\left(-\frac{\Delta x \omega}{V}\right) \\
S_{uw}^{+}(\omega) &= -\frac{2.23 V z \kappa}{(1 + 1.67 \omega z/V)^{7/3}} \exp\left(-\frac{\Delta x \omega}{V}\right)
\end{aligned}
\tag{30}
$$

Here, κ is the roughness coefficient at the site, assumed to be 0.0031; z is the height above the ground, and Δx is the distance between the two points considered. The fluctuating wind velocities have been simulated at 101 points along the girder by the use of Monte Carlo simulations [39–41], with a cut-off frequency of $\omega_u = 5$ rad/s and $\Delta\omega = 0.0002$ rad/s. The time series at point m can then be obtained by

$$
x_m(t) = \sqrt{2\Delta\omega} \operatorname{Re}\left(\sum_{l=1}^{m} \sum_{k=1}^{N} L_{ml}(\omega_k) \exp(i(\omega_k + \phi_{lk}))\right)
\tag{31}
$$

Here, $L_{ml}(\omega_k)$ is the elements in the factorised cross spectral density matrix fulfilling the relation

$$
\mathbf{S}(\omega_k) = \mathbf{L}(\omega_k) \mathbf{L}^*(\omega_k)
\tag{32}
$$

where the elements in $\mathbf{S}(\omega_k)$ represent the cross spectral densities of the fluctuating velocity components at the M points along the girder. The time series of the fluctuating wind velocities at two points with a separation of 117.9 m are shown in Fig. 4, and the average co-spectral densities of 20 time domain simulations and the target co-spectral densities defined in Eq. (30) are shown in Fig. 5. As can be seen from the figure, the time domain simulations correspond very well with the initial co-spectral densities.

3.2. The dynamic equilibrium

The vibration modes from still air are used as generalized coordinates, which implies that the modal dynamic equilibrium conditions may be defined by:

$$
\tilde{\mathbf{M}}_0 \ddot{\boldsymbol{\eta}} + \tilde{\mathbf{C}}_0 \dot{\boldsymbol{\eta}} + \tilde{\mathbf{K}}_0 \boldsymbol{\eta} = \tilde{\mathbf{C}}_{ae} \dot{\boldsymbol{\eta}} + \tilde{\mathbf{K}}_{ae} \boldsymbol{\eta} + \tilde{\mathbf{F}}_{ae} + \tilde{\mathbf{Q}}_{Buff}
\tag{33}
$$

Here, $\tilde{\mathbf{M}}_0$, $\tilde{\mathbf{C}}_0$ and $\tilde{\mathbf{K}}_0$ represent the modal mass damping and stiffness matrices, and the vector $\boldsymbol{\eta}$ contains the generalized degrees of freedom, η_i. A matrix with a zero index indicates that the matrix contains properties from still air, while the index ae implies that the matrix contains aerodynamic properties. The vector $\tilde{\mathbf{F}}_{ae}$ symbolizes

Fig. 3. Artist's view of the Hardanger Bridge across the Hardanger Fjord (www.vegvesen.no, 2010).
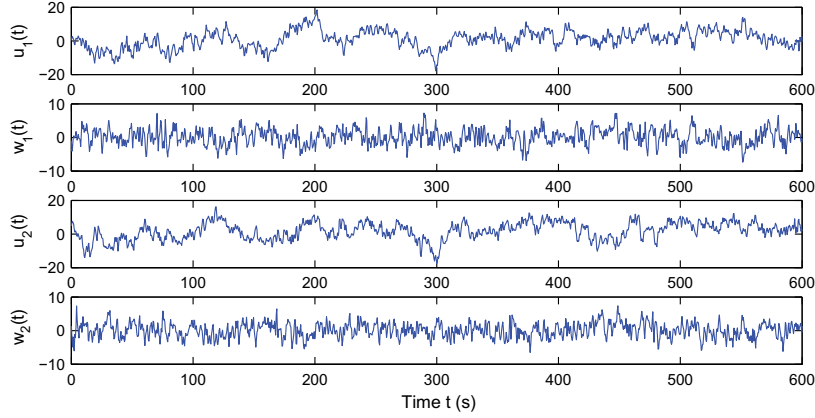
Fig. 4. Time series of the fluctuating velocities at two points along the girder with a separation of 117.9 m; u is the along wind component, while w is the vertical component.

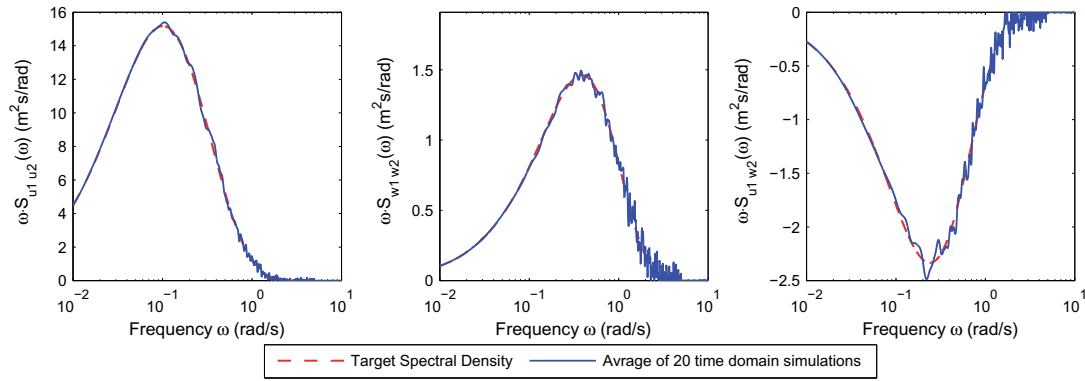Target Spectral Density — — — Avrage of 20 time domain simulations ———

Fig. 5. Comparison of the average co-spectral densities of 20 simulated time series and the target co-spectral densities at two points with a separation 117.9 m. Left figure: The co-spectral density of the u components. Middle figure: The co-spectral density of the w components. Right figure: The co-spectral density of the u and w components.

the history-dependent part of the self-excited forces, and the vector $\tilde{\mathbf{Q}}_{Buff}$ represents the modal buffeting load vector. The elements in the modal aerodynamic damping and stiffness matrices are given by:

$$\tilde{C}_{ij}^{(ae)} = \frac{1}{2}\rho V^2 \frac{B}{V}\left(A_2^{(yy)}G_{ij}^{(yy)} + A_2^{(yz)}G_{ij}^{(yz)} + A_2^{(y\theta)}G_{ij}^{(y\theta)} + A_2^{(zy)}G_{ij}^{(zy)} + A_2^{(zz)}G_{ij}^{(zz)}\right.$$
$$\left. + BA_2^{(z\theta)}G_{ij}^{(z\theta)} + BA_2^{(\theta y)}G_{ij}^{(\theta y)} + BA_2^{(\theta z)}G_{ij}^{(\theta z)} + B^2A_2^{(\theta z)}G_{ij}^{(\theta z)}\right) \quad (34)$$

$$\tilde{K}_{ij}^{(ae)} = \frac{1}{2}\rho V^2 \left(A_1^{(yy)}G_{ij}^{(yy)} + A_1^{(yz)}G_{ij}^{(yz)} + BA_1^{(y\theta)}G_{ij}^{(y\theta)} + A_1^{(zy)}G_{ij}^{(zy)} + A_1^{(zz)}G_{ij}^{(zz)}\right.$$
$$\left. + BA_1^{(z\theta)}G_{ij}^{(z\theta)} + BA_1^{(\theta y)}G_{ij}^{(\theta y)} + BA_1^{(\theta z)}G_{ij}^{(\theta z)} + B^2A_1^{(zy)}G_{ij}^{(\theta z)}\right) \quad (35)$$

respectively, while the elements in the vector $\tilde{\mathbf{F}}_{ae}$ are defined by:

$$F_i = \frac{1}{2}\rho V^2 \sum_{i=1}^{N_{mod}}\int_{-\infty}^{t}\left(G_{ij}^{(yy)}\psi_{yy}(t-\tau)\eta_i^n(\tau) + G_{ij}^{(yz)}\psi_{yz}(t-\tau)\eta_i^n(\tau)\right.$$
$$+ BG_{ij}^{(y\theta)}\psi_{y\theta}(t-\tau)\eta_i^n(\tau) + G_{ij}^{(zy)}\psi_{zy}(t-\tau)\eta_i^n(\tau)$$
$$+ G_{ij}^{(zz)}\psi_{zz}(t-\tau)\eta_i^n(\tau)$$
$$+ BG_{ij}^{(z\theta)}\psi_{z\theta}(t-\tau)\eta_i^n(\tau) + BG_{ij}^{(\theta y)}\psi_{\theta y}(t-\tau)\eta_i^n(\tau)$$
$$\left. + BG_{ij}^{(\theta z)}\psi_{\theta z}(t-\tau)\eta_i^n(\tau) + B^2G_{ij}^{(\theta\theta)}\psi_{\theta\theta}(t-\tau)\eta_i^n(\tau)\right)d\tau \quad (36)$$

Here, ψ_{nm}, n, $m \in \{y, z, \theta\}$, represents the indicial functions; η_i^n symbolizes the nth derivative of the response for generalized coordinate i, and the mode shape integral $G_{ij}^{(nm)}$ is defined as

$$G_{ij}^{(nm)} = \int_0^L \phi_i^{(n)}(x)\phi_j^{(m)}(x)dx \quad (37)$$

where ϕ symbolises the vibration modes. Finally the elements in the modal buffeting load vector can be expressed as:

$$\tilde{Q}_i = \frac{\rho VB}{2}\left(\int_0^L \phi_i^{(y)}(x)\left(2\frac{D}{B}\overline{C}_D u(x,t) + \left(\frac{D}{B}C_D' - \overline{C}_L\right)w(x,t)\right)dx\right.$$
$$+ \int_0^L \phi_i^{(z)}(x)\left(2\overline{C}_L u(x,t) + \left(C_L' + \frac{D}{B}\overline{C}_D\right)w(x,t)\right)dx$$
$$\left. + \int_0^L \phi_i^{(\theta)}(x)\left(2B\overline{C}_M u(x,t) + BC_M'w(x,t)\right)dx\right) \quad (38)$$

Here, $u(x,t)$ and $w(x,t)$ are the fluctuating velocity in the horizontal and vertical direction, respectively.

3.3. Nonlinear curve fitting to the experimental data

Curve fits to the experimental data [42] when force models 1, 2 and 3 are used to model the self-excited forces are shown in Fig. 6
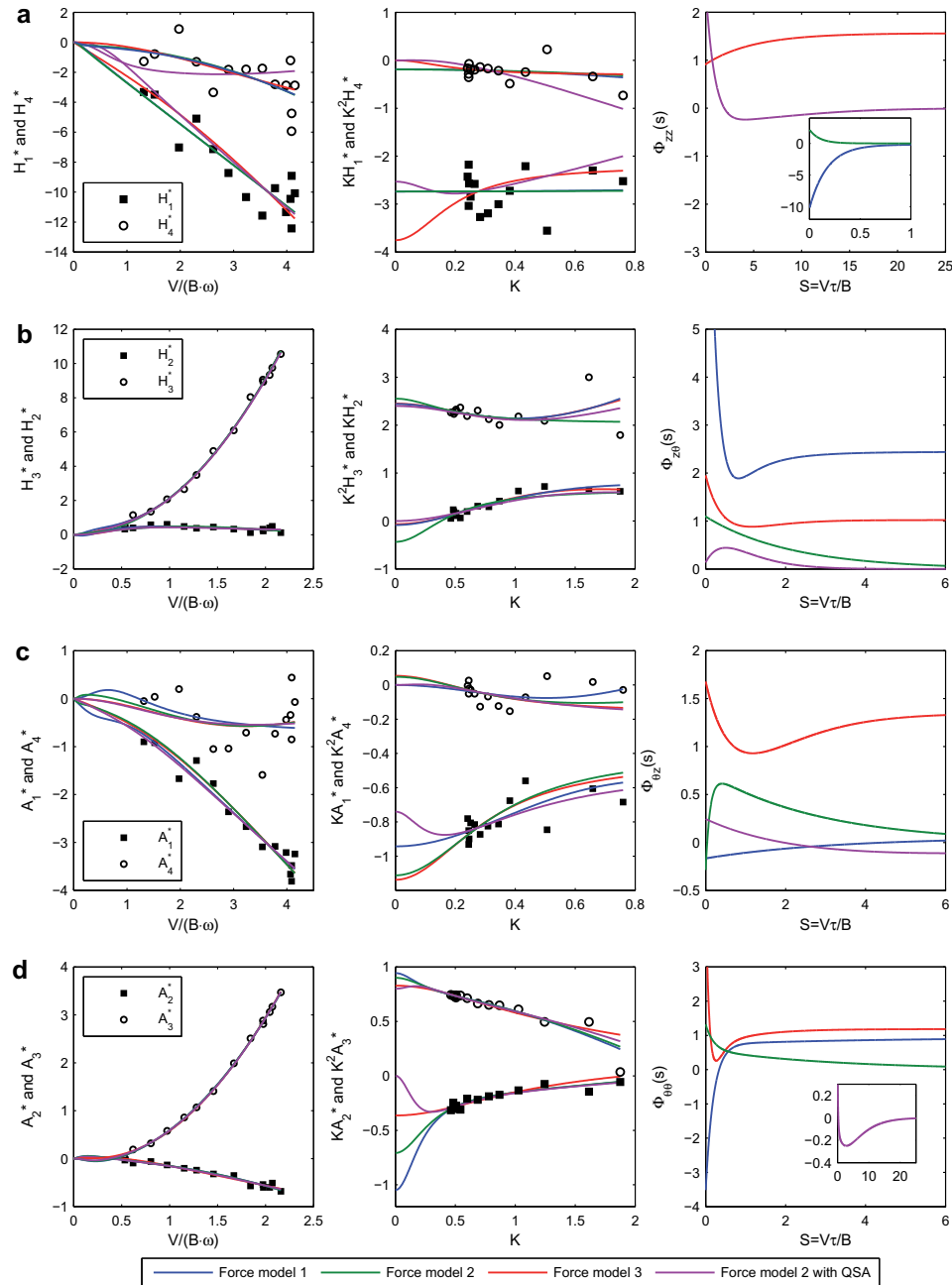
Fig. 6. Curve fits to the experimental data for force model 1 defined in Eq. (6), force model 2 defined in Eq.(11), force model 3 defined in Eq.(18) and force model 2 with quasi-steady asymptotes provided by traditional quasi-steady theory.

The coefficient of determination, R^2, for each of the models, in addition to the second-order polynomials representing the aerodynamic derivatives in the frequency domain, are given in Table 2. The curves representing H_1^* and H_4^* represent the experimental data with apparently fair accuracy. Force models 1 and 2 presented in

Eqs. (8) and (12) provide fits to the data that are identical, and better than those of force model 3 presented in Eq. (21). As can be seen from the central figure, the force coefficients KH_1^* and $K^2H_4^*$ are almost frequency-independent for force models 1 and 2, providing indicial functions with short rise time, while some frequency

Table 2
Coefficient of determination, R^2, for the force models fitted to the experimental data.

Formulation	zz		$z\theta$		θz		$\theta\theta$	
	H_1^*	H_4^*	H_2^*	H_3^*	A_1^*	A_4^*	A_2^*	A_3^*
Aerodynamic derivatives	0.893	0.489	0.502	0.998	0.968	0.148	0.969	0.999
Force model 3, Eq. (21)	0.767	0.405	0.445	0.997	0.953	0.124	0.957	0.999
Force model 1, Eq. (8)	0.818	0.426	0.420	0.997	0.949	0.185	0.963	0.999
Force model 2, Eq. (12)	0.818	0.426	0.297	0.997	0.947	0.196	0.963	0.999
Force model 2 with quasi-steady asymptotes	0.789	−0.042	0.314	0.997	0.954	0.138	0.962	0.999

dependency can be seen for force model 3. Force model 3 provides a less accurate fit to the data than models 1 and 2 since the optimal fit is close to frequency-independent. This is difficult to model with force model 3 since there is no "frequency-independent term" in the expression for H_4^*, which implies that low values of b_{izz} and high values of a_{izz} provide the optimal least squares fit for a frequency-independent case. This will result in an indicial function with a long rise time, such that a very long time series has to be considered before a steady-state solution of the self-excited forces is achieved. All the models considered provide acceptable fits in the range covered by the experimental data, but large discrepancies can be seen in the low reduced-frequency range where experimental data are not available. The traditional quasi-steady theory [25], see also [5], is valid in the low reduced-frequency range. A version of the force model suggested in this article (force model 2) is therefore added, where the coefficients A_1 and A_2 are provided by traditional quasi-steady theory: $A_1^{(zz)} = 0$ and $A_2^{(zz)} = -(C_L^{'} + \bar{C}_D D/B) = -2.53$. This makes the curve fitting slightly more complicated, in particular, since $A_1^{zz} = 0$, which implies that the coefficients in the exponential filters must represent H_4^*. As can be seen from Table 2, force model 2 with quasi-steady asymptotes represents the experimental data for H_1^* with apparently fair accuracy, while the fitting of H_4^* is less accurate. All the curves representing H_2^* and H_3^* are acceptable. The force models considered provide an equally good fit to H_3^*, but as can be seen from the curves representing $K^2 H_3^*$, there are some differences at low reduced frequencies and in the range $K \in \{1.4, \ldots, 2\}$. The quality of the fit to the experimental data of H_2^* is also satisfying. Force model 3 provides the highest coefficient of determination of the time domain models. The curves representing $K H_2^*$ are very similar, but force model 2 has a different quasi-steady asymptote than the other models. A version of force model 2 with quasi-steady asymptotes predicted by traditional quasi-steady theory is also presented, assuming $A_2^{(z\theta)} = 0$ and $A_1^{(z\theta)} = C_L^{'} = 2.4$. As can be seen from the coefficients of determination presented in Table 2, this alternative provides a very good fit to the experimental data for H_3^*, while the coefficient of determination is lower than the other alternatives for H_2^*. The curves representing A_1^* and A_4^* are acceptable. As can be seen from the figure, the curves are notably different at low reduced velocities, and the quasi-steady asymptotes are, in particular for $K A_1^*$, clearly different. Also, for these load coefficients, a version of force model 2 with quasi-steady asymptotes given by traditional quasi-steady theory has been investigated, assuming $A_2^{(\theta z)} = 0$, $A_1^{(\theta z)} = -C_M^{'} = -0.74$. As can be seen from Table 2, this alternative provides a coefficient of determination for A_1^* that is higher than the other alternatives, while the coefficient of determination for A_4^*, is lower than when the coefficients $A_2^{(\theta z)}$ and $A_1^{(\theta z)}$ are determined by the least squares fit. The self-excited force models considered provide very good fits to the experimental data for A_2^* and A_3^*. The coefficient of determination is almost as high as the results achieved by the curves representing the aerodynamic derivatives in the frequency domain. Force model 3 provides results with slightly lower accuracy for A_2^* than the other alternatives, and in the case of A_3^* all models are apparently equally

accurate. As can be seen from the curves representing $K A_2^*$ and $K^2 A_3^*$, the quasi-steady asymptotes are fairly different, in particular for $K A_2^*$. When traditional quasi-steady theory has been used with quasi-steady asymptotes assuming $A_2^{(\theta\theta)} = 0$ and $A_1^{(\theta z)} = C_M^{'} = 0.74$ a least squares fit as accurate as the other alternatives is achieved.

The least squares fit for the different self-excited force models can be summarized as follows: Force model 3 does not have "quasi-steady" terms in all the expressions for the aerodynamic derivatives, which, as has been seen for H_1^*, may be a disadvantage in cases where the experimental data of the aerodynamic derivatives provide a self-excited force model that is close to frequency-independent. Force model 1 is robust and provides fits of good accuracy for all the cases considered, but as has been shown in Eq. (10), the quasi-steady asymptotes are dependent on the coefficients in the exponential filters, which may be a disadvantage. The alternative formulation suggested in Eq. (11) (force model 2) has provided good fits for all the cases considered, and it has been shown that the quasi-steady asymptotes may be easily assigned to values predicted by traditional quasi-steady theory. In most cases this will give a least squares fit with slightly less accuracy since $A_2^{(nm)}$ and $A_1^{(nm)}$ are fixed. The main problem with all the unsteady load models discussed in this section is that the curves representing the experimental data are rather complicated, and since the same coefficients are used for both the real and imaginary part of the transfer functions, two sets of experimental data have to be curve-fitted with the same coefficients. This implies that the least squares fit of the time domain models will become less accurate than the frequency domain approach with the aerodynamic derivatives, since simple polynomial expressions may be used for each aerodynamic derivative separately.

3.4. Dynamic response

The wind-induced dynamic response has been obtained using the well-known Newmark's integration method, applying $\beta = 1/4$ and $\gamma = 1/2$; see, for instance, [43] for further details. The time step Δt has been taken as 0.1 s, and the length of the considered time series is 6000 s. In Fig. 7 the first 600 s of the wind-induced dynamic response at the mid-span of the Hardanger Bridge at a mean wind velocity of 50 m/s is shown. Force model 3 is used to represent the self-excited forces. In Fig. 8 the standard deviations of the horizontal, vertical and torsional responses at several mean wind velocities are shown. The open circles represent the average standard deviation from 20 time domain simulations; the solid lines represent results calculated in the frequency domain using force model 3. The dashed lines represent results obtained in the frequency domain with the aerodynamic derivatives. As can be seen from the figure, the Monte Carlo simulations have converged since the standard deviations predicted by the time domain simulations are very close to the frequency domain results. The results for horizontal and vertical motions are very close to those predicted by the aerodynamic derivatives, while the torsional response is underestimated, compared with the aerodynamic derivatives. The average standard deviations of 20 time domain
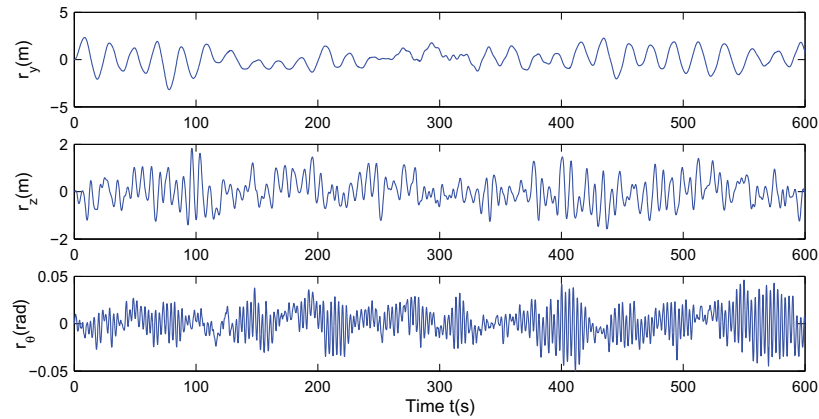
Fig. 7. Wind-induced dynamic response at the mid-span of the Hardanger Bridge at 50 m/s. The self-excited forces have been represented by force model 3.
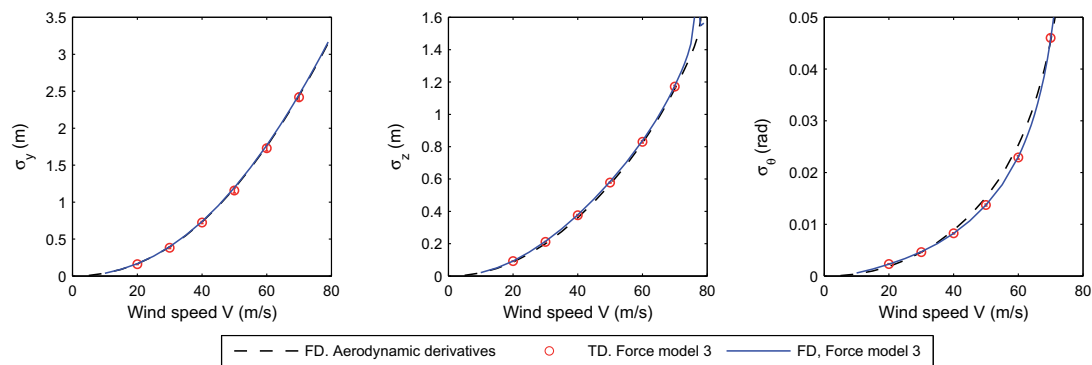

Fig. 8. The standard deviation of the horizontal, vertical, and torsional response predicted using force model 3. The open circles represent the mean value of the standard deviations of 20 time series of 6000 s, the solid blue lines are the frequency domain results while the dashed lines represents the response predicted in the frequency domain using the aerodynamic derivatives. (For interpretation of the references to colour in this figure legend, the reader is referred to the web version of this article.)

simulations, considering all the self-excited force models presented in this article, are presented in Table 3. The response predicted in the frequency domain using the aerodynamic derivatives has been used as a benchmark since the aerodynamic derivatives represent the experimental data with higher accuracy than the other models. Force model 3 provides results with fair accuracy with one exception, which is the torsional response at 20 m/s. The formulation generally underestimates the response slightly. The covariance coefficients of the response components estimated as the mean value of 20 time domain simulations are presented in Table 5, and the covariance coefficients obtained in the frequency domain are provided in Table 6. Force model 3 provides covariance coefficients with acceptable accuracy. When the time domain and frequency domain results are compared, some discrepancies can be observed, indicating that the Monte Carlo simulations have not entirely converged. The co-spectral densities of the response components at a mean wind velocity of 50 m/s are shown in Fig. 9 and as can be seen from the figure; force model 3 captures the co-spectral density of the horizontal and vertical components in good agreement with the results predicted by the aerodynamic derivatives. The estimate of the co-spectral density of the time domain simulations has been obtained by the Welch algorithm and is in good agreement with the frequency domain results. For the co-spectral

density of the vertical and torsional components, the estimate obtained from the time domain simulations contains more scatter than the other estimates, and as can be seen from the frequency domain results, there are some discrepancies at low frequencies, in particular. This is a frequency range that is not covered by the experimental data, which implies that the covariance coefficient of the horizontal and vertical response is uncertain. The estimated co-spectral density of the vertical and torsional components corresponds very well with the results obtained in the frequency domain using force model 3. There are some discrepancies in the results from force model 3 and the aerodynamic derivatives at the peak near 2 rad/s. This is the main source of the discrepancies of the covariance estimates for the vertical and torsional response at 50 m/s.

The standard deviation estimated using force model 1 agrees well with the results predicted using the aerodynamic derivatives. The time domain estimates presented in Table 3 are very close to the corresponding frequency domain results given in Table 4, which implies that the Monte Carlo simulation has converged. The spectral densities of the response components at a mean wind velocity of 50 m/s are shown in Fig. 10. The spectral densities of the time domain simulations have been estimated by the Burg method. As can be seen from the figure, force model 1 captures the spectral

Table 3
Calculated standard deviation of the horizontal, vertical, and torsional response, using different self-excited force models. The standard deviation of the response predicted by the aerodynamic derivatives in the frequency domain is given in the first cell. The mean values of the standard deviation of 20 time domain simulations are given in the next cells together with the percentage difference in the results predicted by the aerodynamic derivatives in the frequency domain.

Mean wind velocity, V (m/s)		20	30	40	50	60	70
Aerodynamic derivatives	Horizontal	0.17	0.39	0.73	1.19	1.76	2.44
	Vertical	0.086	0.200	0.361	0.566	0.823	1.158
	Torsional	0.0019	0.0046	0.0088	0.0152	0.0253	0.0454
Force model 3. Eq. (21)	Horizontal	0.16	0.38	0.72	1.16	1.73	2.42
		−3%	−3%	−1%	−2%	−2%	−1%
	Vertical	0.092	0.212	0.376	0.578	0.830	1.172
		7%	6%	4%	2%	1%	1%
	Torsional	0.0023	0.0046	0.0083	0.0137	0.0229	0.0460
		25%	1%	−7%	−10%	−10%	1%
Force model 1. Eq. (8)	Horizontal	0.16	0.38	0.69	1.15	1.75	2.39
		−1%	−4%	−6%	−3%	0%	−2%
	Vertical	0.088	0.203	0.365	0.565	0.821	1.161
		2%	1%	1%	0%	0%	0%
	Torsional	0.0020	0.0044	0.0084	0.0143	0.0236	0.0426
		6%	−4%	−5%	−6%	−7%	−6%
Force model 2. Eq. (12)	Horizontal	0.16	0.38	0.69	1.15	1.75	2.39
		−1%	−4%	−6%	−3%	0%	−2%
	Vertical	0.088	0.203	0.366	0.566	0.821	1.160
		2%	1%	1%	0%	0%	0%
	Torsional	0.0019	0.0044	0.0083	0.0140	0.0231	0.0418
		5%	−5%	−7%	−8%	−9%	−8%
Force model 2 with QSA	Horizontal	0.16	0.38	0.69	1.15	1.75	2.39
		−1%	−4%	−6%	−3%	0%	−2%
	Vertical	0.097	0.215	0.380	0.586	0.840	1.199
		13%	7%	5%	3%	2%	4%
	Torsional	0.0019	0.0044	0.0083	0.0142	0.0239	0.0481
		4%	−4%	−6%	−7%	−6%	6%
Decoupled system of equations. Eq. (28)	Horizontal	0.16	0.38	0.74	1.16	1.71	2.43
		−5%	−3%	1%	−3%	−3%	−1%
	Vertical	0.085	0.198	0.357	0.560	0.813	1.143
		−1%	−1%	−1%	−1%	−1%	−1%
	Torsional	0.0018	0.0044	0.0085	0.0146	0.0239	0.0429
		−1%	−5%	−4%	−4%	−6%	−5%

Table 4
Calculated standard deviation of the horizontal, vertical, and torsional response in the frequency domain, using the aerodynamic derivatives, force models 1, 2 and 3 and force model 3 with quasi-steady asymptotes given by traditional quasi-steady theory.

Mean wind velocity, V (m/s)		20	30	40	50	60	70
Aerodynamic derivatives	Horizontal	0.17	0.39	0.73	1.19	1.76	2,44
	Vertical	0.09	0.20	0.36	0.57	0.82	1.16
	Torsional	0.0019	0.0046	0.0088	0.0152	0.0253	0.0454
Force model 3. Eq. (21)	Horizontal	0.17	0.40	0.74	1.20	1.77	2,46
		1%	1%	1%	1%	1%	1%
	Vertical	0.093	0.214	0.379	0.584	0.837	1.177
		8%	7%	5%	3%	2%	2%
	Torsional	0.0023	0.0047	0.0082	0.0137	0.0230	0.0457
		23%	2%	−7%	−10%	−9%	1%
Force model 1. Eq. (8)	Horizontal	0.17	0.39	0.73	1.19	1.76	2,45
		0%	0%	0%	0%	0%	0%
	Vertical	0.089	0.206	0.367	0.573	0.830	1.170
		3%	3%	2%	1%	1%	1%
	Torsional	0.0020	0.0045	0.0085	0.0146	0.0243	0.0432
		7%	−2%	−4%	−4%	−4%	−5%
Force model 2. Eq. (12)	Horizontal	0.17	0.39	0.73	1.19	1.76	2,44
		0%	0%	0%	0%	0%	0%
	Vertical	0.089	0.205	0.367	0.573	0.829	1.169
		3%	2%	2%	1%	1%	1%
	Torsional	0.0020	0.0045	0.0084	0.0143	0.0238	0.0430
		7%	−2%	−5%	−6%	−6%	−5%
Force model 2 with QSA	Horizontal	0.17	0.39	0.73	1.19	1.76	2,44
		0%	0%	0%	0%	0%	0%
	Vertical	0.097	0.215	0.377	0.585	0.849	1.208
		13%	7%	5%	3%	3%	4%
	Torsional	0.0020	0.0045	0.0084	0.0144	0.0244	0.0483
		5%	−2%	−4%	−5%	−4%	6%

Table 5
Calculated covariance coefficients, using different self-excited force models. The covariance coefficients predicted using the aerodynamic derivatives in the frequency domain are given in the first cell. The mean values of the covariance coefficients of 20 time domain simulations are given in the next cells together with the percentage difference in the results predicted by the aerodynamic derivatives in the frequency domain.

Mean wind velocity, V (m/s)		20	30	40	50	60	70
Aerodynamic derivatives	yz	−0.18	−0.17	−0.17	−0.16	−0.16	−0.16
	$y\theta$	−0.051	−0.052	−0.053	−0.053	−0.052	−0.047
	$z\theta$	0.2298	0.1998	0.1820	0.1643	0.1297	0.0728
Force model 3. Eq. (21)	yz	−0.17	−0.16	−0.16	−0.17	−0.18	−0.18
		−7%	−8%	−4%	5%	10%	11%
	$y\theta$	−0.043	−0.045	−0.049	−0.059	−0.055	−0.042
		−16%	−15%	−7%	11%	6%	−10%
	$z\theta$	0.1756	0.1831	0.1893	0.1843	0.1446	0.0415
		−24%	−8%	4%	12%	11%	−43%
Force model 1. Eq. (8)	yz	−0.18	−0.16	−0.16	−0.17	−0.18	−0.18
		−3%	−5%	−2%	5%	9%	11%
	$y\theta$	−0.052	−0.049	−0.053	−0.064	−0.065	−0.063
		2%	−5%	0%	22%	26%	34%
	$z\theta$	0.2156	0.2028	0.1962	0.1891	0.1657	0.1362
		−6%	2%	8%	15%	28%	87%
Force model 2. Eq. (12)	yz	−0.18	−0.16	−0.16	−0.17	−0.18	−0.18
		−3%	−5%	−2%	5%	9%	11%
	$y\theta$	−0.053	−0.050	−0.053	−0.064	−0.064	−0.060
		3%	−5%	0%	21%	24%	28%
	$z\theta$	0.2209	0.2061	0.1986	0.1918	0.1666	0.1297
		−4%	3%	9%	17%	28%	78%
Force model 2 with QSA	yz	−0.16	−0.16	−0.16	−0.17	−0.17	−0.17
		−12%	−9%	−4%	3%	9%	8%
	$y\theta$	−0.052	−0.047	−0.049	−0.057	−0.052	−0.040
		2%	−9%	−7%	8%	1%	−14%
	$z\theta$	0.1948	0.1884	0.1837	0.1703	0.1305	0.0442
		−15%	−6%	1%	4%	1%	−39%
Decoupled system of equations. Eq. (28)	yz	−0.18	−0.17	−0.17	−0.17	−0.17	−0.17
		−1%	−3%	−1%	5%	8%	7%
	$y\theta$	−0.051	−0.042	−0.041	−0.048	−0.044	−0.037
		0%	−20%	−22%	−10%	−15%	−21%
	$z\theta$	0.2256	0.1866	0.1670	0.1453	0.1001	0.0348
		−2%	−7%	−8%	−12%	−23%	−52%

Table 6
Calculated covariance coefficients in the frequency domain using the aerodynamic derivatives, force models 1. 2 and 3 and force model 3 with quasi-steady asymptotes given by traditional quasi-steady theory.

| Mean wind velocity, V (m/s)		20	30	40	50	60	70
Aerodynamic derivatives	yz	−0.18	−0.17	−0.17	−0.16	−0.16	−0.16
	$y\theta$	−0.05	−0.05	−0.05	−0.05	−0.05	−0.05
	$z\theta$	0.23	0.20	0.18	0.16	0.13	0.07
Force model 3. Eq. (21)	yz	−0.17	−0.16	−0.16	−0.16	−0.16	−0.16
		7%	6%	4%	2%	−1%	−1%
	$y\theta$	−0.041	−0.049	−0.053	−0.052	−0.048	−0.037
		−21%	−6%	−1%	−2%	−8%	−22%
	$z\theta$	0.1785	0.1862	0.1895	0.1819	0.1466	0.0464
		−22%	−7%	4%	11%	13%	−36%
Force model 1. Eq. (8)	yz	−0.18	−0.17	−0.16	−0.16	−0.16	−0.16
		−3%	−3%	−2%	−1%	0%	1%
	$y\theta$	−0.048	−0.054	−0.056	−0.056	−0.056	−0.054
		−6%	3%	5%	7%	9%	16%
	$z\theta$	0.2113	0.2028	0.1916	0.1796	0.1584	0.1265
		−8%	2%	5%	9%	22%	74%
Force model 2. Eq. (12)	yz	−0.18	−0.17	−0.17	−0.16	−0.16	−0.16
		−3%	−2%	−2%	−1%	0%	1%
	$y\theta$	−0.048	−0.054	−0.056	−0.056	−0.055	−0.051
		−6%	2%	5%	6%	7%	9%
	$z\theta$	0.2149	0.2049	0.1943	0.1841	0.1616	0.1173
		−6%	3%	7%	12%	25%	61%
Force model 2 with QSA	yz	−0.16	−0.16	−0.16	−0.16	−0.16	−0.15
		−11%	−6%	−3%	−1%	−1%	−2%
	$y\theta$	−0.048	−0.051	−0.052	−0.050	−0.045	−0.034
		−7%	−2%	−2%	−6%	−13%	−27%
	$z\theta$	0.1928	0.1901	0.1826	0.1681	0.1276	0.0415
		−16%	−5%	0%	2%	−2%	−43%
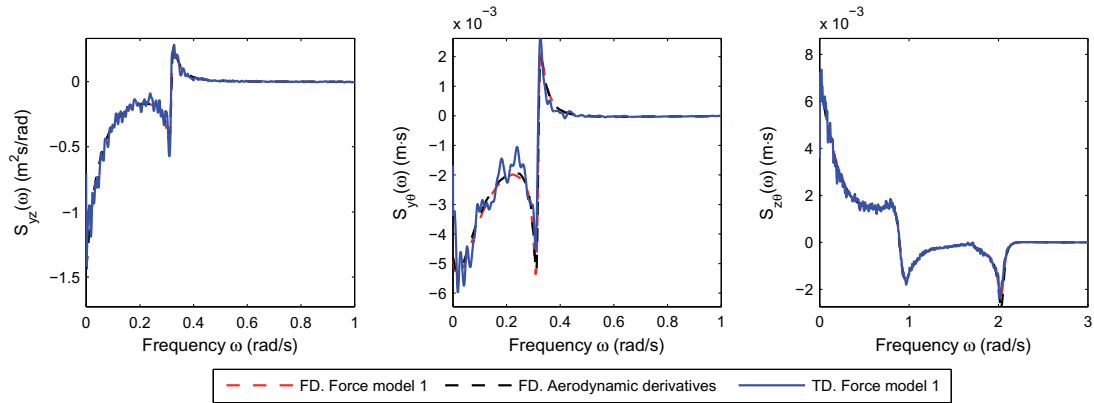
Fig. 9. Comparison of the co-spectral densities of the response components at a mean wind velocity of 50 m/s, using the aerodynamic derivatives and force model 3 in the frequency domain and force model 3 in the time domain. The time domain estimate has been obtained using the Welch algorithm.
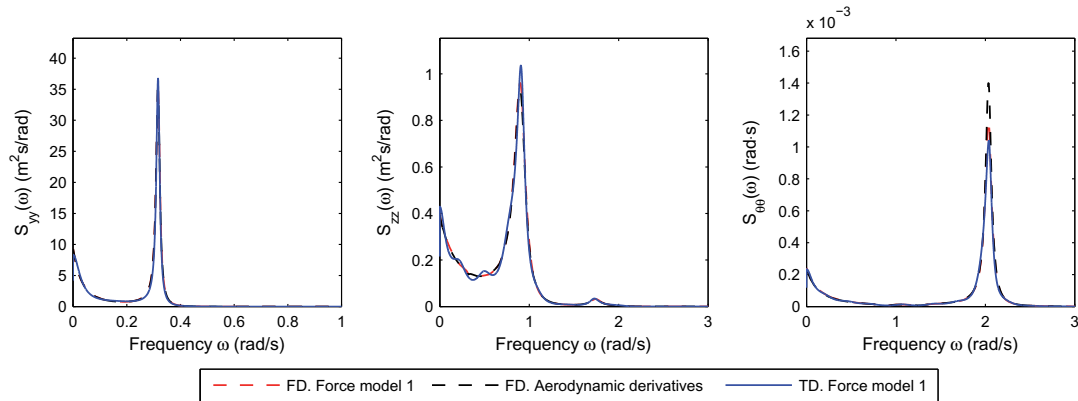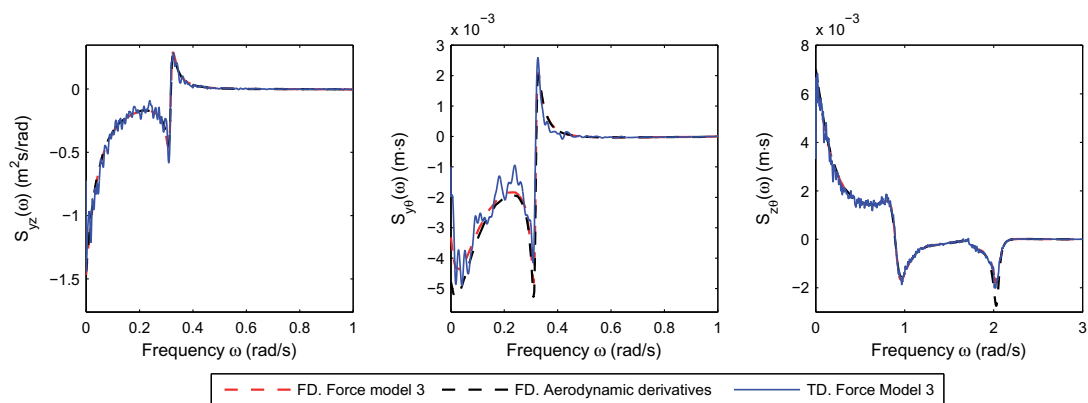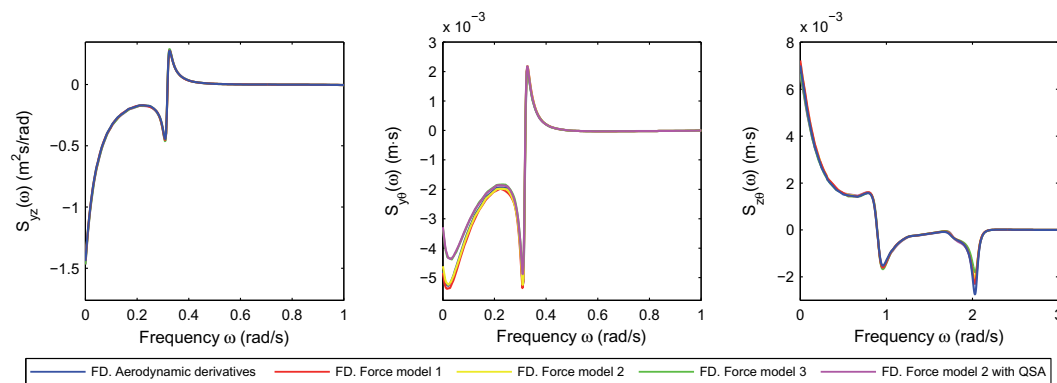

Fig. 10. Comparison of the spectral densities of the response components at a mean wind velocity of 50 m/s, using the aerodynamic derivatives and force model 1 in the frequency domain and force model 1 in the time domain. The time domain estimate has been obtained using the Burg algorithm.

Fig. 11. Comparison of the co-spectral densities of the response components at a mean wind velocity of 50 m/s, using the aerodynamic derivatives and force model 1 in the frequency domain and force model 1 in the time domain. The time domain estimate has been obtained using the Welch algorithm.

density of the horizontal and vertical response very well. The spectral densities estimated from the time domain simulations corresponds very well with the spectral densities for the horizontal

and vertical response obtained in the frequency domain with force model 1, while some discrepancies can be seen for the peak of the spectral density of the torsional response. Force model 1 provides
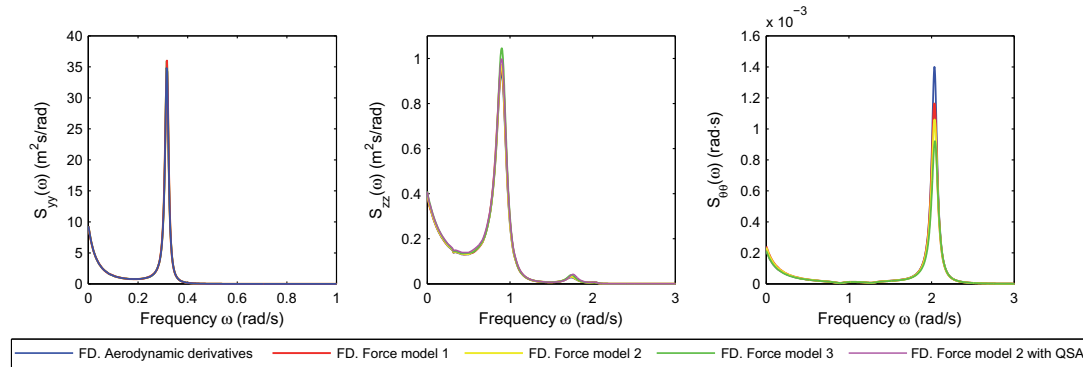
Fig. 12. Comparison of the spectral densities of the response components obtained in the frequency domain at mean wind velocity of 50 m/s using force models 1, 2 and 3 and force model 2 with quasi-steady asymptotes provided by traditional quasi-steady theory.

Fig. 13. Comparison of the co-spectral densities of the response components obtained in the frequency domain at mean wind velocity of 50 m/s, using force model 1, 2 and 3 and force model 2 with quasi-steady asymptotes provided by traditional quasi-steady theory.

higher torsional damping than the aerodynamic derivatives, which is the main reason for the discrepancies of the torsional response presented in Table 3. The covariance coefficients obtained in the time domain are presented in Table 5, and as can be seen, there are some differences between the results predicted using the aerodynamic derivatives and force model 1. The co-spectral densities of the response components at the mid-span at a mean wind velocity of 60 m/s are shown in Fig. 11. The spectral densities estimated from the time series correspond well with the spectral density obtained in the frequency domain when force model 1 is used to model the self-excited forces. The results in the tables indicate that the estimates of the covariance coefficients are less accurate than the estimates of the standard deviations. This is mainly because the correlation of the response components is rather low, and as can be seen from the co-spectral density of the vertical and the torsional components, small differences of the co-spectral densities will result in a large error in the estimate.

Force model 2 provides response estimates of satisfying accuracy. The standard deviation estimated from the time domain simulations in Table 3 corresponds well to the frequency domain results provided in Table 4 and is also in good agreement with the results predicted by the aerodynamic derivatives. The same inaccuracies of the estimates of the covariance coefficients can also

be observed for this force model. When the quasi-steady asymptotes from traditional quasi-steady theory are introduced, it can be seen from Table 3 and Table 4 that results of good accuracy are also achieved for this force model.

To further compare the unsteady time domain models used in this article, the spectral densities of the response components predicted by the unsteady models at a mean wind velocity of 50 m/s is shown in Fig. 12. As can be seen from the figure, the spectral densities do not seem to be sensitive to the discrepancies of the self-excited force models observed in the low reduced frequency range in Fig. 6. The differences are at the peaks of the spectral densities where the curves representing the experimental results are actually more consistent than in the high and low reduced-frequency range. The co-spectral densities of the response components are shown in Fig. 13. The co-spectral density of the horizontal and vertical components are identical for all of the self-excited force models, while some discrepancies can be observed at low frequencies for the co-spectral densities of the horizontal and torsional components. The co-spectral density of the vertical and torsional motion is consistent for all of the self-excited force models considered, but some discrepancies can be observed at the peak near 2 rad/s.

The standard deviation estimated as the average of twenty time domain simulations when the frequency-independent description
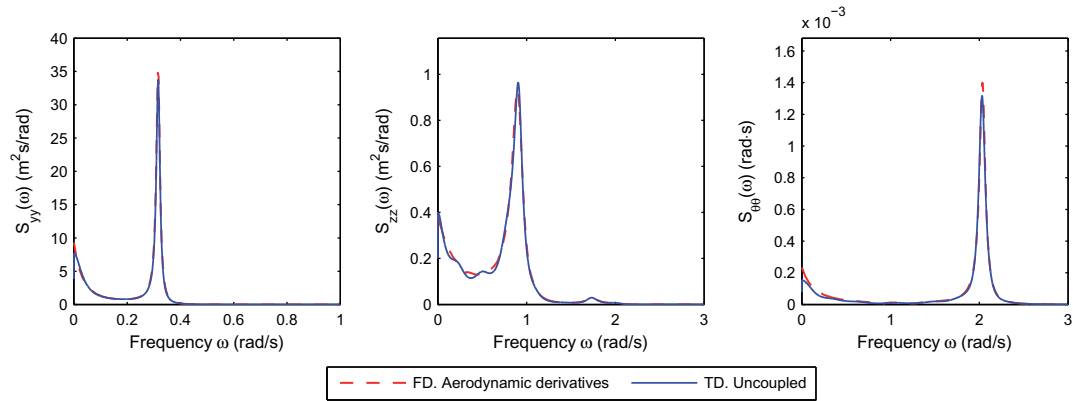
Fig. 14. Comparison of the spectral densities of the response components at mean wind velocity of 50 m/s obtained in the frequency domain, using the aerodynamic derivatives, and in the time domain, using the uncoupled frequency-independent method presented in Eqs. (27) and (29).
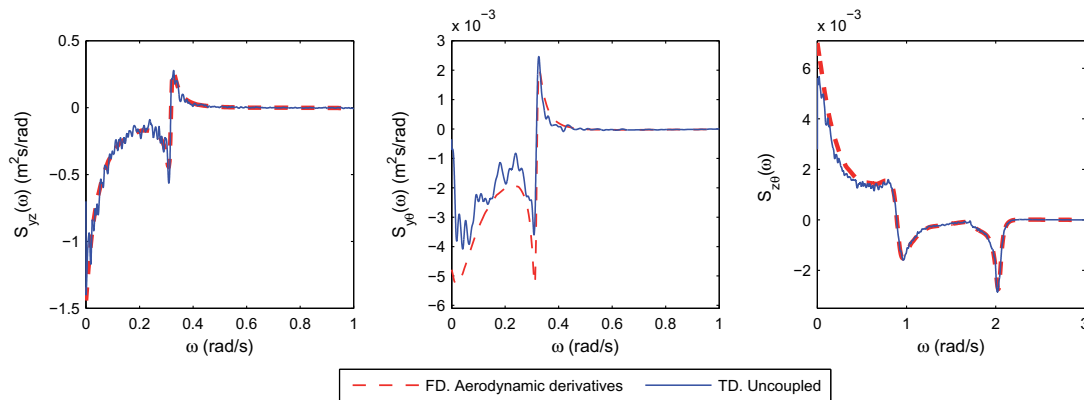

Fig. 15. Comparison of the co-spectral densities of the response components at mean wind velocity of 50 m/s obtained in the frequency domain, using the aerodynamic derivatives, and in the time domain using the uncoupled frequency-independent method presented in Eqs. (27) and (29).

of the self-excited forces outlined in Eqs. (27) and (29) is used to model the self-excited forces is also shown in Table 3. As can be seen from the results, this simplified method provides results as accurate as the more complicated models outlined above. The spectral densities of the response components at the mid-span at a mean wind velocity of 50 m/s are shown in Fig. 14. The results predicted by this method provide spectral densities that are very

Table 7
Calculated critical frequencies and mean wind velocities when the different load formulations discussed in this article have been used to model the self-excited forces.

Formulation	Critical velocity V_{CR} (m/s)	Critical frequency ω_{CR} (rad/s)
Aerodynamic derivatives	79	1.63
Force model 3 Eq. (21)	77	1.68
	−3%	3%
Force model 1, Eq. (8)	79	1.62
	0%	0%
Force model 2. Eq. (12)	79	1.63
	−1%	0%
Force model 2 with	76	1.68
quasi-steady asymptotes	−3%	3%
Decoupled system of	79	1.63
equations. Eq. (28)	0%	0%

similar to the frequency domain results using the aerodynamic derivatives. The peaks where the load coefficients have been obtained are accurately captured. For the torsional response small discrepancies in the results may be observed at low frequencies. The co-spectral density of the response components are shown in Fig. 15. The peaks in the co-spectral densities are accurately captured except for the peak at about 3 rad/s for the co-spectral density of the horizontal and torsional components. Some discrepancies of the co-spectral densities at low frequencies can also be seen.

It is also interesting to investigate the stability limit predicted by the different self-excited force models discussed in this article. The multimode stability limits for the Hardanger Bridge given by the different self-excited force models are presented in Table 7. As can be seen from the results, all the self-excited force models provide stability limits consistent with the results predicted using the aerodynamic derivatives.

4. Concluding remarks

The wind-induced dynamic response of the Hardanger Bridge, emphasizing time domain modeling of self-excited forces, has been

carefully evaluated in this paper. The self-excited forces have been modeled by two commonly applied unsteady force models, an unsteady model suggested in this article and a novel approximate method introduced and explained herein. The unsteady models may be considered as merely a Fourier transform of curves representing the aerodynamic derivatives in the frequency domain and do not introduce any inaccuracies, compared with a frequency domain solution. However, since the nature of the unsteady models implies that two sets of data, representing the imaginary and the real part, have to be curve fitted using the same coefficients, the unsteady time domain methods will normally provide fits to the experimental data of lower accuracy than the curves used in the frequency domain. Significant differences in the results predicted by the considered unsteady models have been observed. The unsteady force model suggested in this article provided results of good accuracy, and it has been shown that the quasi-steady asymptotes provided by traditional quasi-steady theory may easily be introduced in this model. The results presented illustrate that the response spectra are very sensitive to changes in the curves representing the experimental data of the aerodynamic derivatives in the reduced-frequency ranges corresponding to natural frequencies, in particular for H_1^* and A_2^*, while the response spectra seem to have very low sensitivity to changes in the curves in the low reduced-frequency range. For the co-spectral densities of the response components, the same sensitivity at reduced velocities corresponding to the natural frequencies is observed, in addition to an apparently high sensitivity of the co-spectral density of the horizontal and torsional response in the low reduced-frequency range. The integration method suggested for the unsteady models significantly reduced the number of time steps necessary to evaluate the convolution integrals with sufficient accuracy to avoid phase and amplitude distortion of the self-excited forces.

The approximate approach introduced and explained in this article provided standard deviations of very high accuracy. The results are better than some of the unsteady models used in this article. The main reason for this is that the coefficients used to describe the self-excited forces are determined such that self-excited forces related to each natural frequency are accurately modeled. Since the spectral densities of the response components have low sensitivity to the quasi-steady asymptotes, the spectral densities of the response components are accurately captured for the entire frequency range.

Acknowledgements

References

[1] Wyatt TA. Bridge aerodynamics 50 years after Tacoma Narrows – part I: The Tacoma Narrows failure and after. J Wind Eng Ind Aerodyn 1992;40:317–26.
[2] Scanlan RH, Beliveau J-G, Budlong KS. Indicial aerodynamic functions for bridge decks. J Eng Mech Div 1974;100:657–72.
[3] Simiu E, Scanlan RH. Wind effects on structures fundamentals and applications to design. 3rd ed. New York: Wiley; 1996.
[4] Simiu EE, Miyata T. Design of buildings and bridges for wind: a practical guide for ASCE-7 standard users and designers of special structures 2006.
[5] Strømmen EN. Theory of bridge aerodynamics. Berlin: Springer; 2006.
[6] Øiseth O, Rönnquist A, Sigbjörnsson R. Simplified prediction of wind-induced response and stability limit of slender long-span suspension bridges, based on modified quasi-steady theory: acase study. J Wind Eng Ind Aerodyn 2010;98:730–41.
[7] Katsuchi H, Jones NP, Scanlan RH. Multimode coupled flutter and buffeting analysis of the Akashi-Kaikyo bridge. J Struct Eng – ASCE 1999;125:60–70.
[8] Jain A, Jones NP, Scanlan RH. Coupled flutter and buffeting analysis of long-span bridges. J Struct Eng – ASCE 1996;122:716–25.
[9] Scanlan RH, Tomko JJ. Airfoil and bridge deck flutter derivatives. J Eng Mech Div 1971;97:1717–37.
[10] Walshe DE, Wyatt TA. Bridge aerodynamics 50 years after Tacoma Narrows – Part II: A new. J Wind Eng Ind Aerodyn 1992;40:327–36.
[11] Brownjohn JMW, Jakobsen JB. Strategies for aeroelastic parameter identification from bridge deck free vibration data. J Wind Eng Ind Aerodyn 2001;89:1113–36.
[12] Jakobsen JB, Hjorth-Hansen E. Arne Selberg's formula for flutter speed in light of multimodal flutter analysis. In Proceedings of twelfth international conference on wind engineering, Cairns, Australia; 2007.
[13] Theodorsen T. General theory of aerodynamic instability and the mechanism of flutter. NACA report no. 496. Washington, DC; 1934.
[14] Fung YC. An introduction to the theory of aeroelasticity. New York: Wiley; 1955.
[15] Garrick IE. On some reciprocal relations in the theory of nonstationary flows. NACA technical report 629; 1938.
[16] Jakobsen JB, Hjorth-Hansen E. Determination of the aerodynamic derivatives by a system-identification-method. J Wind Eng Ind Aerodyn 1995;57:295–305.
[17] Huang L, Liao H, Wang B, Li Y. Numerical simulation for aerodynamic derivatives of bridge deck. Simul Model Pract Theory 2009;17: 719–29.
[18] Sarwar MW, Ishihara T, Shimada K, Yamasaki Y, Ikeda T. Prediction of aerodynamic characteristics of a box girder bridge section using the LES turbulence model. J Wind Eng Ind Aerodyn 2008;96:1895–911.
[19] Zhu ZW, Gu M, Chen ZQ. Wind tunnel and CFD study on identification of flutter derivatives of a long-span self-anchored suspension bridge. Comput-Aided Civil Infrastruct Eng 2007;22:541–54.
[20] Yagi T. Wind-induced instabilities of structures. Stockholm: Kungl. tekniska högskolan, Institutionen för byggkonstruktion; 1997.
[21] Chen XZ, Matsumoto M, Kareem A. Time domain flutter and buffeting response analysis of bridges. J Eng Mech – ASCE 2000;126:7–16.
[22] Mishra SS, Kumar K, Krishna P. Multimode flutter of long-span cable-stayed bridge based on 18 experimental aeroelastic derivatives. J Wind Eng Ind Aerodyn 2008;96:83–102.
[23] Bucher CG, Lin YK. Stochastic stability of bridges considering coupled modes. J Eng Mech – ASCE 1988;114:2055–71.
[24] Bisplinghoff RL, Ashley H. Principles of aeroelasticity. New York: Wiley; 1962.
[25] Davenport AG. Response of slender line like structures to a gusty wind. The institution of civil engineers. 1962;23:389–408.
[26] Dyrbye C, Hansen SO. Wind loads on structures. Chichester: Wiley; 1997.
[27] Øiseth O, Sigbjörnsson R. An alternative analytical approach to prediction of flutter stability limits of cable supported bridges. J Sound Vib 2011;300:2784–800.
[28] Borri C, Costa C. Quasi-steady analysis of a two-dimensional bridge deck element. Comput Struct 2004;82:993–1006.
[29] Diana G, Bruni S, Cigada A, Collina A. Turbulence effect on flutter velocity in long-span suspended bridges. J Wind Eng Ind Aerodyn 1993;48:329–42.
[30] Diana G, Resta F, Rocchi D. A new numerical approach to reproduce bridge aerodynamic non-linearities in time domain. J Wind Eng Ind Aerodyn 2008;96:1871–84.
[31] Diana G, Rocchi D, Argentini T, Muggiasca S. Aerodynamic instability of a bridge deck section model: linear and nonlinear approach to force modeling. J Wind Eng Ind Aerodyn 2010;98:363–74.
[32] Borri C, Costa C, Zahlten W. Non-stationary flow forces for the numerical simulation of aeroelastic instability of bridge decks. Comput Struct 2002;80:1071–9.
[33] Costa C, Borri C. Application of indicial functions in bridge deck aeroelasticity. J Wind Eng Ind Aerodyn 2006;94:859–81.
[34] Salvatori L, Borri C. Frequency- and time-domain methods for the numerical modeling of full-bridge aeroelasticity. Comput Struct 2007;85:675–87.
[35] Caracoglia L, Jones NP. Time domain vs. frequency domain characterization of aeroelastic forces for bridge deck sections. J Wind Eng Ind Aerodyn 2003;91:371–402.
[36] Chen X, Matsumoto M, Kareem A. Aerodynamic coupling effects on flutter and buffeting of bridges. J Eng Mech 2000;126:17–26.
[37] Humar JL. Dynamics of structures. 2nd ed. Lisse: Balkema; 2002.
[38] Sintef. ALVSAT version 3.7 theory manual, user manual and test manual. Norway: SINTEF Division of Structural Engineering; 1996.
[39] Shinozuka M. Monte Carlo solution of structural dynamics. Comput Struct 1972;2:855–74.
[40] Shinozuka M, Jan CM. Digital simulation of random processes and its applications. J Sound Vib 1972;25:111–28.
[41] Aas-Jakobsen K, Strommen E. Time domain buffeting response calculations of slender structures. J Wind Eng Ind Aerodyn 2001;89:341–64.
[42] Hansen SO, Lollesgaard M, Rex S, Jakobsen JB, Hansen EH. The Hardanger Bridge: static and dynamic wind tunnel tests with a section model. Copenhagen: Svend Ole Hansen ApS; 2006.
[43] Zienkiewicz OC, Taylor RL. The finite element method. 5th ed. Oxford: Butterworth–Heinemann; 2000.

Ole Øiseth, Anders Rönnquist, Ragnar Sigbjörnsson

Finite element formulation of the self-exited forces for time-domain assessment of wind-induced dynamic response and flutter stability limit of cable-supported bridges

Paper IV

Finite element formulation of the self-excited forces for time-domain assessment of wind-induced dynamic response and flutter stability limit of cable-supported bridges

Ole Øiseth, Anders Rönnquist, Ragnar Sigbjörnsson

Department of Structural Engineering, Norwegian University of Science and Technology, 7491 Trondheim, Norway
E-mail: ole.oiseth@ntnu.no

Abstract
In this paper it is shown how unsteady self-excited aerodynamic forces modelled by rational functions can be introduced into a finite element beam model, using the nodal displacement degrees of freedom of the element to characterize the aeroelastic system. The time-dependent part of the self-excited forces is obtained introducing additional degrees of freedom in each node, so-called aerodynamic degrees of freedom. The stability limit and buffeting response obtained in the time domain, using different shape functions to discretise the self-excited forces, are compared with results predicted by a traditional multimode approach. It is concluded that both the stability limit and the buffeting response can be obtained using this aeroelastic element, which implies that structural nonlinearities may be more easily introduced in time-domain analysis of the wind-induced buffeting response.

Key words: Cable-supported bridges, wind loading, aerodynamic derivatives, flutter, FEM

1   Introduction

Wind-induced dynamic response is one of the major concerns when designing long-span bridges. The wind loading may cause unfavourable vibration of the girder, cables, and towers and has to be taken into account in both the ultimate- and serviceability limit states. The wind-induced vibration phenomena of bridges are commonly divided into (*i*) vortex-shedding-induced vibration, (*ii*) buffeting vibration and (*iii*) flutter vibration. Vortex shedding typically occurs at low mean wind velocities, while buffeting and flutter vibration occurs in strong winds. The present state of the art assumes that vortex-induced vibration may be treated separately from the buffeting and flutter vibration, which is a reasonable assumption for common bridges since these phenomena occur at quite different mean wind velocities. [1-7]

The self-excited forces in bridge engineering are commonly modelled by experimentally determined aerodynamic derivatives, as suggested by Scanlan and Tomoko [8]. The experimental data can be conveniently used directly in the frequency domain to obtain the buffeting response and stability limit of the aeroelastic system. The present state of the art is the multimode approach, where selected still-air vibration modes are used as generalized coordinates to characterize the aeroelastic system. [6, 9-12]. Since long-span cable-supported structures are highly nonlinear in nature, a nonlinear approach has to be used in the analysis. In the frequency domain this can be circumvented by

performing the static analyses using a nonlinear approach, and performing a linear dynamic analysis around the dead load equilibrium condition. However, as cable-supported bridges become slenderer, a nonlinear dynamic approach may become necessary. Structural nonlinearities may be taken more easily into account in the time domain than in the frequency domain, which implies that time-domain modelling of self-excited forces will become more important in the future. Several papers on modelling self-excited forces using rational or indicial functions in time domain have been published, e.g., [13-18]. However, it is still common to obtain the dynamic response or the stability limit using still-air vibration modes as generalized coordinates. When material and geometric nonlinearities are considered, it is a clear advantage to perform the calculations using the degrees of freedom of the finite element model directly. There are studies where the element degrees of freedom have been used when assessing the wind-induced dynamic response, e.g., [19-24], but in these articles quasi-steady models have been used to quantify the self-excited forces. There are also examples where the element degrees of freedom have been used to obtain the flutter stability limit, e.g., [25-27]. Here the traditional complex eigenvalue approach has been used for the full system, and the self-excited forces have been modelled directly with experimentally determined aerodynamic derivatives.

In this paper it is shown how self-excited forces may be modelled in time-domain buffeting response analysis using the nodal displacement degrees of freedom instead of using the still-air vibration modes as generalized coordinates. The self-excited forces have been modelled using rational functions, and the time-dependent part of the self-excited forces have been modelled by introducing additional degrees of freedom, termed in the following aerodynamic degrees of freedom, at each end of traditional beam elements. Several alternative element models have been considered, including a consistent model where the same shape functions have been used to characterize the structural and aerodynamic properties of the beam element and hybrid models, where different shape functions have been used to characterize the structural and aerodynamic properties. The stability limit of an idealized model of the Hardanger Bridge has been calculated using the approach suggested in this paper, and the predicted values are compared with the result provided by a traditional multimode approach. The damping at varying mean wind velocities has also been carefully studied and compared with results from the multimodal analysis. Furthermore, the buffeting response at several mean wind velocities has been obtained in time domain, and the results have been compared with the traditional frequency domain multimode approach.

The approach suggested in this paper implies that it is possible to model the time dependency of self-excited forces using the nodal degrees of freedom of a finite element model of a cable-supported bridge. This implies that structural nonlinearities may be taken easily into account. However, the aerodynamic model must be linear, since the self-excited forces have been obtained using the principle of superposition. As long as the mean value of the torsional deformation is taken into account when the aerodynamic derivatives are obtained, and the response is within the limits of linearised aerodynamic theory, structural nonlinearities can be accurately modelled using the approach suggested in this paper. The linear aerodynamic model will provide accurate results during large horizontal and vertical motions, but should be used with care if torsional

deformations become larger than the values considered in wind tunnel experiments. Models exist for large angles of attack, see for instance [28, 29], but only linear aerodynamic models will be discussed in this paper since linear theory is most commonly used.

2 Theory

2.1 Modelling of self-excited forces – a review

The self-excited forces acting on a bridge deck section are commonly represented by aerodynamic derivatives introduced in bridge engineering by Scanlan and Tomoko [8]. For a two-dimensional bridge deck section (see Figure 1) this can be expressed as:

$$q_y^{Se} = \frac{1}{2}\rho V^2 B \left(KP_1^* \frac{\dot{r}_y}{V} + KP_2^* \frac{B\dot{r}_\theta}{V} + K^2 P_3^* r_\theta + K^2 P_4^* \frac{r_y}{B} + KP_5^* \frac{\dot{r}_z}{V} + K^2 P_6^* \frac{r_z}{B} \right)$$

$$q_z^{Se} = \frac{1}{2}\rho V^2 B \left(KH_1^* \frac{\dot{r}_z}{V} + KH_2^* \frac{B\dot{r}_\theta}{V} + K^2 H_3^* r_\theta + K^2 H_4^* \frac{r_z}{B} + KH_5^* \frac{\dot{r}_y}{V} + K^2 H_6^* \frac{r_y}{B} \right) \quad (1)$$

$$q_\theta^{Se} = \frac{1}{2}\rho V^2 B^2 \left(KA_1^* \frac{\dot{r}_z}{V} + KA_2^* \frac{B\dot{r}_\theta}{V} + K^2 A_3^* r_\theta + K^2 A_4^* \frac{r_z}{B} + KA_5^* \frac{\dot{r}_y}{V} + K^2 A_6^* \frac{r_y}{B} \right)$$

Here, V is the mean wind velocity; ρ is the air density; B is the width of the cross section; $K=B\omega/V$ is the reduced circular frequency of motion, and r_n, $n \in \{y, z, \theta\}$ represents the horizontal, vertical and torsional displacements that are positive in the same direction as the forces displayed in Figure 1. P_n^*, H_n^*, A_n^* $n \in \{1, 2, \dots 6\}$ are the dimensionless aerodynamic derivatives, which are characteristic cross-sectional properties given as functions of the reduced-frequency of motion. Eq. (1) is only valid for a single-frequency harmonic motion. However, by introducing the principle of superposition Eq. (1) can be extended to any periodic or aperiodic motion applying Fourier integral representation:

$$G_{q_y^{Se}}(\omega) = \frac{1}{2}\rho B^2 \omega^2 \left[\left(P_1^* i + P_4^*\right) G_y(\omega) + \left(P_5^* i + P_6^*\right) G_z(\omega) + B\left(P_2^* i + P_3^*\right) G_\theta(\omega) \right]$$

$$G_{q_z^{Se}}(\omega) = \frac{1}{2}\rho B^2 \omega^2 \left[\left(H_5^* i + H_6^*\right) G_y(\omega) + \left(H_1^* i + H_4^*\right) G_z(\omega) + B\left(iH_2^* + H_3^* r_\theta\right) G_\theta(\omega) \right] \quad (2)$$

$$G_{q_\theta^{Se}}(\omega) = \frac{1}{2}\rho B^2 \omega^2 \left[B\left(A_5^* i + A_6^*\right) G_y(\omega) + B\left(A_1^* i + A_4^*\right) G_z(\omega) + B^2 \left(A_2^* i + A_3^*\right) G_\theta(\omega) \right]$$

which may be further simplified to:

$$G_{q_n^{Se}}(\omega) = F_{ny}(\omega)G_y(\omega) + F_{nz}(\omega)G_z(\omega) + F_{n\theta}(\omega)G_\theta(\omega) \quad (3)$$
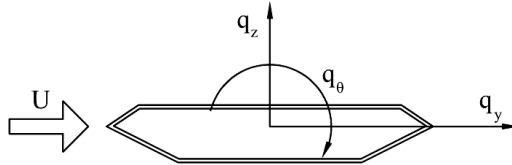

Figure 1: Aerodynamic forces acting on the cross section of the study bridge deck.

3

Here, $n \in \{y, z, \theta\}$; i is the imaginary unit, and $G_X(\omega)$ is the Fourier transform of $X(t)$, where $X(t) \in \{r_y, r_z, r_\theta, q_y, q_z, q_\theta\}$, and $F_{nm}(\omega)$ symbolizes the transfer functions defined in terms of the aerodynamic derivatives, which in this representation are treated as continuous functions of frequency. As shown for instance by [30], the time-domain description of self-excited forces can be obtained applying the inverse Fourier transform. This results in the following equation:

$$q_n^{(Se)}(V,t) = \int_{-\infty}^{t} I_{ny}(t-\tau)r_y(\tau)d\tau + \int_{-\infty}^{t} I_{nz}(t-\tau)r_z(\tau)d\tau + \int_{-\infty}^{t} I_{n\theta}(t-\tau)r_\theta(\tau)d\tau \qquad (4)$$

Here, $n \in \{y, z, \theta\}$. The aerodynamic impulse-response functions can be obtained by the inverse Fourier transform of the aerodynamic transfer functions defined in terms of the aerodynamic derivatives in Eq. (2). The aerodynamic derivatives are commonly known at discrete reduced frequencies and hence must be approximated with a curve fit. To be able to develop a time-domain representation of self-excited forces, the selected expression must be suitable for inverse Fourier transforming. The following expression has frequently been used in the literature, e.g., [6, 18, 30, 31], here exemplified by the vertical self-excited force due to the vertical motion:

$$F_{zz}(V,\omega) = \frac{1}{2}\rho V^2 \left(A_1^{(zz)} + A_2^{(zz)}\frac{i\omega B}{V} + A_3^{(zz)}\left(\frac{i\omega B}{V}\right)^2 + \sum_{l=1}^{m} A_{l+3}^{(zz)}\frac{i\omega B/V}{i\omega B/V + d_l^{(zz)}} \right) \qquad (5)$$

This expression provides the following relation between the transfer function and the experimental data of the aerodynamic derivatives, here exemplified by, H_1^* and H_4^*

$$H_4^* = \hat{V}^2 \left(A_1^{(zz)} + \sum_{l=1}^{L}\frac{A_{l+3}^{(zz)}}{\left[\left(d_l^{(zz)}\hat{V}\right)^2 + 1\right]} \right), \qquad H_1^* = \hat{V} \left(A_2^{(zz)} + \hat{V}^2\sum_{l=1}^{L}\frac{A_{l+3}^{(zz)}d_l^{(zz)}}{\left[\left(d_l^{(zz)}\hat{V}\right)^2 + 1\right]} \right) \qquad (6)$$

Taking the inverse Fourier transform of the transfer function defined in Eq.(5) and inserting the resulting expression into Eq. (4) renders the following expression for the vertical self-excited force induced by vertical motion:

$$q_{zz}^{(se)}(t) = \frac{1}{2}\rho V^2 \left(A_1^{(zz)}r_z(t) + A_2^{(zz)}\frac{B}{V}\dot{r}_z(t) + \sum_{l=1}^{N} A_{l+3}^{(zz)}\left(r_z(t) - \frac{d_l^{(zz)}V}{B}\int_{-\infty}^{t} e^{\left(-\frac{d_l^{(zz)}V}{B}(t-\tau)\right)}r_z(\tau)d\tau \right) \right) \qquad (7)$$

2.2   Finite element representation of self-excited forces
The starting point is the beam element displayed in Figure 2. The element has two nodes, each with six degrees of freedom. This implies that the displacements along the element are defined by the following displacement field:

$$\mathbf{u}(x,t) = \mathbf{N}(x)\mathbf{v}(t)$$
$$\mathbf{u} = \begin{bmatrix} u_x & u_y & u_z & u_\theta \end{bmatrix}^T \qquad (8)$$
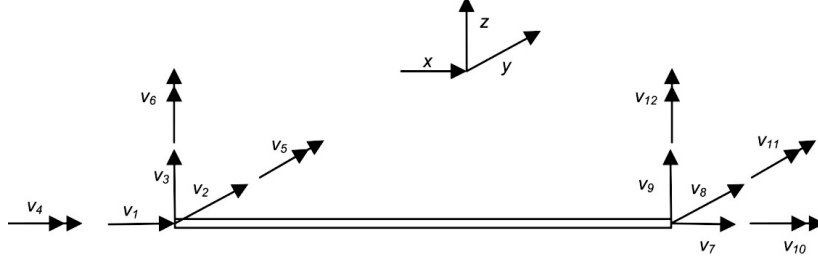
4

Figure 2: A three-dimensional structural beam element with 6 degrees of freedom at each end node

Here, t is time; x is the (local) element coordinate (see, for instance, [32]), and the vector $\mathbf{u}(x,t)$ contains the displacements along the beam element, where u_x symbolizes the longitudinal displacement, u_y, the transverse horizontal displacement u_z, the transverse vertical displacement and, u_Θ, the rotation of the beam element. The matrix $\mathbf{N}(x)$ contains the shape functions, and the vector $\mathbf{v}$ contains the nodal displacement degrees of freedom. The derivation of the mass, damping and stiffness matrices and the load vector is well established and will not be dealt with here, but may be found in several textbooks, e.g., [32-34]. However, it is necessary to explain how the self-excited forces may be introduced into the finite element formulation. The self-excited nodal forces, $\mathbf{F}_{se}$, may be obtained by the principle of virtual work:

$$\delta\mathbf{v}^T\mathbf{F}_{Se}(t) = \delta\mathbf{v}^T\int_0^L \mathbf{N}^T(x)\mathbf{q}(x,t)dx \tag{9}$$

Here, $\delta\mathbf{v}$ symbolizes the virtual nodal displacements, and the vector $\mathbf{q}(x,t)$ contains the self-excited forces along the element, i.e.:

$$\mathbf{q}(x,t) = \begin{bmatrix} 0 & q_y^{(Se)}(x,t) & q_z^{(Se)}(x,t) & q_\theta^{(Se)}(x,t) \end{bmatrix}^T \tag{10}$$

Since the self-excited load in, for instance, the vertical direction is dependent on the horizontal vertical and torsional response, each element in the vector is given by $q_n^{(Se)}(x,t) = q_{ny}^{(Se)} + q_{nz}^{(Se)} + q_{n\theta}^{(Se)}$, where $n \in \{y,\ z,\ \theta\}$. The self-excited forces may be approximated by the following expression (see Eq. (7)):

$$\mathbf{q}(x,t) = \frac{1}{2}\rho V^2\left(\mathbf{A}_1\mathbf{u}(t) + \frac{B}{V}\mathbf{A}_2\dot{\mathbf{u}}(t) + \sum_{l=3}^{N}\left(\mathbf{A}_l\mathbf{u}(t) - \int_{-\infty}^{t}\mathbf{\Phi}_l(t-\tau)\mathbf{u}(\tau)d\tau\right)\right) \tag{11}$$

The content of the matrices $\mathbf{A}_1$, $\mathbf{A}_2$ $\mathbf{A}_l$ and $\mathbf{\Phi}_l$ is given in Appendix A. The self-excited force acting in each degree of freedom may then be expressed as follows:

$$\mathbf{F}_{Se} = \frac{1}{2}\rho V^2\int_0^L\left(\mathbf{N}^T\mathbf{A}_1\mathbf{N}\mathbf{v} + \frac{B}{V}\mathbf{N}^T\mathbf{A}_2\mathbf{N}\dot{\mathbf{v}} + \sum_{l=3}^{N}\left(\mathbf{N}^T\mathbf{A}_l\mathbf{N}\mathbf{v} - \int_{-\infty}^{t}\mathbf{N}^T\mathbf{\Phi}_l(t-\tau)\mathbf{N}\mathbf{v}(\tau)d\tau\right)\right)dx \tag{12}$$

5

The expression can be rewritten as:

$$\mathbf{F}_{Se}(t) = \mathbf{K}_{ae}\mathbf{v}(t) + \mathbf{C}_{ae}\dot{\mathbf{v}}(t) + \mathbf{Z}(t)$$

$$\mathbf{K}_{ae} = \frac{1}{2}\rho V^2 \int_0^L \mathbf{N}^T \mathbf{A}_1 \mathbf{N} \qquad \mathbf{C}_{ae} = \frac{1}{2}\rho V^2 \frac{B}{V}\int_0^L \mathbf{N}^T \mathbf{A}_2 \mathbf{N} \qquad (13)$$

$$\mathbf{Z}(t) = \frac{1}{2}\rho V^2 \sum_{l=3}^N \int_0^L \left(\mathbf{N}^T \mathbf{A}_l \mathbf{N}\mathbf{v} - \int_{-\infty}^t \mathbf{N}^T \mathbf{\Phi}_l(t-\tau)\mathbf{N}\mathbf{v}(\tau)d\tau \right) dx$$

The matrices $\mathbf{K}_{ae}$ and $\mathbf{C}_{ae}$ are referred to as aerodynamic stiffness and aerodynamic damping matrices, respectively. The vector $\mathbf{Z}$ contains the time-history-dependent terms. It is time-consuming to evaluate the convolution integrals numerically. However, this can be avoided by introducing the convolution integrals as unknown in the system of equations. Considering the two-node beam element displayed in Figure 2, the expression for $\mathbf{Z}$ may be rewritten as follows:

$$\mathbf{Z} = \mathbf{Q}\mathbf{X}$$

$$\mathbf{Q} = \begin{bmatrix} \mathbf{W}_1 & \mathbf{W}_2 & \cdots & \mathbf{W}_N \end{bmatrix} \qquad \mathbf{X} = \begin{bmatrix} \mathbf{x}_1 & \mathbf{x}_2 & \cdots & \mathbf{x}_N \end{bmatrix}^T \qquad (14)$$

Here, N is the number of exponential filters used in Eq. (5) to model the self-excited forces. The contents of the matrices $\mathbf{W}_n$ and the vector $\mathbf{x}_n$ are given in Appendix A. The vector $\mathbf{x}_n$ contains convolution integrals, which can be generalized as:

$$x_{nm,0}^{(l)} = A_{l+3}^{(nm)}\left(v_o(t) - \frac{d_l^{(nm)}V}{B}\int_{-\infty}^t e^{\left(-\frac{d_l^{(nm)}V}{B}(t-\tau)\right)}v_o(\tau)d\tau \right) \qquad (15)$$

Here, $n \in \{y,z,\Theta\}$, $m \in \{y,z,\Theta\}$ and $o \in \{1,2\ldots,12\}$. Additional equations are needed if the elements in the vector $\mathbf{X}$ are introduced as unknowns in the system of equations. These equations can be obtained by taking the derivative of Eq. (15):

$$\dot{x}_{nm,o}^{(l)} = A_{l+3}^{(nm)}\dot{v}_o(t) - \frac{d_l^{(nm)}V}{B}x_{nm,o}^{(l)} \qquad (16)$$

In Figure 3 the aerodynamic degrees of freedom needed to model the self-excited forces for one exponential filter are shown. Self-excited forces related to axial displacements of the element have been neglected. This implies that the equations of motion for the aeroelastic beam element may be written as:

$$\mathbf{M}\ddot{\mathbf{v}} + \left(\mathbf{C} - \mathbf{C}_{ae} \right)\dot{\mathbf{v}} + \left(\mathbf{K} - \mathbf{K}_{ae} \right)\mathbf{v} + \mathbf{Q}\mathbf{X} = \mathbf{P}$$

$$\mathbf{A}\dot{\mathbf{v}} + \mathbf{B}\dot{\mathbf{X}} + \mathbf{D}\mathbf{X} = \mathbf{0} \qquad (17)$$

or:

$$\begin{bmatrix} \mathbf{M} & \mathbf{0} \\ \mathbf{0} & \mathbf{0} \end{bmatrix}\begin{bmatrix} \ddot{\mathbf{v}} \\ \ddot{\mathbf{X}} \end{bmatrix} + \begin{bmatrix} (\mathbf{C}-\mathbf{C}_{ae}) & \mathbf{0} \\ \mathbf{A} & \mathbf{B} \end{bmatrix}\begin{bmatrix} \dot{\mathbf{v}} \\ \dot{\mathbf{X}} \end{bmatrix} + \begin{bmatrix} (\mathbf{K}-\mathbf{K}_{ae}) & \mathbf{Q} \\ \mathbf{0} & \mathbf{D} \end{bmatrix}\begin{bmatrix} \mathbf{v} \\ \mathbf{X} \end{bmatrix} = \begin{bmatrix} \mathbf{P} \\ \mathbf{0} \end{bmatrix} \qquad (18)$$
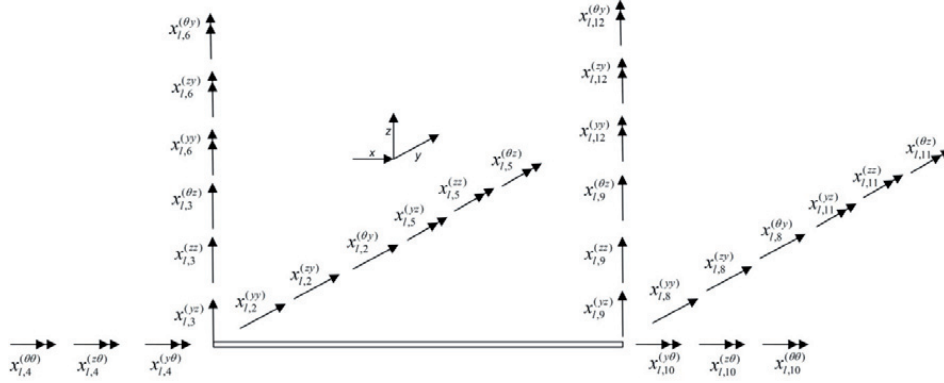
6

Figure 3: The aerodynamic degrees of freedom needed for a consistent aeroelasic beam element when using one exponential filter to model the self-excited forces in the vertical and horizontal direction and in torsion. The self-excited forces due to axial motion have been neglected.

The total number of degrees of freedom for the element is the sum of the displacement degrees of freedom displayed in Figure 2 and the aerodynamic degrees of freedom related to the self-excited forces displayed in Figure 3, multiplied by the number of exponential filters. This implies that if the self-excited forces related to horizontal, vertical, and torsional motion are approximated using two exponential filters in Eq. (5), the total number of degrees of freedom will become $N_{dof} = 12 + 30 \cdot 2 = 72$. This number of degrees of freedom may seem high, but this approach requires far less computational effort than solving the 60 convolution integrals numerically in each time step. The element model displayed in Figure 3 is consistent, which implies that the same shape functions are used to develop all the terms in the equation of motion for the element.
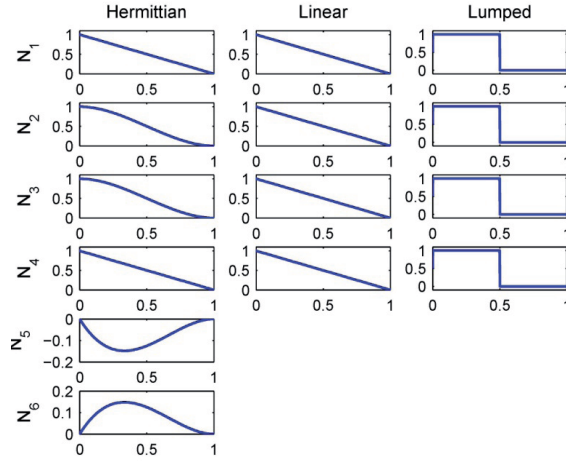
Figure 4: Three types of shape functions used in this paper. The shape functions in the first column are the ones used to obtain the mass and stiffness matrix. The two other columns contain shape functions that have been used to obtain the coefficients related to the self-excited forces if the Hermittian shape functions have not been used.

7

The shape functions often used to develop the equation of motion for beam elements related to the degrees of freedom in the left node of the element are displayed in the left column in Figure 4. The number of degrees of freedom necessary to model the time history-dependent part of the self-excited forces can be effectively reduced by simplifying the displacement field defined in Eq.(8). If the displacements along the element are assumed to be given only by the displacement degrees of freedom in addition to the torsional degree of freedom in each node, the number of degrees of freedom for the example above will become $N_{dof} = 12 + 18 \cdot 2 = 48$. This assumption implies that a linear variation along the element, as displayed in column 2 in Figure 4 or a lumped variation as displayed in column 3 in Figure 4, can be modelled. The aerodynamic degrees of freedom must be taken into account when the system of equations for the global model is established. The displacements at a node that two beam elements have in common are equal. When the aerodynamic degrees of freedom displayed in Figure 3 and defined in Eq.(15) are considered, it is seen that if the two neighbour elements have the same aerodynamic properties, the degrees of freedom will have the same values for both elements. This implies that the commonly applied assembly technique may be used for the aerodynamic degrees of freedom related to the self-excited forces.

3   Numerical results and verification

The simply supported beam shown in Figure 5 is used as a benchmark in the following case study. The properties of the beam are taken such that the beam represents an idealized model of the Hardanger Bridge [6]. The length of the beam L is taken as 1310 m, and the width B is assumed to be 18.3 m. The distributed mass is taken as $m = 12820 \, \text{kg/m}$, and the moment of inertia about the longitudinal axis is assumed $I_P = 426000 \, \text{kgm}^2/\text{m}$. The elastic properties are taken as $EA = 10^{11} \, N$, $EI_y = 3.9 \cdot 10^{14} \, Nm^2$, $EI_z = 6.2 \cdot 10^{13} \, Nm^2$, $GI_x = 3.6 \cdot 10^{11} \, Nm^2$, where E is the modulus of elasticity; G is the shear modulus; A is the cross sectional area, and I_n is the second moment of area about the n axis, where $n \in \{y, z\}$. The undamped horizontal, vertical and torsional vibration modes are given by:

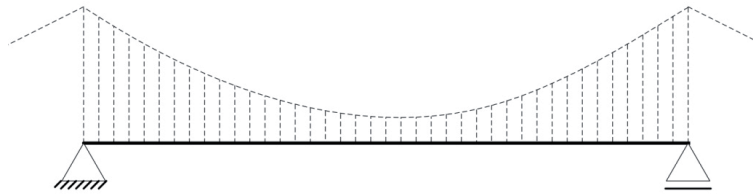$$\phi_m(x) = \sin(\frac{n\pi}{L} x) \qquad (19)$$

Figure 5: Idealized model of the Hardanger Bridge. The mass and stiffness properties have been taken such that the natural frequencies of the first horizontal, vertical and torsional vibration modes correspond to those of the Hardanger Bridge. The length of the beam is assumed to be 1310 m.

Table 1: Natural frequencies and damping ratios for the five first horizontal (H), vertical (V), and torsional (T) vibration modes of the idealized model of the Hardanger Bridge.

Mode:	Type:	Frequency ω rad/s	Damping ratio ξ
1	H	0,40	0,005
2	V	1,00	0,004
3	H	1,60	0,004
4	T	2,20	0,005
5	H	3,60	0,008
6	V	4,00	0,008
7	T	4,40	0,009
8	H	6,41	0,013
9	T	6,60	0,013
10	T	8,80	0,018
11	V	9,01	0,018
12	H	10,01	0,020
13	T	11,01	0,022
14	V	16,02	0,032
15	V	25,03	0,050

Here, $m \in \{y,z,\Theta\}$, $n \in \{1,2,3\ldots\}$. The natural frequencies and damping ratios of the first five horizontal, vertical and torsional vibration modes are given in Table 1. The mass and stiffness matrices of the elements are obtained using Euler-Bernoulli beam theory [32, 33]. This implies that the shape functions for the structural element are third degree Hermittian polynomials, which have been plotted in the left column in Figure 4. Four different elements have been developed and tested (see Table 2). Element 1 uses the Hermittian shape functions to obtain the aerodynamic elemental matrices $\mathbf{K}_{ae}$, $\mathbf{C}_{ae}$ and $\mathbf{Q}$. For element 2, a linear approximation has been used to develop $\mathbf{Q}$, and for element 3 a linear approximation has been used to develop $\mathbf{K}_{ae}$, $\mathbf{C}_{ae}$ and $\mathbf{Q}$, while a lumped approach has been used to develop $\mathbf{K}_{ae}$, $\mathbf{C}_{ae}$ and $\mathbf{Q}$ in the case of element 4. The approximation introduced to develop element 4 actually indicates that the self-excited forces are lumped in the nodal points at each element end. As can be seen in Figure 4 the displacements along half the element length are then assumed to be equal to the response at the corresponding node.

The aerodynamic properties of the cross section of the Hardanger Bridge displayed in Figure 1 have been assumed in the current study. The experimental results of the

Table 2: The four elements tested in this paper. HP stands for Hermittian polynomials; LIN represents linear shape functions, while LUMP implies that the self-excited forces have been "lumped" to each element end. Rayleigh damping has been used to represent still-air damping.

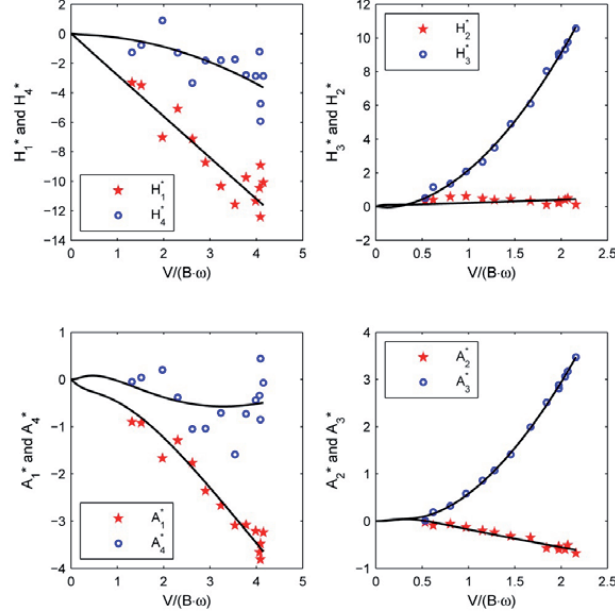| Element	1	2	3	4
Mass and stiffness matrices	HP	HP	HP	HP
Aerodynamic mass and stiffness matrices	HP	HP	LIN	LUMP
Additional state variables	HP	LIN	LIN	LUMP

Figure 6: Curve fits of the rational functions defined in Eq.(5) to the experimentally determined aerodynamic derivatives. The wind tunnel data, marked by circles and dots, are from [35].

aerodynamic derivatives have been obtained by free vibration tests with a scaled section model [35]. Curve fits of the rational functions to the experimental data of the aerodynamic derivatives using four exponential filters are displayed in Figure 6. Since aerodynamic derivatives related to horizontal motion are not available, quasi-steady values have been assumed for the following aerodynamic derivatives:

$$P_1^* = -2\bar{C}_D \frac{D}{B}\left(\frac{1}{K}\right) \qquad P_5^* = \left(\bar{C}_L - C_D' \frac{D}{B}\right)\left(\frac{1}{K}\right) \qquad P_3^* = C_D' \frac{D}{B}\left(\frac{1}{K}\right)^2$$

$$H_5^* = -2\bar{C}_L\left(\frac{1}{K}\right) \quad A_5^* = -2\bar{C}_M\left(\frac{1}{K}\right) \quad P_2^* = P_4^* = P_6^* = H_6^* = A_6^* = 0 \tag{20}$$

where the static force coefficients from [35] are $\bar{C}_D = 0.70$, $C_D' = 0$, $\bar{C}_L = -0.25$, $C_L' = 2.4$, $\bar{C}_M = 0.01$ and $C_M' = 0.74$. For simplicity the still-air damping of the structure has been modelled by Rayleigh damping, assuming a still-air damping matrix given by $\mathbf{C} = 10^{-4}\left(34 \cdot \mathbf{M} + 40 \cdot \mathbf{K}\right)$.

3.1 Stability limit
The stability of the aeroelastic system can be studied by considering its eigenvalues, (see for instance [6, 7, 36, 37]). The eigenvalue problem may be solved by linearization of the aeroelastic system defined below

10

$$\begin{bmatrix} \mathbf{M} & \mathbf{0} \\ \mathbf{0} & \mathbf{0} \end{bmatrix}\begin{bmatrix} \ddot{\mathbf{V}} \\ \ddot{\mathbf{X}} \end{bmatrix} + \begin{bmatrix} (\mathbf{C}-\mathbf{C}_{ae}) & \mathbf{0} \\ \mathbf{A} & \mathbf{B} \end{bmatrix}\begin{bmatrix} \dot{\mathbf{V}} \\ \dot{\mathbf{X}} \end{bmatrix} + \begin{bmatrix} (\mathbf{K}-\mathbf{K}_{ae}) & \mathbf{Q} \\ \mathbf{0} & \mathbf{D} \end{bmatrix}\begin{bmatrix} \mathbf{V} \\ \mathbf{X} \end{bmatrix} = \begin{bmatrix} \mathbf{P} \\ \mathbf{0} \end{bmatrix} \tag{21}$$

$$\begin{bmatrix} \dot{\mathbf{V}} \\ \ddot{\mathbf{V}} \\ \dot{\mathbf{X}} \end{bmatrix} + \begin{bmatrix} \mathbf{0} & -\mathbf{I} & \mathbf{0} \\ \mathbf{M}^{-1}(\mathbf{K}-\mathbf{K}_{ae}) & \mathbf{M}^{-1}(\mathbf{C}-\mathbf{C}_{ae}) & \mathbf{M}^{-1}\mathbf{Q} \\ \mathbf{0} & \mathbf{B}^{-1}\mathbf{A} & \mathbf{B}^{-1}\mathbf{D} \end{bmatrix}\begin{bmatrix} \mathbf{V} \\ \dot{\mathbf{V}} \\ \mathbf{X} \end{bmatrix} = \begin{bmatrix} \mathbf{0} \\ \mathbf{M}^{-1}\mathbf{P} \\ \mathbf{0} \end{bmatrix} \tag{22}$$

The eigenvalues of the system will in general be of the form $S_n = \mu_n + \omega_n i$. A zero imaginary part, $\omega_n = 0$, implies that the response is non-periodic in nature, while a nonzero imaginary part indicates that the response has an oscillatory nature. A positive real part implies that the system is unstable, while a negative real part implies that the system is stable. This implies that the flutter stability limit can be defined as the velocity providing a zero real part for one of the eigenvalues.

The stability limit is evaluated using varying element lengths. Each finer mesh is a regular subdivision of the preceding mesh, implying that the nodes of the coarser mesh are preserved while new nodes and elements are added. The calculated stability limits provided by the element models presented in Table 2, considering different element lengths, have been plotted in Figure 7. As can be seen from the results, all the elements, except element 4, overestimate the stability limit when a coarse mesh is used. This is because few elements result in an overestimated torsional frequency and thus a larger stability limit. However, the results converge to the same solution when the number of elements is increased, and the converged solution corresponds very well with the results obtained using the still-air vibration modes as generalized coordinates to characterize the aeroelastic system. A result that might seem surprising is that the lumped formulation (element 4) seems to provide results that are more accurate than the more comprehensive alternatives where more aerodynamic degrees of freedom are used to model the self-excited forces. The stability limit obtained using element 4 does not provide monotonic convergence. The stability limit is underestimated using a very
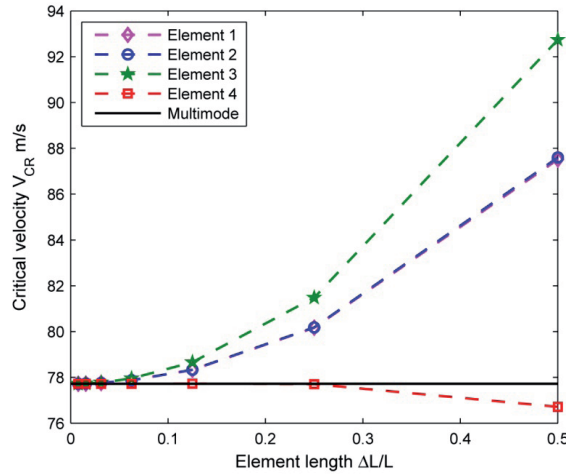

Figure 7: Calculated critical velocities considering different element formulations and element lengths.

11

coarse mesh (only two or four elements), while it is overestimated using denser element nets (eight or sixteen elements). This is because the lumped formulation overestimates the self-excited forces, and the torsional stiffness is overestimated using a coarse mesh, which implies that the two inaccuracies partially cancel each other out. This implies that it is possible that the lumped alternative will underestimate or overestimate the stability limit for some combinations of aerodynamic and structural properties. However, the result will converge to the "exact" solution when the number of elements is increased. Element 3 provides the results with lowest accuracy. This is because the self-excited forces are underestimated. Elements 1 and 2 provide almost the same results, implying that the additional aerodynamic degrees of freedom applied in element 1, compared with element 2, may seem unnecessary. However, this will not be the case if the time-dependent part of the self-excited forces is larger relative to the quasi-steady part than the case tested in this paper.

The critical frequencies obtained considering different element lengths have been plotted in Figure 8. As can be seen from the results, the critical frequency is overestimated for all the cases considered, except element 4, which underestimates the critical frequency using only two elements. However, element 4 provides results of best accuracy for the critical frequencies using a coarse mesh. The critical frequencies provided by element 1 and 2 are almost equally accurate. Elements 3 and 4 also provide results of almost equal accuracy. It can be concluded that all the alternatives tested in this section provide critical velocities and frequencies of good accuracy using rather few elements to model the structure. The converged critical velocities and frequencies correspond very well to the results obtained using the first 15 still-air vibration modes as generalized coordinates. The in-wind frequencies corresponding to the first horizontal, vertical and torsional still-air vibration modes provided using element 2 are shown in Figure 9. The structure has been modelled using 64 elements. The results obtained using the first five horizontal, vertical and torsional vibration modes as generalized coordinates are also given in the figure. Likewise, the total damping of the
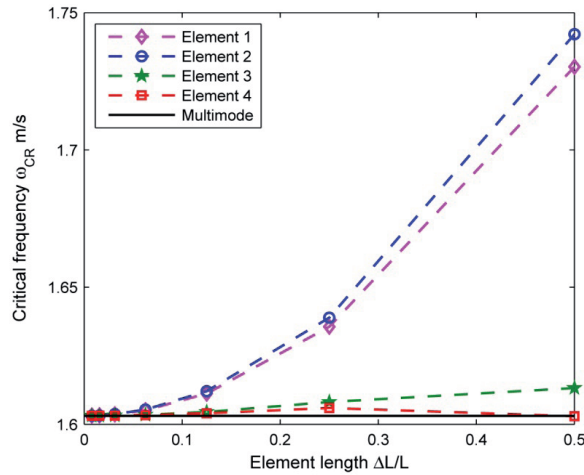

Figure 8: Calculated critical frequencies considering different element formulations and element lengths.
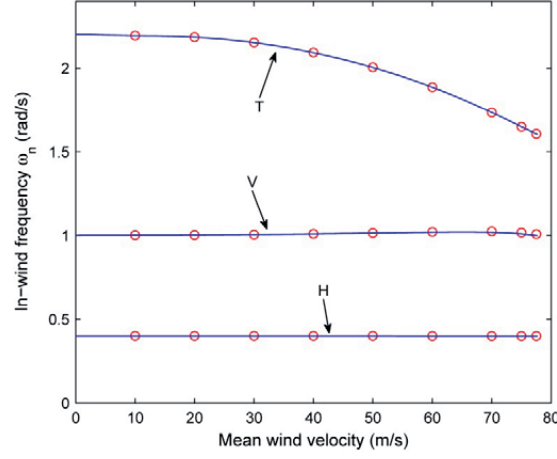
12

Figure 9: The in-wind frequencies of the vibration modes corresponding to the first horizontal (H), vertical (V) and torsional (T) still-air vibration modes. The circles represent results obtained by the finite element solution (Element 2), while the solid lines represent results obtained using the 15 first still-air vibration modes as generalized coordinates to characterize the aeroelastic system.
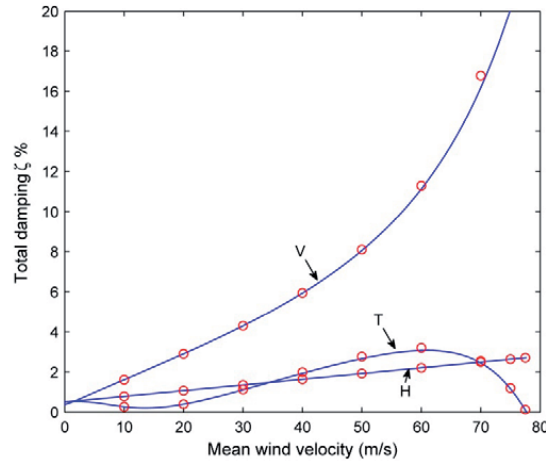

Figure 10: Total damping for the vibration modes corresponding to the first horizontal (H), vertical (V) and torsional (T) still-air vibration modes. The circles represent results obtained by the finite element solution (Element 2) while the solid lines are the solution obtained using the first 15 still-air vibration modes as generalized coordinates.

vibration modes are displayed in Figure 10. As can be seen from the figures, the results obtained using the finite element approach correspond very well to the results obtained by the multimode approach. Excellent results are obtained for the in-wind frequencies corresponding to the horizontal, vertical and torsional vibration modes from still air. The total damping ratios of the first horizontal, vertical and torsional vibration modes provided by the element model correspond very well to the results obtained using still-air vibration modes from still air as generalized coordinates. However, some discrepancies can be seen for the vertical branch close to the stability limit.

13

3.2 Wind-induced buffeting response

The cross-spectral densities of the wind field are assumed to be given by:

$$S_{uu}^+(\omega) = \frac{40.58Vz\kappa}{\left(1+9.74\,\omega z/V\right)^{5/3}}\exp(-1.4\frac{\Delta x\omega}{V}),$$

$$S_{ww}^+(\omega) = \frac{0.82Vz\kappa}{\left(1+0.79\,\omega z/V\right)^{5/3}}\exp(-\frac{\Delta x\omega}{V})$$

$$S_{uw}^+(\omega) = -\frac{2.23Vz\kappa}{\left(1+1.67\,\omega z/V\right)^{7/3}}\exp(-\frac{\Delta x\omega}{V})$$

(23)

Here, $S_{uu}^+(\omega)$ is the cross-spectral density of the along-wind component $u(t)$ at two points along the beam with separation Δx; likewise $S_{ww}^+(\omega)$ is the cross-spectral density of the vertical across-wind component $w(t)$, while $S_{uw}^+(\omega)$ is the cross-spectral density of $u(t)$ and w(t) at the two points. The height above ground is denoted z and is taken as 50 m, while κ is the roughness coefficient at the site, which is assumed to be 0.0031. Time series of the fluctuating turbulence components at 101 points along the beam are obtained by Monte Carlo simulations [22, 38, 39], with a cut-off frequency of ω_u=5 rad/s and $\Delta\omega$=0.0002 rad/s. The time series at point m can then be obtained by

$$x_m(t) = \sqrt{2\Delta\omega}\,\mathrm{Re}\left(\sum_{l=1}^{m}\sum_{k=1}^{N}L_{ml}(\omega_k)\exp\left(i(\omega_k+\phi_{lk})\right)\right)$$

(24)

Here, $L_{ml}(\omega_k)$ denotes the elements of the lower triangular matrix obtained by factorising the cross-spectral density matrix according to the relation

$$\mathbf{S}(\omega_k) = \mathbf{L}(\omega_k)\mathbf{L}^*(\omega_k)$$

(25)

where the elements in $\mathbf{S}(\omega_k)$ represent the cross-spectral densities of the fluctuating velocity components at the 101 points along the girder. An example of simulated time series is shown in Figure 11. The average co-spectral densities of the turbulence components at two points 131m apart, estimated from 20 time series of length 6000s, are shown in Figure 12 together with the target spectral density. As can be seen from the figure, the simulated time series corresponds very well to the assumed spectral densities given in Eq.(23). A contour plot of the fluctuating velocities in the along direction $V+u$, where V is the mean value, and u is the fluctuating component, is shown in Figure 13. The mean wind velocity is 40 m/s. Likewise, the fluctuating vertical turbulence component, w, is displayed in Figure 14. As can be seen from the figures, the 101 points represent the velocity fluctuations along the girder rather well. As expected, the along-wind component is dominated by harmonic components with low frequencies, while the harmonic components with a slightly higher frequency have a stronger influence on the vertical fluctuations. Since the main focus in the current study is modelling of the self-excited forces, the cross sectional admittance functions' influence on the response has been assumed negligible. This implies that the buffeting action at point n is given by [4, 5, 40]:
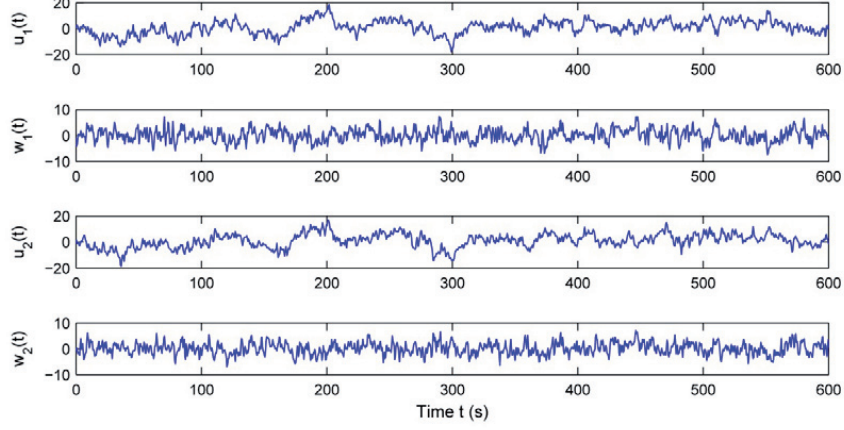
14

Figure 11: Simulated fluctuating wind velocities at two points 131 m apart; u is the along-wind turbulence component, while w is the vertical turbulence component.
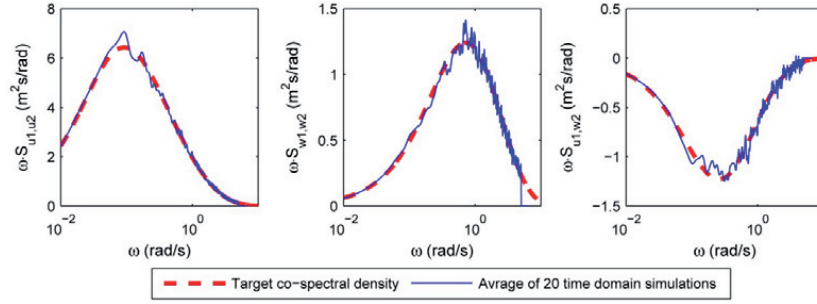

Figure 12: Comparison of the average co-spectral density of 20 simulated times series and the target co-spectral densities at two points with a separation of 1310m. The mean wind velocity is 40 m/s. Left figure: The co-spectral density of the u component. Middle figure: The co-spectral density of the w components. Right figure: The co-spectral density of the u and w components.

$$\mathbf{q}_{Buff} = \begin{bmatrix} q_x & q_y & q_z & q_\theta \end{bmatrix}^T$$

$$\mathbf{q}_{Buff}(x_n,t) = \frac{\rho V B}{2} \begin{bmatrix} 0 & 0 \\ 2(D/B)\overline{C}_D & (D/B)C'_D - \overline{C}_L \\ 2\overline{C}_L & C'_L + (D/B)\overline{C}_D \\ 2B\overline{C}_M & BC'_M \end{bmatrix} \begin{bmatrix} u(t) \\ w(t) \end{bmatrix} \tag{26}$$

Here, q_n $n \in \{x, y, z, \theta\}$ is the buffeting action in the coordinate system of the element; D is the height of the girder, and B symbolizes the width of the girder. C_n, $n \in \{D, L, M\}$ symbolizes the drag lift and overturning moment force coefficient, where a bar represents the mean value, while a prime denotes a derivative with respect to the angle
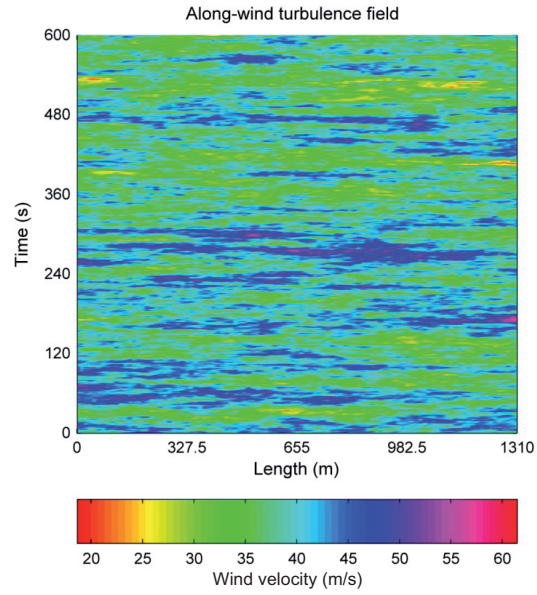
15

Figure 13: Contour plot of the along-wind component, $V+u$, at a mean wind velocity of 40 m/s. Here, V is the mean wind velocity, while u is the fluctuating component.
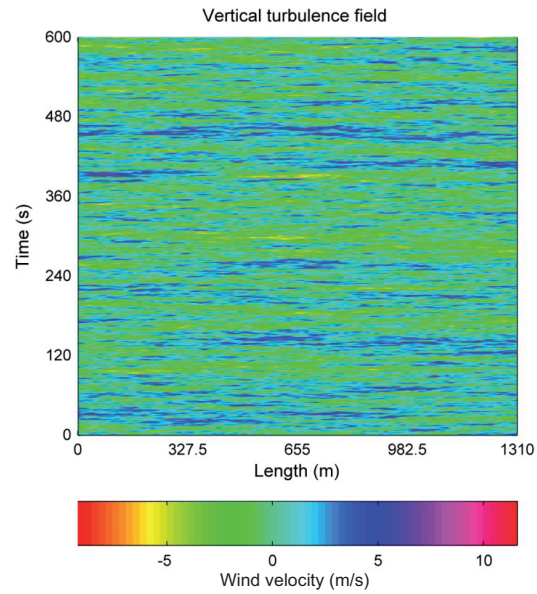

Figure 14: Contour plot of the vertical turbulence component, w, at a mean wind velocity of 40 m/s.

16

of attack. The nodal load vector for the element may then be obtained as:

$$\mathbf{P}(t) = \int_0^L \mathbf{N}^T(x)\mathbf{q}(x,t)dx \tag{27}$$

Since the fluctuating velocities are only known at discrete points along the girder, the distributed loading on half the distance between the points is assumed uniform and equal to the value at the points where the time series have been obtained. The response may be obtained by solving Eq. (22) or (21) by numerical integration. In this study the response will be obtained using the well-known Newmark's method, applying $\gamma = 0.5$ and $\beta = 1/4$; see [33, 41] for further details. Since the matrix related to the double derivative of the dependent variables, $\ddot{v}_n$ and $\ddot{X}_n$, is singular, the initial double derivatives cannot be calculated as usual. This problem may be circumvented by taking the derivative of Eq.(15) twice instead of once. The dynamic equilibrium conditions for the aeroelastic element may then be written as:

$$\begin{bmatrix} \mathbf{M} & \mathbf{0} \\ \mathbf{A} & \mathbf{B} \end{bmatrix}\begin{bmatrix} \ddot{\mathbf{v}} \\ \ddot{\mathbf{X}} \end{bmatrix} + \begin{bmatrix} (\mathbf{C}-\mathbf{C}_{ae}) & \mathbf{0} \\ \mathbf{0} & \mathbf{D} \end{bmatrix}\begin{bmatrix} \dot{\mathbf{v}} \\ \dot{\mathbf{X}} \end{bmatrix} + \begin{bmatrix} (\mathbf{K}-\mathbf{K}_{ae}) & \mathbf{Q} \\ \mathbf{0} & \mathbf{0} \end{bmatrix}\begin{bmatrix} \mathbf{v} \\ \mathbf{X} \end{bmatrix} = \begin{bmatrix} \mathbf{P} \\ \mathbf{0} \end{bmatrix} \tag{28}$$

The system of equations generally has a different structure than usual in structural dynamics analysis, and it is therefore not certain that sufficiently accurate results are obtained by the commonly used integration schemes. The free vibration response at the mid-span of the bridge at a mean wind velocity equal to the stability limit and a mean wind velocity slightly higher than the stability limit is displayed in Figure 15. As can be seen from the figure, the structure behaves as expected. At the stability limit the response seems to be undamped, while negative damping is clearly present when the
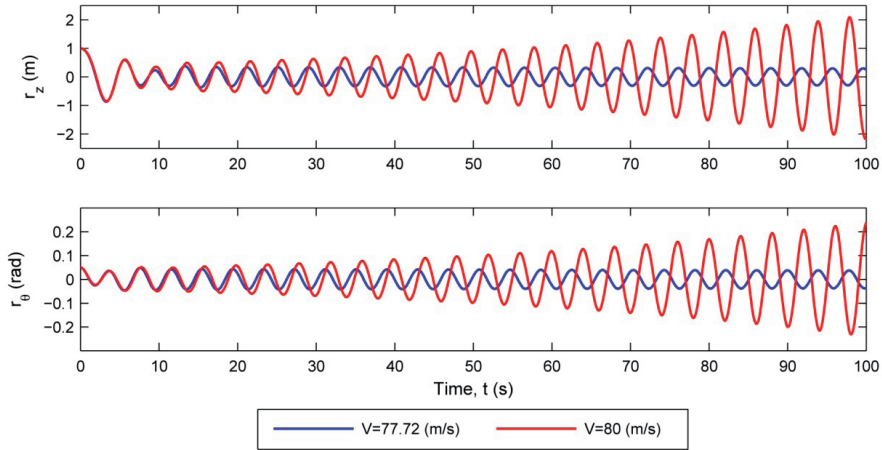

Figure 15: Free vibration response at the mid-span of the bridge at the stability limit (*V*=77.72 m/s) and slightly higher than the stability limit (*V*=80 m/s). 20 finite elements (Element 2) have been used in the analysis.

mean wind velocity is higher than the stability limit. It is also seen that the vertical and torsional motion of the structure is close to 180 degrees out of phase in the flutter motion. The horizontal, vertical and torsional buffeting response at the mid-span of the beam at a mean wind velocity of 40 m/s is shown in Figure 16. Element 2 has been used in the calculations, and the structure has been modelled using 20 elements. The mean values of the standard deviations of 20 response time series at each considered mean wind velocity are shown in Figure 17 together with results obtained in the frequency domain, using the vibration modes presented in Table 1 as generalized coordinates. As can be seen from the results, the finite element formulation developed in this paper provides results that correspond very well with the frequency domain results. The response is accurately captured for all the mean wind velocities considered. The spectral densities estimated as the mean value of the spectral density of 20 time series of the horizontal, vertical and torsional response at the mid-span at a mean wind velocity of 40 m/s are shown in Figure 18 together with the multimode frequency domain results. As can be seen from the results, the spectral density corresponds very well to the spectral density obtained in the frequency domain in the entire frequency range for all the response components. This implies that the properties of the wind field have been captured accurately for the relevant frequency range by the Monte Carlo simulations, and that the finite element model suggested in this paper provides an accurate representation of the self-excited forces. The co-spectral densities of the response components are shown in Figure 19. The co-spectral density of the horizontal and vertical response estimated from the time-domain simulations corresponds very well to the results obtained by the multimode approach in the frequency domain. The co-spectral density of the horizontal and torsional response obtained from the times series corresponds well to the frequency domain results for most of the frequency range, except for the peak at about 0.4 rad/s. The discrepancy observed here may result from the covariance of the horizontal and torsional response being rather low, resulting in uncertainty in the co-spectral estimate. The co-spectral density of the vertical and
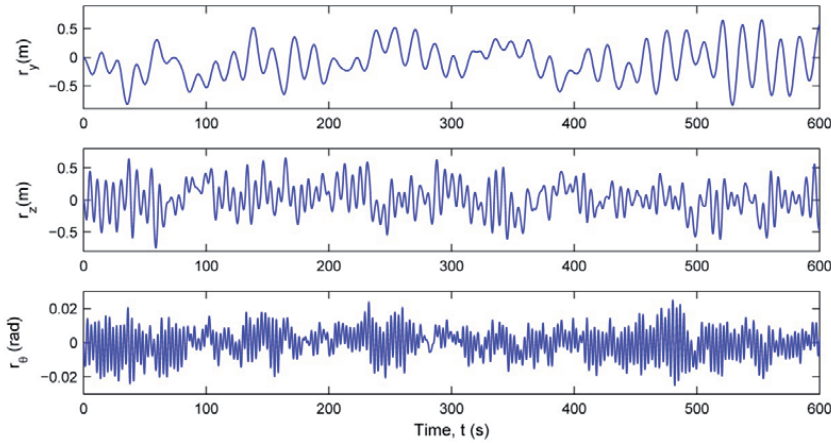

Figure 16: Wind-induced dynamic response at the mid-span of the beam displayed in Figure 5. Upper figure: Horizontal response. Middle figure: Vertical response. Lower figure: Torsional response. The mean wind velocity is V=40 m/s. The length of the obtained time series is 6000 s, but only the first 600 s are displayed in this figure.
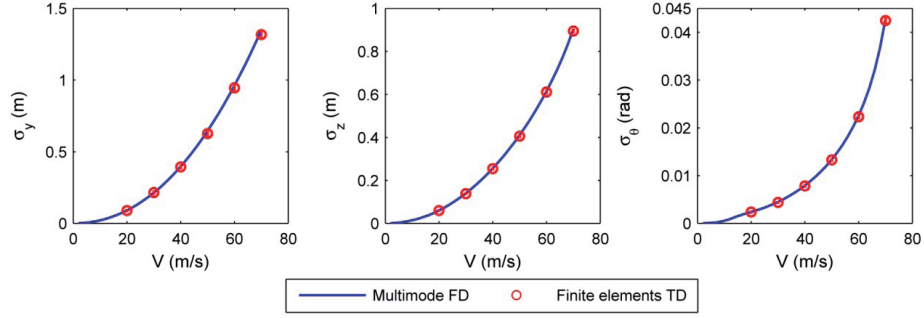
18

Figure 17: Comparison of the standard deviation of the wind-induced dynamic response obtained in the frequency domain, using still-air vibration modes as generalized coordinates (MFD), and in the time domain, using the finite element formulation introduced in this article. Left figure: Horizontal response. Middle figure: Vertical response. Right figure: Torsional response.
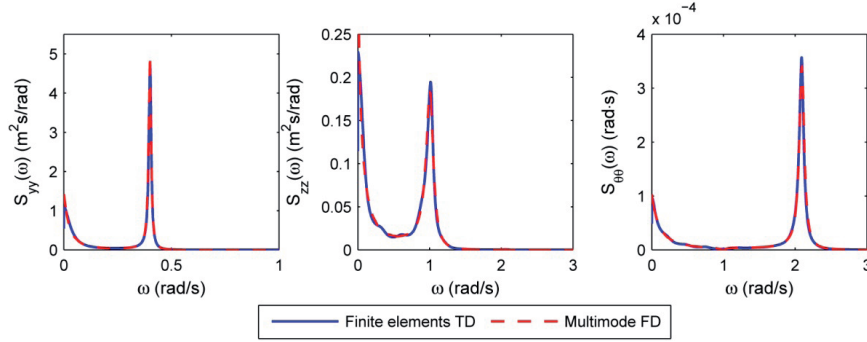

Figure 18 Spectral densities of the response components at a mean wind velocity of V=40 m/s. Left figure: Spectral density of the horizontal response. Middle figure: Spectral density of the vertical response. Right figure: Spectral density of the torsional response.
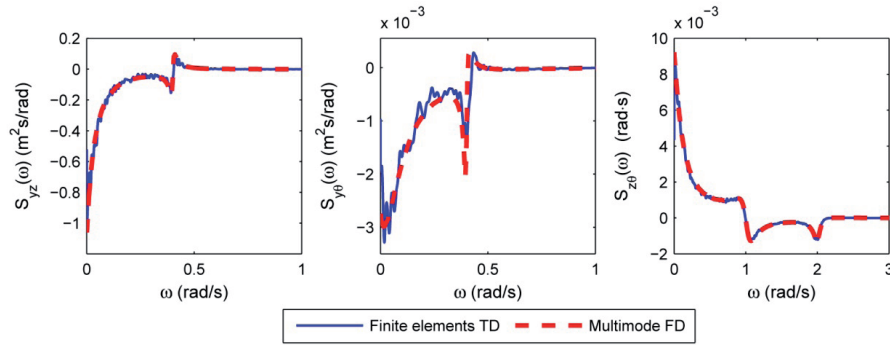

Figure 19: Co-spectral density of the response components at the mid-span of the bridge at a mean wind velocity of 50 m/s. Left figure: Co-spectral density of the horizontal and vertical response. Middle figure: Co-spectral density of the horizontal and torsional response. Right figure: Co-spectral density of the vertical and torsional response.

torsional response is accurately captured for the entire frequency range; both the peak corresponding to the vertical motion at 1 rad/s and the peak corresponding to torsional motion at 2.2 rad/s are accurately captured.

4   Concluding remarks

Four different aeroelastic beam elements for assessment of the buffeting response and flutter stability limit of cable-supported bridges have been developed and tested in this paper. All the alternatives tested have provided results of good accuracy, compared with a traditional multimode approach, where selected still-air vibration modes are used to characterize the aeroelastic system. The stability limit was overestimated for all the element models, except the lumped alternative, when using a coarse mesh, and all the element models tested provided the same stability limit when the number of elements was increased. The converged solution corresponded very well to the stability limit provided by the multimode approach. The consistent model provided results of very good accuracy, but the lumped formulation, where the displacement along half the element length is assumed equal to the displacement at the node for the self-excited forces, seems to provide more accurate results when using a coarse mesh. However, the results provided by the consistent formulation are more reliable than the results provided by the lumped formulation since the lumped formulation overestimates the self-excited forces, and this reduces the effect of a higher torsional frequency, which will increase the predicted critical velocity when using a coarse mesh. The predicted buffeting response corresponded very well to the results obtained in the frequency domain using rather few beam elements. The spectral densities of the horizontal vertical and torsional response corresponded very well with results obtained by the multimode approach in the frequency domain for the entire frequency range. It can be concluded that the elements developed in this paper perform satisfactorily for all the cases considered, and that the modelling technique is convenient when modelling structural nonlinearities in buffeting response analysis of cable-supported bridges.

5   Acknowledgements

6   References

[1]   Dyrbye C, Hansen SO. Wind loads on structures. Chichester: Wiley; 1997.

[2]   Holmes JD. Wind loading of structures. London: Taylor & Francis; 2007.

[3]   Simiu E, Scanlan RH. Wind effects on structures fundamentals and applications to design. 3rd ed. New York: Wiley; 1996.

[4]   Simiu EE, Miyata T. Design of buildings and bridges for wind : a practical guide for ASCE-7 standard users and designers of special structures 2006.

[5]   Strømmen EN. Theory of bridge aerodynamics. Berlin: Springer; 2006.

[6]   Øiseth O, Rönnquist A, Sigbjörnsson R. Simplified prediction of wind-induced response and stability limit of slender long-span suspension bridges, based on modified quasi-steady theory: A case study. Journal of Wind Engineering and Industrial Aerodynamics. 2010;98:730-41.

[7] Øiseth O, Sigbjörnsson R. An alternative analytical approach to prediction of flutter stability limits of cable supported bridges. Journal of Sound and Vibration. 2011;330:2784-800.

[8] Scanlan RH, Tomko JJ. Airfoil and bridge deck flutter derivatives. Journal of the Engineering Mechanics Division. 1971;97:1717-37.

[9] Katsuchi H, Jones NP, Scanlan RH, Akiyama H. Multi-mode flutter and buffeting analysis of the Akashi-Kaikyo bridge. Journal of Wind Engineering and Industrial Aerodynamics. 1998;77-8:431-41.

[10] Jain A, Jones NP, Scanlan RH. Coupled flutter and buffeting analysis of long-span bridges. Journal of Structural Engineering-Asce. 1996;122:716-25.

[11] Katsuchi H, Jones NP, Scanlan RH. Multimode coupled flutter and buffeting analysis of the Akashi-Kaikyo bridge. Journal of Structural Engineering-Asce. 1999;125:60-70.

[12] Jain A, Jones NP, Scanlan RH. Coupled aeroelastic and aerodynamic response analysis of long-span bridges. Journal of Wind Engineering and Industrial Aerodynamics. 1996;60:69-80.

[13] Salvatori L, Borri C. Frequency- and time-domain methods for the numerical modeling of full-bridge aeroelasticity. Computers & Structures. 2007;85:675-87.

[14] Costa C, Borri C. Application of indicial functions in bridge deck aeroelasticity. Journal of Wind Engineering and Industrial Aerodynamics. 2006;94:859-81.

[15] Caracoglia L, Jones NP. Time domain vs. frequency domain characterization of aeroelastic forces for bridge deck sections. Journal of Wind Engineering and Industrial Aerodynamics. 2003;91:371-402.

[16] Chen XZ, Matsumoto M, Kareem A. Time domain flutter and buffeting response analysis of bridges. Journal of Engineering Mechanics-Asce. 2000;126:7-16.

[17] Mishra SS, Kumar K, Krishna P. Multimode flutter of long-span cable-stayed bridge based on 18 experimental aeroelastic derivatives. Journal of Wind Engineering and Industrial Aerodynamics. 2008;96:83-102.

[18] Øiseth O, Rönnquist A, Sigbjörnsson R. Time domain modeling of self-excited aerodynamic forces for cable-supported bridges: A comparative study. Computers & Structures. 2011;In Press, Corrected Proof.

[19] Salvatori L, Spinelli P. Effects of structural nonlinearity and along-span wind coherence on suspension bridge aerodynamics: Some numerical simulation results. Journal of Wind Engineering and Industrial Aerodynamics. 2006;94:415-30.

[20] Petrini F, Giuliano F, Bontempi F. Comparison of time domain techniques for the evaluation of the response and the stability in long span suspension bridges. Computers and Structures. 2007;85:1032-48.

[21] Su C, Fan X, He T. Wind-induced vibration analysis of a cable-stayed bridge during erection by a modified time-domain method. Journal of Sound and Vibration. 2007;303:330-42.

[22] Aas-Jakobsen K, Strommen E. Time domain buffeting response calculations of slender structures. Journal of Wind Engineering and Industrial Aerodynamics. 2001;89:341-64.

[23] Kim HK, Shinozuka M, Chang SP. Geometrically nonlinear buffeting response of a cable-stayed bridge. Journal of Engineering Mechanics. 2004;130:848-57.

[24] Matheson MJ, Holmes JD. Simulation of the dynamic response of transmission lines in strong winds. Engineering Structures. 1981;3:105-10.

[25] Hua XG, Chen ZQ. Full-order and multimode flutter analysis using ANSYS. Finite Elements in Analysis and Design. 2008;44:537-51.

[26] Hua XG, Chen ZQ, Ni YQ, Ko JM. Flutter analysis of long-span bridges using ANSYS. Wind and Structures, An International Journal. 2007;10:61-82.

[27] Ge YJ, Tanaka H. Aerodynamic flutter analysis of cable-supported bridges by multi-mode and full-mode approaches. Journal of Wind Engineering and Industrial Aerodynamics. 2000;86:123-53.

[28] Diana G, Resta F, Rocchi D. A new numerical approach to reproduce bridge aerodynamic non-linearities in time domain. Journal of Wind Engineering and Industrial Aerodynamics. 2008;96:1871-84.

[29] Diana G, Rocchi D, Argentini T, Muggiasca S. Aerodynamic instability of a bridge deck section model: Linear and nonlinear approach to force modeling. Journal of Wind Engineering and Industrial Aerodynamics. 2010;98:363-74.

[30] Bucher CG, Lin YK. Stochastic stability of bridges considering coupled modes. Journal of Engineering Mechanics-Asce. 1988;114:2055-71.

[31] Borri C, Costa C, Zahlten W. Non-stationary flow forces for the numerical simulation of aeroelastic instability of bridge decks. Computers & Structures. 2002;80:1071-9.

[32] Cook RD. Concepts and applications of finite element analysis. New York: Wiley; 2002.

[33] Zienkiewicz OC, Taylor RL. The finite element method. 5th ed. Oxford: Butterworth-Heinemann; 2000.

[34] Humar JL. Dynamics of structures. 2nd ed. Lisse: Balkema; 2002.

[35] Hansen SO, Lollesgaard M, Rex S, Jakobsen JB, Hansen EH. The Hardanger Bridge: Static and dynamic wind tunnel tests with a section model. Copenhagen: Svend Ole Hansen ApS; 2006.

[36] Jakobsen JB, Hjorth-Hansen E. Arne Selberg's formula for flutter speed in light of multimodal flutter analysis. Proceedings of Twelfth international confrence on wind engineering Cairns, Australia2007.

[37] Agar TJA. Aerodynamic flutter analysis of suspension bridges by a modal technique. Engineering Structures. 1989;11:75-82.

[38] Shinozuka M. Monte Carlo solution of structural dynamics. Computers and Structures. 1972;2:855-74.

[39] Shinozuka M, Jan CM. Digital simulation of random processes and its applications. Journal of Sound and Vibration. 1972;25:111-28.

[40] Davenport AG. Response of slender line like structures to a gusty wind. The institution of civil engineers. 1962;23:389-408.

[41] Chopra AK. Dynamics of structures: theory and applications to earthquake engineering. Upper Saddle River, N.J.: Pearson Prentice Hall; 2007.

Appendix A

In this appendix the matrices used to obtain the equations of motions is presented. The matrices introduced in Eq.(11) are defined by

$$
\mathbf{A}_1 = \begin{bmatrix} 0 & 0 & 0 & 0 \\ 0 & A_1^{(yy)} & A_1^{(yz)} & BA_1^{(y\theta)} \\ 0 & A_1^{(zy)} & A_1^{(zz)} & BA_1^{(z\theta)} \\ 0 & BA_1^{(\theta y)} & BA_1^{(\theta z)} & B^2 A_1^{(\theta\theta)} \end{bmatrix}, \qquad
\mathbf{A}_2 = \begin{bmatrix} 0 & 0 & 0 & 0 \\ 0 & A_2^{(yy)} & A_2^{(yz)} & BA_2^{(y\theta)} \\ 0 & A_2^{(zy)} & A_2^{(zz)} & BA_2^{(z\theta)} \\ 0 & BA_2^{(\theta y)} & BA_2^{(\theta z)} & B^2 A_2^{(\theta\theta)} \end{bmatrix}, \quad (29)
$$

$$
\mathbf{A}_l = \begin{bmatrix} 0 & 0 & 0 & 0 \\ 0 & A_{l+3}^{(yy)} & A_{l+3}^{(yz)} & BA_{l+3}^{(y\theta)} \\ 0 & A_{l+3}^{(zy)} & A_{l+3}^{(zz)} & BA_{l+3}^{(z\theta)} \\ 0 & BA_{l+3}^{(\theta y)} & BA_{l+3}^{(\theta z)} & B^2 A_{l+3}^{(\theta\theta)} \end{bmatrix}, \qquad
\mathbf{\Phi} = \begin{bmatrix} 0 & 0 & 0 & 0 \\ 0 & \Phi^{(yy)} & \Phi^{(yz)} & B\Phi^{(y\theta)} \\ 0 & \Phi^{(zy)} & \Phi^{(zz)} & B\Phi^{(z\theta)} \\ 0 & B\Phi^{(\theta y)} & B\Phi^{(\theta z)} & B^2\Phi^{(\theta\theta)} \end{bmatrix} \quad (30)
$$

$$
\Phi^{(nm)} = \sum_{l=1}^{N} A_{l+3}^{(nm)} \left(r_m(t) - \frac{d_l^{(nm)}V}{B} \int_{-\infty}^{t} e^{\left(-\frac{d_l^{(nm)}V}{B}(t-\tau) \right)} r_m(\tau) d\tau \right) \quad (31)
$$

The matrix $\mathbf{W}$ introduced in Eq. (14) is given by

$$
\mathbf{W}_i = \frac{1}{2}\rho V^2 \int_0^L \begin{bmatrix} \mathbf{w}_{11} & \mathbf{w}_{12} \\ \mathbf{w}_{21} & \mathbf{w}_{22} \end{bmatrix} dx \quad (32)
$$

$$
\mathbf{W}_{11} = \begin{bmatrix}
0 & 0 & 0 & 0 & 0 & 0 & 0 & 0 & 0 & 0 & 0 & 0 & 0 & 0 & 0 \\
N_2^2 & 0 & 0 & N_2 N_3 & 0 & 0 & N_2 N_4 & 0 & 0 & N_2 N_5 & 0 & 0 & N_2 N_6 & 0 & 0 \\
0 & N_3 N_2 & 0 & 0 & N_3^2 & 0 & 0 & N_3 N_4 & 0 & 0 & N_3 N_5 & 0 & 0 & N_3 N_6 & 0 \\
0 & 0 & N_4 N_2 & 0 & 0 & N_4 N_3 & 0 & 0 & N_4^2 & 0 & 0 & N_4 N_5 & 0 & 0 & N_4 N_6 \\
0 & N_5 N_2 & 0 & 0 & N_5 N_3 & 0 & 0 & N_5 N_4 & 0 & 0 & N_5^2 & 0 & 0 & N_5 N_6 & 0 \\
N_2 N_6 & 0 & 0 & N_6 N_3 & 0 & 0 & N_6 N_4 & 0 & 0 & N_6 N_5 & 0 & 0 & N_6^2 & 0 & 0
\end{bmatrix} \quad (33)
$$

$$
\mathbf{W}_{12} = \begin{bmatrix}
0 & 0 & 0 & 0 & 0 & 0 & 0 & 0 & 0 & 0 & 0 & 0 & 0 & 0 & 0 \\
N_2 N_8 & 0 & 0 & N_2 N_9 & 0 & 0 & N_2 N_{10} & 0 & 0 & N_2 N_{11} & 0 & 0 & N_2 N_{12} & 0 & 0 \\
0 & N_3 N_8 & 0 & 0 & N_3 N_9 & 0 & 0 & N_3 N_{10} & 0 & 0 & N_3 N_{11} & 0 & 0 & N_3 N_{12} & 0 \\
0 & 0 & N_4 N_8 & 0 & 0 & N_4 N_9 & 0 & 0 & N_4 N_{10} & 0 & 0 & N_4 N_{11} & 0 & 0 & N_4 N_{12} \\
0 & N_5 N_8 & 0 & 0 & N_5 N_9 & 0 & 0 & N_5 N_{10} & 0 & 0 & N_5 N_{11} & 0 & 0 & N_5 N_{12} & 0 \\
N_6 N_8 & 0 & 0 & N_6 N_9 & 0 & 0 & N_6 N_{10} & 0 & 0 & N_6 N_{11} & 0 & 0 & N_6 N_{12} & 0 & 0
\end{bmatrix} \quad (34)
$$

$$
\mathbf{W}_{21} = \begin{bmatrix}
0 & 0 & 0 & 0 & 0 & 0 & 0 & 0 & 0 & 0 & 0 & 0 & 0 & 0 & 0 \\
N_2 N_8 & 0 & 0 & N_8 N_3 & 0 & 0 & N_8 N_4 & 0 & 0 & N_8 N_5 & 0 & 0 & N_6 N_8 & 0 & 0 \\
0 & N_9 N_2 & 0 & 0 & N_3 N_9 & 0 & 0 & N_9 N_4 & 0 & 0 & N_5 N_9 & 0 & 0 & N_9 N_6 & 0 \\
0 & 0 & N_{10} N_2 & 0 & 0 & N_{10} N_3 & 0 & 0 & N_{10} N_4 & 0 & 0 & N_{10} N_5 & 0 & 0 & N_{10} N_6 \\
0 & N_{11} N_2 & 0 & 0 & N_3 N_{11} & 0 & 0 & N_{11} N_4 & 0 & 0 & N_5 N_{11} & 0 & 0 & N_{11} N_6 & 0 \\
N_{12} N_2 & 0 & 0 & N_{12} N_3 & 0 & 0 & N_{12} N_4 & 0 & 0 & N_{12} N_5 & 0 & 0 & N_6 N_{12} & 0 & 0
\end{bmatrix} \quad (35)
$$

$$
\mathbf{W}_{22} = \begin{bmatrix}
0 & 0 & 0 & 0 & 0 & 0 & 0 & 0 & 0 & 0 & 0 & 0 & 0 & 0 & 0 \\
N_8^2 & 0 & 0 & N_8 N_9 & 0 & 0 & N_8 N_{10} & 0 & 0 & N_8 N_{11} & 0 & 0 & N_8 N_{12} & 0 & 0 \\
0 & N_9 N_8 & 0 & 0 & N_9 N_9 & 0 & 0 & N_9 N_{10} & 0 & 0 & N_9 N_{11} & 0 & 0 & N_9 N_{12} & 0 \\
0 & 0 & N_{10} N_8 & 0 & 0 & N_{10} N_9 & 0 & 0 & N_{10} N_{10} & 0 & 0 & N_{10} N_{11} & 0 & 0 & N_{10} N_{12} \\
0 & N_{11} N_8 & 0 & 0 & N_{11} N_9 & 0 & 0 & N_{11} N_{10} & 0 & 0 & N_{11} N_{11} & 0 & 0 & N_{11} N_{12} & 0 \\
N_8 N_{12} & 0 & 0 & N_{11} N_9 & 0 & 0 & N_{11} N_{10} & 0 & 0 & N_{11} N_{11} & 0 & 0 & N_{11} N_{12} & 0 & 0
\end{bmatrix} \quad (36)
$$

The vector $\mathbf{x}_n$ introduced in Eq. (14) is defined by

$$\mathbf{x}_n = \begin{bmatrix} x_{l,2}^{(yy)} & x_{l,2}^{(zy)} & x_{l,2}^{(\theta y)} & x_{l,3}^{(yz)} & x_{l,3}^{(zz)} & x_{l,3}^{(\theta z)} & x_{l,4}^{(y\theta)} & x_{l,4}^{(z\theta)} & x_{l,4}^{(\theta\theta)} & x_{l,5}^{(yz)} & \cdots \\ & x_{l,5}^{(zz)} & x_{l,5}^{(\theta z)} & x_{l,6}^{(yy)} & x_{l,6}^{(zy)} & x_{l,6}^{(\theta y)} & x_{l,8}^{(yy)} & x_{l,8}^{(zy)} & x_{l,8}^{(\theta y)} & x_{l,9}^{(yz)} & x_{l,9}^{(zz)} & \cdots \\ & & x_{l,9}^{(\theta z)} & x_{l,10}^{(y\theta)} & x_{l,10}^{(z\theta)} & x_{l,10}^{(\theta\theta)} & x_{l,11}^{(yz)} & x_{l,11}^{(zz)} & x_{l,11}^{(\theta z)} & x_{l,12}^{(yy)} & x_{l,12}^{(zy)} & x_{l,12}^{(\theta y)} \end{bmatrix} \tag{37}$$

Here, each element is given by the expression

$$x_{l,o}^{(nm)} = A_{l+3}^{(nm)} \left(v_o(t) - \frac{d_l^{(nm)} V}{B} \int_{-\infty}^{t} e^{\left(-\frac{d_l^{(nm)} V}{B}(t-\tau)\right)} v_o(\tau) d\tau \right) \tag{38}$$

The matrix **D** introduced in Eq. (17) is a diagonal matrix and defined by the following expression.

$$\mathbf{D} = \frac{V}{B} \begin{bmatrix} \mathbf{d}_1 & 0 & \cdots & 0 \\ 0 & \mathbf{d}_2 & \cdots & 0 \\ \vdots & \vdots & \ddots & \vdots \\ 0 & 0 & \cdots & \mathbf{d}_l \end{bmatrix} \tag{39}$$

The sub-matrix **d** is defined as

$$\mathbf{d}_l = diag\left[d_l^{(yy)} \quad d_l^{(zy)} \quad d_l^{(\theta y)} \quad d_l^{(yz)} \quad d_l^{(zz)} \quad d_l^{(\theta z)} \quad d_l^{(y\theta)} \quad d_l^{(z\theta)} \quad d_l^{(\theta\theta)} \quad d_l^{(yz)} \quad \cdots \right.$$
$$d_l^{(zz)} \quad d_l^{(\theta z)} \quad d_l^{(yy)} \quad d_l^{(zy)} \quad d_l^{(\theta y)} \quad d_l^{(yy)} \quad d_l^{(zy)} \quad d_l^{(\theta y)} \quad d_l^{(yz)} \quad d_l^{(zz)} \quad \cdots$$
$$\left. d_l^{(\theta z)} \quad d_l^{(y\theta)} \quad d_l^{(z\theta)} \quad d_l^{(\theta\theta)} \quad d_l^{(yz)} \quad d_l^{(zz)} \quad d_l^{(\theta z)} \quad d_l^{(yy)} \quad d_l^{(zy)} \quad d_l^{(\theta y)} \right] \tag{40}$$

The matrix **B** introduced in Eq. (17) is diagonal

$$\mathbf{B} = \begin{bmatrix} \mathbf{I}_1 & 0 & \cdots & 0 \\ 0 & \mathbf{I}_2 & \cdots & 0 \\ \vdots & \vdots & \ddots & \vdots \\ 0 & 0 & \cdots & \mathbf{I}_l \end{bmatrix} \tag{41}$$

$$\mathbf{I}_l = diag[1 \quad 1] \tag{42}$$

The matrix **A** introduced in Eq. (17) is defined as

$$\mathbf{A} = \begin{bmatrix} \begin{bmatrix} \mathbf{a}_1 & 0 \\ 0 & \mathbf{a}_1 \end{bmatrix} \\ \begin{bmatrix} \mathbf{a}_2 & 0 \\ 0 & \mathbf{a}_2 \end{bmatrix} \\ \vdots \\ \begin{bmatrix} \mathbf{a}_l & 0 \\ 0 & \mathbf{a}_l \end{bmatrix} \end{bmatrix} \tag{43}$$

Here the submatrices $\mathbf{a}_l$ are defined by

$$\mathbf{a}_l = \begin{bmatrix} 0 & A_{l+3}^{(yy)} & 0 & 0 & 0 & 0 \\ 0 & A_{l+3}^{(zy)} & 0 & 0 & 0 & 0 \\ 0 & A_{l+3}^{(\theta y)} & 0 & 0 & 0 & 0 \\ 0 & 0 & A_{l+3}^{(yz)} & 0 & 0 & 0 \\ 0 & 0 & A_{l+3}^{(zz)} & 0 & 0 & 0 \\ 0 & 0 & A_{l+3}^{(\theta z)} & 0 & 0 & 0 \\ 0 & 0 & 0 & A_{l+3}^{(y\theta)} & 0 & 0 \\ 0 & 0 & 0 & A_{l+3}^{(z\theta)} & 0 & 0 \\ 0 & 0 & 0 & A_{l+3}^{(\theta\theta)} & 0 & 0 \\ 0 & 0 & 0 & 0 & A_{l+3}^{(yz)} & 0 \\ 0 & 0 & 0 & 0 & A_{l+3}^{(zz)} & 0 \\ 0 & 0 & 0 & 0 & A_{l+3}^{(\theta z)} & 0 \\ 0 & 0 & 0 & 0 & 0 & A_{l+3}^{(yy)} \\ 0 & 0 & 0 & 0 & 0 & A_{l+3}^{(zy)} \\ 0 & 0 & 0 & 0 & 0 & A_{l+3}^{(\theta y)} \end{bmatrix} \qquad (44)$$

Ole Øiseth, Anders Rönnquist, Ragnar Sigbjörnsson

Effects of cross-spectral densities of atmospheric turbulence on the dynamic response of cable-supported bridges: A case study

Paper V

Is not included due to copyright

"Nonlinear Analysis of Reinforced Concrete Structures Exposed to Transient Loading",
K. V. Høiseth, 1992:15, ISBN 82-7119-364-3, ISSN 0802-3271.

"Finite Element Formulations and Solution Algorithms for Buckling and Collapse
Analysis of Thin Shells",
R. O. Bjærum, 1992:30, ISBN 82-7119-380-5, ISSN 0802-3271.

"Response Statistics of Nonlinear Dynamic Systems",
J. M. Johnsen, 1992:42, ISBN 82-7119-393-7, ISSN 0802-3271.

"Digital Models in Engineering. A Study on why and how engineers build and operate
digital models for decisison support",
J. Høyte, 1992:75, ISBN 82-7119-429-1, ISSN 0802-3271.

"Sparse Solution of Finite Element Equations",
A. C. Damhaug, 1992:76, ISBN 82-7119-430-5, ISSN 0802-3271.

"Some Aspects of Floating Ice Related to Sea Surface Operations in the Barents Sea",
S. Løset, 1992:95, ISBN 82-7119-452-6, ISSN 0802-3271.

"Modelling of Cyclic Plasticity with Application to Steel and Aluminium Structures",
O. S. Hopperstad, 1993:7, ISBN 82-7119-461-5, ISSN 0802-3271.

"The Free Formulation: Linear Theory and Extensions with Applications to Tetrahedral
Elements with Rotational Freedoms",
G. Skeie, 1993:17, ISBN 82-7119-472-0, ISSN 0802-3271.

"Høyfast betongs motstand mot piggdekkslitasje. Analyse av resultater fra prøving i
Veisliter'n",
T. Tveter, 1993:62, ISBN 82-7119-522-0, ISSN 0802-3271.

"A Nonlinear Finite Element Based on Free Formulation Theory for Analysis of
Sandwich Structures",
O. Aamlid, 1993:72, ISBN 82-7119-534-4, ISSN 0802-3271.

"The Effect of Curing Temperature and Silica Fume on Chloride Migration and Pore
Structure of High Strength Concrete",
C. J. Hauck, 1993:90, ISBN 82-7119-553-0, ISSN 0802-3271.

"Failure of Concrete under Compressive Strain Gradients",
G. Markeset, 1993:110, ISBN 82-7119-575-1, ISSN 0802-3271.

"An experimental study of internal tidal amphidromes in Vestfjorden",
J. H. Nilsen, 1994:39, ISBN 82-7119-640-5, ISSN 0802-3271.

"Structural analysis of oil wells with emphasis on conductor design",
H. Larsen, 1994:46, ISBN 82-7119-648-0, ISSN 0802-3271.

"Adaptive methods for non-linear finite element analysis of shell structures",
K. M. Okstad, 1994:66, ISBN 82-7119-670-7, ISSN 0802-3271.

"On constitutive modelling in nonlinear analysis of concrete structures",
O. Fyrileiv, 1994:115, ISBN 82-7119-725-8, ISSN 0802-3271.

"Fluctuating wind load and response of a line-like engineering structure with emphasis on motion-induced wind forces",
J. Bogunovic Jakobsen, 1995:62, ISBN 82-7119-809-2, ISSN 0802-3271.

"An experimental study of beam-columns subjected to combined torsion, bending and axial actions",
A. Aalberg, 1995:66, ISBN 82-7119-813-0, ISSN 0802-3271.

"Scaling and cracking in unsealed freeze/thaw testing of Portland cement and silica fume concretes",
S. Jacobsen, 1995:101, ISBN 82-7119-851-3, ISSN 0802-3271.

"Damping of water waves by submerged vegetation. A case study of laminaria hyperborea",
A. M. Dubi, 1995:108, ISBN 82-7119-859-9, ISSN 0802-3271.

"The dynamics of a slope current in the Barents Sea",
Sheng Li, 1995:109, ISBN 82-7119-860-2, ISSN 0802-3271.

"Modellering av delmaterialenes betydning for betongens konsistens",
Ernst Mørtsell, 1996:12, ISBN 82-7119-894-7, ISSN 0802-3271.

"Bending of thin-walled aluminium extrusions",
Birgit Søvik Opheim, 1996:60, ISBN 82-7119-947-1, ISSN 0802-3271.

"Material modelling of aluminium for crashworthiness analysis",
Torodd Berstad, 1996:89, ISBN 82-7119-980-3, ISSN 0802-3271.

"Estimation of structural parameters from response measurements on submerged floating tunnels",
Rolf Magne Larssen, 1996:119, ISBN 82-471-0014-2, ISSN 0802-3271.

"Numerical modelling of plain and reinforced concrete by damage mechanics",
Mario A. Polanco-Loria, 1997:20, ISBN 82-471-0049-5, ISSN 0802-3271.

"Nonlinear random vibrations - numerical analysis by path integration methods",
Vibeke Moe, 1997:26, ISBN 82-471-0056-8, ISSN 0802-3271.

 "Numerical prediction of vortex-induced vibration by the finite element method",
Joar Martin Dalheim, 1997:63, ISBN 82-471-0096-7, ISSN 0802-3271.

"Time domain calculations of buffeting response for wind sensitive structures",
Ketil Aas-Jakobsen, 1997:148, ISBN 82-471-0189-0, ISSN 0802-3271.

"A numerical study of flow about fixed and flexibly mounted circular cylinders",
Trond Stokka Meling, 1998:48, ISBN 82-471-0244-7, ISSN 0802-3271.

"Estimation of chloride penetration into concrete bridges in coastal areas",
Per Egil Steen, 1998:89, ISBN 82-471-0290-0, ISSN 0802-3271.

"Stress-resultant material models for reinforced concrete plates and shells",
Jan Arve Øverli, 1998:95, ISBN 82-471-0297-8, ISSN 0802-3271.

"Chloride binding in concrete. Effect of surrounding environment and concrete composition",
Claus Kenneth Larsen, 1998:101, ISBN 82-471-0337-0, ISSN 0802-3271.

"Rotational capacity of aluminium alloy beams",
Lars A. Moen, 1999:1, ISBN 82-471-0365-6, ISSN 0802-3271.

"Stretch Bending of Aluminium Extrusions",
Arild H. Clausen, 1999:29, ISBN 82-471-0396-6, ISSN 0802-3271.

"Aluminium and Steel Beams under Concentrated Loading",
Tore Tryland, 1999:30, ISBN 82-471-0397-4, ISSN 0802-3271.

"Engineering Models of Elastoplasticity and Fracture for Aluminium Alloys",
Odd-Geir Lademo, 1999:39, ISBN 82-471-0406-7, ISSN 0802-3271.

"Kapasitet og duktilitet av dybelforbindelser i trekonstruksjoner",
Jan Siem, 1999:46, ISBN 82-471-0414-8, ISSN 0802-3271.

"Etablering av distribuert ingeniørarbeid; Teknologiske og organisatoriske erfaringer fra en norsk ingeniørbedrift",
Lars Line, 1999:52, ISBN 82-471-0420-2, ISSN 0802-3271.

"Estimation of Earthquake-Induced Response",
Símon Ólafsson, 1999:73, ISBN 82-471-0443-1, ISSN 0802-3271.

"Coastal Concrete Bridges: Moisture State, Chloride Permeability and Aging Effects"
Ragnhild Holen Relling, 1999:74, ISBN 82-471-0445-8, ISSN 0802-3271.

"Capacity Assessment of Titanium Pipes Subjected to Bending and External Pressure",
Arve Bjørset, 1999:100, ISBN 82-471-0473-3, ISSN 0802-3271.

"Validation of Numerical Collapse Behaviour of Thin-Walled Corrugated Panels",
Håvar Ilstad, 1999:101, ISBN 82-471-0474-1, ISSN 0802-3271.

"Strength and Ductility of Welded Structures in Aluminium Alloys",
Miroslaw Matusiak, 1999:113, ISBN 82-471-0487-3, ISSN 0802-3271.

"Thermal Dilation and Autogenous Deformation as Driving Forces to Self-Induced
Stresses in High Performance Concrete",
Øyvind Bjøntegaard, 1999:121, ISBN 82-7984-002-8, ISSN 0802-3271.

"Some Aspects of Ski Base Sliding Friction and Ski Base Structure",
Dag Anders Moldestad, 1999:137, ISBN 82-7984-019-2, ISSN 0802-3271.

"Electrode reactions and corrosion resistance for steel in mortar and concrete",
Roy Antonsen, 2000:10, ISBN 82-7984-030-3, ISSN 0802-3271.

"Hydro-Physical Conditions in Kelp Forests and the Effect on Wave Damping and
Dune Erosion. A case study on Laminaria Hyperborea",
Stig Magnar Løvås, 2000:28, ISBN 82-7984-050-8, ISSN 0802-3271.

"Random Vibration and the Path Integral Method",
Christian Skaug, 2000:39, ISBN 82-7984-061-3, ISSN 0802-3271.

"Buckling and geometrical nonlinear beam-type analyses of timber structures",
Trond Even Eggen, 2000:56, ISBN 82-7984-081-8, ISSN 0802-3271.

"Structural Crashworthiness of Aluminium Foam-Based Components",
Arve Grønsund Hanssen, 2000:76, ISBN 82-7984-102-4, ISSN 0809-103X.

"Measurements and simulations of the consolidation in first-year sea ice ridges, and
some aspects of mechanical behaviour",
Knut V. Høyland, 2000:94, ISBN 82-7984-121-0, ISSN 0809-103X.

"Kinematics in Regular and Irregular Waves based on a Lagrangian Formulation",
Svein Helge Gjøsund, 2000-86, ISBN 82-7984-112-1, ISSN 0809-103X.

"Self-Induced Cracking Problems in Hardening Concrete Structures",
Daniela Bosnjak, 2000-121, ISBN 82-7984-151-2, ISSN 0809-103X.

"Ballistic Penetration and Perforation of Steel Plates",
Tore Børvik, 2000:124, ISBN 82-7984-154-7, ISSN 0809-103X.

"Freeze-Thaw resistance of Concrete. Effect of: Curing Conditions, Moisture Exchange
and Materials",
Terje Finnerup Rønning, 2001:14, ISBN 82-7984-165-2, ISSN 0809-103X

Structural behaviour of post tensioned concrete structures. Flat slab. Slabs on ground",
Steinar Trygstad, 2001:52, ISBN 82-471-5314-9, ISSN 0809-103X.

"Slipforming of Vertical Concrete Structures. Friction between concrete and slipform panel",
Kjell Tore Fosså, 2001:61, ISBN 82-471-5325-4, ISSN 0809-103X.

"Some numerical methods for the simulation of laminar and turbulent incompressible flows",
Jens Holmen, 2002:6, ISBN 82-471-5396-3, ISSN 0809-103X.

"Improved Fatigue Performance of Threaded Drillstring Connections by Cold Rolling",
Steinar Kristoffersen, 2002:11, ISBN: 82-421-5402-1, ISSN 0809-103X.

"Deformations in Concrete Cantilever Bridges: Observations and Theoretical Modelling",
Peter F. Takâcs, 2002:23, ISBN 82-471-5415-3, ISSN 0809-103X.

"Stiffened aluminium plates subjected to impact loading",
Hilde Giæver Hildrum, 2002:69, ISBN 82-471-5467-6, ISSN 0809-103X.

"Full- and model scale study of wind effects on a medium-rise building in a built up area",
Jónas Thór Snæbjørnsson, 2002:95, ISBN82-471-5495-1, ISSN 0809-103X.

"Evaluation of Concepts for Loading of Hydrocarbons in Ice-infested water",
Arnor Jensen, 2002:114, ISBN 82-417-5506-0, ISSN 0809-103X.

"Numerical and Physical Modelling of Oil Spreading in Broken Ice",
Janne K. Økland Gjøsteen, 2002:130, ISBN 82-471-5523-0, ISSN 0809-103X.

"Diagnosis and protection of corroding steel in concrete",
Franz Pruckner, 20002:140, ISBN 82-471-5555-4, ISSN 0809-103X.

"Tensile and Compressive Creep of Young Concrete: Testing and Modelling",
Dawood Atrushi, 2003:17, ISBN 82-471-5565-6, ISSN 0809-103X.

"Rheology of Particle Suspensions. Fresh Concrete, Mortar and Cement Paste with Various Types of Lignosulfonates",
Jon Elvar Wallevik, 2003:18, ISBN 82-471-5566-4, ISSN 0809-103X.

"Oblique Loading of Aluminium Crash Components",
Aase Reyes, 2003:15, ISBN 82-471-5562-1, ISSN 0809-103X.

"Utilization of Ethiopian Natural Pozzolans",
Surafel Ketema Desta, 2003:26, ISSN 82-471-5574-5, ISSN:0809-103X.

"Behaviour and strength prediction of reinforced concrete structures with discontinuity regions", Helge Brå, 2004:11, ISBN 82-471-6222-9, ISSN 1503-8181.

"High-strength steel plates subjected to projectile impact. An experimental and numerical study", Sumita Dey, 2004:38, ISBN 82-471-6282-2 (printed version), ISBN 82-471-6281-4 (electronic version), ISSN 1503-8181.

"Alkali-reactive and inert fillers in concrete. Rheology of fresh mixtures and expansive reactions."
Bård M. Pedersen, 2004:92, ISBN 82-471-6401-9 (printed version), ISBN 82-471-6400-0 (electronic version), ISSN 1503-8181.

"On the Shear Capacity of Steel Girders with Large Web Openings".
Nils Christian Hagen, 2005:9 ISBN 82-471-6878-2 (printed version), ISBN 82-471-6877-4 (electronic version), ISSN 1503-8181.

"Behaviour of aluminium extrusions subjected to axial loading".
Østen Jensen, 2005:7, ISBN 82-471-6873-1 (printed version), ISBN 82-471-6872-3 (electronic version), ISSN 1503-8181.

"Thermal Aspects of corrosion of Steel in Concrete".
Jan-Magnus Østvik, 2005:5, ISBN 82-471-6869-3 (printed version), ISBN 82-471-6868 (electronic version), ISSN 1503-8181.

"Mechanical and adaptive behaviour of bone in relation to hip replacement." A study of bone remodelling and bone grafting.
Sébastien Muller, 2005:34, ISBN 82-471-6933-9 (printed version), ISBN 82-471-6932-0 (electronic version), ISSN 1503-8181.

"Analysis of geometrical nonlinearities with applications to timber structures".
Lars Wollebæk, 2005:74, ISBN 82-471-7050-5 (printed version), ISBN 82-471-7019-1 (electronic version), ISSN 1503-8181.

"Pedestrian induced lateral vibrations of slender footbridges",
Anders Rönnquist, 2005:102, ISBN 82-471-7082-5 (printed version), ISBN 82-471-7081-7 (electronic version), ISSN 1503-8181.

"Initial Strength Development of Fly Ash and Limestone Blended Cements at Various Temperatures Predicted by Ultrasonic Pulse Velocity",
Tom Ivar Fredvik, 2005:112, ISBN 82-471-7105-8 (printed version), ISBN 82-471-7103-1 (electronic version), ISSN 1503-8181.

"Behaviour and modelling of thin-walled cast components",
Cato Dørum, 2005:128, ISBN 82-471-7140-6 (printed version), ISBN 82-471-7139-2 (electronic version), ISSN 1503-8181.

"Behaviour and modelling of selfpiercing riveted connections",
Raffaele Porcaro, 2005:165, ISBN 82-471-7219-4 (printed version), ISBN 82-471-7218-6 (electronic version), ISSN 1503-8181.

"Behaviour and Modelling og Aluminium Plates subjected to Compressive Load",
Lars Rønning, 2005:154, ISBN 82-471-7169-1 (printed version), ISBN 82-471-7195-3 (electronic version), ISSN 1503-8181.

"Bumper beam-longitudinal system subjected to offset impact loading",
Satyanarayana Kokkula, 2005:193, ISBN 82-471-7280-1 (printed version), ISBN 82-471-7279-8 (electronic version), ISSN 1503-8181.

"Control of Chloride Penetration into Concrete Structures at Early Age",
Guofei Liu, 2006:46, ISBN 82-471-7838-9 (printed version), ISBN 82-471-7837-0 (electronic version), ISSN 1503-8181.

"Modelling of Welded Thin-Walled Aluminium Structures",
Ting Wang, 2006:78, ISBN 82-471-7907-5 (printed version), ISBN 82-471-7906-7 (electronic version), ISSN 1503-8181.

"Time-variant reliability of dynamic systems by importance sampling and probabilistic analysis of ice loads",
Anna Ivanova Olsen, 2006:139, ISBN 82-471-8041-3 (printed version), ISBN 82-471-8040-5 (electronic version), ISSN 1503-8181.

"Fatigue life prediction of an aluminium alloy automotive component using finite element analysis of surface topography".
Sigmund Kyrre Ås, 2006:25, ISBN 82-471-7791-9 (printed version), ISBN 82-471-7791-9 (electronic version), ISSN 1503-8181.

"Constitutive models of elastoplasticity and fracture for aluminium alloys under strain path change",
Dasharatha Achani, 2006:76, ISBN 82-471-7903-2 (printed version), ISBN 82-471-7902-4 (electronic version), ISSN 1503-8181.

"Simulations of 2D dynamic brittle fracture by the Element-free Galerkin method and linear fracture mechanics",
Tommy Karlsson, 2006:125, ISBN 82-471-8011-1 (printed version), ISBN 82-471-8010-3 (electronic version), ISSN 1503-8181.

"Penetration and Perforation of Granite Targets by Hard Projectiles",
Chong Chiang Seah, 2006:188, ISBN 82-471-8150-9 (printed version), ISBN 82-471-8149-5 (electronic version), ISSN 1503-8181.

"Deformations, strain capacity and cracking of concrete in plastic and early hardening phases",
Tor Arne Hammer, 2007:234, ISBN 978-82-471-5191-4 (printed version), ISBN 978-82-471-5207-2 (electronic version), ISSN 1503-8181.

"Crashworthiness of dual-phase high-strength steel: Material and Component behaviour", Venkatapathi Tarigopula, 2007:230, ISBN 82-471-5076-4 (printed version), ISBN 82-471-5093-1 (electronic version), ISSN 1503-8181.

"Fibre reinforcement in load carrying concrete structures",
Åse Lyslo Døssland, 2008:50, ISBN 978-82-471-6910-0 (printed version), ISBN 978-82-471-6924-7 (electronic version), ISSN 1503-8181.

"Low-velocity penetration of aluminium plates",
Frode Grytten, 2008:46, ISBN 978-82-471-6826-4 (printed version), ISBN 978-82-471-6843-1 (electronic version), ISSN 1503-8181.

"Robustness studies of structures subjected to large deformations",
Ørjan Fyllingen, 2008:24, ISBN 978-82-471-6339-9 (printed version), ISBN 978-82-471-6342-9 (electronic version), ISSN 1503-8181.

"Constitutive modelling of morsellised bone",
Knut Birger Lunde, 2008:92, ISBN 978-82-471-7829-4 (printed version), ISBN 978-82-471-7832-4 (electronic version), ISSN 1503-8181.

"Experimental Investigations of Wind Loading on a Suspension Bridge Girder",
Bjørn Isaksen, 2008:131, ISBN 978-82-471-8656-5 (printed version), ISBN 978-82-471-8673-2 (electronic version), ISSN 1503-8181.

"Cracking Risk of Concrete Structures in The Hardening Phase",
Guomin Ji, 2008:198, ISBN 978-82-471-1079-9 (printed version), ISBN 978-82-471-1080-5 (electronic version), ISSN 1503-8181.

"Modelling and numerical analysis of the porcine and human mitral apparatus",
Victorien Emile Prot, 2008:249, ISBN 978-82-471-1192-5 (printed version), ISBN 978-82-471-1193-2 (electronic version), ISSN 1503-8181.

"Strength analysis of net structures",
Heidi Moe, 2009:48, ISBN 978-82-471-1468-1 (printed version), ISBN 978-82-471-1469-8 (electronic version), ISSN1503-8181.

"Numerical analysis of ductile fracture in surface cracked shells",
Espen Berg, 2009:80, ISBN 978-82-471-1537-4 (printed version), ISBN 978-82-471-1538-1 (electronic version), ISSN 1503-8181.

"Subject specific finite element analysis of bone – for evaluation of the healing of a leg lengthening and evaluation of femoral stem design",
Sune Hansborg Pettersen, 2009:99, ISBN 978-82-471-1579-4 (printed version), ISBN 978-82-471-1580-0 (electronic version), ISSN 1503-8181.

"Evaluation of fracture parameters for notched multi-layered structures",
Lingyun Shang, 2009:137, ISBN 978-82-471-1662-3 (printed version), ISBN 978-82-471-1663-0 (electronic version), ISSN 1503-8181.

"Modelling of Dynamic Material Behaviour and Fracture of Aluminium Alloys for Structural Applications"
Yan Chen, 2009:69, ISBN 978-82-471-1515-2 (printed version), ISBN 978-82 471-1516-9 (electronic version), ISSN 1503-8181.

"Nanomechanics of polymer and composite particles"
Jianying He 2009:213, ISBN 978-82-471-1828-3 (printed version), ISBN 978-82-471-1829-0 (electronic version), ISSN 1503-8181.

"Mechanical properties of clear wood from Norway spruce"
Kristian Berbom Dahl 2009:250, ISBN 978-82-471-1911-2 (printed version) ISBN 978-82-471-1912-9 (electronic version), ISSN 1503-8181.

"Modeling of the degradation of TiB_2 mechanical properties by residual stresses and liquid Al penetration along grain boundaries"
Micol Pezzotta 2009:254, ISBN 978-82-471-1923-5 (printed version) ISBN 978-82-471-1924-2 (electronic version) ISSN 1503-8181.

"Effect of welding residual stress on fracture"
Xiabo Ren 2010:77, ISBN 978-82-471-2115-3 (printed version) ISBN 978-82-471-2116-0 (electronic version), ISSN 1503-8181.

"Pan-based carbon fiber as anode material in cathodic protection system for concrete structures"
Mahdi Chini 2010:122, ISBN 978-82-471-2210-5 (printed version) ISBN 978-82-471-2213-6 (electronic version), ISSN 1503-8181.

"Structural Behaviour of deteriorated and retrofitted concrete structures" Irina Vasililjeva Sæther 2010:171, ISBN 978-82-471-2315-7 (printed version) ISBN 978-82-471-2316-4 (electronic version) ISSN 1503-8181.

"Prediction of local snow loads on roofs" Vivian Meløysund 2010:247, ISBN 978-82-471-2490-1 (printed version) ISBN 978-82-471-2491-8 (electronic version) ISSN 1503-8181.

"Behaviour and modelling of polymers for crash applications" Virgile Delhaye 2010:251, ISBN 978-82-471-2501-4 (printed version) ISBN 978-82-471-2502-1 (electronic version) ISSN 1503-8181.

"Blended cement with reduced CO_2 emission – Utilizing the Fly Ash-Limestone Synergy", Klaartje De Weerdt 2011:32, ISBN 978-82-471-2584-7 (printed version) ISBN 978-82-471-2584-4 (electronic version) ISSN 1503-8181.

"Chloride induced reinforcement corrosion in concrete" Concept of critical chloride content – methods and mechanisms. Ueli Angst 2011:113, ISBN 978-82-471-2769-9 (printed version) ISBN 978-82-471-2763-6 (electronic version) ISSN 1503-8181.

"A thermo-electric-Mechanical study of the carbon anode and contact interface for Energy savings in the production of aluminium". Dag Herman Andersen 2011:157, ISBN 978-82-471-2859-6 (printed version) ISBN 978-82-471-2860-2 (electronic version) ISSN 1503-8181.

"Structural Capacity of Anchorage Ties in Masonry Veneer Walls Subjected toEarthquake". The implications of Eurocode 8 and Eurocode 6 on a typical Norwegain veneer wall. Ahmed Mohamed Yousry Hamed 2011:181, ISBN 978-82-471-2911-1 (printed version) ISBN 978-82-471-2912-8 (electronic ver.) ISSN 1503-8181.